NASA Technical Paper 3202

1992

Survey and Analysis of Research on Supersonic Drag-Due-to-Lift Minimization With Recommendations for Wing Design

Harry W. Carlson
Lockheed Engineering & Sciences Company
Hampton, Virginia

Michael J. Mann
Langley Research Center
Hampton, Virginia

National Aeronautics and Space Administration

Office of Management

Scientific and Technical Information Program

Contents

Abstract

A survey of research on drag-due-to-lift minimization at supersonic speeds, including a study of the effectiveness of current design and analysis methods, has been conducted. The results show that a linearized theory analysis with estimated attainable thrust and vortex force effects can predict with reasonable accuracy the lifting efficiency of flat wings. Significantly better wing performance can be achieved through the use of twist and camber. Although linearized theory methods tend to overestimate the amount of twist and camber required for a given application and provide an overly optimistic performance prediction, these deficiencies can be overcome by implementation of recently developed empirical corrections. Numerous examples of the correlation of experiment and theory are presented to demonstrate the applicability and limitations of linearized theory methods with and without empirical corrections. The use of an Euler code for the estimation of aerodynamic characteristics of a twisted and cambered wing and its application to design by iteration are discussed.

Introduction

At supersonic speeds, airplane aerodynamic efficiency, as measured by the lift-drag ratio, cannot approach subsonic levels because of the appearance of wave drag. Theoretical studies such as references 1 and 2, however, have shown the potential for relatively high levels of efficiency provided wing leading edges are swept behind the Mach line and a substantial portion of the theoretical leading-edge thrust is realized. The indicated lift-drag values, if achievable, are high enough so that the airplane range, which is related to the product of lift-drag ratio and speed, can be competitive with subsonic values. Unfortunately, the attainment of any substantial portion of the theoretical leading-edge thrust has not been demonstrated in practice. Other theoretical and experimental studies, for example references 3 to 5, have pointed out that wing twist and camber may be employed as an alternate means of achieving relatively high levels of efficiency. Theoretically, a properly twisted and cambered wing can have performance equal to or better than a wing with full theoretical leading-edge thrust. In effect, a distributed thrust due to lift loadings acting over much of the wing in the region of the leading edge is substituted for the concentrated leading-edge force. Experimental studies of this approach have shown more encouraging results than studies confined to wings without twist and camber. Even with this approach, however, the attainable performance levels fall well below the theoretical potential.

This paper reviews and analyzes a variety of experimental investigations providing measurements of wing lifting efficiency at supersonic speeds. Some of these studies (refs. 6 and 7) were designed to evaluate attainable levels of leading-edge thrust. Others (refs. 8 to 17) were devoted to evaluation of the benefits of wing twist and camber. The analysis is performed with the aid of the modified linearized theory computer code of reference 18. This code provides for both the design and analysis of twisted and cambered wings at supersonic speeds. It is used primarily in the analysis mode for this study. The code is well suited to this purpose because it provides for estimates of attainable thrust and separated leading-edge vortex forces as well as the forces due to the basic pressure loadings.

The extensive correlations of theory and experiment given in this paper are intended to provide an assessment of the applicability and limitations of theoretical design and analysis methods. A prime goal of the study is the establishment of guidelines for application to the design methods which take into account and compensate for shortcomings of the theory so as to more closely define optimum designs and more accurately estimate achievable performance.

The paper provides first a discussion of theoretical wing-design and analysis concepts and their use in the computer code. This is followed by comparisons of theoretical and experimental results for flat wings (wings without twist or camber) and for wings with twist and camber. Results from these comparisons are then used in derivation of an empirical method for better employment of linearized theory in twisted and cambered wing design and more accurate estimation of achievable performance. The reader interested in application of the empirical method and not its justification may want to proceed directly to the

section "Empirical Design Guidelines." Other design considerations applicable to complete airplane configurations are also discussed. Finally, one example of the application of an Euler code method to twisted and cambered wing analysis is given. Brian E. McGrath of the Lockheed Engineering & Sciences Company, Hampton, Virginia, and Kenneth M. Jones of the Langley Research Center provided an understanding of the Euler code computational process, recommended the appropriate solution strategy, and in general oversaw this part of the design study.

Symbols

AR	aspect ratio, b^2/S
b	span, in.
C_A	axial- or chord-force coefficient
C_D	drag coefficient
ΔC_D	drag coefficient due to lift, $C_D - C_{D,0}$
$C_{D,0}$	drag coefficient at $\alpha = 0°$ for configuration with no camber or twist
C_L	lift coefficient
$C_{L,\mathrm{des}}$	design lift coefficient
C_{L_α}	theoretical lift-curve slope at $\alpha = 0°$, per deg
C_m	pitching-moment coefficient
$C_{m,\mathrm{des}}$	design pitching-moment coefficient
C_N	normal-force coefficient
C_p	pressure coefficient
ΔC_p	lifting pressure coefficient
c	local chord, in.
$\bar{c}$	mean aerodynamic chord, in.
c_A	section axial-force coefficient
c_{le}	streamwise chord length for leading-edge design area
c_N	section normal-force coefficient
c_r	wing root chord, chord at $y = 0$, in.
c_t	section leading-edge thrust coefficient
$c_{t,a}$	section attainable leading-edge thrust coefficient
c_{te}	streamwise chord length for trailing-edge design area
$c_{t,t}$	section theoretical leading-edge thrust coefficient
K_D	design lift-coefficient factor, $\frac{(C_{L,\mathrm{des,opt}})_{\mathrm{exp}}}{(C_{L,\mathrm{des,opt}})_{\mathrm{th}}}$
K_S	suction parameter factor, $\frac{(S_{s,\mathrm{max}})_{\mathrm{exp}}}{(S_{s,\mathrm{max}})_{\mathrm{th}}}$
k	arbitrary constant used in definition of pressure distribution
k_n	arrow wing notch ratio (see fig. 1)
L/D	lift-drag ratio
l	overall wing length
M	Mach number
R	Reynolds number based on mean aerodynamic chord
r	leading-edge radius, in.
S	reference area, in^2
S_s	suction parameter, $\frac{C_L \tan(C_L/C_{L_\alpha}) - \Delta C_D}{C_L \tan(C_L/C_{L_\alpha}) - C_L^2/(\pi \mathrm{AR})}$
t	section thickness, in.
x, y, z	Cartesian coordinates, positive aft, right, and up, respectively
x'	distance in x direction measured from leading edge, in.
x^*	wing shear parameter, distance behind wing apex at which camber surface ordinates are set to zero, in. (see fig. 30)
Y_0	limiting value of the singularity parameter, $\Delta C_p \sqrt{x'}$, at $x' = 0$
α	angle of attack, deg
α_{des}	angle of attack corresponding to design lift coefficient
α_{zt}	angle of attack for zero thrust
α_0	angle of attack corresponding to zero lift
$\Delta\alpha_{\mathrm{ft}}$	range of angle of attack for full leading-edge thrust
β	$= \sqrt{M^2 - 1}$
γ	ratio of specific heats, 1.4
η	$= x'/c$ for $(t/c)_{\mathrm{max}}$
Λ_{le}	wing leading-edge sweep angle

Λ_{te}	wing trailing-edge sweep angle

Subscripts:

ave	average
c	cambered wing
exp	experiment
f	flat wing
fc	flat wing-cambered wing interference
ft	full thrust
le	leading edge
max	maximum
opt	optimum
th	theoretical
te	trailing edge
u	upper surface
v	vortex
vac	vacuum

Theoretical Considerations

This review of drag-due-to-lift reduction technology for supersonic flight encompasses an examination of a variety of experimental test programs. For consistency in the comparisons of theoretical and measured lifting efficiencies, one computer code for the estimation of wing aerodynamic characteristics is applied in all cases. That code, designated WINGDES2 which is described in reference 18, provides an estimate of attainable leading-edge thrust and separated leading-edge vortex forces as well as the forces associated with the basic attached flow pressure distributions. The code, which is further described in the appendix, provides both design and analysis capabilities. In this paper, the code is used primarily in the analysis mode. Similar results would be expected from the code described in references 19 and 20, which has been updated to include thrust and vortex forces and is part of the Boeing complex of supersonic design and analysis codes (refs. 21 to 24).

Theoretical Drag Breakdown

Sketch A depicts a typical supersonic lift-drag polar curve and shows the main contributions to the drag. For efficient flight, at a lift coefficient which maximizes the lift-drag ratio, the drag due to lift is about half the total. This is the contribution which is estimated by the WINGDES2 code. The code evaluates the drag by an integration of pressures acting on the lifting surface. However, linearized theory concepts also allow a separation of the drag due to lift

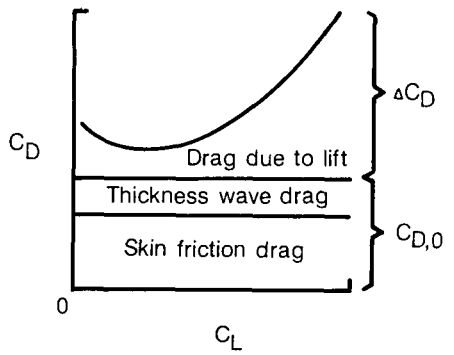

Sketch A

into two fundamental components: vortex drag associated with the spanwise distribution of the lifting force and the resultant downwash behind the wing and wave drag due to lift, which arises only for supersonic flow, associated with the longitudinal distribution of lift and the resultant disturbance waves propagating into the surrounding air. This separation of drag contributions can be of value in analysis of wing performance and in the search for optimum designs.

The combination of thickness wave drag and skin friction drag ($C_{D,0}$) represents the drag of a configuration without twist and camber at zero lift and zero angle of attack. Because the purpose of this study is the evaluation of lifting efficiency, an experimental evaluation of $C_{D,0}$ is used when available rather than a theoretical estimate. For the few test programs which did not provide data for comparable configurations without twist and camber, $C_{D,0}$ is estimated with methods described in references 21 to 25.

The WINGDES2 computer code of reference 18 actually works with forces perpendicular and tangent to a wing reference plane rather than lift and drag directly. The relationship between these forces is depicted in sketch B. The use of C_N and C_A rather than C_L and C_D permits a more elementary separation of the contributions to wing forces. As shown in subsequent analysis, curves of C_A versus α are

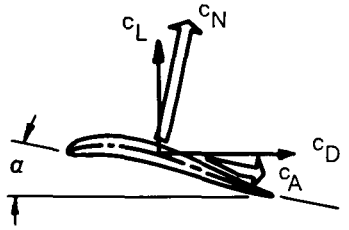

Sketch B

particularly useful in comparisons of twisted and cambered wing performance with that of the corresponding flat wing.

Perturbation Velocities and Pressure Distribution

The WINGDES2 code evaluation of lifting surface perturbation velocities and pressure distributions follows procedures originally developed in reference 19. The techniques for application of linearized theory vortex lattice solutions in reference 19 were later modified as described in reference 20 to provide a better method, "aft element sensing," for controlling pressure distribution oscillation tendencies. A further modification, described in reference 18, provided an additional smoothing of pressure distributions, which is especially valuable for very highly swept wing leading edges.

Basic Force Integration

The force integration techniques applied to the basic pressure loadings were originally developed for subsonic speeds and are described in some detail in reference 26. Their adaptation to supersonic speeds for use in the WINGDES2 code is not adequately described in reference 18. Because of that omission and because some of the concepts involved are vital to an understanding of the code features, a brief description of the process is given.

Force characteristics for lifting wings could be determined from individual solutions for each of a series of wing angles of attack. The superposition characteristics of linearized theory, however, provide for a more economical process that actually can give a more exact numerical evaluation of the theory. In the evaluation of basic wing forces due to pressure loadings on the wing surfaces, contributions from a cambered wing with its reference plane at zero angle of attack are combined with contributions from a flat wing surface at angle of attack. This separation allows the selection of integration techniques appropriate to each of the two different types of pressure distributions.

Typical contributions to normal force as evaluated by the lifting surface solutions of reference 18 are shown in sketch C. The basic loading for a flat wing section at an angle of attack of 1°, with a typical leading-edge singularity associated with a subsonic leading edge, is shown at the top of the sketch. Loadings at other angles of attack are assumed to be proportional to the sine of the angle. The sine of the angle rather than the angle itself is used because the theory does not distinguish between the

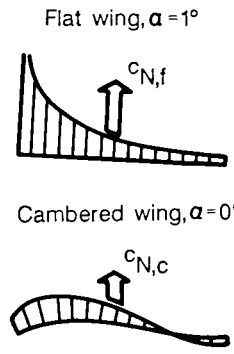

Sketch C

two ($\sin\alpha = \alpha$ in radians) and because experience has shown that the sine variation agrees better with measured results. The basic loading for a camber surface which displays no leading-edge singularity is shown at the bottom of the sketch. The total lifting pressure coefficient at angle of attack is

$$\Delta C_p = \Delta C_{p,c} + \frac{\sin\alpha}{\sin 1^\circ}\Delta C_{p,f}$$

Section normal-force coefficients representing these two contributions are found by numerical solutions of the following integral equations:

$$c_{N,f} = \frac{1}{c_{\text{ave}}}\int_0^c \Delta C_{p,f}\, dx'$$

$$c_{N,c} = \frac{1}{c_{\text{ave}}}\int_0^c \Delta C_{p,c}\, dx'$$

Special integration techniques designed to account for the leading-edge singularity are used in the calculation of the flat wing contribution to normal force illustrated at the top of sketch C. For any segment of the wing chord, the flat wing pressure distribution is assumed to have the form

$$\Delta C_{p,f} = k \qquad (M > 1, \beta\cot\Lambda_{\text{le}} \geq 1)$$

$$\Delta C_{p,f} = \frac{k}{\sqrt{x'}} \qquad (M > 1, \beta\cot\Lambda_{\text{le}} < 1)$$

$$\Delta C_{p,f} = k\sqrt{\frac{c}{x'} - 1} \qquad (M < 1)$$

with the particular value of the arbitrary constant k defined by the value of $\Delta C_{p,f}$ at a solution control point being applicable only to that segment. At subsonic speeds and at supersonic speeds for wings with subsonic leading edges, the pressure distribution near the leading edge tends to vary inversely with $\sqrt{x'}$. The product $\Delta C_{p,f}\sqrt{x'}$ which has a limiting

value at the leading edge ($x' = 0$) is a measure of the singularity strength.

The cambered wing section loading shown at the bottom of sketch C is smooth with no evidence of a singularity. Departures from this idealized condition which generally arise are treated later. For any segment of the wing chord, the cambered wing pressure distribution without singularities is assumed to have the form

$$\Delta C_{p,c} = k \qquad (M > 1, \beta \cot \Lambda_{le} \geq 1)$$

$$\Delta C_{p,c} = k\sqrt{x'} \qquad (M > 1, \beta \cot \Lambda_{le} < 1)$$

$$\Delta C_{p,c} = k\sqrt{x'(c - x')} \qquad (M < 1)$$

with the particular value of k being applicable only to that segment. Contributions from integrations of the cambered wing and the flat wing loading with the variation in $\sin \alpha$ taken into account are added to obtain the section normal force for the cambered wing at angle of attack:

$$c_N = c_{N,c} + \frac{\sin \alpha}{\sin 1^\circ} c_{N,f}$$

Typical contributions to axial or chord force are shown in sketch D. The loading of a cambered wing section at zero angle of attack, again in the absence of singularities, is shown at the top of the sketch. The same form of pressure distribution as previously described is allowed to act on the camber surface slopes in the integration to obtain the cambered wing section axial- or chord-force coefficient $c_{A,c}$ at $\alpha = 0^\circ$:

$$c_{A,c} = \frac{-1}{c_{ave}} \int_0^c \Delta C_{p,c} \left(\frac{dz}{dx} \right) dx'$$

The flat wing generates no axial force since by definition its surface is coincident with the reference plane. The flat wing loading, however, generates an interference loading on the surface of the cambered wing

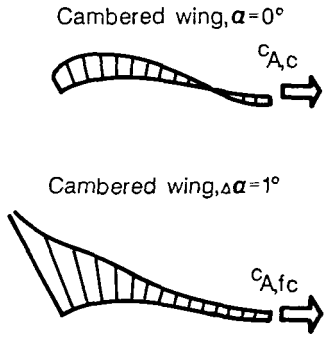

Sketch D

which is of critical importance in estimating the cambered wing aerodynamic performance at angle of attack. As shown in the bottom of sketch D, an interference term, $c_{A,fc}$, is found by performing an integration in which the flat wing pressure distribution of $\alpha = 1^\circ$ is allowed to act on the cambered wing surface slopes:

$$c_{A,fc} = \frac{-1}{c_{ave}} \int_0^c \Delta C_{p,f} \left(\frac{dz}{dx} \right) dx'$$

The section axial-force coefficient for the cambered wing at angle of attack (excluding friction and thickness contributions) given by

$$c_A = c_{A,c} + \frac{\sin \alpha}{\sin 1^\circ} c_{A,fc}$$

is a linear function of $\sin \alpha$.

Leading-Edge Thrust

The basic lifting surface pressure distributions and resultant forces previously discussed do not include a theoretical leading-edge thrust force which arises from the velocities generated by a flow around the leading edge from a stagnation point on the wing lower surface. This force, which at supersonic speeds arises only for wings with subsonic leading edges ($\beta \cot \Lambda_{le} < 1$), is calculated by methods described in reference 27 which were later modified for use in reference 18. The magnitude of the force is directly dependent on the previously mentioned leading-edge singularity strength parameter $\Delta C_p \sqrt{x'}$. Wing performance is critically dependent on the amount of this theoretical force which can actually be realized. In reference 28, a study of the factors which place limits on theoretical thrust was made, and a semi-empirical method for estimation of attainable thrust was developed. This estimation technique is employed in the WINGDES2 code.

For a flat wing, the full theoretical thrust at a given span station is a function of the square of the angle of attack as shown in sketch E. The attainable thrust, however, has a more complex dependence on angle of attack. Up to the critical angle, designated $\Delta\alpha_{ft}$, attainable thrust equal to the full theoretical thrust is predicted. Beyond that point, although the attainable thrust increases, it becomes a smaller and smaller fraction of the theoretical thrust. Actually, at some angle of attack the attainable thrust will fail to increase and could even drop precipitously, an event which the attainable thrust method does not predict.

A typical spanwise variation of both theoretical and attainable thrusts for a flat wing is shown in sketch F. For an arrow wing with subsonic leading edges ($\beta \cot \Lambda_{le} < 1$) and supersonic trailing edges

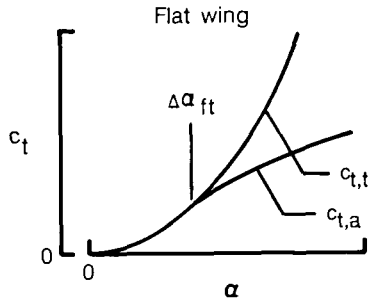

Sketch E

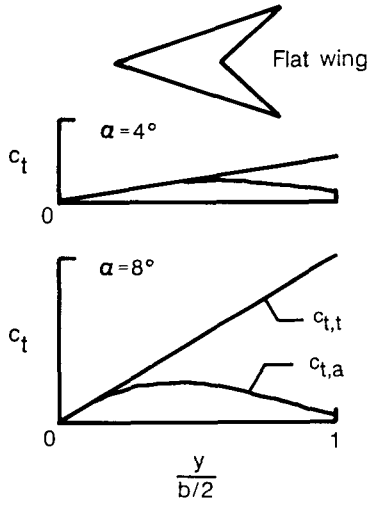

Sketch F

($\beta \cot \Lambda_{te} > 1$), the theoretical thrust increases linearly with increasing span position. The attainable thrust estimate, however, can display a rather arbitrary variation with span position. Notice that for an angle of attack of 4°, full thrust is estimated to be achievable for about half of the semispan. For an angle of attack of 8°, full thrust is estimated to be achievable for about 15 percent of the semispan. Thus at the 15-percent station, the range of full thrust is about 8°, but at the mid semispan station this range is only about 4°. The decrease of the range of full thrust with increasing span station is due to the more rapid growth of theoretical leading-edge thrust with angle of attack and the earlier encounter of limiting pressures. Stated another way, the rapid growth of upwash in the spanwise direction makes it more difficult for the flow to remain attached and can result in the onset of flow separation and the failure to achieve theoretical thrust at smaller angles of attack.

The spanwise variation of this range of full thrust shown in sketch G is an important consideration in the evaluation of flat wing performance and, as is

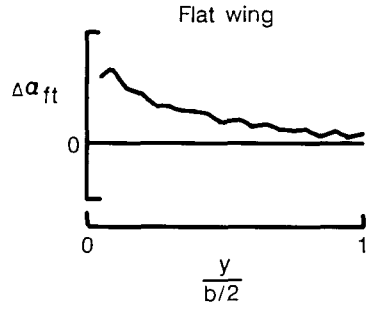

Sketch G

shown later, in the design and evaluation of twisted and cambered wings.

For a twisted and cambered wing, zero thrust will not occur at an angle of attack of 0° but at an angle of attack which produces an alignment of the local upwash with the local wing surface. In order to estimate theoretical and attainable leading-edge thrust for twisted and cambered wings, it is first necessary to define that angle. Sketches H and I are helpful in a discussion of the evaluation of the angle of attack for zero thrust. Sketch H shows code results that might be found for one spanwise station of a representative cambered wing at three different angles of attack. With the wing reference plane at an angle of attack of 0°, a negative leading-edge pressure singularity is shown. At some larger angle of attack this singularity will go through 0 and at even larger angles will become a positive singularity. For the example shown here the singularity and the associated leading-edge thrust vanish at $\alpha = 2°$. This important condition can play a significant role in both wing analysis and wing design. The angle of zero thrust, identified as α_{zt}, could be determined by iteration coupled with visual inspection. However, a more direct method that is adaptable to computer implementation is available.

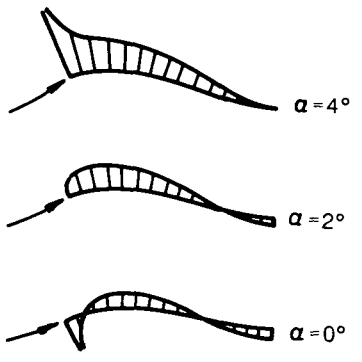

Sketch H

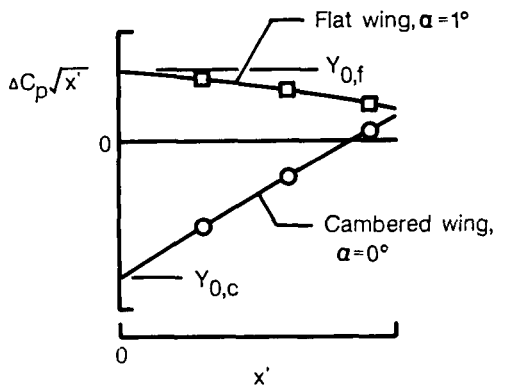

Sketch I

A fully automated method used in the computer code of reference 18 for definition of the angle of zero thrust may be explained with the aid of sketch I. Here the leading-edge singularity strength parameter $\Delta C_p\sqrt{x'}$ from code data for both the flat wing and the cambered wing (with a singularity) is shown as a function of the distance behind the wing leading edge. For a flat wing, the pressure behind the singularity drops off at a rate such that near the leading edge, the singularity parameter tends to be constant. A wing with pure camber (no singularity at all) would have a singularity parameter that approaches 0 as x' approaches 0. Generally, however, the cambered wing singularity parameter at $x' = 0$ is not 0 but has a value designated as $Y_{0,c}$. The cambered wing singularity parameter could, however, be made to equal 0 by a change in angle of attack, which produces a compensating leading-edge singularity increment. The required angle, the angle of attack for zero thrust, may be expressed simply as

$$\alpha_{zt} = -\frac{Y_{0,c}}{Y_{0,f}}$$

because this represents the number of 1° increments needed to produce a singularity parameter of 0.

The angle of attack for zero thrust is not a single value that may be assigned to a given wing but generally varies with the wing spanwise station. Therefore, a redefinition of the wing reference plane to simplify force calculations is not practical. Instead, the local angle of attack for zero thrust is used in a separation of cambered wing loadings into two components, one with a singularity and one without. This separation allows the previously described integration techniques to be applied to each of the components for a better evaluation of $C_{N,c}$ and $C_{A,c}$ when a residual singularity is present.

For twisted and cambered wings, theoretical and attainable leading-edge thrusts are assumed to act equally on either side of the previously discussed angle of zero thrust. This is similar to the assumption that upper and lower surface pressure distribution increments for a twisted and cambered wing due to a change in angle of attack are of equal magnitude but opposite sign. A typical variation of section thrust coefficient with angle of attack for a twisted and cambered wing is shown in sketch J. This variation with α is the same as that shown for a flat wing in sketch E, except that it is centered on α_{zt} instead of $\alpha = 0°$. Actually there is one other difference between the leading-edge thrust characteristics of flat and twisted and cambered wings. As shown in sketch K the force acts tangent to the wing lifting surface of the leading edge not tangent to the wing reference plane and thus introduces both incremental axial and normal forces.

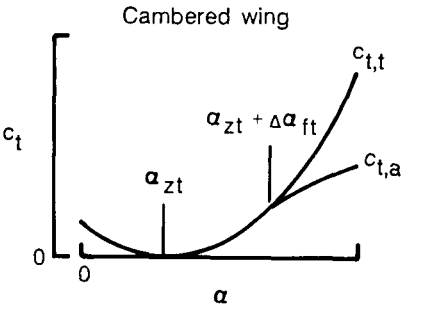

Sketch J

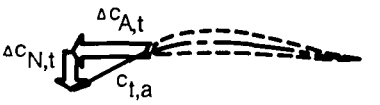

Sketch K

Because, for a twisted and cambered wing, α_{zt} varies with span position, for example as illustrated in sketch L, the range of full thrust could take on the appearance illustrated in sketch M. If the wing operating angle of attack is less than the upper curve $(\alpha_{zt} + \Delta\alpha_{ft})$ and is greater than the lower curve $(\alpha_{zt} - \Delta\alpha_{ft})$ for the entire wingspan, full theoretical thrust is estimated to be achievable. Failure to achieve full theoretical thrust, indicated by a range of full thrust that does not include the wing angle of attack, also implies the onset of flow separation which can lead to performance penalties not covered by the theory even with the inclusion of attainable thrust and vortex force estimates. Information such as that illustrated in sketch M will be of value in the design and analysis of twisted and cambered wings.

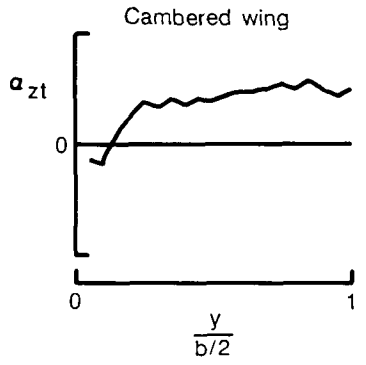

Sketch L

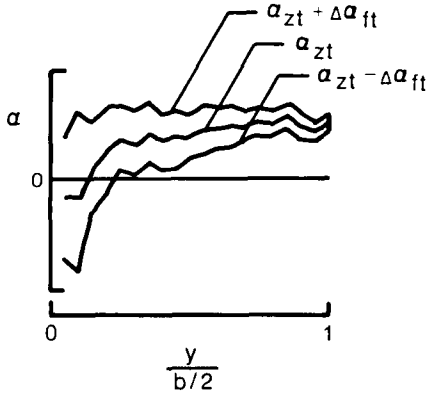

Sketch M

Design With Attainable Thrust Considerations

The design process employed in the WINGDES2 code as described in reference 18 is generally initiated by input of a flat lifting surface (the code default). Analysis of this initial surface provides values of the spanwise variation of $\Delta\alpha_{ft}$ and an initial estimate of the angle of attack at which the design lift is developed. For this flat surface, the angle of attack for zero thrust α_{zt} is 0° at all span stations. For wings with subsonic leading edges, good performance depends on the development of as large a portion of the theoretical flat wing leading-edge thrust as circumstances allow and on the substitution of a distributed thrust for the theoretical thrust that cannot be realized. This distribution of thrust is accomplished by creation of a camber surface with an α_{zt} spanwise distribution which with the addition of the $\Delta\alpha_{ft}$ distribution matches the design angle of attack α_{des}.

Tailoring of the wing shape in the leading-edge region is accomplished by use of special leading-edge surfaces (described in ref. 18) designed to have their largest effect at the leading edge itself. A series of leading-edge surfaces is provided, each of which is centered on a particular computational span station in order to provide the necessary adjustment to α_{zt}. The change in the weighting factor for each surface is proportional to the quantity $\alpha_{des} - (\alpha_{zt} + \Delta\alpha_{ft})$ at the span station for that surface.

These changes in the wing shape change the wing lift and pitching moment. It is therefore necessary to use additional general camber surfaces which affect the entire wing to restore the wing lift and pitching-moment coefficients to their design values. The method of Lagrange multipliers is used to determine the surface shape which provides the required lift and pitching-moment increments with a minimum axial force. The new wing shape has a new design angle of attack and a new spanwise distribution of zero thrust angle. This new information necessitates a redesign of the leading-edge shape and a subsequent redefinition of the general surfaces to again restore lift and pitching-moment coefficients to their proper values. The solution therefore requires iteration. A more complete description of the design method is in reference 18.

Attainment of some portion of the flat wing theoretical leading-edge thrust reduces the need for complete alignment of the leading edge with the local oncoming flow and results in a wing with a milder camber surface. The benefits of such a design are better performance at off-design conditions and a reduction of the nonlinear penalties discussed later.

Vortex Forces

For wings with sharp leading edges, for which no leading-edge thrust is assumed to develop, Polhamus (ref. 29) established a relationship between the normal force induced by separated vortex flow and the theoretical leading-edge thrust. According to the Polhamus suction analogy, the suction vector $c_t/\cos\Lambda_{le}$ is assumed to rotate to a position normal to the wing surface, where it affects the normal force rather than the chord force. Because the WINGDES2 code treats a partially developed leading-edge thrust, it is logical to consider a partial development of the vortex force in which

$$c_{N,v} = \frac{c_{t,t} - c_{t,a}}{\cos\Lambda_{le}}$$

The WINGDES2 code provides three options for the estimation of the magnitude and distribution of forces generated by detached leading-edge vortices, which are assumed to form when there is a failure to achieve full theoretical leading-edge thrust. These options are outlined in the appendix.

Code Application to Arrow Wings

The linearized theory computer code WINGDES2 was used in the preparation of figure 1, which illustrates the effect of wing leading-edge sweep and wing planform on drag due to lift. The parameters used allow the results to be applicable to a continuous spectrum of Mach number and sweep-angle combinations. Similar plots derived from closed form linearized theory expressions have appeared in various published documents including references 1, 2, and 5.

Figure 1(a) shows curves for a flat wing without leading-edge thrust or vortex force having a typical section flow pattern as shown in sketch N. The very high drag values for small values of the $\beta \cot \Lambda_{le}$ parameter result from the small wingspan and the resultant increase of vortex drag. These drag levels are somewhat unrealistic because some amount of leading-edge thrust and/or vortex force would be expected. Generally for thin wings, the vortex force arising from the separated leading-edge flow depicted in sketch O would be realized and would reduce to some degree the required angle of attack and high levels of drag associated with subsonic leading edges ($\beta \cot \Lambda_{le} < 1$). Drag levels, however, would still be too high to make subsonic leading edges attractive. In spite of this element of pessimism, the drag of a flat wing without leading-edge thrust or vortex forces provides a useful and easily calculated point of reference.

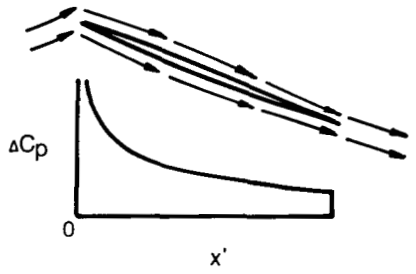

Sketch N

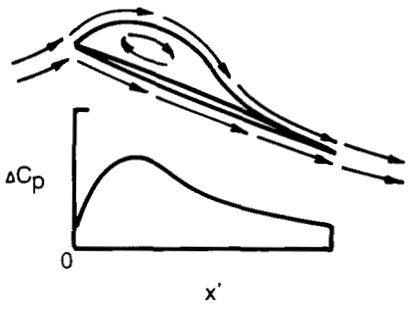

Sketch O

The curves of figure 1(b) show the dramatic improvement offered if the theoretical potential of leading-edge thrust could be fully realized. The flow pattern of sketch N still applies, but it does not show in sufficient detail the flow around the leading edge from a stagnation point on the lower surface which gives rise to the thrust. This leading-edge thrust makes subsonic leading edges appear attractive. The tendency of highly swept wings to have relatively low values of thickness wave drag is another factor which increases the interest. Unfortunately, only small portions of this large benefit have been demonstrated experimentally. Reference 28 presents a study of the factors limiting the achievement of full theoretical leading-edge thrust and provides a means of estimating attainable leading-edge thrust.

The curves of figure 1(c) show the performance potential of wings which employ twist and camber defined by use of the design mode of the WINGDES2 computer code of reference 18. Flow patterns for typical sections of such wings might appear as shown in sketch P. For values of k_n of 0 and 0.4, the code default options were used, but for $k_n = 0.8$, restricting the leading-edge candidate surfaces to the wing area itself was necessary to better account for the complexity introduced by Mach lines from the root chord trailing edge crossing the wing leading edge. The wings represented in figure 1(c) have a surface which, in the region of the leading edge, produces finite loadings instead of the flat wing singularities. In effect, a distributed thrust force over much of the wing planform in the vicinity of the leading edge replaces the flat wing leading-edge thrust, which is concentrated at the leading edge itself. Drag levels are similar to but not identical with those of a flat wing with full thrust. There are several reasons for the differences. Errors in the numerical solutions for the two classes of wings prevent complete agreement, but there are two more important reasons. There will be a tendency for the drag of twisted and cambered wings to be higher because of the limited area near the tips over which the distributed thrust can be developed. This is countered by a general tendency for the twisted and cambered wing drags to be lower because of improved longitudinal lift distributions which reduce supersonic wave drag due to lift. As pointed out in reference 5, the net result is that twisted and cambered wing drag can often be lower than that of the corresponding flat wing with full thrust.

The wings of figure 1(c) represent a collection of point designs. For each of these wings, a flat wing with its flow field shown in sketch Q is replaced by a twisted and cambered wing with its flow field shown in sketch R. The most important characteristic of

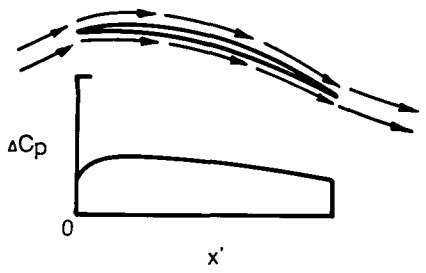

Sketch P

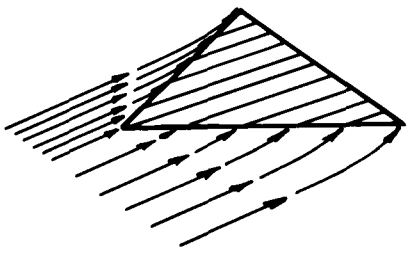

Sketch Q

a properly shaped wing with twist and camber is a leading edge shaped to meet the upwash so that leading-edge pressures remain finite. This shape depends on the Mach number and to an even greater extent on the lift coefficient. At any point on the wing, surface ordinate departures from the reference plane are proportional to the design lift coefficient. As depicted in sketch S, an envelope curve representing a minimum drag-due-to-lift factor is formed about a family of wings, each of which is designed for a specific lift coefficient and Mach number.

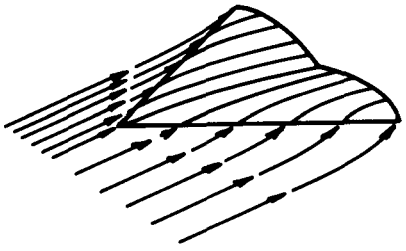

Sketch R

As with most twisted and cambered wing designs, the designs of figure 1(c) are optimized only in a limited sense. Each member of the family is designed so that, compared with other members of the family, it has the lowest drag. The absolute value of the minimized drag thus depends on the size and variety of the family (in this case composed of candidate

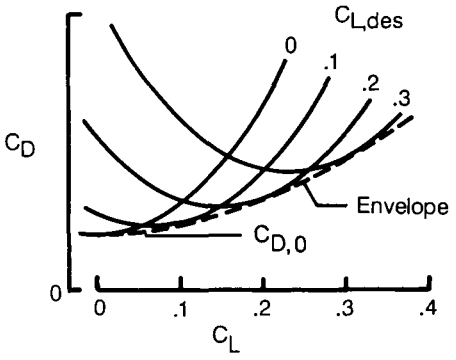

Sketch S

surfaces, and in other cases composed of candidate loadings).

In the application of linearized theory to twisted and cambered wing design, some serious real flow limitations are ignored. A prime example is the limitation on distributed thrust forces imposed by achievable upper surface pressure loadings. For a twisted and cambered wing designed for a uniform load, the lifting surface ΔC_p everywhere is equal to the design lift coefficient. For a more optimally designed twisted and cambered wing the maximum ΔC_p which occurs at the wing leading edge may be about 40 percent greater than the uniform load value. Because linearized theory gives an equal division of lift between upper and lower surfaces, the leading-edge upper surface pressure coefficient for a well-designed twisted and cambered wing would be

$$(C_{p,\mathrm{le}})_u = -\frac{1}{2}\Delta C_{p,\mathrm{le}} \approx -\frac{1.4}{2}C_{L,\mathrm{des}}$$

The vacuum pressure coefficient imposes an absolute limit on achievable upper surface pressures. Thus, the maximum negative upper surface pressure coefficient would be

$$(C_{p,\mathrm{le}})_u \approx C_{p,\mathrm{vac}} \approx \frac{-2}{\gamma M^2}$$

and the maximum design lift coefficient may be approximated as

$$(C_{L,\mathrm{des}})_{\max} \approx \frac{2}{M^2}$$

This relationship is illustrated in sketch T. Real flow limitations are much more severe than this idealized limit, especially at low Reynolds numbers. The shaded band in the sketch represents an "educated guess" of real flow limits for typical wind tunnel Reynolds numbers of 2×10^6 to 4×10^6. The guess

is based in part on the analysis of reference 28. This clearly illustrates the difficulty of effectively applying twist and camber at high supersonic Mach numbers.

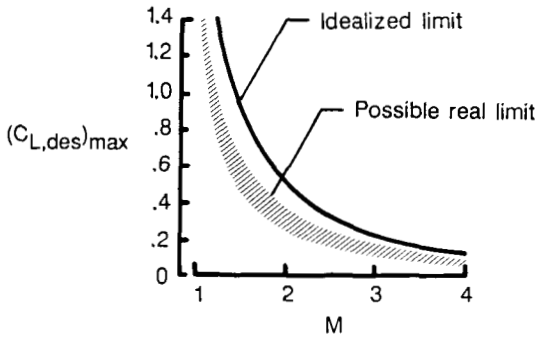

Sketch T

Suction Parameter

In comparing the aerodynamic performance of various wing designs, a common figure of merit is convenient. The lift-drag ratio which is often used for this purpose is affected by thickness as well as pure lift effects and is not used here. Because this study is designed to concentrate on lifting efficiency, the suction parameter is used for the purpose of rating the performance. The suction parameter which is defined by the equation

$$S_s = \frac{C_L \tan\left(C_L/C_{L_\alpha}\right) - \Delta C_D}{C_L \tan\left(C_L/C_{L_\alpha}\right) - C_L^2/\pi \mathrm{AR}}$$

may be explained with the aid of sketch U. With this parameter, the wing drag is compared with upper and lower bounds. The upper bound $C_{D,0} + C_L \tan\left(C_L/C_{L_\alpha}\right)$ is the drag of a flat wing with no leading-edge thrust and no vortex forces. Actually, flat wings develop some degree of leading-edge thrust and/or some degree of vortex force and generally have somewhat lower drags than given by the upper limit. A prime advantage of this upper limit is its simplicity and repeatability. The lower bound $C_{D,0} + C_L^2/\pi \mathrm{AR}$ is the drag of a wing with an elliptical span load distribution (a uniform downwash) and the full amount of any theoretical leading-edge thrust that might be called for. There is no supersonic wave drag-due-to-lift contribution. This limit is a carryover from subsonic speeds where the limit is reasonably achievable. At supersonic speeds, the presence of wave drag due to lift prevents a close approach to this value. Again the simplicity and repeatability make it a logical choice. As shown by the equation and the sketch, the suction parameter is a measure of the departure from the upper limit and approach to the lower bound.

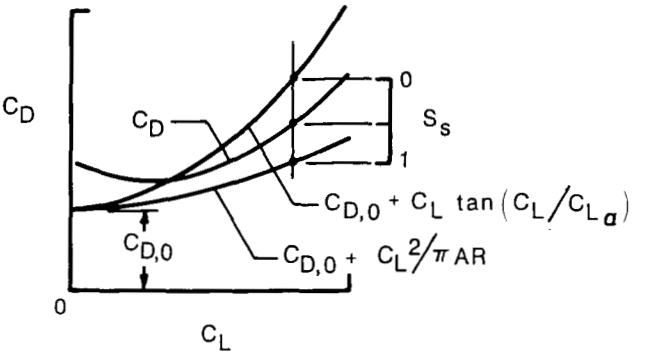

Sketch U

Analysis of Flat Wing Data

As mentioned in the section "Theoretical Considerations," the WINGDES2 code provides an estimate of attainable thrust and vortex forces. A comparison of the theory with measured data for flat wings (wings without twist or camber) provides a test of the accuracy of the prediction for baseline configurations uncomplicated by the presence of twist and camber. In addition, the examination of such data helps illustrate the need for twist and camber to overcome performance penalties due to the failure to develop the theoretical leading-edge thrust.

60° Swept Arrow Wings

Figure 2 presents data from reference 6 for 60° swept arrow wings with various wing sections tested at Mach numbers from 1.60 to 2.16. The flat wings were tested in both an upright and an inverted attitude; data for these two conditions indicate to some degree the repeatability and accuracy of the measurements. The most notable effect of the model attitude (upright or inverted) is in the axial-force data and the suction parameter. Only small differences are seen in the normal force. Differences in pitching moment and drag are so small that only upright data are shown.

For the "sharp" leading edge shown in figure 2(a), the model actually had a small amount of bluntness estimated to correspond to a constant radius of about 0.004 in. along the whole leading edge. This value was used in the code estimation of attainable thrust. The theory overestimates the axial force (underestimates the thrust) and overestimates the normal force. The net result is that through compensating errors the drag and suction parameter agreement is quite good.

For the standard section with $r/c = 0.0026$ shown in figure 2(b), there is still some underestimation of the thrust and some overestimation of the normal force, but again drag and suction parameter are in close agreement. For the blunt section with $r/c = 0.00470$ shown in figure 2(c), the theory gives a better estimate of the thrust, but the suction parameter is overestimated. Considering some uncertainties in the experimental data, reasonable agreement occurs between theory and experiment, especially for the suction parameter figure of merit.

If full theoretical leading-edge thrust (the dashed line) could be achieved, the wings of figures 2(a) to (c) would have a theoretical suction parameter of about 0.64 over the entire lift-coefficient range instead of only at $C_L = 0$. The measured values clearly fall far short of this ideal except for very small lift coefficients.

The wing with the standard section when tested at higher Mach numbers (figs. 2(d) to (f)) showed decreasing thrust and decreasing suction parameter. The theory gives zero thrust for Mach numbers of 2.00 and greater. The experiment however indicates the presence of some effective thrust, perhaps due in part to a detached wing bow shock which allows a subsonic type of flow at the leading edge. Again, in spite of some discrepancies in force components, the prediction of suction parameter variation with Mach number is reasonably good.

Modified Arrow Wings

Another set of flat wing data is shown in figure 3. These data for a wing with aspect ratio of 1.83 and various sections tested at Mach numbers of 1.60 and 2.36 are taken from reference 7. As shown in figure 3(a), the wing section characterized as sharp leading edge displays an axial-force decrease (an attainable leading-edge thrust increase) with angle of attack. The theory gives a good estimate of this force by using an assumed constant leading-edge radius of 0.004 in. All the other measured aerodynamic characteristics including drag and suction parameter are also in good agreement with the theory. Data for the wing with a standard section (NACA 65A004) with $r/c = 0.001$ shown in figure 3(b) also agree well with the theory. The aerodynamic efficiency of this wing, however, is only marginally better than that of the sharp-leading-edge wing. For the blunt-leading-edge wing of figure 3(c), which has a maximum value of r/c of 0.004, the theory predicts a larger amount of thrust and a greater suction parameter than actually is realized. In fact, the measured data are almost the same as those of the wing with the standard section.

The wings whose data are shown in figures 3(a) to (c) would produce suction parameters of about 0.62 for all lift coefficients if full theoretical leading-edge thrust could be achieved. Again the measured lifting efficiency is well below this level.

Data for these same three wings at a Mach number of 2.36 are shown in figures 3(d) to (f). Even at this high Mach number, part of the leading edge is subsonic ($\beta \cot \Lambda_{le} < 1$) and some thrust is developed. Again in spite of some discrepancies, the theory provides a reasonable prediction of the measured performance.

A significant observation for these and the previous flat wings is that sharp leading edges actually have some effective leading-edge radius and may have only small performance penalties relative to the standard sections. Also blunt leading edges fail to offer any improvement in performance relative to that of the standard sections. An examination of geometric data for a large number of NACA airfoil sections shows that leading-edge radius is related to the section maximum thickness and location of maximum thickness η by the simple expression

$$\frac{r}{c} \approx \frac{0.28}{\eta} \left(\frac{t}{c}\right)^2_{\max}$$

Two-dimensional experimental airfoil data for NACA wing sections were used in the calibration of the attainable thrust prediction method; thus, it is not surprising that the method is more accurate for "standard sections" than for arbitrary shapes.

These observations lead to the following suggestion for selection of leading-edge radius for use in code predictions of attainable thrust. First, make as accurate as possible an estimate of the actual leading-edge radius with stated ratios for standard sections and measured values or estimates for nonstandard sections. Then compare this radius with that given by the preceding expression and use whichever is smaller. Application of this procedure to an appropriate selection of wingspan stations gives a spanwise distribution of leading-edge radius that should improve prediction capabilities.

Aspect Ratio 2 Wing–Body Combination

Additional flat wing data (ref. 8) presented in figure 4 provide a further test of the prediction ability of the theory. Figures 4(a) to (c) show data for the aspect ratio 2 wing at three different Reynolds numbers. The theory predicts a small increase in the amount of thrust attainable as the Reynolds number increases. The experiment also shows a

small but noticeable improvement in the wing lifting efficiency, as measured by the suction parameter, with increasing Reynolds number.

Reference 8 provides data and an analysis, which points out some hazards in evaluating wing lifting efficiency at wind tunnel Reynolds numbers. At low Reynolds numbers, there may be regions of laminar flow at small angles of attack and a transition to more nearly turbulent flow as the angle increases. Such changes obscure attempts to evaluate increases in lifting efficiency brought about by measures taken to increase attainable thrust or by the introduction of twist and camber. The results shown in figure 4 and throughout this paper are from tests which used transition strips, which attempt to simulate a fully turbulent boundary layer.

Figures 4(d) and (e) illustrate the influence of Mach number on attainable thrust and wing performance at a Reynolds number of 5.6×10^6. The thrust and the other performance characteristics are well predicted by the theory.

The data in figure 4(d) for a configuration with a 3-percent-thick airfoil may be compared with the data for the 5-percent-thick airfoil shown in figure 4(b). The thinner airfoil has a lower value of $C_{D,0}$ because of its lower wave drag but also develops less thrust which results in little noticeable change in drag at the higher lift coefficients.

In general, the flat wings examined in this section displayed relatively low levels of aerodynamic efficiency as measured by the suction parameter, even though predicted levels of attainable thrust were achieved. There is clearly a need to explore the use of twist and camber to substitute distributed thrust forces for the unattained concentrated thrust.

Analysis of Twisted and Cambered Wing Data

A wide variety of representative twisted and cambered wing data has been examined to assess achievable levels of supersonic lifting efficiency. For consistency in the analysis of the data, one computer code, the WINGDES2 code previously discussed, is applied to all the data. Linearized theory methods, even modified methods such as WINGDES, have certain deficiencies in application to twisted and cambered wings. Specifically the tendency is to overestimate the performance levels achievable and to overestimate the amount of twist and camber required for a particular application. More accurate alternate methods, however, have not yet been developed to the point where they can easily and quickly be applied to the volume of cases treated herein.

Data for the twisted and cambered wings are presented in the same fashion as for the flat wing with one exception. Axial and normal forces are calculated and plotted as a function of the quantity $\alpha - \alpha_0$ instead of α. The angle α_0 as shown in sketch V is the theoretical angle of attack at which the twisted and cambered wing produces a lift coefficient of zero. This conversion permits a clear visualization of the prime characteristic of efficient twisted and cambered wings, which, as shown in sketch W, is an axial force with a negative slope so that for design conditions, an axial force associated with a flat wing with full thrust may be replaced by an axial force resulting from a distributed thrust.

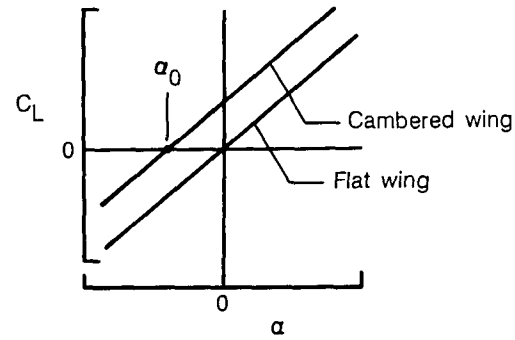

Sketch V

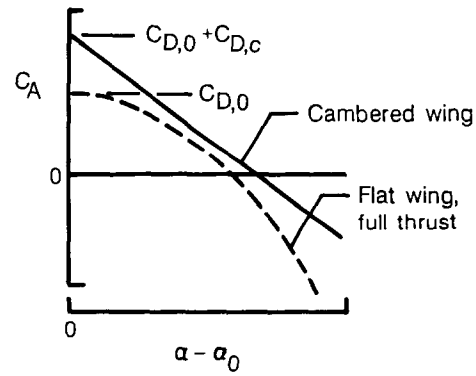

Sketch W

Aspect Ratio 2 Wing–Body Combination With Conical Camber

Figure 5 shows data from reference 8 for an aspect ratio 2 wing–body combination with conical camber designed for a Mach number of 1.00 and a lift coefficient of 0.215. Data for this wing tested at a Mach number of 1.30 and a Reynolds number of 5.6×10^6 are shown in figure 5(a). A value of $C_{D,0}$ of 0.0122 taken from the experimental data of figure 4(d) was used in applying the theory to the twisted and

cambered wing body. Even though this wing surface was designed for different conditions than those of the test, it performed quite well. The decrease of axial force with increasing angle of attack indicates an effective substitution of distributed thrust for the theoretical leading-edge thrust. Realization of this thrust force results in a measured peak suction parameter of about 0.55 at a lift coefficient of about 0.20. which is a considerable improvement over the corresponding value of about 0.20 for the flat wing. The theory gives a good estimate of the actual performance.

Data for the conically cambered wing at a Mach number of 1.70 shown in figure 5(b) show a much poorer performance, only slightly better than the corresponding flat wing (fig. 4(e)). Also a sizable discrepancy exists between the theory and the measured data. This tendency for poorer performance and poorer theoretical prediction ability as Mach number increases is seen throughout this paper.

Aspect Ratio 1.57 Wing–Body Combination Designed for $M = 1.62$

Data from reference 4 for wings twisted and cambered for three different lift coefficients at a Mach number of 1.62 are shown in figure 6. The wings were designed to carry a uniform load at lift coefficients of 0.08 and 0.20. The third wing in the series, a flat wing, may be considered to have a design lift coefficient of 0. Shown in figure 6(a) for the flat wing is some evidence of a partially laminar flow for α near zero (the decrease in C_A as $\alpha = 0$ is approached) which makes selection of the proper value of $C_{D,0}$ a bit more difficult. Also raised is a question about the stability of the flow over the other wings. Thus, some uncertainty exists regarding the performance levels actually achieved. The negative slopes of the axial-force curves and the close agreement of experiment and theory shown in figures 6(b) and (c) indicate that the goal of the design was largely achieved. The measured suction parameters are probably reasonably accurate despite the $C_{D,0}$ uncertainty, and measured suction parameter peaks approach theoretical values.

The existence of data for three design lift coefficients permits an examination of the dependence of lifting efficiency as measured by the suction parameter on the severity of the surface warping. Such information is presented in figure 7, where suction parameter at each of three designated lift coefficients is shown as a function of the design lift coefficient. At any given point on the wing planform, the camber surface ordinates are directly proportional to the design lift coefficient. In this plot and all subsequent plots of experimental suction parameter versus design lift coefficient, the fairing is based on three data points even if only two appear in the figure. For an operational lift coefficient of 0.08, shown at the top of the figure, the theory predicts a peak suction parameter of about 0.53 at or near the lift coefficient of 0.08. The experimental data indicate a somewhat lower peak of about 0.47 at a lower design lift coefficient. The same pattern occurs for the other operating lift coefficients. The theory not only overestimates the attainable suction parameters but also provides a surface that is too severe for a given operational lift coefficient. These characteristics of the theory are explored in greater depth in succeeding examples.

Arrow Wings Designed for $M = 2.00$

The twisted and cambered wings of reference 9 were designed to carry an optimum combination of three candidate loadings subject to the limiting of leading-edge loadings to values no more than 40 percent greater than the average loading over the whole wing. This was done to allow a greater theoretical lifting efficiency than a uniform loading while still avoiding transonic flow in the cross-flow plane for the chosen leading-edge sweep angles of 70° and 75° at the design conditions of $M = 2.00$ and $C_{L,\text{des}} = 0.16$. The design was accomplished by application of methods described in references 30 and 31 in a laborious process of hand calculation. Those methods later formed the basis for the computer implemented design method of reference 19.

Data from tests of arrow wings with a 70° leading-edge sweep are shown in figure 8. These semispan models were tested on a boundary-layer bypass plate mounted on the tunnel sting support, which was found to produce a flow of Mach number 2.05 instead of the design value of 2.00. Data are shown for a flat wing ($C_{L,\text{des}} = 0$), a wing twisted and cambered for the design lift coefficient of 0.16, and a wing with an intermediate design lift coefficient of 0.08. The wing with $C_{L,\text{des}} = 0.08$ has camber surface ordinates which for any given point on the planform are one half those for the wing with $C_{L,\text{des}} = 0.16$. As shown by the flat wing axial-force data of figure 8(a), a small amount of effective leading-edge thrust is developed even though the 3-percent-thick circular-arc sections have a theoretical leading-edge radius of 0. For the theoretical calculations, an estimated leading-edge radius of 0.004 in. at all span stations was used. From the appearance of the axial-force plot, it may be assumed that $C_{D,0}$ can be established with acceptable accuracy. Data for the wing with $C_{L,\text{des}} = 0.16$ of figure 8(c) show a noticeable failure

to achieve the theoretical values of C_A at and near the angle of attack for $C_L = 0.16$. The suction parameter also shows a considerable discrepancy between the theoretical and measured lifting efficiencies. Causes of these discrepancies are addressed subsequently. Note that the closest approach of the theoretical and experimental suction parameter is not at the design lift coefficient but at a higher C_L. Data for the wing with the milder camber surface in figure 8(b) show a closer agreement of theory and experiment than for the wing with $C_{L,\text{des}} = 0.16$. At a lift coefficient of 0.16, the suction parameter for this wing is somewhat higher than that for the wing with $C_{L,\text{des}} = 0.16$. For the wing with $C_{L,\text{des}} = 0.08$, the maximum lift-drag ratio, which occurs at $C_L \approx 0.14$, was found to be about 8.8, which compares with a value of about 8.1 for the flat wing and about 8.3 for the wing with $C_{L,\text{des}} = 0.16$. After the publication of these data in reference 9, many supersonic wing designers began to apply a rule of thumb in which design lift coefficients equal to some fraction of the operational lift coefficient (usually 0.5 to 0.8) were used in the theoretical design.

Figure 9 shows suction parameter at each of three selected lift coefficients as a function of the design lift coefficient. Although theoretical peak suction parameters of about 0.56 are predicted, measured peaks are about 0.38 or less. As in the data for the aspect ratio 1.57 wing–body at $M = 1.62$ shown in figure 7, the measured peaks also occur at lower design lift coefficients. At this higher Mach number, the ratio of measured and theoretical peaks and the lift coefficients at which they occur are lower than at $M = 1.62$.

To further explore the characteristics of twisted and cambered wings, the 70° swept wings were subjected to pressure distribution tests reported in reference 10. Sample data from these tests are reproduced in figure 10. Upper and lower surface pressure coefficients are shown as a function of nondimensionalized distance behind the wing leading edge for selected semispan stations and for selected angles of attack. The angles were selected so that data would be shown for an angle near that at which a theoretical C_L of 0.16 is reached and at angles 4° lower and 4° higher. The experimental distributions can be compared with linearized theory distributions, also taken directly from reference 10. The WINGDES2 code gives results that differ very little from those shown when the vortex pressure loadings are disregarded.

For the flat wing data of figure 10(a), experiment and theory agree reasonably well for small angles of attack and inboard stations. At high angles of attack, the discrepancies can get very large, particularly near the wingtip. The primary cause is the theoretical leading-edge singularity which of course cannot exist in the real flow. Also present is evidence of a leading-edge flow separation (very noticeable for $\alpha = 8°$ and $\frac{y}{b/2} = 0.3$) which is not predicted by the basic linearized theory.

In the data for the wing with $C_{L,\text{des}} = 0.08$ of figure 10(b), reasonable agreement of experiment and theory is seen out to the 0.7 span station for $\alpha = 2°$ which corresponds to a theoretical lift coefficient of about 0.15. This is in accord with the relatively good performance of this wing compared with the other two. For this angle of attack, little or no evidence of the separated leading-edge flow noted for the flat wing is seen.

For the data for the wing with $C_{L,\text{des}} = 0.16$ in figure 10(c), there is a notable failure to produce the theoretical loadings in the vicinity of the leading edge for the $\alpha = 0°$ ($C_L = 0.16$) design condition. In fact at the outboard station, a negative rather than a positive loading is realized. This failure can have disastrous effects on twisted and cambered wing performance because the indicated theoretical loadings are required if the flat wing theoretical leading-edge thrust is to be recovered.

The pressure distribution data just examined can be very useful in diagnosing the failures of the linearized theory in wing design and in providing remedies. An analysis of the pressure distribution data for the wing with $C_{L,\text{des}} = 0.16$, which may be illustrated with the aid of figure 11, shows how an improved wing design may be devised. The basis of the analysis is an assumption that for reasonably efficient performance of the twisted and cambered wing, leading-edge ΔC_p loadings close to the theoretical level of $C_{L,\text{des}} = 1.4$ are required and that these loadings may be controlled by a properly selected incremental twist distribution. As illustrated by the sketch at the top of the figure, the data of figure 10(c) were used in defining a leading-edge lifting pressure coefficient for each span station and angle of attack. When assembled and faired as shown in the middle of the figure, these data provide the information necessary to define the required twist distribution. The plot for $\Delta C_{p,\text{le}}$ versus α has superimposed on it the design value of $\Delta C_{p,\text{le}}$ of 0.22 which is equal to $1.4 C_{L,\text{des}}$. From this plot, for each span station the angle of attack at which $\Delta C_{p,\text{le}} = 0.22$ is achieved may be read. The results are shown at the bottom of the figure in a plot which shows the local angle of attack at which $\Delta C_{p,\text{le}}$ of 0.22 would be achieved. As shown by the dashed line, an

incremental twist distribution closely corresponding to that derived from the analysis of experimental data can be produced by a change of 0.04 in design lift coefficient, a reduction from 0.16 to 0.12. This incremental twist distribution was found by using camber surface ordinates from the wing with $C_{L,\mathrm{des}} = 0.16$ to define its spanwise twist distribution and then applying a factor (based on the linear dependence of z ordinates on $C_{L,\mathrm{des}}$) to fit the experimentally derived twist distribution. The implication of this diagnosis is that the linearized theory overestimates the magnitude of the upwash ahead of the leading edge and, because of this overestimation, calls for an amount of camber that is too large to provide a near-tangent onset flow at the leading edge in the real flow. In this case, the effective upwash that actually developed apparently is only about 75 percent (0.12/0.16) of the theoretical values.

In this analysis, an assumption is implied that local leading-edge flow is primarily influenced by the local geometry and is not critically dependent on geometry changes elsewhere. This assumption is probably reasonable if the geometry changes are small and gradual. Results of the preceding analysis are reinforced by the data of figure 9, which shows that for a lift coefficient of 0.16 the actual suction parameter maximized not at $C_{L,\mathrm{des}} = 0.16$ but near $C_{L,\mathrm{des}} = 0.12$. The preceding analysis thus indicates not only that the proper reduction in design lift coefficient will offer improved performance but also that there is not likely to be any appreciably better adjustment applicable to linearized theory design methods.

The observed tendency of the actual upwash to fall short of the linearized theory prediction is not surprising. The theory gives large values of upwash in the vicinity of the leading edge and an infinite value at the leading edge itself, which is of course unattainable. In addition the bow wave created by the wing thickness will cause the upwash generation to begin farther ahead of the leading edge than indicated by the theoretical Mach line. Thus the actual flow vertical velocities will develop more gradually than the theory indicates and will achieve smaller maximum values.

Data from tests of the wing with a 75° swept leading edge reported in reference 9 are given in figure 12. Only a flat wing and a wing with $C_{L,\mathrm{des}} = 0.16$ were tested, and no subsequent pressure distribution tests were conducted. Therefore, an extensive analysis as was made for the 70° swept wing cannot be performed. As for the 70° swept wings, the twisted and cambered wing offered an improved performance over that of the flat wing at the design lift coefficient and at higher lift coefficients.

Modified Arrow Wings Designed for $M = 2.60$

A systematic study of the effects of leading-edge sweep angle and design lift coefficient on the performance of twisted and cambered arrow wings is reported in reference 11. These wings had clipped tips because, as discussed in reference 11 and elsewhere in this report, the regions removed provide little or no improvement in lifting efficiency but do contribute to thickness and skin friction drag. A series of nine wings composing a matrix of three leading-edge sweep angles ($\beta \cot \Lambda_{\mathrm{le}} = 0.60$, 0.75, and 0.90) and three design lift coefficients ($C_{L,\mathrm{des}} = 0$, 0.08, and 0.12) at a Mach number of 2.60 was designed by use of the method of reference 20. Data from tests of those wings are presented in figures 13 to 15.

Data for a 75.96° swept wing ($\beta \cot \Lambda_{\mathrm{le}} = 0.60$) are shown in figure 13, data for a 72.65° swept wing ($\beta \cot \Lambda_{\mathrm{le}} = 0.75$) are shown in figure 14, and data for a 69.44° swept wing ($\beta \cot \Lambda_{\mathrm{le}} = 0.90$) are shown in figure 15. Qualitative results are similar to those found for the previously discussed arrow wings tested at a Mach number of 2.05.

In figures 13 to 15, notice that as the sweep angle decreases, the suction parameter associated with full recovery of the flat wing theoretical leading-edge thrust (the dashed line) also decreases. This decrease occurs not only because of the reduced leading-edge thrust for $\beta \cot \Lambda_{\mathrm{le}}$ approaching 1 but also because of the increased wave drag due to lift. Wave drag due to lift tends to vary inversely with the square of the wing lifting length in the streamwise direction. The wing with $\beta \cot \Lambda_{\mathrm{le}} = 0.90$ has only 82 percent of the lifting length of the wing with $\beta \cot \Lambda_{\mathrm{le}} = 0.60$ and thus would have a wave drag due to lift about 50 percent higher. The improvement in the longitudinal lift distribution offered by well-designed twist and camber is more important for the wing with $\beta \cot \Lambda_{\mathrm{le}} = 0.90$ and results in a theoretical performance considerably better than that of the flat wing with full leading-edge thrust.

The twisted and cambered wings offer performance improvements but not as much as predicted by the theory. Peak measured suction parameters fall well below the theory and generally occur at higher lift coefficients. The primary value of these data is their use in defining the dependence of wing performance as measured by the suction parameter on sweep angle as well as design lift coefficient. Figure 16 shows suction parameter at three selected

lift coefficients for the three different wing planforms plotted as a function of design lift coefficient. Both theoretical and experimental data show decreasing suction parameters with increasing values of the parameter $\beta \cot \Lambda_{le}$, which is similar to the trends shown in figures 1(b) and (c). As for the previous arrow wings tested at $M = 2.05$ (fig. 9), measured suction parameter peaks are well below the theoretical peaks and occur at lower design lift coefficients. The experimental peak is generally a smaller fraction of the theoretical peak than was true for the data at $M = 2.05$. The value of C_L for the experimental peak is also a smaller fraction of C_L for the theoretical peak than it was for the data at $M = 2.05$.

Figure 17 shows maximum suction parameter at each of three lift coefficients as a function of the leading-edge sweep-angle parameter. Fairing of the data for the three wing planforms indicates that a sweep-angle parameter near $\beta \cot \Lambda_{le} = 0.60$ gives the greatest lifting efficiency. Similar plots in reference 11 in which maximum lift-drag ratio was the dependent variable showed an optimum $\beta \cot \Lambda_{le}$ between 0.60 and 0.70.

Delta Wing–Body Combination Designed for $M = 3.50$

Tests of delta wings twisted and cambered to support an optimum combination of three loads at a Mach number of 3.50 reported in reference 12 failed to show any appreciable benefit of departures from the flat surface. These data are shown in figure 18. However, plots of suction parameter versus design lift coefficient shown in figure 19 indicate that design lift coefficients somewhat lower than the intermediate value of 0.05 should offer some small improvement over the flat wing.

Arbitrary Planform Wing–Body Combination Designed for $M = 2.40$

Reference 13 presents a study of the effect of leading-edge lifting pressure constraints on the performance of twisted and cambered wings designed for a lift coefficient of 0.08 at a Mach number of 2.40. A basic twisted and cambered wing was designed by use of methods described in references 21 to 24 with no constraints applied. The design employed an optimum combination of an apparently large, but unspecified, number of candidate loadings. A second design with a moderate constraint restricted leading-edge pressures so that, at design conditions, the flow component normal to the leading edge would have a Mach number less than 1.00. A third design with a severe constraint restricted leading-edge lifting pressures to zero for the whole wingspan.

Data for these three twisted and cambered wings and for a flat wing of the same planform are shown in figure 20. All the twisted and cambered wings offer a small but measurable performance improvement over the flat wing for lift coefficients at which the twisted and cambered wing suction parameter reaches its maximum value. The unconstrained design offers its maximum improvement at and near the design C_L of 0.08. The severely constrained wing, on the other hand, offers an advantage only for lift coefficients in excess of 0.12.

A detailed examination of the relative merits of each of these designs is made simpler by the use of figure 21 which enlarges the suction parameter plots and provides sketches depicting a mid semispan loading and surface for the design lift coefficient and for a lift coefficient twice that. According to the experimental data, the design with no constraint produces a maximum suction parameter of about 0.36 at a lift coefficient of about 0.09. At this lift coefficient, the mid semispan loading and surface shape are close to those depicted in the sketch for the design C_L. For the moderate constraint, the peak measured parameter of about 0.30 occurs for a lift coefficient of about 0.14. For the severely constrained design, the peak measured suction parameter is slightly less than 0.30 but is reached only when the lift coefficient is about 0.16, or more than twice the design value. Measured suction parameter for the flat wing shows a considerable degree of scatter but does stabilize at the higher lift coefficients. A fairing of the experimental data for this wing takes into consideration the characteristics of other flat wings treated in this study.

These data indicate that the imposition of pressure restraints more severe than those given by the theoretical optimum combination of loads is counterproductive. Leading-edge pressures of zero at the leading edge itself and not much greater than zero at locations behind the leading edge conflict with the goal of substituting a distributed thrust force for the theoretical leading-edge force. Such a strategy can work only if the loading behind the leading edge is permitted to increase rapidly to high levels so that a substantial thrusting force can be developed. Apparently, the candidate loadings used in the design process did not include any with this characteristic. Notice that for the severely constrained wing design, both theory and experiment show improved performance at lift coefficients above the design value. At these higher lift coefficients, flat plate ΔC_p increments result in much larger theoretical loadings in the vicinity of the wing leading edge. The restricted design thus behaves somewhat like an unrestricted design for higher lift coefficients but in all likelihood

produces a lower performance level than would the unrestricted design.

Note that for the design of sharp leading edges, the WINGDES2 code attempts to provide an alignment of leading-edge surface slope with the local upwash at design conditions so that leading-edge pressure loadings are near zero. This code, however, includes candidate surfaces which allow a rapid curvature away from the alignment condition so that pressure loadings and thrust forces in the vicinity of the wing leading edge can be substantial.

74° Swept Arrow Wing–Body Combination

Data from reference 14 for an arrow wing designed for a lift coefficient of 0.1 and a Mach number of 2.50 are presented in figure 22. For the flat wing of figure 22(a), good correlation of experiment and theory occurs for most of the lift coefficient range. For the twisted and cambered wing, however, the measured performance again falls short of theoretical expectations. A flow breakdown starting at an angle of attack of about 4° and a lift coefficient of about 0.1 is shown by the axial-force curve.

75° Swept Modified Arrow Wing–Body Combination

Figure 23 presents data from reference 15 for a modified arrow wing designed for a lift coefficient of 0.1 at a Mach number of 3.00. The methods of references 30 and 31 were employed to define a surface corresponding to an optimum combination of loads. The number of candidate loadings used in the design is not specified. Apparently no limitations were placed on the magnitude of the total local loading.

The surface has a severe slope in the region of the wing apex, which is clearly shown in the photographs of reference 15. This characteristic in combination with the modified arrow wing planform produces an artistic shape which is represented in the original NASA logo. From a purely theoretical standpoint, the wing apex shape would be beneficial in producing a large amount of forward lift which would in turn create a large upwash along the outboard wing leading edge resulting in increased distributed thrust. However, as indicated by the data of figure 23, the measured performance falls far short of the theoretical potential. Because no flat wing tests were conducted, the Boeing complex of codes (refs. 21 to 24) was employed to provide a $C_{D,0}$ estimate. The wave drag coefficient at zero lift was calculated to be 0.0023, and the skin friction drag coefficient was 0.0048. An estimated additional drag coefficient of 0.0006 was added to these two components to account for the use of grit strips to ensure a turbulent boundary layer. For the estimated total $C_{D,0}$ of 0.0077, the maximum measured suction parameter is only slightly more than zero. Based on observations of data for other configurations treated in this paper, this wing is unlikely to give an aerodynamic performance better than that of a flat wing.

One possible reason for the poor performance may be illustrated by sketch X which has been prepared with data provided by the WINGDES2 code. This plot shows the effect of the severe surface slope in the region of the wing apex on the leading-edge flow conditions. As shown in the sketch, the angle of attack for zero thrust for an inboard semispan location is 6° or more negative compared with a design angle of attack of 0°. As described elsewhere in this paper, for a well-designed wing the range of full thrust should cover the design angle. Failure to provide the proper leading-edge surface alignment with the flow ahead prevents the recovery of the theoretical leading-edge thrust on which the wing efficiency depends. Large discrepancies such as shown in sketch X also indicate the possibility of severe flow separation which invalidates the theory. In particular, flow separation in the wing apex region would reduce the local lift and the resultant upwash field on which the theoretical performance depends.

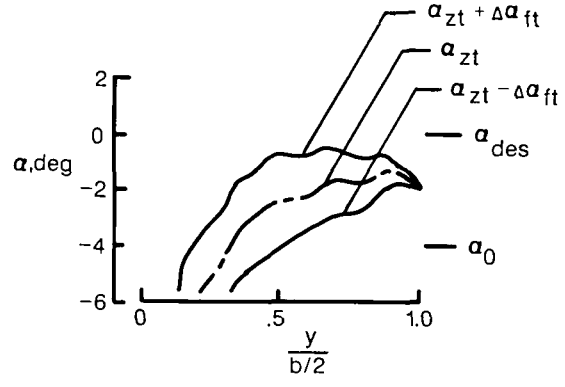

Sketch X

Supersonic Transport Wing–Body Combination

The wing–body combination whose planform is shown in the sketch of figure 24 is one of a large number of candidate supersonic transport configurations studied by NASA beginning in the midsixties. As described in references 32 and 33, a complete vehicle model known as the SCAT 15F, built on a similar baseline configuration, was assembled and tested to

serve as a demonstration of the integration of various techniques for design optimization that were then being developed. One of the key techniques was the use of wing twist and camber. Data from reference 16 for a wing designed by the method of reference 19 for a lift coefficient of 0.08 and a Mach number of 2.70 are shown in figure 24. For this configuration, no data for a comparable flat configuration were obtained; therefore, a value of $C_{D,0}$ was estimated. The Boeing complex of codes (refs. 21 to 24) was used to evaluate a skin friction component of 0.0060 and a zero lift wave drag of 0.0010. An additional increment of 0.0006 due to the grit strips used to ensure a turbulent boundary was estimated from data supplied in reference 16. An estimated total $C_{D,0}$ of 0.0076 is included in the theory shown in figure 24. The theory agrees reasonably well with all the experimental data up to an angle of attack of about 5° or a lift coefficient of about 0.12. As might now be expected, however, there is some failure to achieve the theoretically predicted suction parameter. The value achieved (about 0.30) though is relatively good for a Mach number this high.

60° Swept Wing–Body Combination

In reference 17, a different and more difficult class of design problem was undertaken. In this exercise, a relatively mild camber surface for a lift coefficient of 0.05 at a Mach number of 1.80 was subject to a mission adaptive redesign in an attempt to improve performance at a maneuver lift coefficient of 0.36 and a Mach number of 1.60. Such a design presents a difficult problem not only because of the more severe surfaces required for high lift coefficients but also because only a limited area of the wing surface is available for the redesign. Only the front 20 percent of the local wing chord could be altered to provide a surface shape and loading for recovery of the theoretical leading-edge thrust. The higher-than-normal pressure loadings required may in fact be physically unattainable if they approach the vacuum pressure limit. A further complication is the possible inadequacy of the code numerical representation of the wing surface and loadings in the critical areas. For much of the outer wing panel, the modified surface may be represented by only one or two chordwise code elements which could lead to errors in calculation of local pressure loadings and in definition of optimized surfaces. The latter problem could be avoided by an expansion of the code to handle a much larger number of elements. With the additional storage and higher speeds available with advanced computers, this should be possible. In design problems such as this, every possibility of using larger chord redesign areas should be explored.

Figure 25(a) shows data at $M = 1.60$ for the cruise wing surface designed for a lift coefficient of 0.05 at a Mach number of 1.80. As might be expected, for such a mild surface, there is a reasonable correlation of experiment and theory for most of the angle of attack and lift coefficient ranges.

An early version of the WINGDES2 code was used to provide a mission adaptive surface design. In an attempt to provide the desired performance gains with a camber surface as mild as possible, the attainable thrust code features were utilized, and a design lift coefficient of 0.30 slightly less than the maneuver lift coefficient of 0.36 was used. The maneuver wing data shown in figure 25(b) show a large discrepancy between theory and experiment and a failure of the redesign to offer any improved performance at design conditions. An analysis in the following section of this paper explores in greater detail this particular design problem.

In general, well-designed twisted and cambered wings are found to give an improved lifting efficiency compared with the corresponding flat wings. The performance as measured by the suction parameter, however, is below the theoretical potential given by linearized theory. The nature of these discrepancies is addressed in greater detail in the following section.

Empirical Design Guidelines

The preceding comparisons of theory and experiment for twisted and cambered wings revealed some consistent qualitative patterns. The maximum suction parameters actually achieved were lower than those predicted by the theory, and the required surface for given design conditions was less severe (smaller departures from a flat surface) than that given by the design methods. In addition, these differences become more pronounced with increasing Mach number. In this section, an attempt is made to quantify the differences and devise empirical adjustments to more closely define optimum designs and to more accurately estimate achievable performance.

Derivation of Empirical Design and Estimation Method

Four of the experiments used in the analysis included data for a series of three wings with varying degrees of camber surface severity dictated by the design lift coefficient. Because the results of each of these experiments indicated a successful application of twist and camber, these data can be used in quantifying some empirical guidelines for application of linearized theory design methods. Data from plots of suction parameter versus design lift coefficient for a given operational lift coefficient (figs. 7, 9, 16,

and 19) have been assembled in figure 26. As shown in the sketch at the top of the figure, the important data points are the maximum values of the suction parameter $S_{s,\max}$ for a given lift coefficient and the design lift coefficient $C_{L,\text{des,opt}}$ at which it is achieved.

The plot in the middle of figure 26 permits a comparison of the camber surface severity corresponding to the experimental maximum $((C_{L,\text{des,opt}})_{\text{exp}})$ and the camber surface severity corresponding to the theoretical maximum $((C_{L,\text{des,opt}})_{\text{th}})$. If the theory accurately represented the experimental data, these two values would be identical as shown by the dashed line. The plot shows that the actual surface required is always less severe than the theoretically generated surface and that the Mach number exerts a strong influence on the relative values. For a given Mach number, there is, for practical purposes, just one ratio of experimentally determined optimum design lift coefficient to theoretical optimum design lift coefficient. This ratio is independent of the operational lift coefficient. Of particular significance are the data for the tests at $M = 2.60$ which cover various sweep angles ($\beta \cot \Lambda_{\text{le}} = 0.60$ to 0.90). The empirical ratios are applicable to a wide range of lift coefficients which should be greater than the C_L range used in their derivation (0.08 to 0.16). However, at very low C_L values, where attainable concentrated leading-edge thrust may have a significant contribution, the wing performance is not critically dependent on the small amount of twist and camber that may be required, and a flat wing may perform as well as a wing with twist and camber corresponding to the indicated empirical ratios.

The results of these correlations suggest the use of a design factor K_D shown at the top of figure 27 in determining a design lift coefficient for use in theoretical wing design to replace the actual operational or cruise lift coefficient. Such a strategy is not new; it has been used before (for example, refs. 32 and 33). The present data, however, provide a firm base for the practice and demonstrate the dependence of the design factor on Mach number. The previous analysis of the pressure data for the 70° arrow wing including the effect of wing twist and $C_{L,\text{des}}$ on leading-edge loadings also supports the strategy. It indicates not only that a change in $C_{L,\text{des}}$ is an effective measure in providing a more realistic optimum surface, but also that there is not likely to be a better approach of comparable simplicity.

The bottom of figure 26 shows the relationship between maximum measured suction parameters and maximum theoretical suction parameters. These ratios are not as well defined as the ratios of $C_{L,\text{des}}$ but still can be useful. The greatest scatter is for the wings with $\beta \cot \Lambda_{\text{le}} = 0.90$ tested by Mack (ref. 11). For these wings with a near sonic leading edge, suction parameter tends to be relatively small and can be affected by variations in attainable thrust as influenced by a wing-thickness-generated bow shock, which is not included in the theory. A factor expressing the ratio between measured and theoretical maximum suction parameters is shown at the bottom of figure 27. This curve should be interpreted as an approximate upper bound for wings designed according to the principles outlined in this paper. These principles include not only the selection of the appropriate design lift coefficient but also the selection of design surfaces that provide the proper leading-edge onset flow conditions for thrust recovery and the prevention of flow separation.

Application of Empirical Design and Estimation Method

Use of the plots of figure 27 in selecting a design lift coefficient and estimating wing performance may be summarized as follows. First, for the selected design Mach number read the corresponding factor K_D from the top plot to define a design lift coefficient

$$C_{L,\text{des}} = K_D C_{L,\text{cruise}}$$

for use in computer code definition of the lifting surface ordinates and theoretical performance including $(S_{s,\max})_{\text{th}}$. Then read K_S from the bottom plot to estimate the suction parameter

$$S_{s,\text{cruise}} = K_S (S_{s,\max})_{\text{th}}$$

that can actually be achieved. The code value of $(S_{s,\max})_{\text{th}}$ for $C_{L,\text{des}}$ is used in this expression even though $C_{L,\text{des}}$ differs from $C_{L,\text{cruise}}$. As illustrated in sketch Y for a wing-design family of various $C_{L,\text{des}}$ values, very little change in $S_{s,\max}$ occurs. The drag coefficient at cruise lift coefficient can be estimated by use of the expression

$$C_{D,\text{cruise}} = C_{D,0} + \frac{\left(C_L^2\right)_{\text{cruise}}}{\pi \text{AR}} + (1 - S_{s,\text{cruise}}) \times \left[C_{L,\text{cruise}} \tan \frac{C_{L,\text{cruise}}}{C_{L_\alpha}} - \frac{\left(C_L^2\right)_{\text{cruise}}}{\pi \text{AR}} \right]$$

which is derived from a rewriting of the suction parameter definition. The lift-drag polar near the cruise lift coefficient may be approximated as

$$C_D = C_{D,0} + \frac{C_L^2}{\pi \text{AR}} + (1 - S_s) \left[C_L \tan \frac{C_L}{C_{L_\alpha}} - \frac{C_L^2}{\pi \text{AR}} \right]$$

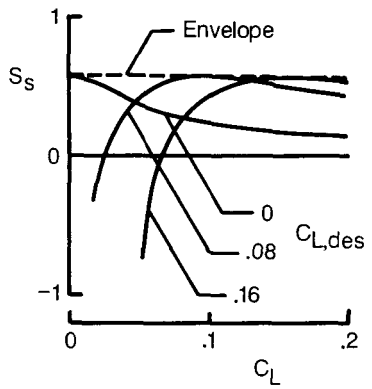

Sketch Y

where the suction parameter S_s is found from the curve for theoretical S_s versus C_L for a value of C_L equal to K_D times the actual C_L and is corrected for the overestimation tendency by subtracting an increment between theoretical and experimental peak suction parameter, which is assumed to be constant over a range of C_L. In equation form,

$$S_s = S_{s,\text{th}}\Big|_{K_D C_L} - (1 - K_S)(S_{s,\max})_{\text{th}}$$

Sketch Z illustrates a typical application of the procedure.

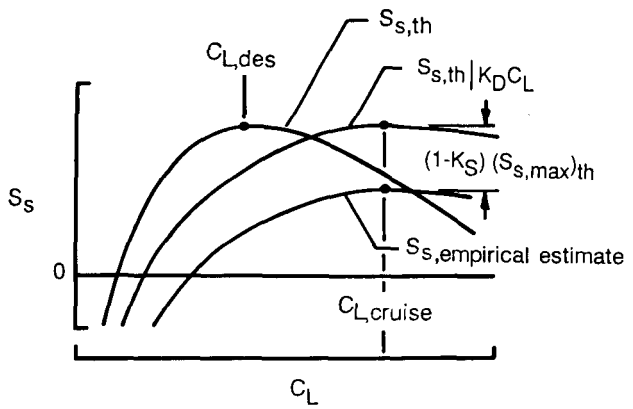

Sketch Z

For small values of $C_{L,\text{des}}$, the factor will properly define the mild surface required, but application of the factor K_S may underestimate the performance. The suction parameter for a properly designed twisted and cambered wing will not be less than S_s for a flat wing at the same C_L. For a better performance estimate, use whichever value is greater. When the WINGDES code is used in the design mode with a flat initial surface (the code default), the first design iteration provides data for a flat wing.

Although the empirical design and estimation factors were derived from data for wings designed without attainable thrust considerations, they may also be applied to designs using the default option of the WINGDES2 code in which camber surface requirements are reduced to a degree consistent with the estimated development of leading-edge thrust. The same tendency for the linearized theory to overestimate the local upwash is present in both cases. Application of the factor K_D will provide a better design where local camber surface slopes are appreciable and will have little or no influence where slopes are small or zero. The purpose of the attainable thrust design is not so much to improve performance as it is to give a comparable performance with a milder camber surface. Thus, the factor K_S is still applicable. However, as previously mentioned, an estimated S_s value less than that of a flat wing at the same C_L should be replaced by the flat wing value.

If the need to impose moment restraints on an optimum combination of loadings arises, the following expression can be used:

$$C_{m,\text{des}} = C_{m,\text{cruise}} - \frac{\partial C_m}{\partial C_L}\left(C_{L,\text{cruise}} - C_{L,\text{des}}\right)$$

This expression provides a design moment at $C_{L,\text{des}}$, which in combination with a moment increment due to the difference between $C_{L,\text{cruise}}$ and $C_{L,\text{des}}$ yields the desired $C_{m,\text{cruise}}$.

Although wing-design codes provide for the design of surfaces meeting specified moment restraints, this capability should be used cautiously for supersonic cruise vehicles. As shown in figure 28, the imposition of seemingly mild $C_{m,\text{des}}$ restraints can have large effects on lifting efficiency. This example is for a 70° swept arrow wing designed for a lift coefficient of 0.16 at a Mach number of 2.05 by use of the WINGDES2 code, but the results are typical. If, for example, twist and camber were employed to shift the center of pressure from the unrestrained design location of about $0.50\bar{c}$ to a location of about $0.25\bar{c}$ to be more consistent with the presumed subsonic location, a design moment coefficient of zero would be required. This requirement would result in about a 35-percent reduction in suction parameter or about a 10-percent reduction in $(L/D)_{\max}$. Consideration in providing trim for supersonic cruise flight should be given to configuration center-of-gravity selection, to fuel management, or to other nonaerodynamic means. Combating the aerodynamic-center

shift from subsonic to supersonic speeds will generally be accomplished with less penalty by the use of subsonic rather than supersonic aerodynamic devices. See reference 34 for a study of subsonic moment control systems including flaps, canards, and horizontal tails.

Test Cases of Empirical Method

Existing experimental data such as those reproduced in this paper can be used to assess the validity of the empirical design and evaluation methods. For an existing wing surface, it is first necessary to establish a design lift coefficient by use of an evaluation code (in this case the evaluation mode of WINGDES2). Then the factor K_D is applied to find the cruise lift coefficient for which this surface would have been designed if the empirical design selection method had been applied directly. In a certain sense, it is an inverse application of the empirical design and estimation method.

Such an application for the 70° swept arrow wing originally designed for a cruise lift coefficient of 0.08 at a Mach number of 2.00 (tested at $M = 2.05$) is illustrated in figure 29(a). Because data for this wing (shown in fig. 8) were included in the derivation of the method, good correlation would be expected; therefore, this example does not provide a true test of the applicability of the method. It does, however, offer a good example of factors to be considered in the use of the method. The key theoretical data as generated by the WINGDES2 code in its evaluation mode are shown at the left of the figure. The effective design lift coefficient is established by the peak of the suction parameter curve which in this case occurs at a lift coefficient of about 0.085 only slightly different from the original design value. A reference to the curve for K_D of figure 27 shows that for the test Mach number of 2.05, an appropriate cruise lift coefficient would be

$$C_{L,\text{cruise}} = \frac{1}{K_D} C_{L,\text{des}} = 0.12$$

In other words, if the desired cruise lift coefficient had been 0.12, the proper design lift coefficient would be 0.085, and an appropriate wing surface design (found by the WINGDES2 code or any other valid linearized theory method) would display the characteristics shown here. The plot of α versus span station shows that for most of the span α_{zt} is only slightly less than α_{des} (the angle of attack corresponding to the design lift coefficient). This is an indication of a good design for effective recovery of theoretical leading-edge thrust by a sharp leading-edge wing. The range of full thrust (the whole space between the curves for $\alpha_{zt} + \Delta\alpha_{ft}$ and $\alpha_{zt} - \Delta\alpha_{ft}$) shows a substantial margin of error which should ensure relatively good performance. Application of the empirical estimation method to the theoretical data provides an estimate of actual performance which as shown at the right of the figure agrees well with the experimental data. Note that good performance as measured by the suction parameter extends well beyond the value for $C_{L,\text{cruise}}$. The measured suction parameter of about 0.35 for the cruise lift coefficient represents a relatively efficient lifting surface for this Mach number. Full recovery of the theoretical flat wing leading-edge thrust would yield a suction parameter of about 0.56.

The second example, also from data used in derivation of the empirical method, is included to illustrate a design similar to that produced by the WINGDES2 code in the default mode where the range of attainable thrust is used to an advantage in achieving a milder camber surface than would otherwise be required. Figure 29(b) shows data for a 72.65° swept wing ($\beta \cot \Lambda_{le} = 0.75$) from reference 11. The plot of α versus span station shows that for most of the span the upper limit of the range of full thrust is only slightly greater than the design angle of attack. This fits the description of a wing designed for the mildest possible camber surface yielding a performance comparable with that of a flat wing with full theoretical leading-edge thrust. As might be expected, the empirical estimate agrees well with the measured data. Note that above $C_{L,\text{cruise}}$, the measured suction parameter decreases at a more rapid rate than for the previous wing because the design approach is aimed at production of a mild camber surface.

Illustrations of the application of the empirical methods in figures 29(c) to (l) are for data not included in the derivation, and thus they provide a valid test. Data for a 75° swept arrow wing designed for a lift coefficient of 0.16 at a Mach number of 2.00 (tested at $M = 2.05$) are shown in figure 29(c). Data for this wing were first shown in figure 12. The theoretical data for this wing in combination with the empirical factor K_D indicate that it would be an appropriate design for a cruise lift coefficient of about 0.25 not 0.16. There also must be some reservation about the degree of thrust recovery beyond a span station of about 0.8 as indicated by the plot of α versus span station. Unfortunately, this region is where the numerical solution is least accurate because of the small number of elements used to represent the surface. As pointed out previously, there is good reason to employ clipped tips for arrow wings. In spite of this reservation, the empirical

estimate gives a reasonable prediction of the actual performance. For a lift coefficient of about 0.2 where the experimental suction parameter data reach a maximum and flatten out, the corresponding α is about $-1.3°$. At this angle, code results indicate that thrust recovery would be complete to about 95 percent of the span.

Data for the aspect ratio 2 wing–body with conical camber at a Mach number of 1.30 in figure 29(d) show a very good empirical estimate of the measured performance. Actually at a supersonic Mach number this low, the empirical factor is very close to 1.0 and the theory alone gives a good estimate of the expected performance. (See fig. 5(a).) The curve for $\alpha_{zt} + \Delta\alpha_{ft}$ and its close correspondence with the α_{des} value for most of the semispan indicate a good design for thrust recovery. The dip in the curve near the 0.15 semispan station is caused by the inadequate numerical representation of the wing–body juncture and is not of any practical significance.

Data for the conically cambered wing at a Mach number of 1.70 in figure 29(e) show a relatively poor performance. For values of C_L in excess of about 0.16, the measured suction parameter is well below the empirical estimate because of a poor design for thrust recovery at the cruise C_L, which is indicated by the plot of α versus span station. At all span stations, $\alpha_{zt} + \Delta\alpha_{ft}$ is considerably below the design angle of attack for $C_{L,cruise}$.

Measured suction parameter for the arbitrary planform wing–body wing design with no restraint shown in figure 29(f) agrees well with the empirical estimate. The failure of the range of full thrust to match α_{des} outboard of the 0.85 semispan station is of no consequence because the leading edge is supersonic and there is no theoretical thrust to be recovered. Data in figure 29(g) for a wing of the same planform designed with a severe restraint ($\Delta C_p = 0$ at the leading edge and only a gradual buildup with increasing distance behind the leading edge) do not quite fit the definition of a good design as described in this paper. The good prediction of suction parameter shown here may be somewhat fortuitous.

The 74° swept arrow wing–body whose data are shown in figure 29(h) has a pronounced upsweep of the wing apex (a large local angle of attack), which is responsible for the large negative values of α_{zt} for the inboard semispan positions. Large differences between α_{des} and the upper limit of the range of full thrust $\alpha_{zt} + \Delta\alpha_{ft}$ could easily imply a separated flow. This separation in turn could prevent the development of an upwash field like that predicted by the theory and could have a serious detrimental effect on wing performance. The α_{zt} and range of full thrust distribution also suggest that distributed thrust loadings in the vicinity of the wingtip would not be achieved. It is thus not surprising that the estimated performance is not realized.

The 75° swept modified arrow wing–body treated in figure 29(i) has an even more pronounced upsweep of the wing apex, which was first noticed in the discussion of figure 23. The large discrepancy between the design angle of attack and the upper limit of the attainable thrust range gives a strong indication of the probability of flow separation which could not only prevent thrust recovery at the inboard stations but also could adversely affect the relationship between the developed upwash and the surface shape of the outboard stations. The measured suction parameter data confirm this assessment. As discussed previously, the estimated suction parameter derived from the curve for K_S of figure 27 represents an approximate upper limit of performance achievable only with a properly designed surface.

Data for the supersonic transport wing–body first treated in figure 24 are shown in figure 29(j). At the estimated cruise lift coefficient, there is close agreement of the estimated and measured suction parameters. The somewhat larger experimental suction parameters at lower lift coefficients may be the result of the selection of too high a value of $C_{D,0}$ in the absence of flat wing data. The importance of flat wing reference data to the proper evaluation of lifting efficiency cannot be overstated. The cruise C_L suction parameter of about 0.22 represents a relatively efficient design for this planform and a cruise Mach number this high. The supersonic leading edge of the outboard 25-percent of the wing semispan produces no theoretical leading-edge thrust and no opportunity for thrust recovery design.

In figure 29(k), data are shown for a 60° swept wing–body with a wing surface designed for a lift coefficient of 0.05 at a Mach number of 1.80 (tested at $M = 1.60$). For this mild camber surface, with sections which produce a relatively large range of full thrust, good correlation of estimated and measured suction parameters would be expected.

Results for the mission adaptive design of the same wing planform for $C_L = 0.30$ at $M = 1.60$ shown in figure 29(l) are quire different. The previous discussion of data for this design when first introduced in figure 25 explained the difficult design problem that is represented here. The curves for the range of full thrust in figure 29(l) reveal some additional possibilities to explain the failure of the design. The characteristics shown are similar to those shown

in figure 29(i). As in the previous case, the desired recovery of theoretical leading-edge thrust would be thwarted by the poor alignment of the wing surface with the upwash field. For this mission adaptive design, the design surface extends from the 0.13 semispan station to the wingtip, and over this range control of the leading-edge flow matchup should be possible. However, only for a very limited portion of the wing semispan does the upper limit of the range of full thrust approach the design angle of attack. This suggests that the TAFIX feature of the WINGDES2 code was not employed. Implementation of this adjustment as described in reference 18 compensates at least in part for failures of the numerical solution to provide the proper leading-edge camber (a coincidence of the upper limit of full thrust $\alpha_{zt} + \Delta\alpha_{ft}$ with the design angle of attack α_{des}). In most cases, this is merely a "fine tuning" operation, but for special cases such as this mission adaptive design where candidate design surfaces are restricted to a small portion of the wing chord, its application may be essential. In addition, in order to give a representation of the restricted areas as accurate as possible, the maximum allowable number of code wing elements should be employed.

In accordance with the preceding suggestions, a new design of the mission adaptive surface was undertaken. The numerical solution employed 32 semispan elements (JBYMAX = 32) and 1902 total elements, the maximum allowable for this planform and Mach number with the present version of the code. In addition the TAFIX option was employed by using the suggested values provided by the first run in a second run. As in the original application, no C_m restraint was applied. The plot for range of full thrust shown in sketch AA displays a much more reasonable match of the leading-edge surface with the upwash field. The code does not provide a sufficiently detailed representation of the lifting surface to avoid the abrupt changes in the vicinity of $\frac{y}{b/2} = 0.13$ caused by the wing-fuselage juncture. A design using only the wing planform and excluding the fuselage forebody would yield a better behaved solution. The remaining mismatch in the vicinity of the wingtip is probably caused by a still inadequate representation of the mission adaptive surface. Near the wingtip only 1.1 elements (on the average) are included in the 20-percent chord of the mission adaptive surface. Results from previous examples of application of the empirical method indicate that this new design should offer improved performance.

The data of figure 25(b) in combination with the plot of α in figure 29(l) may be used to illustrate the effects of flow separation on drag. As illustrated in

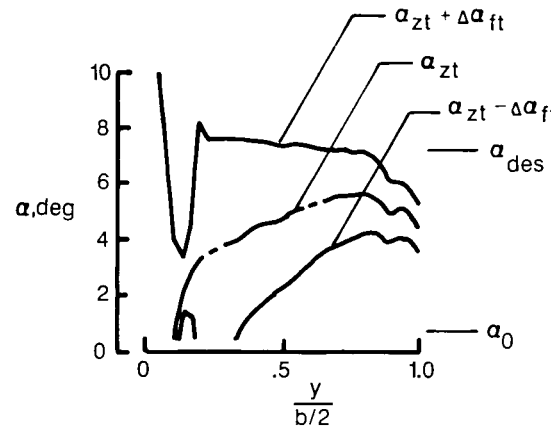

Sketch AA

the plot of α, there is no angle of attack at which attached flow is indicated for the full wingspan. The best matchup is for angles in the range from 3° to 5° or lift coefficients of about 0.1 to 0.2, where some agreement between theory and experiment exists. At higher lift coefficients, the failure to provide conditions favorable to thrust recovery and the maintenance of attached flow can produce severe drag penalties. At low lift coefficients, the theoretical performance which is predicated on an assumption of attached flow indicates a substantial drag penalty relative to that of a milder surface properly designed for that lift coefficient. At $C_L = 0$, for example, a flat wing ($C_{L,des} = 0$) would have a drag coefficient of 0.0250. If flow on the severely warped wing remains attached, the theory indicates a drag level considerably higher (about 0.0310). However, measured values are not that high (about 0.0280). Under these circumstances separation causes drag reduction. For the theoretically attached flow, the total lift would be zero, but high levels of localized lift (both positive and negative) would be present to contribute to the drag. Thus, the failure to realize this local lift as a result of flow separation also prevents the occurrence of the associated drag.

In general, the empirical methods give a reasonable prediction of the relationship of the measured performance (both the maximum suction parameter and the lift coefficient at which it occurs) to the theoretical prediction. Even for those cases where the agreement with experimental data is poorer than would be desired, the empirical estimate offers a considerable improvement over the use of linearized theory alone. Failure of the designed wing surface to provide a reasonable leading-edge matchup with the upwash field ($\alpha_{zt} + \Delta\alpha_{ft} \approx \alpha_{des}$) provides a warning of a serious deterioration in wing performance. Not only will the theoretical potential be reduced,

but more important, such a mismatch could lead to flow separation which would result in drastic losses in performance.

Use of the empirical guidelines in conjunction with computer-code-generated wing data such as those shown in figure 1(c) should provide a valuable preliminary design tool for wing planform trade studies. The linearized theory methods require little effort in preparation of input data and can be executed in a relatively short period of time. Data for the curves of figure 1(c) (21 computer runs) were assembled in an elapsed time of about 2 days. When applied to such data, the empirical factors provide realistic estimates of actual performance and the required surfaces for use in trade-off studies.

Integration of Wing Design Into Complete Airplane Configurations

A number of published works, for example references 35 to 44, have addressed the problem of combining a well-designed wing camber surface with other airplane components so as to retain or even enhance the wing performance. In this section, some of the more important of these considerations are described and explained.

Shearing of Design Surface

The linearized theory, on which most of the current methods of twisted and cambered wing design are based, sets specific requirements for the surface slope with respect to the flight direction (chordwise) but imposes no restrictions on the slope with respect to lateral direction (spanwise). Results from an experimental investigation reported in reference 36 which illustrate the importance of lateral-slope considerations are shown in figure 30. The models were variations of the basic wing design for a Mach number of 2.0 and a lift coefficient of 0.08 described in reference 10. Data for this wing at a Mach number of 2.05 were shown in figure 8. These wings have been sheared to provide a flat lateral section at various stations x^* along the root chord of the wing, as shown in the inset sketch in figure 30. The variation of measured $(L/D)_{\max}$ with the shear parameter x^*/c_r is shown, along with sketches of the side views of the semispan wings. The experimental data indicate that maximum performance is attained for values of x^*/c_r near 0.5. The best results appear to be obtained when the surface is arranged to lie in as nearly a single plane as possible without changing the streamwise slopes. The results of an experimental study in which wing dihedral is the variable (ref. 37) lead to a similar conclusion. Those results have lead to a rule which might be called the "minimum packing case theory."

Fuselage Integration

An important consideration in the application of twisted and cambered wing design is the manner in which the wing and the fuselage are combined. Reference 38 gives maximum lift-drag ratios at a Mach number of 2.02 for wing-fuselage combinations employing the basic cambered wing of figure 30, and these data are presented in figure 31. Also, for reference purposes, data are presented for a combination in which the uncambered (flat) wing is used. The theory values are those given by the WINGDES2 code. At one time the belief was that a fuselage aligned with the free stream (configuration A) would be beneficial because it would cover up the troublesome inboard wing region having large surface slopes. Experimental data for the first of the cambered and twisted configurations in figure 31 indicate, however, that the combination with a fuselage so aligned has a maximum lift-drag ratio only slightly larger than that of the flat configuration. Another possible way of combining the wing and fuselage is to align the fuselage with the wing root chord (configuration B). As shown in figure 31, the maximum lift-drag ratio for this combination is considerably larger than that for the flat configuration. Configuration C in this figure has a fuselage which is aligned with the root chord but has a reflex at the wing apex and at the root-chord trailing edge. In effect, the thickness of this configuration, both wing and fuselage, is displaced symmetrically about the camber surface defined for the wing planform. For the design condition of $C_L = 0.08$, the fuselage ahead of and behind the wing surface is aligned with the free stream and carries little or no lift. This wing-fuselage combination produced the highest maximum lift-drag ratio of the test configurations; the ratio was about 10 percent better than that of configuration A. Such an arrangement of the configuration volume appears to preserve the distribution of wing loading prescribed by the wing theory. Theoretical maximum lift-drag ratios evaluated by use of the mean-camber-surface concept, which is discussed in the following paragraph, predict reasonably well the performance gains of B and C in figure 31 but fail to properly assess the penalties associated with the streamwise fuselage alignment. Additional information on the influence of fuselage camber on the performance of twisted and cambered wing-fuselage configurations is given in reference 39. As depicted in figure 31, a normal whole wing design calls for a root chord with some positive incidence, which could result in an undesirable cabin floor angle. This incidence can be reduced with some

small penalty in lifting efficiency by use of optional features of the WINGDES2 code described in the appendix in the section "Notes on Code Application."

Mean Camber Surface

The concept of a mean camber surface is quite useful in analyzing the characteristics of a wing–body configuration with appreciable thickness. An application of this kind of analysis to the prediction of interference effects for a delta wing–wedge body model at $M = 2.00$ (ref. 40) is shown in figure 32. Lift-drag polars and curves for angle of attack as a function of lift coefficient are shown for a high-wing and a low-wing configuration. The lift characteristics have been estimated from program calculations for a warped surface formed by the locus of points midway between the upper and lower model surfaces. Since the numerical solution cannot work with discontinuous slopes, it is necessary in this example to approximate the mean camber surface with a surface that varies gradually from element to element. The step in the surface is thus replaced by a series of ramps extending over a number of grid elements. This modeling is obviously an extreme case of a warped wing surface. The data show that the high-wing configuration has lower drag at the lifting condition than does the low-wing configuration and that the theory correctly predicts this drag. The mean camber surface used to represent the high-wing model more nearly corresponds to the surface required for an optimum combination of loads. The use of favorable-interference concepts, as exemplified by the high-wing model, is in a sense a special case of twist and camber. As shown at the right of the figure, the theory somewhat overestimates the influence of the wedge in the generation of interference lift, perhaps because in real flow the body pressure field extends some distance ahead of the theoretically sonic leading-edge wing. Since a mean camber surface may be used to represent the lifting effects of a wing–body combination, it would be expected that, conversely, lifting effects for a theoretically determined mean camber surface would be best retained with a symmetrical distribution of thickness above and below that surface.

Nacelle Alignment

Positioning of engine nacelles or stores has an important influence on configuration aerodynamic characteristics. Substantial variations in wave drag at zero lift can result from variations of nacelle location relative to the wing-fuselage. As illustrated in figure 33, nacelle alignment also influences the drag. This figure presents data from reference 41 and shows the variation of ΔC_D for the wing-nacelle combination with alignment or cant angle at $C_L = 0.16$. By definition, the drag increment is zero for zero cant angle. As shown in the inset sketch, a nacelle-pylon installation experiences a side force due to the flow angularity produced by the wing. A component of the force acts in the drag direction. When the nacelle is aligned with the local flow, no side force and no drag components are present. When the nacelle is aligned with the airplane axis or the free stream, a side force normal to the nacelle is present but the drag component is zero. For a cant angle larger than the flow angle, the side-force vector reverses and considerable drag can result. Also, for negative cant angles, the drag penalties can become large. Note that a thrust, not a drag, is indicated for cant angles between the free stream and the local flow, with the maximum thrust halfway between the two. Setting a nacelle-pylon combination at such an angle results in somewhat higher drag at zero lift but produces, as does a twisted or cambered wing, a reduction in drag at design conditions. Calculation of local flow angle is not now a part of the WINGDES2 computer code but may be handled by a graphical integration of pressure to obtain velocity potential and a subsequent differentiation to obtain surface velocities. When calculated surface angles are used to optimize nacelle-pylon alignment, some correction should be made for the tendency to overestimate flow angularity off the wing surface at the pylon location. In the example given in figure 33 the measured flow angle at the nacelle was only about two thirds the predicted surface angle. These considerations are also applicable to any vertical surfaces displaced from the airplane axis (e.g., outboard vertical fins). This rather simplified analysis of a complex situation has proved effective in obtaining drag reduction.

Other Considerations

Other considerations involved in integrating twisted and cambered wing technology into complete supersonic cruise vehicles are discussed in references 32, 33, and 42 to 45. Foremost among the topics treated in those references, but not here, is the use of fuselage shaping in the reduction of wave drag at zero lift. These references also treat the problem of shaping and locating engine nacelles for minimum wave drag. Another technique also discussed is the use of wing camber surface reflexing in the vicinity of the nacelles to produce favorable interference effects. A numerical method for implementing nacelle interference wing surface design is given in references 21 to 24 and 46. The WINGDES code can also be used for wing reflexing design. The code user, however, must first provide a nacelle interference pressure field as described in the appendix and must also describe

an input trailing-edge design surface matching the boundary of the nacelle pressure field.

Euler Code Analysis

Modified linearized methods, even the calibrated system previously described, are not sufficiently accurate to replace wind tunnel testing in the final stages of engineering development for complex airplane configurations. This study includes an assessment of the applicability of a more advanced analysis method to one set of wind tunnel data. An Euler equation numerical solution described in references 47 and 48 has been applied to the data for the 70° swept arrow wing of references 9 and 10, which have been previously treated in this paper. The Euler code known as EMTAC (Euler marching technique for accurate computation) is valid for low and high supersonic Mach number flows with strong shocks and rotational effects.

Mathematical Model and Code Parameters

The surfaces of the 70° arrow wings were defined for the code as a series of cross sections at different longitudinal stations along the wing centerline. The cross sections were divided into upper and lower surface patches. Typical cross-section grids for the wing with $C_{L,\text{des}} = 0.16$ are shown in figure 34. As shown in these sections, the grid is clustered in the region of the wing leading edge, which for this solution was considered to be sharp. Consideration of the blunted leading edge with an estimated constant leading-edge radius of 0.004 in. used in the analysis with modified linearized theory would have presented a much more difficult problem. The consequences of the decision to use a sharp leading-edge solution are discussed later.

A flow-field grid resolution study was performed by varying the number of grid points in the circumferential and normal directions at the wing cross sections. The grid was varied from a minimum density of 30 points along the circumference to a maximum of 60 points and from a minimum density of 15 points normal to the surface to a maximum of 27 points. In trial solutions involving various combinations of circumferential and normal densities, the solution was more sensitive to grid density in the circumferential direction than the normal direction. Figure 35 shows the code-evaluated lift, drag, and pitching-moment coefficients as a function of the cross-section grid density expressed as the product of the number of circumferential points and the number of normal points. Data points for a variety of combinations of circumferential and normal points fell close to the plotted curve. As shown in the figure, the calculated coefficients have essentially converged for a grid density of 1200. A grid of 60 circumferential and 25 normal points (1500 cross-section grid points) depicted in figure 34 was used in derivation of the code data presented in this paper. The longitudinal step size was varied between 0.02 and 0.05 in. (model length of 30 in.), depending on wing geometry and angle of attack. The computed forces and moments were not significantly affected by step size variation within this range.

The EMTAC code uses a space-marching technique which proceeds down the length of the wing. A conical solution is used as a starting solution for the input geometry. The longitudinal location at which the conical solution terminates and the solution on the actual wing geometry begins is specified by the user. A stable solution is dependent on this starting location. Most solutions were obtained with a starting location of 0.75 in. (2.5 percent of model length); however in some cases for the higher angles of attack, a starting location of 2.0 in. (6.7 percent of model length) was required.

Correlation of Euler Code and Experimental Results

Pressure distributions provided by the Euler code and experimental measurements from reference 10 are provided in figure 36. Similar comparisons for the basic linearized theory were given in figure 10. In general, for all three design lift coefficients (figs. 36(a), (b), and (c)), the Euler code results give an improved correlation with the measurements. Improvements over the linearized theory results are particularly noticeable at the higher lift coefficients in the region of the wing leading edge, where the linearized theory singularity is obviously incorrect. Euler code results are questionable only for the outermost wing semispan stations where even a very small grid increment can extend over a substantial portion of the wing section chord.

Figure 37 shows the experimental results and the Euler code forces and moments obtained by integration of code surface pressures. The curves labeled Euler code (the long-dash line) include a skin friction component determined by subtraction of the Euler code drag coefficient for the flat wing at $\alpha = 0°$ from the experimental $C_{D,0}$. This skin friction component was added to all the Euler code drag coefficients. The results show a reasonable but not exact correspondence of the code predictions with the experimental data. Normal-force and pitching-moment predictions are quite good, a noticeable improvement over the modified linearized theory prediction shown

in figure 8. However, a significant overestimation of the measured axial force and drag occurs with a corresponding underestimation of the suction parameter. The net result is that the performance estimate of the more advanced code is little better than that of the modified linearized theory. (See fig. 8.)

Analysis of Theoretical-Experimental Discrepancies

In the modified linearized theory used in this paper, any departure from an axial force that is invariant with angle of attack for a flat wing is interpreted as an attainment of some amount of leading-edge thrust. Euler code data for the flat wing shown in figure 37(a), however, show some variation of axial force with angle of attack even though the sharp leading-edge solution eliminates the possibility of a calculated leading-edge thrust. The Euler code prediction of a small variation of axial force with angle of attack results from integration of surface pressures which depart from the linearized theory behavior in which upper and lower surface pressure increments due to angle of attack are of equal magnitude and opposite sign. Because this change in axial force is associated with pressures acting over the whole of the airfoil section rather than a concentrated force in the immediate vicinity of the leading edge, it does not represent a leading-edge thrust. This force is included as a part of the attainable thrust estimate described in reference 28, because calibration of the system is based on measured axial-force data which account for all departures from linearized theory.

For the flat wing at all angles other than zero and for the twisted and cambered wings at angles above and below those corresponding to the design lift coefficients, the experimental data of figure 37 show direct evidence of an actual attained leading-edge thrust. An estimate of the forces that might result from inclusion of a leading-edge thrust in an Euler code solution may be obtained by applying a correction for the presence of attainable leading-edge thrust derived from the WINGDES2 code. First an average angle of attack for zero thrust ($\Delta C_{p,\mathrm{le}} = 0$) over the wing semispan was found from an examination of the pressure data of figure 36. Then attainable thrust estimates for a flat wing from the WINGDES2 code were subtracted from the Euler code axial force symmetrically about the angle of attack for zero thrust. This adjustment would be expected to overestimate the thrust force because, as discussed in the previous paragraph, the estimated attainable thrust increment includes a contribution already accounted for by the Euler code solution. As shown in figure 37, Euler code results with the adjustment (the short-dash line) give an improved correlation with the measured axial-force, drag, and suction parameter relative to the unadjusted results (the long-dash line). The thrust is not overestimated because, as shown in figure 8(a), the attainable thrust estimate does not fully predict the measured flat wing thrust.

A further explanation for the behavior of the Euler code force data relative to the experimental force data may be seen in the pressure data of figure 36. Measured upper surface pressures in the vicinity of the leading edge for C_L greater than $C_{L,\mathrm{des}}$ are generally greater (more negative) than the code results. Higher than predicted peak pressures just behind the leading edge may be associated with the attainment of some degree of leading-edge thrust. Higher pressures which peak aft of the leading edge (for example, the data at the semispan station of 0.3 for the flat wing) indicate the possibility of a larger contribution of a separated leading-edge vortex flow than predicted by the Euler code.

One difficulty that may be encountered in application of Euler codes to problems of this nature is an inability to correctly predict a partial development of leading-edge thrust and a partial development of a separated vortex flow. As indicated in reference 49, a fully attached flow solution can be achieved for blunt leading edges with proper attention to grid refinement and the selection of an appropriate finite-difference scheme. The resultant leading-edge force will very likely be less than the linearized theory full thrust value but could still give an overly optimistic estimate of the thrust that can actually be achieved if some degree of separation is present. As indicated in references 49 and 50, a Navier-Stokes solution appears to be a more promising method for the accurate prediction of leading-edge thrust and wing performance levels. However, in the case of one of the wings examined in reference 50, the assumption of a laminar or turbulent boundary-layer model determined whether the flow at the leading edge was separated or attached. Perhaps, as with linearized theory, advanced computational aerodynamic methods will have to rely on empirical criteria to account for leading-edge flow separation and its effect on leading-edge thrust.

Comparison of Euler Code and Linearized Theory Camber Surface Selection

As previously shown, linearized theory without benefit of a correction based on a large collection of experimental data is incapable of selecting the proper amount of twist and camber for a particular application and fails in estimation of the achievable

performance. The following example is presented to test the ability of the Euler code to serve this purpose. Figure 38 shows suction parameter at each of the three selected lift coefficients as a function of the design lift coefficient designating the amount of twist and camber. As previously mentioned in the discussion of figure 9, the linearized theory predicts a greater level of efficiency (higher suction parameter) than is actually achieved and calls for a more severe surface (greater departures from a flat surface) than is actually required. In contrast, the Euler code predicts a lower level of efficiency than is realized. With the addition of the attainable thrust estimate, however, the predicted optimum design lift coefficient and suction parameter more nearly match the experimental results.

The results of this study of the application of an Euler code to a representative wing analysis problem indicate that the Euler code employed herein and other computational fluid dynamics methods offer much promise. However the results found here also indicate that extensive correlations with reliable experimental data are required to firmly establish the applicability and limitations of the new techniques. For this purpose, pressure distribution correlations alone can be misleading. The appearance of the pressure distribution correlation plots for the examples treated here led to anticipation of an agreement with force data that was not realized. An analysis of the discrepancies indicated that much of the problem is associated with the handling of the leading-edge radius of a "sharp" wing section which actually has a degree of bluntness and results in achievement of an appreciable amount of leading-edge thrust.

The supersonic wing designer can resort to corrected linearized theory methods while new computational fluid dynamics methods are being developed and verified. These simpler and faster strategies may continue to be employed well into the foreseeable future, particularly for configuration selection and preliminary design. They also may be useful in providing initial designs for use in design processes employing computational fluid dynamics analysis methods coupled with optimization techniques.

The modified linearized theory evaluation method with nonlinear corrections (LTSTAR) shown in figure 39 is described in reference 51. In this case, the LTSTAR method provides a good estimate of the achievable performance and the required twist and camber. The method, however, does not always provide this degree of correlation, as shown by other correlations presented in reference 51. In selection of the proper design lift coefficient and in estimation of the wing performance, the LTSTAR method does not offer any significant improvement over the simpler strategy described in the section "Empirical Design Guidelines." As might be expected for a set of data used to calibrate the system, the semi-empirical method results shown in figure 39 give a good indication of the optimum design lift coefficient and the achievable performance level. From examples given previously, similar prediction abilities should apply to other wing designs that meet the requirements for thrust recovery and prevention of flow separation.

Conclusions

A survey of research on drag-due-to-lift minimization at supersonic speeds including a study of the effectiveness of current wing design and analysis methods has yielded the following conclusions:

1. Measured levels of lifting efficiency for wings without twist or camber fall far short of the theoretical potential because only a small fraction of the full theoretical leading-edge thrust is actually realized and the vortex forces that result from flow separation have little beneficial effect on performance.

2. The lifting efficiency of wings without twist or camber (as measured by the suction parameter) can be predicted with reasonable accuracy by a modified linearized theory computer code which accounts for attainable thrust and vortex force contributions.

3. Wings with twist and camber, which substitute a distributed thrust over a broad leading-edge region for the concentrated flat wing leading-edge thrust, generally offer better performance than that of the flat wing but at levels still short of the theoretical potential.

4. Extensive comparisons of theory and experiment for twisted and cambered wings reveal a consistent qualitative pattern in which maximum suction parameter is overestimated by the linearized theory, and the required surface for given flight conditions is less severe than that given by the theory.

5. Analysis of data including pressure distributions indicates that an unrealistic theoretical prediction of the magnitude of the wing upwash field is the primary cause of the discrepancy and that the use of a theoretical design lift coefficient less than the desired operational lift coefficient offers an appropriate correction for linearized theory design methods.

6. A further analysis of the data led to the development of an empirical method for the selection of the proper design lift coefficient and for the estimation of achievable aerodynamic performance.

7. Information provided by the WINGDES2 code was found to give an indication of the required

matchup of the leading-edge surface with the local upwash for effective recovery of leading-edge thrust and the prevention of appreciable flow separation with its associated performance penalties.

8. Application of the empirical estimation method to a series of sample cases showed that reasonable prediction of the measured performance (both the maximum suction parameter and the lift coefficient at which it occurs) was given provided that leading-edge matchup conditions were met.

9. Use of the empirical method in conjunction with computer code data should provide a valuable preliminary design tool for wing planform trade-off studies. The modified linearized theory methods require little effort in preparation of input data and can be executed in a relatively short period of time.

10. Additional suggestions for implementation of linearized theory wing-design methods for complete configurations were reviewed.

11. Application of an Euler code to evaluation of aerodynamic characteristics for one wing series resulted in improved correlation between predicted and measured pressure distributions. However, the improvement in prediction of overall aerodynamic efficiency was less than anticipated. An analysis of the discrepancies indicated that much of the problem is associated with the handling of the leading-edge radius of a sharp wing section which actually has a degree of bluntness and results in achievement of an appreciable amount of leading-edge thrust.

NASA Langley Research Center
Hampton, VA 23681-0001
May 1, 1992

Appendix

Wing-Design Computer Code

The wing-design code introduced in reference 18 generates an optimized twisted and cambered lifting surface for a given wing planform operating at specified flight conditions, provides the corresponding lifting-pressure distribution, and gives wing force and moment data. The code provides an analysis of the designed surface and may be operated in an analysis-only mode. Supersonic and subsonic speeds can be handled, but it is not a transonic code. Because the solution is based on the use of candidate surfaces, it can provide a twisted and cambered surface restricted to specified wing regions (a mission adaptive design) as well as a whole-wing design.

The numerical method is based on linearized theory potential flow solutions for a zero thickness lifting surface represented by an array of horseshoe vortices. A solution by iteration rather than by a matrix inversion is used. The code also provides for an estimate of attainable leading-edge thrust and of the forces caused by separated leading-edge vortices. Attainable leading-edge thrust considerations play a direct part in the design process, but vortex force estimates do not except for a reduction of design lift coefficient (and camber surface severity) caused by the vortex lift contribution.

The computer code WINGDES2—Wing-Design and Analysis Code—may be obtained for a fee from

Computer Software Management Information Center (COSMIC)
The University of Georgia
382 East Broad Street
Athens, GA 30602
Telephone: (404) 542-3265

Request the code by the designation LAR-13995. This code is written in FORTRAN V for use on the CDC® 6600 computer system and on the CDC® CYBER computer system.

The first record in the input is a code run identification that accepts up to 80 characters. The remainder of the input is placed in NAMELIST format under the name INPT1.

Wing Planform—Required Input

The wing planform information is specified by a series of leading-edge and trailing-edge breakpoints for a right-hand wing panel. Up to 30 pairs of coordinates may be used to describe the leading edge and up to 30 pairs to describe the trailing edge. The planform input data in program terminology are as follows:

NLEY	number of leading-edge breakpoints (limit of 30)
TBLEY (NLEY)	table of leading-edge y values; beginning at $y = 0$; increasing order of y from root to tip
TBLEX (NLEY)	table of leading-edge x values that corresponds to TBLEY table
NTEY	number of trailing-edge break points (limit of 30)
TBTEY (NTEY)	table of trailing-edge y values; beginning at $y = 0$; increasing order of y from root to tip
TBTEX (NTEY)	table of trailing-edge x values that corresponds to TBTEY table
XMAX	largest x ordinate anywhere on planform
SREF	wing reference area for use in aerodynamic force and moment coefficients

CBAR	wing reference chord for use in aerodynamic moment coefficients
XMC	x location of moment reference center
ELAR	element aspect ratio (default 1.0 for subsonic cases, $1.0/\beta$ for supersonic cases)
JBYMAX	integer designating number of elements in spanwise direction (limit of 50)

For subsonic speeds the element aspect ratio ELAR is chosen by the user (default 1.0). At supersonic speeds, a fixed value of ELAR = $1.0/\beta$ is imposed to avoid computational difficulties and the user has no option. For flat and mildly cambered wings at subsonic speeds, an element aspect ratio one half the full wing aspect ratio or greater is recommended. For wings with small chord leading-edge or trailing-edge design areas, it may be necessary to use a large element aspect ratio to place at least two elements within the chord. The number of elements in a given chord, c_{le} or c_{te}, may be approximated as

$$N = \frac{c_{le}}{b/2}\,(\text{JBYMAX})(\text{ELAR})$$

or

$$N = \frac{c_{te}}{b/2}\,(\text{JBYMAX})(\text{ELAR})$$

Because computational costs tend to increase as the fourth power of JBYMAX and the second power of ELAR, an increase in the element aspect ratio is the more efficient means of providing for improved definition. At supersonic speeds, where ELAR is fixed, the only recourse is to increase JBYMAX. This parameter controls the size of the wing in code dimensions.

The necessary scaling is done within the code by use of a scale factor, 2(JBYMAX)/(SPAN (β)). The number of complete wing elements N corresponding to a given JBYMAX may be approximated as

$$N = 4(\text{JBYMAX})^2\left(\frac{\text{ELAR}}{\text{AR}}\right)$$

The code has been written to accommodate 1000 right-hand panel elements (2000 complete wing elements). Generally, the JBYMAX integer is less than the limit of 50. The normal range is 10 to 20 for subsonic speeds and 20 to 40 for supersonic speeds. Computational costs tend to increase as the square of the number of elements.

Sketch A1 illustrates a typical wing planform and its representation in the code. Pairs of leading-edge and trailing-edge break points are selected to represent with reasonable accuracy the actual planform as a series of connected straight lines. For a supersonic solution with a small number of semispan elements (JBYMAX = 8), the code-generated planform would appear as shown. For a supersonic solution with a more usual number of semispan elements (JBYMAX = 20 to 40), the code-generated planform would much more closely resemble the code input. The step nature of the leading and trailing edges is a result of the requirement for unswept horseshoe elements to provide a stable supersonic solution. For subsonic speeds, swept leading and trailing edges can be handled and a reasonable code-generated planform requires far fewer semispan elements.

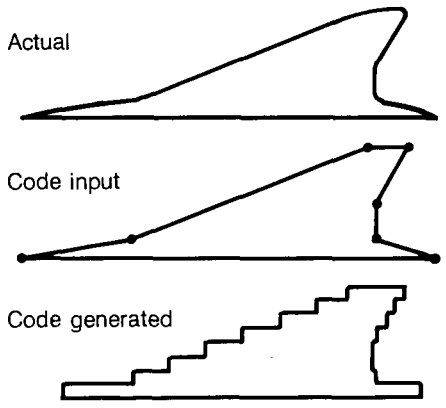

Sketch A1

Wing Camber Surface—Optional Input

A wing mean camber surface may be specified by a set of tabular entries. However, if a flat wing analysis is to be performed or if a flat wing is to be used as the initial surface in a design process, these entries are not required. If a wing surface is input, the section mean camber surface must be specified by exactly 26 chordwise ordinates at up to 52 span stations. When fewer than 26 camber coordinates are used to define the sections, the ordinate tables must be filled with enough zeros to complete the list of 26. The necessary section information is as follows:

NYC	number of spanwise stations at which chordwise sections are used to define mean camber surface (limit of 52)
TBYC (NYC)	table of y values for chordwise camber surface sections; beginning at $y = 0$; increasing order of y from root to tip
NPCTC	number of chordwise stations used in definition of mean camber surface (limit of 26)
TBPCTC (NPCTC)	table of chordwise stations, in percent chord, at which mean camber surface ordinates are defined; increasing order from leading edge to trailing edge
TZORDC (NPCTC, NYC)	table of mean camber surface z ordinates that corresponds to TBPCTC table; the full 26 values for root chord (including zeros for values in excess of NPCTC) are given first, followed by similar information for NYC spanwise stations in increasing order of y
TZSCALE	multiplying factor applied to TZORDC table to change camber surface ordinates

The TZORDC table may be multiplied by a scale factor TZSCALE. This factor may be useful if the original tabulated ordinates are nondimensionalized with respect to a single measurement (e.g., the wing root chord) or if it is necessary to evaluate the effect of change in camber surface severity.

Attainable Thrust and Vortex Force Data—Required Input

The following wing section information is required for the calculation of attainable leading-edge thrust and leading-edge separation forces:

NYR	number of spanwise stations at which information on airfoil sections is supplied (limit of 30)
TBYR (NYR)	table of y values for airfoil section information; beginning at $y = 0$; increasing order of y values from root to tip
TBTOC (NYR)	table of airfoil maximum thickness as a fraction of chord, t/c
TBETA (NYR)	table of section locations of maximum thickness as a fraction of chord, η
TBROC (NYR)	table of leading-edge radii as a fraction of chord, r/c
IVOROP	vortex location option as follows:
	0 full vortex force acts normal to wing reference plane at wing leading edge; does not contribute to axial force
	1 vortex center given by empirical relationships derived from delta wing experimental data (default)
	2 vortex center given by method of Lan (ref. 52)
YAPEX	spanwise location of vortex flow-field origin (default 0.0)

For special planforms such as forward-swept wings or other wings with an apex away from the centerline, the YAPEX input can help provide a better estimate of vortex-induced flow fields and forces.

The design procedure employed in the code is intended to provide the mildest possible camber surface that will yield an aerodynamic lifting efficiency comparable with that of a flat wing with full theoretical leading-edge thrust by utilizing to the fullest extent any thrust that may actually be developed. For such a design, as shown in sketch A2, the upper limit of the range of full thrust is made to coincide with the design angle of attack. For a more conservative design, one more comparable with previous design methods such as reference 19, an alternate approach may be taken. In this alternate approach, the wing design is performed with TBROC set to zero for the entire semispan. Then after the design run, a second run with actual values of TBROC is performed to estimate the wing performance. As indicated by sketch A3, for this design, the range of attainable thrust provides a factor of safety on either side of the design to minimize the effect of failures of the design procedures to properly match the surface to the upwash field in the vicinity of the leading edge.

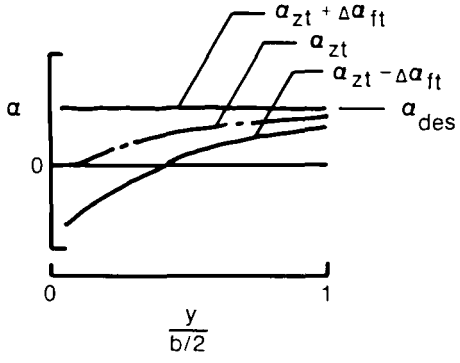

Sketch A2

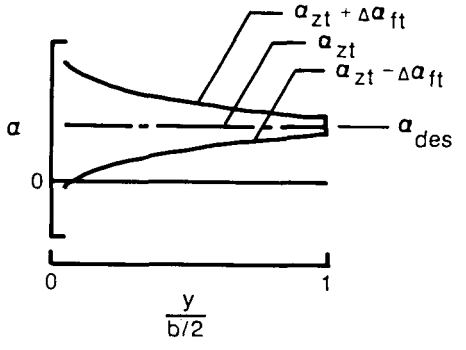

Sketch A3

For wing spanwise stations at which the leading edge is supersonic ($\beta \cot \Lambda_{le} > 1$), no theoretical leading-edge thrust is developed and the range of full thrust is zero. In the design process, however, the code still makes use of the calculated α_{zt} quantity, which for a twisted and cambered wing

is generally not zero. For this situation the α_{zt} value may be considered to represent the zero leading-edge loading condition resulting from an alignment of the leading-edge surface with the local flow ahead of it. Maintenance of the same flow alignment condition as for subsonic leading edges ($\alpha_{zt} + \Delta\alpha_{ft} = \alpha_{des}$) was found to yield a more efficient surface than other strategies and was adapted for supersonic leading edges also.

Flight Conditions—Required Input

The flight or test conditions are specified as follows:

XM	free-stream Mach number
RN	free-stream Reynolds number (based on $\bar{c}$) $\times 10^{-6}$
NALPHA	number of angles of attack to be calculated (limit of 19)
TALPHA	table of angles of attack to be calculated, deg

The commonly accepted practice of performing subsonic calculations for a Mach number of 0 is not appropriate for this code. Realistic estimates of attainable thrust can be made only if both the Mach number and the Reynolds number correspond to actual conditions. In fact, the code stops and writes an error message when XM = 0 is input. A wide range of angle of attack is required in order to use the code in the design mode. This range must cover the angle of attack for $C_{L,des}$ of the original and all subsequent surfaces. An error message is written when the angle of attack range is too small.

Solution Convergence Criteria—Optional Input

To determine perturbation velocity distributions for the input camber surface, the flat wing surface at an angle of attack of 1°, and the candidate camber surfaces used in the design mode, a maximum of 70 iterations are provided. If this number is reached without the convergence criteria being met, the results for the 70th iteration are printed with an appropriate message. The maximum number of iterations may be changed by the entry

ITRMAX	maximum number of perturbation velocity iterations (default 70)

The code convergence criteria are met when, for all wing surfaces, the average difference in perturbation velocity between successive iterations is less than one half of 1 percent of the average velocity over the wing. If the average velocity for any of the wing surfaces is less than the average velocity for the flat surface at $\alpha = 1°$, the flat wing surface value is used instead. In many instances, these criteria may be more stringent than necessary. If desired, the convergence criteria may be changed by the entry

CNVGTST	perturbation velocity convergence criteria (default 0.005)

Design Specifications—Required Input for Design Mode

The following entries control the solution for the optimized surface in the program design mode. For the analysis of a specified wing surface, omit these entries.

CLDES	design lift coefficient (if CLDES is not specified, the code defaults to CLDES = 0.0, which triggers an analysis-only solution)
CMDES	design pitching-moment coefficient (if CMDES is not specified, the code defaults to CMDES = 1000.0, which triggers an optimization solution without moment restraint)
ITRDESM	maximum number of design iterations (default 20)

See the section "Empirical Design Guidelines" of the text for comments on performance penalties that can result from imposition of CMDES restraints. This capability should not generally be used for supersonic cruise designs.

In attempting to meet the convergence criteria for wing design, the code provides for a maximum of 20 iterations. If this number is reached without the convergence criteria being met, the results for the 20th iteration are printed with a warning of the failure to meet the criteria. If desired, the maximum number of design iterations may be increased or decreased by the ITRDESM entry. The user has no control over the design convergence criteria.

Design Specifications—Optional Input for Design Mode

The rest of the design mode entries are optional. These can be valuable for program user control of the design process but are covered by program defaults if the user chooses not to exercise the options.

The user may select the number of general camber surfaces to be used in the optimization process as follows. These surfaces are described in reference 18.

NGCS	number of general camber surfaces covering the entire wing (limit of 8, default 8)

In addition, the user may select exponents that control the shape of the various surfaces by use of the following entries:

EXPY1, EXPY2, EXPY3, EXPY4	exponents of y used in definition of general camber surfaces (defaults: EXPY1 = 0.0, EXPY2 = 1.0, EXPY3 = 2.0, and EXPY4 = 3.0)
EXPX1, EXPX2	exponents of x' used in definition of general camber surfaces (defaults: EXPX1 = 1.5, EXPX2 = 2.0)

To preserve the original surface between the leading-edge modification surfaces and the trailing-edge modification surfaces for a mission adaptive design, NGSC may be set to zero. In this case, user options for both leading-edge and trailing-edge modifications must be employed.

The following entries control the region of the wing affected by the leading-edge modification surfaces. Because wing aerodynamic performance is critically dependent on the surface shape and pressure loading in the leading-edge region, these surfaces are essential to the optimization process.

NLEC	number of break points used in definition of area of wing to be affected by leading-edge modification surfaces (limit of 30, default 2)
TBLECY (NLEC)	table of y values at break points used in definition of area of wing to be affected by leading-edge modification surfaces; increasing order of y from wing root to wingtip (default 0.0, TBLEY (NLEY))
TBLEC (NLEC)	table of c_{le} values corresponding to TBLECY table (default TBTEX(1)—TBLEX(1) for both entries); see note under ELAR entry regarding definition of leading-edge areas; it may be necessary to change ELAR or to place limits on nonzero c_{le} values

The following entries control the region of the wing affected by the trailing-edge modification surfaces and the streamwise section shape of these surfaces. The code defaults exclude these surfaces.

NTES	number of trailing-edge modification surfaces (limit of 4)
NTEC	number of break points used in definition of area of wing affected by trailing-edge modification surfaces (limit of 30)
TBTECY (NTEC)	table of y values at break points used in definition of area of wing affected by trailing-edge modification surfaces; increasing order of y from root to tip
TBTEC (NTEC)	table of c_{te} values corresponding to the TBTECY table; see note for ELAR entry regarding definition of trailing-edge areas; it may be necessary to change ELAR or to place limits on nonzero c_{te} values
EXPXTE	exponent of $(x' - (c - c_{te}))$ used in definition of trailing-edge modification surfaces (exponents of y are the same as those used in definition of general camber surfaces) (default: EXPXTE = 1.5)

Sketch A4 shows a typical representation of leading-edge and trailing-edge modification surfaces for a supersonic mission adaptive design. The design areas are represented by hatching. Leading- and trailing-edge surface chords must be specified for the entire wing semispan even if the chords are zero. Where there is an abrupt change in chord, values of the chord should be specified for semispan stations just inboard and just outboard of the break. For a supersonic solution with a small number of semispan elements (JBYMAX = 8), the code-generated planform would appear as shown. For a supersonic solution with a more usual number of semispan elements (JBYMAX = 20 to 40), the code-generated design area planform would more closely resemble the code input. For a subsonic mission adaptive design, swept leading and trailing edges can be handled, and reasonable code-generated design areas require far fewer spanwise elements.

Program defaults provide candidate surfaces which generally provide a camber surface design with good aerodynamic efficiency. The program user, however, may want to tailor a camber surface solution more appropriate to the problem at hand and may want to search for solutions offering greater efficiency.

The code provides for an automated graphical flap-fitting technique, described in reference 53, which is activated by the following input:

IFLPDES	flap design index (set this index to 1 if the code is to be used to define a spanwise distribution of leading- and trailing-edge flap deflections which approximate the designed camber surface; use this option only for a design in which leading- and trailing-edge modification surfaces are specified; code defaults to an index of 0, which bypasses the flap-design feature)

When the flap-design feature is to be used, leading-edge and/or trailing-edge modification surfaces must be employed and NGCS must be set at zero. The chords of these surfaces are input as the chords of the flaps themselves. The code then designs a restricted-area camber surface for leading- and trailing-edge areas whose chords are set to 1.5 times the flap chords. (See sketch A5.) The original camber surface (a flat surface or a milder camber design such as for supersonic cruise) is then superimposed by rotation and translation on the new design. Differences in leading- and trailing-edge ordinates are then used to calculate flap deflections which approximate the designed camber surface. It must be emphasized that the flap deflections thus obtained are not necessarily optimum deflections but only approximations. The code aerodynamic characteristics do not apply to the configuration with flaps but to the smooth designed surface from which the flap geometry was derived. For subsonic cases, use of the evaluation code described in references 34 and 53

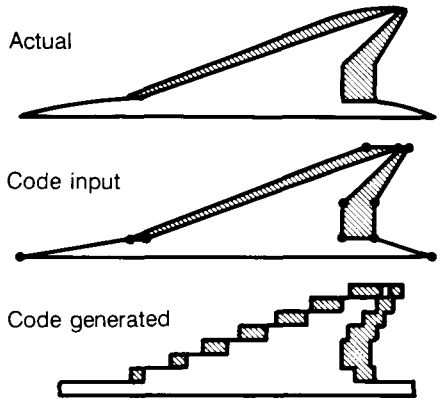

Sketch A4

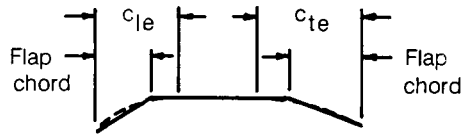

Sketch A5

can help provide a better estimate of true optimum deflections and the flap system aerodynamic characteristics.

Design Surface Smoothness Control—Optional Input

The following user option provides a degree of control over the smoothness of the camber surface solution. Code-determined weighting factors for the leading-edge modification surfaces are subject to numerical inaccuracies which may produce z ordinates that do not have a smooth variation with respect to the y dimension. See pages 19 to 23 of reference 18 for a discussion of the role of leading-edge modification surfaces in the design process and of the selection and use of leading-edge surface factors. In addition to the leading-edge surface weighting factors used in the design, the code also provides a listing of suggested replacement values that, as described in reference 18, may lead to improved performance. By using this option, the user may substitute a smoothed set of leading-edge surface factors for the code-tabulated values. With the present program, two runs are required: the first finds the nonsmoothed values and the second operates with the smoothed values.

IAFIX	smoothing operation indicator: set IAFIX = 1 if smoothed values are to be supplied (default 0)
TAFIX (JBYMAX)	table of smoothed surface weighting factors replacing code-generated table in same order of increasing span stations

Interference Flow Field—Optional Input

The computer code permits the design of a wing lifting surface with flow fields of other airplane components, such as fuselage, nacelles, or canards, taken into account. This design may be accomplished by the addition of a table describing the interference lifting pressure distribution on the wing surface generated by the other airplane components. This pressure field and the surface on which it acts, described by an input table, enter into the optimization process but, unlike the other surfaces and loadings, remain unchanged throughout the design.

The interference pressure field must be supplied by the user; normally, it is found by the use of some other aerodynamic analysis program capable of handling the desired airplane components. In most cases, two computer runs of this other program are required: one has all the airplane components represented, and one has only a mean camber surface that matches as closely as possible the fixed input camber surface (surface 1) of the wing-design code. The wing-design code interference lifting pressure field is then defined as the difference between these two loadings. By using the appropriate wing-design code options, the design surface may include only the wing outboard of the wing-fuselage juncture or may include the complete lifting surface, in which case a new fuselage camber surface is generated.

The following additional input data provide for a wing design with other airplane component-induced pressure fields taken into account. For normal program operation, simply omit these entries. If an interference pressure field is input, the distribution must be specified by exactly 26 chordwise positions at up to 52 span stations. When fewer than 26 chordwise positions are used to define the interference pressure field, the table for ΔC_p must be filled with enough zeros to complete the list of 26.

ICP	other airplane component-induced pressure field indicators; set ICP = 1 if this option is used (default 0)
NYCP	number of spanwise stations at which chordwise sections are used to define interference pressure field (limit of 52)
TBYCP (NYCP)	table of y values for interference pressure field chordwise sections; beginning at $y = 0$; increasing order of y from root to tip
NPCTCP	number of chordwise stations used in interference pressure field definition (limit of 26)
TBPCTCP (NPCTCP)	table of chordwise stations, in percent of chord, at which interference pressure field distributions are defined; increasing order from leading edge to trailing edge
TCP (NPCTCP, NYCP)	table of interference pressure field coefficients corresponding to TBPCTCP table; full 26 values for root chord (including zeros for values in excess of NPCTCP) are given first, followed by similar information for spanwise stations in increasing order of y
YFUS	spanwise station of wing-fuselage juncture; this entry limits wing general camber surfaces to values of y greater than that specified; leading- and trailing-edge camber surfaces may be limited by existing options; use of these limitations yields a design lifting surface confined to the wing outboard of the fuselage (default 0.0)

Code Output Data

The code is constructed so that successive runs may be made with a given computer entry. To make additional runs, it is only necessary to add an identification record and name list data that are to be changed from the previous run. An additional capability is provided by the entry NEWDES. When the code is run in the design mode and NEWDES is set to 1, a design camber surface is found, the input set of camber surface ordinates is replaced by camber surface ordinates for the new design, and this new design is treated as an evaluation case. In the original code, the default for the entry NEWDES was 0, which provided for a design of the wing surface but not for a subsequent evaluation. Now, however, because this feature has been found to be so useful, the default has been changed to NEWDES = 1. When the NEWDES option is used, successive runs may be employed to evaluate the new surface at off-design conditions.

The wing-design camber surface ordinates are printed for a reference angle of attack defined by an entry of ALPZPR (reference angle of attack) or CLZPR (reference lift coefficient). The default is ALPZPR = 0.0. When CLZPR is specified, the code calculates the corresponding ALPZPR and uses it in the determination of ordinates.

If the code user desires, span load distribution data may be printed. If the index IPRSLD is set to 1, section aerodynamic characteristics, including the separate contributions of basic pressure

loadings, attainable thrust, and vortex forces for each entry in the angle of attack table, are printed. These data are printed only for the evaluation mode or when the NEWDES option is used in the design mode.

The printed code results include the following items:

1. An iteration-by-iteration history of the convergence parameters for the longitudinal perturbation velocity solution; in the design mode, data are given only for the most critical surface of up to 64 surfaces which may be used and for the flat surface at $\alpha = 1°$; for the supersonic solution in which iteration is not used, this printout is omitted
2. A listing of the spanwise distribution of the leading-edge surface factor, the angle of attack range for full thrust, and the angle of attack for zero thrust; these data are given for the evaluation mode and for all iterations in the design mode from the first (input surface) to the last (optimized surface); for the evaluation mode, leading-edge surface factors are all zero
3. A listing of overall wing aerodynamic characteristics as a function of angle of attack; these data are given for the evaluation mode and for all iterations in the design mode from the first (input surface) to the last (optimized surface)
4. A listing of the spanwise distribution of wing-section aerodynamic characteristics, including the separate contributions of basic pressure loadings, attainable thrust, and vortex forces; these data are given only for the evaluation mode (or when the NEWDES option is used in the design mode) and are given only if the print option IPRSLD is set to 1
5. A listing of the wing-surface ordinates as a function of chord position for each of the span stations used in the program solution
6. Listings of lifting pressure distributions for the camber surface at $\alpha = 0°$ and for the flat surface at $\alpha = 1°$
7. A listing of the leading-edge surface factors used in the design and a listing of suggested replacement values which may lead to improved performance when the NEWDES option is used; generally, the need for this replacement arises only when it has not been possible to provide a sufficiently detailed numerical representation of the wing to give closely matched aerodynamic characteristics in the design and evaluation modes
8. A listing of a suggested spanwise distribution of flap deflection angles to approximate the designed camber surface and to approach its aerodynamic performance when the IFLPDES option is used and flap chord information is supplied

Notes on Code Application

The code in its present form offers the user a wide variety of options in the way a particular design problem is attacked. Experience in application of the code has led to the following recommendations for some specific tasks.

For the design of a camber surface covering the whole wing planform (not a mission adaptive design) in which moment restraints are imposed, a straightforward application of the code will yield a reasonable solution. However, for more than mild moment restraints a somewhat better performance is obtained by using the following steps:

1. Perform a whole wing design at the design lift coefficient, Mach number, and Reynolds number conditions but impose no moment restraint
2. Perform a second whole wing design at the same conditions but with the desired moment restraint; for this case, also impose a set of leading-edge surface weighting factors TAFIX as defined in a table of suggested values given by the first design (with appropriate smoothing)

This process will produce a more nearly optimum surface in the critical leading-edge region. The required moment increment is supplied by the general surfaces covering the entire wing. The leading-edge surface is thus compromised to a lesser degree by the moment requirement.

For the design of mission adaptive surfaces and the selection of flap geometry, a straightforward application of the code tends to underemphasize the contribution of loadings provided by the camber surface or flaps in the region of the wing trailing edge. This results in only a small penalty in theoretical performance because the wing leading-edge shape is still proper for the design conditions. As a practical matter, however, additional loading of the trailing-edge surfaces will reduce the need for leading-edge camber which, as discussed previously, introduces drag penalties not fully covered by the linearized theory. A recommended procedure that utilizes trailing-edge camber and/or flap deflections to increase the theoretical performance and produce a more practical design is as follows:

1. Perform a whole wing design for the entire wing planform at the design lift coefficient, Mach number, and Reynolds number conditions. Use no moment restraint if performance alone is the concern, but specify a design moment if trim conditions must also be considered. This design provides an indication of performance potential and aids in the selection of local design area chords within limitations imposed by wing structural restraints. Generally, chords should be as large as structural considerations allow; however, the whole wing solution sometimes shows areas where leading-edge design area or flap chords may be reduced or eliminated

2. Perform a restricted area wing design for the same flight conditions and for a moment coefficient $C_{m,\mathrm{des}}$ at the design lift coefficient as given by the whole wing solution. Imposition of the design moment ensures that adequate consideration is given to trailing-edge contributions to lifting efficiency. For a mission adaptive design, input the desired design area chords subject to the considerations discussed in the first step. To perform a flap design, input a design area chord equal to the actual flap chord and activate the flap design (FLPDES) feature of the code to provide a spanwise flap deflection schedule

3. For flap design cases, examine the code output flap deflection schedule and modify it as necessary to meet design restraints such as those imposed by spanwise segmentation. Also, since the theoretically recommended deflections are only approximations not true optimums, experience may be applied in modifying results, particularly in the reduction of large indicated angles. For subsonic cases, application of the wing evaluation code (refs. 34 and 53) to the selected flap system will help in defining more accurately the optimum deflections and the flap system performance

The wing-design code provides a number of options which can be used to control the character of the designed surface. For special design problems, the user may want to explore various alternate design approaches. For example, to reduce the wing root chord incidence and the cabin floor angle, a special trailing-edge design area illustrated in sketch A6 may be used. For a normal whole wing

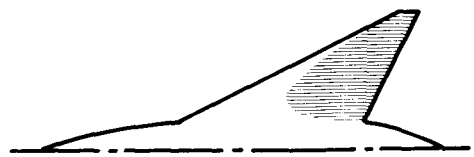

Sketch A6

design, the wing root chord will have a larger incidence than that of a flat wing developing the same lift. This occurs because the leading-edge surface changes required for thrust recovery also result in a loss of lift which must be compensated by increased lifting forces elsewhere. If the wing area providing this compensating lift is limited as shown (with NTES = 4 and EXPXTE = 1.5), the root

chord incidence will not be as large as for a whole wing design. Because the special trailing-edge surface is substituted for the general surfaces, it is necessary to eliminate those surfaces by setting NGCS = 0. Generally, a drag penalty is associated with this alternate design.

The table of suggested TAFIX values may in some cases show negative values. These are provided to apply to design cases in which the initial surface is already twisted and cambered. If this initial surface has too severe a leading-edge camber for the new design conditions, it may need to be reduced, and a negative factor is appropriate. For the usual design cases (the code default, for example), occasional negative values should be disregarded.

In use of the suggested replacement leading-edge surface weighting factors TAFIX, one particular situation requires an additional explanation. For the standard automated design process which attempts to achieve a surface with minimum distortion from a flat surface, suggested redesign TAFIX values may take on the appearance shown in sketch A7. Strict adherence to the suggested distribution would produce a surface slope discontinuity which is neither necessary nor desirable. A better distribution is indicated by the dashed line. This not only provides a smooth surface but also represents a design with a greater margin of safety. The suggested TAFIX values shown in sketch A7 result from a wing design with α_{zt} and $\Delta\alpha_{ft}$ values shown in sketch A8. Inboard of the 30-percent semispan station, the range of full thrust $\Delta\alpha_{ft}$ is greater than the design angle of attack and no camber or twist is required. However, a moderate amount of camber and twist dictated by the TAFIX distribution shown by the dashed line will give an equally good design phase aerodynamic efficiency and will provide a design surface that will not suffer as severe performance penalties if evaluation phase results do not completely meet the design goals. Recall that for maximum factor of safety in design, the leading-edge matchup would appear as in sketch A3.

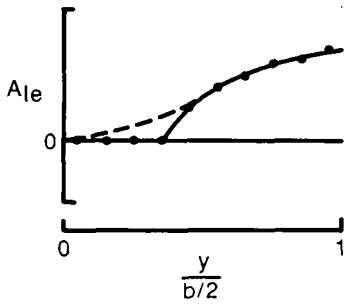

Sketch A7

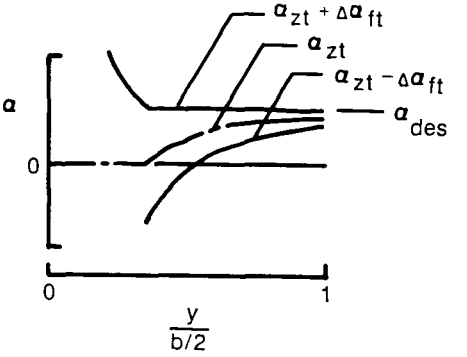

Sketch A8

As discussed in the section "Code Output Data," provision has been made for successive runs of the code with a single computer entry. Under some circumstances, the following input data quantities may be changed during a computer run. The new values will be used for subsequent runs unless reset by the code user.

JBYMAX — may be reduced to keep the number of elements within code limits; the new value which depends on the Mach number will be retained unless respecified

CLDES — is reset to 0.0 after a design run is performed; subsequent runs will be for evaluation only, unless CLDES is respecified

NEWDES — is reset to zero after the evaluation of a newly designed surface is performed; the original input camber surface description (z = zero everywhere for the default) is replaced with new values of NYC, TBYC, NPCTC, TBPCTC, and TZORDC for the designed surface which are retained unless respecified

TZSCALE	is reset to 1.0 after the rescaling operation is performed; any subsequent rescaling activated by setting TZSCALE to a value other than 1.0 will be applied to the newly rescaled surface
TBLEC	is multiplied by 1.5 when the flap design option (IFLPDES = 1) is employed; TBLEC must be respecified if a subsequent design is to be performed
CLZPR	is reset to 1000 at the completion of each computer run; for the following run, the camber surface ordinates will be printed for an angle of attack of zero unless CLZPR is respecified

For reference purposes it my be desirable to have full theoretical thrust performance estimates which the code does not normally supply. Such a result, however, may be obtained by setting the input RN to a very high value such as 1.0 E20, letting TBTOC = 1.0, and TBROC = 0.5. The code C_A values will represent full theoretical thrust for a range of angle of attack from the largest value of $\alpha_{zt} - \Delta\alpha_{\text{ft}}$ at any spanwise station (the lower limit) to the smallest value of $\alpha_{zt} + \Delta\alpha_{\text{ft}}$ at any spanwise station (the upper limit).

Table I presents sample input data for the WINGDES2 code for each of the test configurations studied. The fuselage and the wing are represented in the planform submitted to the code. The camber ordinates TZORDC were determined from the mean ordinates of both the wing and fuselage. Generally, the whole wing–body planform was represented by 25 to 30 semispan elements JBYMAX and by 700 to 1200 total elements. The first 16 examples are evaluation cases and the last 4 are design cases.

To obtain estimates of attainable leading-edge thrust, input values of RN and XM are both specified and the wing section geometric characteristics of t/c, r/c, and η are entered in the appropriate tables. For evaluation of the estimated forces caused by leading-edge vortex separation, the vortex location option IVOROP = 1 was chosen. This option has been found to be more accurate for the conventional swept wings of this study than the other two options.

References

1. Jones, Robert T.: *Estimated Lift-Drag Ratios at Supersonic Speed.* NACA TN 1350, 1947.

2. Puckett, A. E.; and Stewart, H. J.: Aerodynamic Performance of Delta Wings at Supersonic Speeds. *J. Aeronaut. Sci.*, vol. 14, no. 10, Oct. 1947, pp. 567–578.

3. Madden, Robert T.: *Aerodynamic Study of a Wing-Fuselage Combination Employing a Wing Swept Back 63° — Investigation at a Mach Number of 1.53 To Determine the Effects of Cambering and Twisting the Wing for Uniform Load at a Lift Coefficient of 0.25.* NACA RM A9C07, 1949.

4. Brown, Clinton E.; and Hargrave, L. K.: *Investigation of Minimum Drag and Maximum Lift-Drag Ratios of Several Wing-Body Combinations Including a Cambered Triangular Wing at Low Reynolds Numbers and at Supersonic Speeds.* NACA TN 4020, 1958. (Supersedes NACA RM L51E11.)

5. Brown, Clinton E.; and McLean, Francis E.: The Problem of Obtaining High Lift-Drag Ratios at Supersonic Speeds. *J. Aero/Sp. Sci.*, vol. 26, no. 5, May 1959, pp. 298–302.

6. Mack, Robert J.: *Wind-Tunnel Investigation of Leading-Edge Thrust on Arrow Wings in Supersonic Flow.* NASA TP-2167, 1983.

7. Wood, Richard M.; and Miller, David S.: *Experimental Investigation of Leading-Edge Thrust at Supersonic Speeds.* NASA TP-2204, 1983.

8. Boyd, John W.; Migotsky, Eugene; and Wetzel, Benton E.: *A Study of Conical Camber for Triangular and Sweptback Wings.* NACA RM A55G19, 1955.

9. Carlson, Harry W.: *Aerodynamic Characteristics at Mach Number 2.05 of a Series of Highly Swept Arrow Wings Employing Various Degrees of Twist and Camber.* NASA TM X-332, 1960.

10. Carlson, Harry W.: *Pressure Distributions at Mach Number 2.05 on a Series of Highly Swept Arrow Wings Employing Various Degrees of Twist and Camber.* NASA TN D-1264, 1962.

11. Mack, Robert J.: *Effects of Leading-Edge Sweep Angle and Design Lift Coefficient on Performance of a Modified Arrow Wing at a Design Mach Number of 2.6.* NASA TN D-7753, 1974.

12. Sorrells, Russell B., III; and Landrum, Emma Jean: *Theoretical and Experimental Study of Twisted and Cambered Delta Wings Designed for a Mach Number of 3.5.* NASA TN D-8247, 1976.

13. Darden, Christine M.: *Effect of Leading-Edge Load Constraints on the Design and Performance of Supersonic Wings.* NASA TP-2446, 1985.

14. Hasson, Dennis F.; Fichter, Ann B.; and Wong, Norman: *Aerodyamic Characteristics at Mach Numbers From 1.6 to 2.8 of 74° Swept Arrow Wings With and Without Camber and Twist.* NASA TM X-8, 1959.

15. Hallissy, Joseph M., Jr.; and Hasson, Dennis F.: *Aerodynamic Characteristics at Mach Numbers 2.36 and 2.87 of an Airplane Configuration Having a Cambered Arrow Wing With a 75° Swept Leading Edge.* NACA RM L58E21, 1958.

16. Morris, Odell A.; Fuller, Dennis E.; and Watson, Carolyn B.: *Aerodynamic Characteristics of a Fixed Arrow-Wing Supersonic Cruise Aircraft at Mach Numbers of 2.30, 2.70, and 2.95.* NASA TM-78706, 1978.

17. Johnson, Matthew E.: *A Design and Analysis of Maneuver Wing Flaps at Supersonic Speeds With Attainable Leading-Edge Thrust Considerations.* NASA CR-3939, 1985.

18. Carlson, Harry W.; and Walkley, Kenneth B.: *Numerical Methods and a Computer Program for Subsonic and Supersonic Aerodynamic Design and Analysis of Wings With Attainable Thrust Considerations.* NASA CR-3808, 1984.

19. Middleton, Wilbur D.; and Carlson, Harry W.: Numerical Method of Estimating and Optimizing Supersonic Aerodyamic Characteristics of Arbitrary Planform Wings. *J. Aircr.*, vol. 2, no. 4, July–Aug. 1965, pp. 261–265.

20. Carlson, Harry W.; and Miller, David S.: *Numerical Methods for the Design and Analysis of Wings at Supersonic Speeds.* NASA TN D-7713, 1974.

21. Middleton, W. D.; and Lundry, J. L.: *A System for Aerodynamic Design and Analysis of Supersonic Aircraft. Part 1 — General Description and Theoretical Development.* NASA CR-3351, 1980.

22. Middleton, W. D.; Lundry, J. L.; and Coleman, R. G.: *A System for Aerodynamic Design and Analysis of Supersonic Aircraft. Part 2—User's Manual.* NASA CR-3352, 1980.

23. Middleton, W. D.; Lundry, J. L.; and Coleman, R. G.: *A System for Aerodynamic Design and Analysis of Supersonic Aircraft. Part 3—Computer Program Description.* NASA CR-3353, 1980.

24. Middleton, W. D.; and Lundry, J. L.: *A System for Aerodyamic Design and Analysis of Supersonic Aircraft. Part 4 — Test Cases.* NASA CR-3354, 1980.

25. Harris, Roy V., Jr.: *An Analysis and Correlation of Aircraft Wave Drag.* NASA TM X-947, 1964.

26. Carlson, Harry W.; and Walkley, Kenneth B.: *A Computer Program for Wing Subsonic Aerodynamic Performance Estimates Including Attainable Thrust and Vortex Lift Effects.* NASA CR-3515, 1982.

27. Carlson, Harry W.; and Mack, Robert J.: *Estimation of Leading-Edge Thrust for Supersonic Wings of Arbitrary Planform.* NASA TP-1270, 1978.

28. Carlson, Harry W.; Mack, Robert J.; and Barger, Raymond L.: *Estimation of Attainable Leading-Edge Thrust for Wings at Subsonic and Supersonic Speeds.* NASA TP-1500, 1979.

29. Polhamus, Edward C.: Predictions of Vortex-Lift Characteristics by a Leading-Edge Suction Analogy. *J. Aircr.*, vol. 8, no. 4, Apr. 1971, pp. 193–199.

30. Tucker, Warren A.: *A Method for the Design of Swept-back Wings Warped To Produce Specified Flight Characteristics at Supersonic Speeds.* NACA Rep. 1226, 1955. (Supersedes NACA RM L51F08.)

31. Grant, Frederick C.: *The Proper Combination of Lift Loadings for Least Drag on a Supersonic Wing.* NACA Rep. 1275, 1956. (Supersedes NACA TN 3533.)

32. Robins, A. Warner; Morris, Odell A.; and Harris, Roy V., Jr.: Recent Research Results in the Aerodynamics of Supersonic Vehicles. *J. Aircr.*, vol. 3, no. 6, Nov.–Dec. 1966, pp. 573–577.

33. Baals, Donald D.; Robins, A. Warner; and Harris, Roy V., Jr.: Aerodynamic Design Integration of Supersonic Aircraft. AIAA Paper 68-1018, Oct. 1968.

34. Carlson, Harry W.; Darden, Christine M.; and Mann, Michael J.: *Validation of a Computer Code for Analysis of Subsonic Aerodynamic Performance of Wings With Leading- and Trailing-Edge Flaps With a Canard or Horizontal-Tail Surface and an Application to Optimization.* NASA TP-2961, 1990.

35. Carlson, Harry W.; and McLean, F. Edward: *Current Methods for Prediction and Minimization of Lift-Induced Drag at Supersonic Speeds.* NASA TM X-1275, 1966.

36. Landrum, Emma Jean; and Shrout, Barrett L.: *Effect of Shape Changes on the Aerodynamic Characteristics of a Twisted and Cambered Arrow Wing at Mach Number 2.03.* NASA TN D-4796, 1968.

37. Middleton, Wilbur D.; and Carlson, Harry W.: *Supersonic Longitudinal Aerodynamic Characteristics of Two Wing-Body Configurations Employing Warped Arrow Wings of Varying Dihedral.* NASA TM X-897, 1963.

38. Carlson, Harry W.: *Longitudinal Aerodynamic Characteristics at Mach Number 2.02 of a Series of Wing-Body Configurations Employing a Cambered and Twisted Arrow Wing.* NASA TM X-838, 1963.

39. Dollyhigh, Samuel M.; Morris, Odell A.; and Adams, Mary S.: *Experimental Effects of Fuselage Camber on Longitudinal Aerodynamic Characteristics of a Series of Wing-Fuselage Configurations at a Mach Number of 1.41.* NASA TM X-3411, 1976.

40. Morris, Odell A.: *Aerodynamic Characteristics in Pitch at a Mach Number of 2.01 of Several Wing-Body Combinations With Wedge-Shaped Bodies Located Above and Below a 54.5° Swept Delta Wing.* NASA TN D-1823, 1963.

41. Landrum, Emma Jean: *Effect of Nacelle Orientation on the Aerodynamic Characteristics of an Arrow Wing-Body Configuration at Mach Number 2.03.* NASA TN D-3284, 1966.

42. Sigalla, Armand; and Hallstaff, Thomas H.: Aerodynamics of Powerplant Installation on Supersonic Aircraft. *J. Aircr.*, vol. 4, no. 4, July–Aug. 1967, pp. 273–277.

43. Nichols, Mark R.: *Aerodynamics of Airframe-Engine Integration of Supersonic Aircraft.* NASA TN D-3390, 1966.

44. Loftin, Laurence K., Jr.: Research Relating to Large Supersonic Cruising Aircraft. AIAA Paper 67-748, Oct. 1967.

45. Kulfan, R. M.; and Sigalla, A.: Airframe-Propulsion System Aerodynamic Interference Predictions at High Transonic Mach Numbers Including Off-Design Engine Airflow Effects. *Aerodynamics of Power Plant Installation*, AGARD-CP-301, Sept. 1981, pp. 35-1–35-23.

46. Mack, Robert J.: *A Numerical Method for Evaluation and Utilization of Supersonic Nacelle-Wing Interference.* NASA TN D-5057, 1969.

47. Szema, Kuo-Yen; Chakravarthy, Sukumar; and Shankar, Vijaya: *Supersonic Flow Computations Over Aerospace Configurations Using an Euler Marching Solver.* NASA CR-4085, 1987.

48. Chakravarthy, Sukumar R.; and Szema, Kuo-Yen: Euler Solver for Three-Dimensional Supersonic Flows With Subsonic Pockets. *J. Aircr.*, vol. 24, no. 2, Feb. 1987, pp. 73–83.

49. Newsome, Richard W.; and Thomas, James L.: Computation of Leading-Edge Vortex Flows. *Vortex Flow Aerodynamics*, Volume I, James F. Campbell, Russell F. Osborn, and Jerome T. Foughner, Jr., eds., NASA CP-2416, 1986, pp. 305–330.

50. McMillin, S. Naomi; Thomas, James L.; and Murman, Earll M.: *Navier-Stokes and Euler Solutions for Lee-Side Flows Over Supersonic Delta Wings—A Correlation With Experiment.* NASA TP-3035, 1990.

51. Carlson, Harry W.; and Mack, Robert J.: *Estimation of Wing Nonlinear Aerodynamic Characteristics at Supersonic Speeds.* NASA TP-1718, 1980.

52. Lan, C. Edward; and Chang, Jen-Fu: *Calculation of Vortex Lift Effect for Cambered Wings by the Suction Analogy.* NASA CR-3449, 1981.

53. Carlson, Harry W.; and Darden, Christine M.: *Validation of a Pair of Computer Codes for Estimation and Optimization of Subsonic Aerodynamic Performance of Simple Hinged-Flap Systems for Thin Swept Wings.* NASA TP-2828, 1988.

Table I. Sample Input Data for WINGDES2 Code

(a) 60° flat swept arrow wing with standard wing section

```
ATTAINABLE THRUST WINGS - MACK,TP 2167  STD SECTION
$INPT1 XM=1.6,RN=2.0,JBYMAX=25,IVOROP=1,IPRSLD=0,
SREF=300.0,CBAR=12.252,XMC=12.48,XMAX=28.27,
NLEY=2,TBLEY=0.000,16.32,
       TBLEX=0.000,28.27,
NTEY=2,TBTEY=0.000,16.32,
       TBTEX=18.38,28.27,
NYR=2,TBYR=0.000,16.32,
     TBTOC=.0400,.0400,
     TBROC=.0024,.0024,
     TBETA=.4500,.4500,
NALPHA=13,TALPHA=0.0,1.0,2.0,3.0,4.0,5.0,6.0,7.0,8.0,9.0,
10.0,11.0,12.0,    $
M=1.8
$INPT1 XM=1.8,     $
M=2.0
$INPT1 XM=2.0,     $
M=2.16
$INPT1 XM=2.16,    $
```

(b) Flat modified arrow wing–body combination with sharp-leading-edge wing section

```
THRUST WING - WOOD,TP2204  SHARP L E SECTION R=.004  M=1.6
$INPT1 XM=1.6,RN=2.0,JBYMAX=25,IPRSLD=1,
SREF=324.6,CBAR=15.86,XMC=22.53,XMAX=36.32,
NLEY=9,
TBLEY=0.000,0.815,1.627,2.442,3.663,5.494,7.326,9.767,12.21,
TBLEX=4.531,5.148,6.710,9.088,13.03,18.67,23.32,28.76,33.79,
NTEY=9,
TBTEY=0.000,0.815,1.627,2.442,3.663,5.494,7.326,9.767,12.21,
TBTEX=30.93,30.77,30.61,30.46,30.74,31.93,33.13,34.72,36.32,
NYR=7,
 TBYR=0.0000,0.8150,2.4420,5.4940,7.3260,9.7670,12.209,
TBTOC=.04000,.04000,.04000,.04000,.04000,.04000,.04000,
TBROC=.00100,.00100,.00020,.00030,.00040,.00070,.00100,
TBETA=.42500,.42500,.42500,.42500,.42500,.42500,.42500,
NALPHA=11,TALPHA=0.0,1.0,2.0,3.0,4.0,5.0,6.0,7.0,8.0,9.0,10.0,
$
M=2.0
$INPT1 XM=2.0,     $
M=2.36
$INPT1 XM=2.36,     $
```

Table I. Continued

(c) Aspect ratio 2 wing–body combination with conical camber for $C_L = 0.215$ and $M = 1.00$

```
AR 2  DELTA WING  CONICAL CAMBER - BOYD,RM A55G19  3 PCT
$INPT1 XM=1.3,RN=5.6,JBYMAX=25,IPRSLD=1,
SREF=2.00,CBAR=1.333,XMC=2.242,XMAX=3.556,
NLEY=3,TBLEY=0.000,0.200,1.000,
       TBLEX=0.000,1.642,3.242,
NTEY=4,TBTEY=0.000,0.150,0.160,1.000,
       TBTEX=3.556,3.556,3.242,3.242,
NYR=2,TBYR=0.0000,1.0000,
     TBTOC=0.0300,0.0300,
     TBROC=.00047,.00047,
     TBETA=0.5000,0.5000,
NYC=8,TBYC=0.0,.19,.20,.40,.60,.80,.90,1.00,
NPCTC=8,
TBPCTC=0.0000,5.0000,10.000,20.000,40.000,60.000,80.000,100.00,
TZORDC=0.0000,0.0000,0.0000,0.0000,0.0000,0.0000,0.0000,0.0000,18*0.0
       0.0000,0.0000,0.0000,0.0000,0.0000,0.0000,0.0000,0.0000,18*0.0,
       -.0084,0.0000,0.0000,0.0000,0.0000,0.0000,0.0000,0.0000,18*0.0,
       -.0167,-.0055,-.0016,0.0000,0.0000,0.0000,0.0000,0.0000,18*0.0,
       -.0250,-.0148,-.0093,-.0032,0.0000,0.0000,0.0000,0.0000,18*0.0,
       -.0334,-.0269,-.0221,-.0157,-.0077,-.0033,-.0007,0.0000,18*0.0,
       -.0385,-.0347,-.0312,-.0266,-.0195,-.0145,-.0104,-.0073,18*0.0,
       -.0425,-.0425,-.0425,-.0425,-.0425,-.0425,-.0425,-.0425,18*0.0,
NALPHA=17,TALPHA=-6.0,-5.0,-4.0,-3.0,-2.0,-1.0,0.0,1.0,2.0,3.0,4.0,
                 5.0,6.0,7.0,8.0,9.0,10.0,    $
XM=1.7,RN=5.6
$INPT1 XM=1.7,RN=5.6,    $
```

Table I. Continued

(d) Aspect ratio 1.57 wing–body combination twisted and cambered for uniform load at $C_L = 0.20$ and $M = 1.62$

```
TRIANGULAR WING - BROWN,TN 4020  CLD=.20
$INPT1 XM=1.62,RN=1.45,JBYMAX=25,IPRSLD=1,
SREF=14.10,CBAR=4.00,XMC=5.875,XMAX=7.875,
NLEY=3,TBLEY=0.000,0.380,2.350,
       TBLEX=0.000,2.845,7.875,
NTEY=2,TBTEY=0.000,2.350,
       TBTEX=7.875,7.875,
NYR=3,TBYR=0.000,1.763,2.350,
     TBTOC=.0200,.0307,.0340,
     TBROC=.0004,.0009,.0011,
     TBETA=0.300,0.300,0.300,
NYC=11,TBYC=0.000,0.470,0.705,0.940,1.175,1.410,1.645,
            1.880,2.115,2.256,2.350,
NPCTC=8,
TBPCTC=0.000,10.00,20.00,30.00,40.00,60.00,80.00,100.0,
TZORDC=0.232,0.134,0.037,-.061,-.159,-.354,-.549,-.744,18*0.0,
       0.014,0.024,0.002,-.032,-.072,-.175,-.292,-.408,18*0.0,
       0.022,0.038,0.032,0.015,-.010,-.078,-.155,-.240,18*0.0,
       0.029,0.050,0.052,0.044,0.033,-.006,-.060,-.120,18*0.0,
       0.036,0.059,0.065,0.064,0.059,0.038,0.005,-.030,18*0.0,
       0.043,0.065,0.073,0.076,0.077,0.071,0.060,0.042,18*0.0,
       0.050,0.068,0.078,0.085,0.089,0.090,0.085,0.078,18*0.0,
       0.057,0.070,0.079,0.085,0.092,0.099,0.102,0.102,18*0.0,
       0.065,0.073,0.078,0.083,0.088,0.092,0.096,0.098,18*0.0,
       0.069,0.072,0.075,0.077,0.080,0.084,0.087,0.090,18*0.0,
       0.072,0.072,0.072,0.072,0.072,0.072,0.072,0.072,18*0.0,
NALPHA=15,TALPHA=-4.0,-3.0,-2.0,-1.0,0.0,1.0,2.0,3.0,4.0,5.0,
                6.0,7.0,8.0,9.0,10.0,
CLZPR=0.20,    $
CLD=.08
$INPT1 TZSCALE=0.4,CLZPR=.08,    $
CLD=0.0
$INPT1 TZSCALE=0.0,CLZPR=0.0,    $
```

Table I. Continued

(e) 70° swept arrow wing twisted and cambered for optimum combination of loads at $C_L = 0.16$ and $M = 2.00$

```
70 DEG ARROW WING - CARLSON,TMX-332 AND TN D-1264  CLD=,16
$INPT1 XM=2.05,RN=4.4,JBYMAX=30,IVOROP=1,IPRSLD=1,
SREF=212.94,CBAR=13.00,XMC=13.25,XMAX=30.00,
NLEY=2,TBLEY=0.000,10.92,
       TBLEX=0.000,30.00,
NTEY=2,TBTEY=0.000,10.92,
       TBTEX=19.50,30.00,
NYR=5,TBYR=0.0000,5.4600,7.6440,8.7360,10.920,
     TBTOC=0.0300,0.0300,0.0300,0.0300,0.0300,
     TBROC=.00020,.00042,.00050,.00050,.00050,
     TBETA=0.5000,0.5000,0.5000,0.5000,0.5000,
NYC=9,TBYC=0.000,1.092,3.276,5.460,7.644,9.828,10.37,10.70,10.92,
NPCTC=9,
TBPCTC=0.000,5.000,10.00,20.00,30.00,40.00,60.00,80.00,100.0,
TZORDC=6.800,6.790,6.470,5.210,3.770,2.000,-1.60,-5.13,-8.31,17*0.0,
       4.700,4.780,4.600,3.700,2.620,1.290,-1.60,-4.30,-6.89,17*0.0,
       0.510,0.770,0.870,0.690,0.330,-.120,-1.27,-2.65,-4.05,17*0.0,
       0.840,1.040,1.200,1.370,1.350,1.200,0.750,0.120,-.640,17*0.0,
       1.140,1.340,1.500,1.700,1.800,1.860,1.800,1.620,1.260,17*0.0,
       1.440,1.520,1.600,1.720,1.830,1.940,2.070,2.180,2.240,17*0.0,
       1.530,1.590,1.640,1.730,1.800,1.870,1.980,2.050,2.120,17*0.0,
       1.590,1.610,1.640,1.680,1.730,1.760,1.820,1.860,1.900,17*0.0,
       1.590,1.590,1.590,1.590,1.590,1.590,1.590,1.590,1.590,17*0.0,
TZSCALE=.16,CLZPR=0.16,
NALPHA=17,TALPHA=-6.0,-5.0,-4.0,-3.0,-2.0,-1.0,0.0,1.0,2.0,3.0,4.0,
                 5.0,6.0,7.0,8.0,9.0,10.0,    $
CLD=.08
$INPT1 TZSCALE=.50,CLZPR=.16,    $
CLD=0.0
$INPT1 TZSCALE=0.0,CLZPR=.16,    $
```

Table I. Continued

(f) 75° swept arrow wing twisted and cambered for optimum combination of loads at $C_L = 0.16$ and $M = 2.00$

```
75 DEG ARROW WING - CARLSON,TMX-332
$INPT1 XM=2.05,RN=4.4,JBYMAX=30,IVOROP=1,
SREF=156.78,CBAR=13.0,XMC=13.25,XMAX=30.0,
NLEY=2,TBLEY=0.000,8.040,
       TBLEX=0.000,30.00,
NTEY=2,TBTEY=0.000,8.040,
       TBTEX=19.50,30.00,
NYR=5,TBYR=0.0000,4.0200,5.6280,6.4320,8.0400,
     TBTOC=.03000,.03000,.03000,.03000,.03000,
     TBROC=.00020,.00042,.00050,.00050,.00050,
     TBETA=.50000,.50000,.50000,.50000,.50000,
NYC=8,TBYC=0.000,1.608,3.216,4.842,6.432,7.236,7.638,8.040,
NPCTC=9,
TBPCTC=0.000,5.000,10.00,20.00,30.00,40.00,60.00,80.00,100.0,
TZORDC=.0789,.0740,.0681,.0559,.0427,.0293,.0018,-.031,-.065,17*0.0,
       .0129,.0153,.0162,.0140,.0099,.0042,-.007,-.021,-.036,17*0.0,
       .0081,.0105,.0119,.0127,.0120,.0105,.0060,-.001,-.010,17*0.0,
       .0120,.0138,.0152,.0173,.0180,.0183,.0172,.0150,.0123,17*0.0,
       .0155,.0166,.0175,.0195,.0208,.0219,.0225,.0225,.0218,17*0.0,
       .0171,.0178,.0185,.0196,.0206,.0215,.0228,.0235,.0238,17*0.0,
       .0179,.0184,.0189,.0197,.0203,.0208,.0217,.0226,.0235,17*0.0,
       .0187,.0187,.0187,.0187,.0187,.0187,.0187,.0187,.0187,17*0.0,
NALPHA=17,TALPHA=-6.0,-5.0,-4.0,-3.0,-2.0,-1.0,0.0,1.0,2.0,3.0,
                 4.0,5.0,6.0,7.0,8.0,9.0,10.0,
TZSCALE=30.0,CLZPR=.16,    $
FLAT WING
$INPT1 TZSCALE=0.0,    $
```

Table I. Continued

(g) 75.96° swept modified arrow wing twisted and cambered for optimum combination of loads at $C_L = 0.12$ and $M = 2.60$

```
CLIPPED TIP ARROW WING - MACK,TN D-7753  BCOT=.60,CLD=.12
$INPT1 XM=2.60,RN=5.12,JBYMAX=25,IVOROP=1,IPRSLD=1,
SREF=1935.48,CBAR=52.08,XMC=46.15,XMAX=97.74,
NLEY=2,TBLEY=0.000,23.03,
       TBLEX=0.000,92.31,
NTEY=3,TBTEY=0.000,20.81,23.03,
       TBTEX=76.93,97.74,92.31,
NYR=4,TBYR=0.0000,11.510,18.420,23.030,
     TBTOC=0.0300,0.0300,0.0300,0.0300,
     TBROC=.00012,.00024,.00046,.00050,
     TBETA=0.5000,0.5000,0.5000,0.5000,
NYC=12,TBYC=0.00,2.30,4.60,6.90,9.21,11.51,13.81,16.12,
           18.42,20.77,21.88,23.03,
NPCTC=9,
TBPCTC=0.000,5.000,10.00,20.00,30.00,40.00,60.00,80.00,100.0,
TZORDC=.6627,.6107,.5587,.4558,.3508,.2469,.0387,-.169,-.273,17*0.0,
       .4050,.3994,.3833,.3053,.2166,.1278,-.048,-.216,-.355,17*0.0,
       .1949,.2098,.2144,.1775,.1200,.0546,-.081,-.214,-.325,17*0.0,
       .0747,.0983,.1107,.0886,.0574,.0162,-.080,-.182,-.276,17*0.0,
       .0206,.0439,.0587,.0520,.0347,.0076,-.064,-.141,-.216,17*0.0,
       0.000,.0241,.0407,.0422,.0347,.0162,-.033,-.088,-.149,17*0.0,
       0.000,.0225,.0390,.0465,.0455,.0360,.0087,-.031,-.072,17*0.0,
       0.000,.0180,.0325,.0455,.0487,.0477,.0325,.0102,-.017,17*0.0,
       0.000,.0139,.0260,.0412,.0485,.0520,.0477,.0399,.0260,17*0.0,
       0.000,.0083,.0162,.0310,.0433,.0481,.0541,.0559,.0524,17*0.0,
       0.000,.0050,.0100,.0190,.0250,.0310,.0400,.0480,.0520,17*0.0,
       0.000,0.000,0.000,0.000,0.000,0.000,0.000,0.000,0.000,17*0,0,
TZSCALE=11.729,CLZPR=0.12,
NALPHA=18,TALPHA=-12.0,-10.0,-8.0,-6.0,-4.0,-2.0,-1.0,0.0,1.0,2.0,
                 3.0,4.0,6.0,8.0,10.0,12.0,14.0,16.0,    $
CLD=.08
$INPT1 TZSCALE=.666,CLZPR=0.12    $
CLD=0.0
$INPT1 TZSCALE=0.0,CLZPR=0.12     $
```

Table I. Continued

(h) 72.65° swept modified arrow wing twisted and cambered for optimum combination of loads at $C_L = 0.12$ and $M = 2.60$

```
CLIPPED TIP ARROW WING - MACK,TN D-7753  BCOT=.75 CLD=.12
$INPT1 XM=2.60,RN=5.12,JBYMAX=25,IVOROP=1,IPRSLD=1,
SREF=1935.48,CBAR=46.51,XMC=41.29,XMAX=87.67,
NLEY=2,TBLEY=0.000,25.79,
       TBLEX=0.000,82.51,
NTEY=3,TBTEY=0.000,23.64,25.79,
       TBTEX=68.76,87.67,82.51,
NYR=4,TBYR=0.0000,12.890,20.630,25.790,
     TBTOC=0.0316,0.0316,0.0316,0.0316,
     TBROC=.00014,.00026,.00050,.00050,
     TBETA=0.5000,0.5000,0.5000,0.5000,
NYC=12,TBYC=0.00,2.79,5.15,7.73,10.31,12.89,15.47,18.05,
           20.63,23.64,24.50,25.79,
NPCTC=9,
TBPCTC=0.000,5.000,10.00,20.00,30.00,40.00,60.00,80.00,100.0,
TZORDC=.7413,.6896,.6378,.5342,.4306,.3274,.1202,-.087,-.294,17*0.0,
       .3646,.3575,.3429,.2801,.2040,.1256,-.029,-.173,-.284,17*0.0,
       .1690,.1756,.1750,.1412,.0917,.0386,-.072,-.174,-.267,17*0.0,
       .0664,.0800,.0857,.0640,.0290,-.006,-.088,-.165,-.243,17*0.0,
       .0305,.0319,.0386,.0302,.0097,-.014,-.077,-.139,-.198,17*0.0,
       0.000,.0116,.0193,.0181,.0097,-.010,-.053,-.101,-.145,17*0.0,
       0.000,.0112,.0193,.0229,.0229,.0121,-.018,-.053,-.087,17*0.0,
       0.000,.0108,.0193,.0265,.0302,.0265,.0097,-.014,-.039,17*0.0,
       0.000,.0105,.0193,.0290,.0338,.0338,.0290,.0145,0.000,17*0.0,
       0.000,.0089,.0159,.0222,.0271,.0290,.0314,.0300,.0280,17*0.0,
       0.000,.0025,.0050,.0100,.0160,.0200,.0230,.0260,.0300,17*0.0,
       0.000,0.000,0.000,0.000,0.000,0.000,0.000,0.000,0.000,17*0.0,
TZSCALE=10.520,CLZPR=0.12,
NALPHA=18,TALPHA=-12.0,-10.0,-8.0,-6.0,-4.0,-2.0,-1.0,0.0,
                 1.0,2.0,3.0,4.0,6.0,8.0,10.0,12.0,14.0,16.0,    $
CLD=.08
$INPT1 TZSCALE=.666,CLZPR=0.12    $
CLD=0.0
$INPT1 TZSCALE=0.0,CLZPR=0.12    $
```

Table I. Continued

(i) 69.44° swept modified arrow wing twisted and cambered for optimum combination of loads at $C_L = 0.12$ and $M = 2.60$

```
CLIPPED TIP ARROW WING - MACK,TN D-7753  BCOT=.90,CLD=.12
$INPT1 XM=2.60,RN=5.12,JBYMAX=25,IVOROP=1,IPRSLD=1,
SREF=1935.48,CBAR=42.514,XMC=37.702,XMAX=80.20,
NLEY=2,TBLEY=0.000,28.23,
       TBLEX=0.000,75.29,
NTEY=3,TBTEY=0.000,26.19,28.23,
       TBTEX=62.74,80.20,75.29,
NYR=4,TBYR=0.0000,14.110,22.580,28.230,
     TBTOC=.03350,.03350,.03350,.03350,
     TBROC=.00015,.00030,.00050,.00050,
     TBETA=0.5000,0.5000,0.5000,0.5000,
NYC=12,TBYC=0.00,2.82,5.64,8.47,11.29,14.11,16.94,19.76,
            22.58,26.18,27.38,28.23,
NPCTC=9,
TBPCTC=0.000,5.000,10.00,20.00,30.00,40.00,60.00,80.00,100.0,
TZORDC=.7839,.7324,.6806,.5772,.4743,.3710,.1643,-.042,-.249,17*0.0,
       .3232,.3070,.2877,.2349,.1715,.1029,-.032,-.156,-.243,17*0.0,
       .1597,.1558,.1478,.1135,.0726,.0277,-.066,-.157,-.232,17*0.0,
       .0726,.0742,.0713,.0475,.0211,-.011,-.080,-.149,-.216,17*0.0,
       .0211,.0242,.0238,.0079,-.013,-.037,-.084,-.138,-.194,17*0.0,
       0.000,.0041,.0053,-.005,-.022,-.040,-.075,-.116,-.156,17*0.0,
       0.000,.0049,.0066,-.001,-.006,-.022,-.048,-.076,-.107,17*0.0,
       0.000,.0053,.0079,.0027,-.003,-.011,-.026,-.046,-.067,17*0.0,
       0.000,.0053,.0079,.0053,.0040,.0000,-.011,-.021,-.036,17*0.0,
       0.000,.0021,.0037,.0045,.0045,.0037,.0008,-.002,-.006,17*0.0,
       0.000,.0005,.0010,.0016,.0018,.0018,.0015,.0002,-.001,17*0.0,
       0.000,0.000,0.000,0.000,0.000,0.000,0.000,0.000,0.000,17*0.0,
TZSCALE=9.623,CLZPR=0.12,
NALPHA=18,TALPHA=-12.0,-10.0,-8.0,-6.0,-4.0,-2.0,-1.0,0.0,
                 1.0,2.0,3.0,4.0,6.0,8.0,10.0,12.0,14.0,16.0,    $
CLD=.08
$INPT1 TZSCALE=.666,CLZPR=0.12    $
CLD=0.0
$INPT1 TZSCALE=0.0,CLZPR=0.12    $
```

Table I. Continued

(j) 76° swept delta wing–body combination twisted and cambered for optimum combination of loads at $C_L = 0.10$ and $M = 3.50$

```
M=3.5 T AND C WING - SORRELLS,TN D-8247  CLDES=.1
$INPT1 XM=3.5,RN=4.9,JBYMAX=25,IPRSLD=1,
SREF=2045.2,CBAR=60.58,XMC=51.3,XMAX=90.17,
NLEY=2,TBLEY=0.000,21.39,
       TBLEX=0.000,85.85,
NTEY=2,TBTEY=0.000,21.39,
       TBTEX=90.17,90.17,
NYR=7,TBYR=0.0000,4.2800,8.5600,12.830,17.110,19.250,21.390,
     TBTOC=.04000,.04000,.04000,.04000,.04000,.04000,.04000,
     TBROC=.00011,.00013,.00018,.00026,.00047,.00079,.00090,
     TBETA=.50000,.50000,.50000,.50000,.50000,.50000,.50000,
NYC=13,TBYC=0.000,1.080,2.154,2.540,4.305,6.459,8.611,10.76,
            12.92,15.07,17.22,19.38,21.39,
NPCTC=10,
TBPCTC=0.000,2.500,5.000,10.00,20.00,30.00,40.00,60.00,80.00,100.0,
TZORDC=5.606,5.461,5.258,4.780,3.607,2.385,1.473,.0460,-.460,-.041,16*0.0,
       4.524,4.321,4.176,3.848,2.921,1.969,1.173,-.089,-.457,-.069,16*0.0,
       2.891,2.814,2.733,2.573,2.047,1.496,.9500,-.066,-.495,.0710,16*0.0,
       2.443,2.395,2.357,2.217,1.824,1.359,.8660,-.112,-.437,.0080,16*0.0,
       .9830,1.044,1.105,1.184,1.105,.8920,.5820,-.084,-.691,-1.23,16*0.0,
       .3860,.4780,.5640,.6580,.7320,.6730,.5330,.0840,-.424,-.960,16*0.0,
       .2590,.3510,.4240,.5360,.7060,.7440,.6680,.4040,.0430,-.399,16*0.0,
       .6120,.7090,.7670,.8860,1.054,1.097,1.082,.9860,.7870,.3530,16*0.0,
       1.247,1.313,1.351,1.430,1.577,1.669,1.725,1.768,1.638,1.308,16*0.0,
       1.831,1.897,1.933,2.014,2.164,2.286,2.365,2.433,2.418,2.195,16*0.0,
       2.431,2.479,2.517,2.583,2.718,2.842,2.908,3.023,3.058,2.954,16*0.0,
       3.007,3.040,3.071,3.117,3.205,3.299,3.373,3.505,3.551,3.510,16*0.0,
       3.564,3.576,3.589,3.612,3.653,3.696,3.734,3.820,3.889,3.909,16*0.0,
NALPHA=17,TALPHA=-4.0,-3.0,-2.0,-1.0,0.0,1.0,2.0,3.0,4.0,5.0,6.0,7.0,8.0,
                 9.0,10.0,11.0,12.0,
CLZPR=.10,    $
CLDES=.05
$INPT1 TZSCALE=.5,CLZPR=.1,    $
CLDES=0.0
$INPT1 TZSCALE=0.0,CLZPR=.1,    $
```

Table I. Continued

(k) Arbitrary planform wing–body combination twisted and cambered for optimum combination of loads with no constraint at $C_L = 0.08$ and $M = 2.40$

```
CURVED L E WING - DARDEN TP-2446  NO CONSTRAINT
$INPT1 XM=2.4,RN=2.0,JBYMAX=25,IVOROP=1,IPRSLD=1,
SREF=2.5375,CBAR=1.6861,XMC=1.431,XMAX=3.29,
NLEY=11,
TBLEY=0.00,0.10,0.20,0.30,0.40,0.50,0.60,0.70,0.80,0.90,1.00,
TBLEX=0.00,0.12,0.48,1.08,1.55,1.85,2.09,2.31,2.53,2.75,2.96,
NTEY=11,
TBTEY=0.00,0.10,0.20,0.30,0.40,0.50,0.60,0.70,0.80,0.90,1.00,
TBTEX=2.58,2.60,2.64,2.71,2.79,2.87,2.96,3.04,3.13,3.21,3.29,
NYR=4,TBYR=0.0000,0.5000,0.8000,1.0000,
     TBTOC=0.0300,0.0300,0.0300,0.0300,
     TBROC=.00010,.00030,.00050,.00050,
     TBETA=0.5000,0.5000,0.5000,0.5000,
NYC=11,TBYC=0.00,0.10,0.20,0.30,0.40,0.50,0.60,0.70,0.80,0.90,1.00,
NPCTC=9,
TBPCTC=0.000,5.000,10.00,20.00,30.00,40.00,60.00,80.00,100.0,
TZORDC=.1182,.1083,.0965,.0721,.0494,.0307,.0063,-.004,-.013,17*0.0,
       .1345,.1290,.1195,.0968,.0727,.0501,.0139,-.012,-.035,17*0.0,
       .1099,.1156,.1127,.0972,.0764,.0544,.0151,-.012,-.027,17*0.0,
       .0357,.0487,.0557,.0560,.0485,.0374,.0122,-.011,-.028,17*0.0,
       .0059,.0123,.0157,.0184,.0176,.0148,.0054,-.006,-.017,17*0.0,
       .0026,.0053,.0073,.0090,.0088,.0075,.0029,-.003,-.010,17*0.0,
       .0018,.0029,.0039,.0048,.0046,.0040,.0015,-.002,-.005,17*0.0,
       .0007,.0013,.0018,.0023,.0023,.0019,.0008,-.001,-.002,17*0.0,
       .0000,.0003,.0007,.0013,.0015,.0016,.0014,.0010,.0006,17*0.0,
       .0000,.0002,.0005,.0010,.0013,.0016,.0019,.0022,.0023,17*0.0,
       .0000,.0001,.0002,.0004,.0015,.0025,.0050,.0075,.0102,17*0.0,
CLZPR=.08,
NALPHA=17,TALPHA=-6.0,-5.0,-4.0,-3.0,-2.0,-1.0,0.0,1.0,2.0,3.0,
                 4.0,5.0,6.0,7.0,8.0,9.0,10.0,
$
ZSCALE=.5
$INPT1 TZSCALE=0.5,CLZPR=.08,    $
ZSCALE=0.0
$INPT1 TZSCALE=0.0,CLZPR=.08,    $
```

Table I. Continued

(l) Arbitrary planform wing–body combination twisted and cambered for optimum combination of loads with severe constraint at $C_L = 0.08$ and $M = 2.40$

```
CURVED L E WING - DARDEN TP-2446  SEVERE CONSTRAINT
$INPT1 XM=2.4,RN=2.0,JBYMAX=25,IVOROP=1,IPRSLD=1,
SREF=2.5375,CBAR=1.6861,XMC=1.431,XMAX=3.29,
NLEY=11,
TBLEY=0.00,0.10,0.20,0.30,0.40,0.50,0.60,0.70,0.80,0.90,1.00,
TBLEX=0.00,0.12,0.48,1.08,1.55,1.85,2.09,2.31,2.53,2.75,2.96,
NTEY=11,
TBTEY=0.00,0.10,0.20,0.30,0.40,0.50,0.60,0.70,0.80,0.90,1.00,
TBTEX=2.58,2.60,2.64,2.71,2.79,2.87,2.96,3.04,3.13,3.21,3.29,
NYR=4,TBYR=0.0000,0.5000,0.8000,1.0000,
     TBTOC=0.0300,0.0300,0.0300,0.0300,
     TBROC=.00010,.00030,.00050,.00050,
     TBETA=0.5000,0.5000,0.5000,0.5000,
NYC=11,TBYC=0.00,0.10,0.20,0.30,0.40,0.50,0.60,0.70,0.80,0.90,1.00,
NPCTC=9,
TBPCTC=0.000,5.000,10.00,20.00,30.00,40.00,60.00,80.00,100.0,
TZORDC=.1395,.1387,.1366,.1272,.1109,.0882,.0302,-.026,-.048,17*0.0,
       .1217,.1213,.1200,.1132,.1002,.0811,.0290,-.027,-.059,17*0.0,
       .0740,.0748,.0757,.0754,.0704,.0601,.0240,-.026,-.075,17*0.0,
       .0000,.0032,.0074,.0161,.0238,.0294,.0322,.0221,-.001,17*0.0,
       .0000,.0021,.0045,.0097,.0147,.0193,.0259,.0278,.0242,17*0.0,
       .0000,.0010,.0023,.0047,.0073,.0094,.0125,.0134,.0117,17*0.0,
       .0000,.0006,.0012,.0025,.0036,.0046,.0056,.0052,.0033,17*0.0,
       .0000,.0003,.0007,.0013,.0018,.0022,.0025,.0017,.0000,17*0.0,
       .0000,.0002,.0004,.0007,.0011,.0013,.0014,.0009,.0000,17*0.0,
       .0000,.0001,.0002,.0004,.0006,.0007,.0009,.0006,.0002,17*0.0,
       .0000,.0001,.0001,.0002,.0003,.0004,.0009,.0017,.0025,17*0.0,
CLZPR=.08,
NALPHA=17,TALPHA=-6.0,-5.0,-4.0,-3.0,-2.0,-1.0,0.0,1.0,2.0,3.0,
                 4.0,5.0,6.0,7.0,8.0,9.0,10.0,
$
ZSCALE=.5
$INPT1 TZSCALE=0.5,CLZPR=.08,    $
ZSCALE=0.0
$INPT1 TZSCALE=0.0,CLZPR=.08,    $
```

Table I. Continued

(m) 74° swept arrow wing–body combination with twist and camber for $C_L = 0.10$ and $M = 2.50$

```
T AND C ARROW WING - HASSON TM X8
$INPT1 XM=2.5,RN=5.0,JBYMAX=25,IVOROP=1,IPRSLD=1,
SREF=216.0,CBAR=15.492,XMC=19.584,XMAX=32.532
NLEY=2,TBLEY=0.000,9.294,
       TBLEX=0.000,32.53,
NTEY=2,TBTEY=0.000,9.294,
       TBTEX=23.24,32.53,
NYR=6,TBYR=0.0000,1.8588,3.7176,5.5764,7.4352,9.294,
     TBTOC=.03000,.03000,.03000,.03000,.03000,.03000,
     TBROC=.00017,.00022,.00029,.00043,.00050,.00050,
     TBETA=.50000,.50000,.50000,.50000,.50000,.50000,
NYC=12,TBYC=0.000,0.929,1.858,2.788,3.718,4.647,5.576,
           6.506,7.435,8.365,8.829,9.294,
NPCTC=9,
TBPCTC=0.000,5.000,10.00,20.00,30.00,40.00,60.00,80.00,100.0,
TZORDC=2.117,1.861,1.615,1.150,0.723,0.339,-.290,-.711,-.897,17*0.0,
       1.075,0.996,0.908,0.707,0.481,0.243,-.236,-.657,-.939,17*0.0,
       0.638,0.621,0.589,0.489,0.351,0.184,-.190,-.547,-.798,17*0.0,
       0.429,0.429,0.416,0.356,0.260,0.138,-.146,-.423,-.618,17*0.0,
       0.286,0.294,0.291,0.257,0.192,0.105,-.112,-.325,-.475,17*0.0,
       0.175,0.191,0.196,0.182,0.141,0.077,-.085,-.249,-.361,17*0.0,
       0.102,0.121,0.131,0.129,0.103,0.058,-.064,-.187,-.260,17*0.0,
       0.053,0.072,0.084,0.089,0.073,0.041,-.046,-.132,-.172,17*0.0,
       0.006,0.032,0.042,0.055,0.049,0.029,-.032,-.089,-.102,17*0.0,
       -.015,0.001,0.008,0.020,0.020,0.012,-.015,-.041,-.047,17*0.0,
       -.018,-.004,0.002,0.010,0.010,0.007,-.007,-.020,-.024,17*0.0,
       0.000,0.000,0.000,0.000,0.000,0.000,0.000,0.000,0.000,17*0.0,
NALPHA=16,TALPHA=-8.0,-6.0,-4.0,-2.0,-1.0,
                 0.0,1.0,2.0,3.0,4.0,5.0,6.0,7.0,8.0,9.0,10.0,    $
FLAT WING
$INPT1 TZSCALE=0.0,    $
```

Table I. Continued

(n) 75° swept modified arrow wing–body combination with twist and camber for $C_L = 0.10$ and $M = 3.00$

```
BROWN BOMBER - HALLISSY,RM L58E21
$INPT1 XM=2.87,RN=4.2,JBYMAX=25,IVOROP=1,
SREF=502.56,CBAR=20.43,XMC=27.98,XMAX=56.00,
NLEY=2,TBLEY=0.000,15.00,
       TBLEX=0.000,56.00,
NTEY=8,TBTEY=0.000,2.590,5.180,7.760,10.35,12.94,13.97,15.00,
       TBTEX=28.00,34.56,40.92,46.58,51.24,54.60,55.46,56.00,
NYR=6,TBYR=0.000,2.580,5.180,7.760,11.65,15.00,
     TBTOC=.0186,.0227,.0227,.0289,.0289,.0165,
     TBROC=.0003,.0005,.0005,.0007,.0007,.0002,
     TBETA=.4000,.4000,.4000,.4000,.4000,.4000,
NYC=8,TBYC=0.000,2.590,5.180,7.760,10.35,12.94,13.97,15.00,
NPCTC=9,
TBPCTC=0.000,5.000,10.00,20.00,30.00,40.00,60.00,80.00,100.0,
TZORDC=3.040,2.630,2.150,1.240,0.410,-.150,-.900,-1.49,-1.92,17*0.0,
       0.210,0.238,0.215,0.060,-.140,-.380,-.880,-1.39,-1.88,17*0.0,
       0.106,0.159,0.169,0.130,0.047,-.070,-.420,-.780,-1.15,17*0.0,
       0.117,0.168,0.191,0.187,0.148,0.090,-.050,-.220,-.380,17*0.0,
       0.061,0.109,0.138,0.170,0.177,0.169,0.120,0.050,-.020,17*0.0,
       -.030,-.005,0.012,0.045,0.068,0.088,0.113,0.130,0.137,17*0.0,
       -.075,-.055,-.047,-.024,-.008,0.007,0.031,0.049,0.063,17*0.0,
       -.134,-.134,-.134,-.134,-.134,-.134,-.134,-.134,-.134,17*0.0,
NALPHA=17,TALPHA=-8.0,-6.0,-4.0,-3.0,-2.0,-1.0,0.0,1.0,2.0,
                 3.0,4.0,5.0,6.0,7.0,8.0,9.0,10.0,
CLZPR=.10,    $
FLAT WING
$INPT1 TZSCALE=0.0,    $
```

Table I. Continued

(o) Supersonic transport wing–body combination with twist and camber for $C_L = 0.08$ and $M = 2.70$

```
ARROW WING SST - MORRIS,TM 78706
$INPT1 XM=2.7,RN=3.19,JBYMAX=25,IVOROP=1,IPRSLD=1,
SREF=320.69,CBAR=19.155,XMC=33.405,XMAX=54.0,
NLEY=4,TBLEY=0.000,0.856,8.533,11.41,
       TBLEX=0.000,14.83,41.61,47.78,
NTEY=6,TBTEY=0.000,0.856,2.370,4.980,8.533,11.41,
       TBTEX=54.00,43.93,43.93,44.84,47.47,49.13,
NYR=6,TBYR=0.000,0.856,0.857,8.533,8.534,11.41,
     TBTOC=.0300,.0300,.0300,.0300,.0300,.0300,
     TBROC=.0005,.0005,.0005,.0005,.0005,.0005,
     TBETA=.6000,.6000,.6000,.5000,.5000,.5000,
NYC=13,TBYC=0.000,0.856,1.712,2.370,2.853,3.994,4.980,6.297,
            7.418,8.533,9.130,10.27,11.41,
NPCTC=10,
TBPCTC=0.000,2.500,5.000,10.00,20.00,30.00,40.00,60.00,80.00,100.0,
TZORDC=2.300,2.300,2.300,2.300,2.300,2.040,1.450,0.250,-.720,-1.52,16*0.0,
       0.000,-.017,-.048,-.164,-.470,-.833,-1.17,-1.80,-2.31,-2.62,16*0.0,
       0.000,.0150,.0180,-.026,-.176,-.380,-.591,-1.04,-1.44,-1.72,16*0.0,
       0.000,.0250,.0320,.0130,-.090,-.236,-.395,-.742,-1.08,-1.30,16*0.0,
       0.000,.0220,.0340,.0300,-.051,-.166,-.300,-.598,-.893,-1.12,16*0.0,
       0.000,.0190,.0360,.0510,.0270,-.050,-.131,-.327,-.541,-.708,16*0.0,
       0.000,.0170,.0310,.0550,.0550,.0220,-.032,-.177,-.281,-.417,16*0.0,
       0.000,.0170,.0330,.0540,.0700,.0630,.0450,-.032,-.114,-.210,16*0.0,
       0.000,.0180,.0300,.0530,.0860,.0920,.0800,.0610,.0140,-.035,16*0.0,
       0.000,.0080,.0150,.0270,.0480,.0700,.0740,.0700,.0570,.0460,16*0.0,
       0.000,.0030,.0040,.0070,.0190,.0320,.0360,.0250,.0170,.0150,16*0.0,
       0.000,.0010,.0010,.0000,.0000,-.004,-.009,-.021,-.036,-.050,16*0.0,
       0.000,.0000,.0000,.0000,-.001,-.001,-.002,-.003,-.004,-.005,16*0.0,
NALPHA=19,TALPHA=-8.0,-7.0,-6.0,-5.0,-4.0,-3.0,-2.0,-1.0,
                 0.0,1.0,2.0,3.0,4.0,5.0,6.0,7.0,8.0,9.0,10.0,
CLZPR=.08,    $
CLD=0.0
$INPT1 TZSCALE=0.0,CLZPR=.08,    $
```

Table I. Continued

(p) 60° swept wing–body combination twisted and cambered for $C_L = 0.05$ and $M = 1.80$

```
CRUISE SURFACE - JOHNSON,CR 3939
$INPT1 XM=1.6,RN=1.66,JBYMAX=25,IPRSLD=1,
SREF=148.6,CBAR=9.96,XMC=20.64,XMAX=33.50,
NLEY=4,TBLEY=0.000,1.190,1.200,9.200,
       TBLEX=0.000,4.400,13.43,27.29,
NTEY=5,TBTEY=0.000,1.190,1.200,5.200,9.200,
       TBTEX=33.50,33.50,26.64,27.16,29.29,
NYR=2,TBYR=0.000,9.200,
     TBTOC=.0400,.0400,
     TBROC=.0011,.0011,
     TBETA=.4000,.4000,
NYC=11,TBYC=0.00,1.19,1.20,2.20,3.20,4.20,5.20,6.20,7.20,8.20,9.20,
NPCTC=10,
TBPCTC=0.000,2.481,4.975,9.965,19.95,29.95,39.95,59.96,79.80,100.0,
TZORDC=0.000,0.000,0.000,0.000,0.000,0.000,0.000,0.000,0.000,0.000,16*0.0,
       0.000,0.000,0.000,0.000,0.000,0.000,0.000,0.000,0.000,0.000,16*0.0,
       0.000,-.012,-.023,-.039,-.061,-.081,-.100,-.116,-.080,-.019,16*0.0,
       0.000,.0030,.0020,.0010,-.003,-.007,-.007,.0020,.0230,.0460,16*0.0,
       0.000,.0090,.0150,.0260,.0390,.0430,.0460,.0630,.0850,.1090,16*0.0,
       0.000,.0090,.0160,.0290,.0490,.0560,.0610,.0830,.1060,.1310,16*0.0,
       0.000,.0060,.0120,.0220,.0390,.0520,.0650,.0890,.1120,.1370,16*0.0,
       0.000,.0060,.0110,.0200,.0350,.0490,.0610,.0850,.1070,.1320,16*0.0,
       0.000,.0050,.0090,.0170,.0300,.0420,.0530,.0740,.0950,.1150,16*0.0,
       0.000,.0030,.0060,.0120,.0240,.0330,.0430,.0600,.0770,.0950,16*0.0,
       0.000,.0015,.0022,.0060,.0140,.0240,.0330,.0520,.0720,.0910,16*0.0,
NALPHA=15,TALPHA=-4.0,-3.0,-2.0,-1.0,0.0,1.0,2.0,3.0,4.0,5.0,6.0,7.0,8.0,
9.0,10.0,
CLZPR=.30,    $
FLAT WING
$INPT1 TZSCALE=0.0,CLZPR=.30,    $
```

Table I. Continued

(q) 60° swept wing–body with mission adaptive twist and camber for $C_L = 0.30$ and $M = 1.60$

```
MISSION ADAPTIVE SURFACE - JOHNSON,CR 3939
$INPT1 XM=1.6,RN=1.66,JBYMAX=25,IPRSLD=1,
SREF=148.6,CBAR=9.96,XMC=20.64,XMAX=33.50,
NLEY=4,TBLEY=0.000,1.190,1.200,9.200,
       TBLEX=0.000,4.400,13.43,27.29,
NTEY=5,TBTEY=0.000,1.190,1.200,5.200,9.200,
       TBTEX=33.50,33.50,26.64,27.16,29.29,
NYR=2,TBYR=0.000,9.200,
     TBTOC=.0400,.0400,
     TBROC=.0011,.0011,
     TBETA=.4000,.4000,
NYC=11,TBYC=0.00,1.19,1.20,2.20,3.20,4.20,5.20,6.20,7.20,8.20,9.20,
NPCTC=10,
TBPCTC=0.000,2.467,4.947,9.925,19.90,29.90,39.91,59.93,79.97,100.0,
TZORDC=0.000,0.000,0.000,0.000,0.000,0.000,0.000,0.000,0.000,0.000,16*0.0,
       0.000,0.000,0.000,0.000,0.000,0.000,0.000,0.000,0.000,0.000,16*0.0,
       0.000,-.011,-.021,-.038,-.065,-.085,-.104,-.120,-.084,-.023,16*0.0,
       0.000,.0160,.0290,.0440,.0450,.0410,.0410,.0500,.0710,.0940,16*0.0,
       0.000,.0370,.0670,.1060,.1340,.1360,.1390,.1560,.1770,.2020,16*0.0,
       0.000,.0450,.0830,.1340,.1760,.1830,.1880,.2100,.2330,.2580,16*0.0,
       0.000,.0470,.0870,.1450,.1920,.2050,.2180,.2420,.2650,.2900,16*0.0,
       0.000,.0500,.0920,.1510,.1990,.2130,.2250,.2490,.2710,.2960,16*0.0,
       0.000,.0470,.0870,.1430,.1930,.2040,.2160,.2370,.2580,.2780,16*0.0,
       0.000,.0370,.0690,.1150,.1560,.1650,.1740,.1920,.2090,.2270,16*0.0,
       0.000,.0260,.0480,.0760,.1100,.1200,.1290,.1480,.1680,.1870,16*0.0,
NALPHA=15,TALPHA=-4.0,-3.0,-2.0,-1.0,0.0,1.0,2.0,3.0,4.0,5.0,6.0,7.0,8.0,
9.0,10.0,
CLZPR=.30,    $
FLAT WING
$INPT1 TZSCALE=0.0,CLZPR=.30,    $
```

Table I. Continued

(r) Design of wing surface for 70° swept arrow wing at $C_L = 0.16$ and $M = 2.05$ with no moment restraint

```
70 DEG ARROW WING - CARLSON,TMX-332 AND TN D-1264  CLD=.16
$INPT1 XM=2.05,RN=0.0,JBYMAX=30,IVOROP=1,IPRSLD=0,
CLDES=0.16,CLZPR=0.16,NEWDES=1,
CMDES=0.0,
SREF=212.94,CBAR=13.00,XMC=13.25,XMAX=30.00,
NLEY=2,TBLEY=0.000,10.92,
       TBLEX=0.000,30.00,
NTEY=2,TBTEY=0.000,10.92,
       TBTEX=19.50,30.00,
NYR=5,TBYR=0.0000,5.4600,7.6440,8.7360,10.920,
     TBTOC=0.0300,0.0300,0.0300,0.0300,0.0300,
     TBROC=.00010,.00021,.00034,.00050,.00050,
     TBETA=0.5000,0.5000,0.5000,0.5000,0.5000,
NALPHA=17,TALPHA=-6.0,-5.0,-4.0,-3.0,-2.0,-1.0,0.0,1.0,2.0,3.0,4.0,
                 5.0,6.0,7.0,8.0,9.0,10.0,    $
```

(s) Design of wing surface for 70° swept arrow wing at $C_L = 0.16$ and $M = 2.05$ with $C_{M,\text{des}} = 0.0$ and with TAFIX option employed

```
70 DEG ARROW WING - CARLSON,TMX-332 AND TN D-1264  CLD=,16 CMD=0.0
$INPT1 XM=2.05,RN=0.0,JBYMAX=30,IVOROP=1,IPRSLD=0,
CLDES=0.16,CLZPR=0.16,NEWDES=1,
CMDES=0.0,
SREF=212.94,CBAR=13.00,XMC=13.25,XMAX=30.00,
NLEY=2,TBLEY=0.000,10.92,
       TBLEX=0.000,30.00,
NTEY=2,TBTEY=0.000,10.92,
       TBTEX=19.50,30.00,
NYR=5,TBYR=0.0000,5.4600,7.6440,8.7360,10.920,
     TBTOC=0.0300,0.0300,0.0300,0.0300,0.0300,
     TBROC=.00010,.00021,.00034,.00050,.00050,
     TBETA=0.5000,0.5000,0.5000,0.5000,0.5000,
IAFIX=1,
TAFIX=1.894,4.269,4.925,5.271,5.442,5.599,5.836,6.257,6.385,6.276,
      6.151,6.040,5.974,5.884,5.855,5.862,5.905,5.983,6.142,6.424,
      6.933,7.252,7.406,7.521,7.547,7.543,7.705,8.211,9.046,10.06,
NALPHA=17,TALPHA=-6.0,-5.0,-4.0,-3.0,-2.0,-1.0,0.0,1.0,2.0,3.0,4.0,
                 5.0,6.0,7.0,8.0,9.0,10.0,    $
```

Table I. Continued

(t) Design of revised mission adaptive surface for a 60° swept wing–body combination at $C_L = 0.30$ and $M = 1.60$ without TAFIX

```
MISSION ADAPTIVE WING REDESIGN CL=.3 - JOHNSON,CR 3939
$INPT1 XM=1.6,RN=1.66,JBYMAX=50,IPRSLD=1,
CLDES=0.30,IFLPDES=1,
SREF=148.6,CBAR=9.96,XMC=20.64,XMAX=33.50,
NLEY=4,TBLEY=0.000,1.190,1.200,9.200,
       TBLEX=0.000,4.400,13.43,27.29,
NTEY=5,TBTEY=0.000,1.190,1.200,5.200,9.200,
       TBTEX=33.50,33.50,26.64,27.16,29.29,
NYR=2,TBYR=0.000,9.200,
     TBTOC=.0400,.0400,
     TBROC=.0011,.0011,
     TBETA=.4000,.4000,
NYC=11,TBYC=0.00,1.19,1.20,2.20,3.20,4.20,5.20,6.20,7.20,8.20,9.20,
NPCTC=10,
TBPCTC=0.000,2.481,4.975,9.965,19.95,29.95,39.95,59.96,79.80,100.0,
TZORDC=0.000,0.000,0.000,0.000,0.000,0.000,0.000,0.000,0.000,0.000,16*0.0,
       0.000,0.000,0.000,0.000,0.000,0.000,0.000,0.000,0.000,0.000,16*0.0,
       0.000,-.012,-.023,-.039,-.061,-.081,-.100,-.116,-.080,-.019,16*0.0,
       0.000,.0030,.0020,.0010,-.003,-.007,-.007,.0020,.0230,.0460,16*0.0,
       0.000,.0090,.0150,.0260,.0390,.0430,.0460,.0630,.0850,.1090,16*0.0,
       0.000,.0090,.0160,.0290,.0490,.0560,.0610,.0830,.1060,.1310,16*0.0,
       0.000,.0060,.0120,.0220,.0390,.0520,.0650,.0890,.1120,.1370,16*0.0,
       0.000,.0060,.0110,.0200,.0350,.0490,.0610,.0850,.1070,.1320,16*0.0,
       0.000,.0050,.0090,.0170,.0300,.0420,.0530,.0740,.0950,.1150,16*0.0,
       0.000,.0030,.0060,.0120,.0240,.0330,.0430,.0600,.0770,.0950,16*0.0,
       0.000,.0015,.0022,.0060,.0140,.0240,.0330,.0520,.0720,.0910,16*0.0,
NGCS=0,
NTES=2,
NTEC=5,TBTECY=0.000,1.190,1.200,5.200,9.200,
        TBTEC=0.000,0.000,1.360,1.360,.4000,
NLEC=4,TBLECY=0.000,1.190,1.200,9.200,
        TBLEC=0.000,0.000,2.320,.4000,
NALPHA=15,TALPHA=-4.0,-3.0,-2.0,-1.0,0.0,1.0,2.0,3.0,4.0,5.0,6.0,7.0,8.0,
9.0,10.0,
CLZPR=.30,     $
```

Table I. Concluded

(u) Design of revised mission adaptive surface for 60° swept wing–body combination at $C_L = 0.30$ and $M = 1.60$ with TAFIX

```
MISSION ADAPTIVE WING REDESIGN WITH TAFIX CL=.3 - JOHNSON,CR 3939
$INPT1 XM=1.6,RN=1.66,JBYMAX=50,IPRSLD=1,
CLDES=0.30,IFLPDES=1,
SREF=148.6,CBAR=9.96,XMC=20.64,XMAX=33.50,
NLEY=4,TBLEY=0.000,1.190,1.200,9.200,
       TBLEX=0.000,4.400,13.43,27.29,
NTEY=5,TBTEY=0.000,1.190,1.200,5.200,9.200,
       TBTEX=33.50,33.50,26.64,27.16,29.29,
NYR=2,TBYR=0.000,9.200,
     TBTOC=.0400,.0400,
     TBROC=.0011,.0011,
     TBETA=.4000,.4000,
NYC=11,TBYC=0.00,1.19,1.20,2.20,3.20,4.20,5.20,6.20,7.20,8.20,9.20,
NPCTC=10,
TBPCTC=0.000,2.481,4.975,9.965,19.95,29.95,39.95,59.96,79.80,100.0,
TZORDC=0.000,0.000,0.000,0.000,0.000,0.000,0.000,0.000,0.000,0.000,16*0.0,
       0.000,0.000,0.000,0.000,0.000,0.000,0.000,0.000,0.000,0.000,16*0.0,
       0.000,-.012,-.023,-.039,-.061,-.081,-.100,-.116,-.080,-.019,16*0.0,
       0.000,.0030,.0020,.0010,-.003,-.007,-.007,.0020,.0230,.0460,16*0.0,
       0.000,.0090,.0150,.0260,.0390,.0430,.0460,.0630,.0850,.1090,16*0.0,
       0.000,.0090,.0160,.0290,.0490,.0560,.0610,.0830,.1060,.1310,16*0.0,
       0.000,.0060,.0120,.0220,.0390,.0520,.0650,.0890,.1120,.1370,16*0.0,
       0.000,.0060,.0110,.0200,.0350,.0490,.0610,.0850,.1070,.1320,16*0.0,
       0.000,.0050,.0090,.0170,.0300,.0420,.0530,.0740,.0950,.1150,16*0.0,
       0.000,.0030,.0060,.0120,.0240,.0330,.0430,.0600,.0770,.0950,16*0.0,
       0.000,.0015,.0022,.0060,.0140,.0240,.0330,.0520,.0720,.0910,16*0.0,
NGCS=0,
NTES=2,
NTEC=5,TBTECY=0.000,1.190,1.200,5.200,9.200,
        TBTEC=0.000,0.000,1.360,1.360,.4000,
NLEC=4,TBLECY=0.000,1.190,1.200,9.200,
        TBLEC=0.000,0.000,2.320,.4000,
NALPHA=15,TALPHA=-4.0,-3.0,-2.0,-1.0,0.0,1.0,2.0,3.0,4.0,5.0,6.0,7.0,8.0,
9.0,10.0,
IAFIX=1,
TAFIX=1.0,2.8,6.0,10.3,14.5,15.0,12.0,9.5,8.3,8.0,7.8,8.0,8.2,
      8.5,9.0,9.5,10.3,11.2,12.0,13.0,14.0,15.0,16.0,17.0,
      18.3,20.0,21.3,23.2,25.5,27.3,30.3,34.0,
CLZPR=.30,    $
```

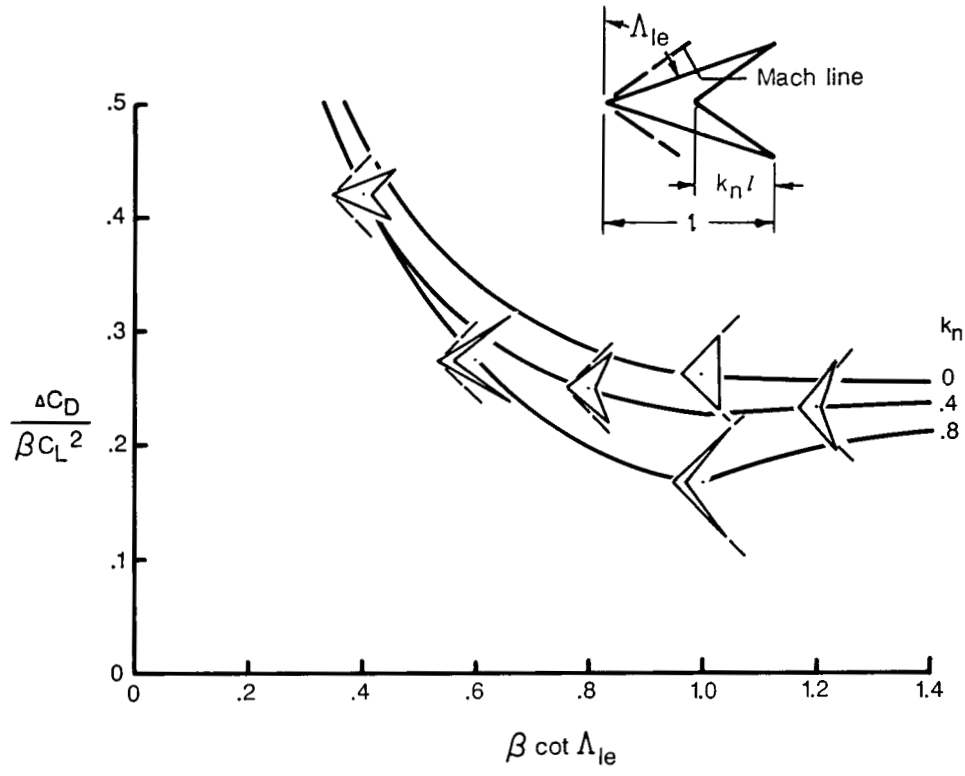

(a) Flat wing without leading-edge thrust or vortex forces.

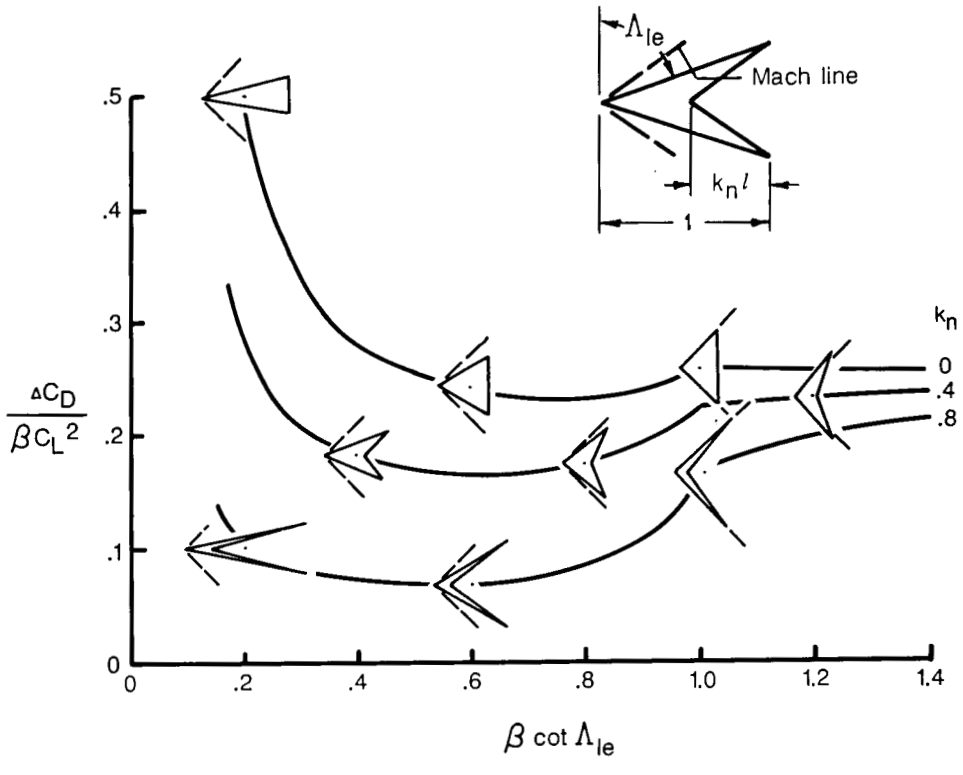

(b) Flat wing with full theoretical leading-edge thrust.

Figure 1. Drag due to lift for arrow wings given by linearized theory computer code.

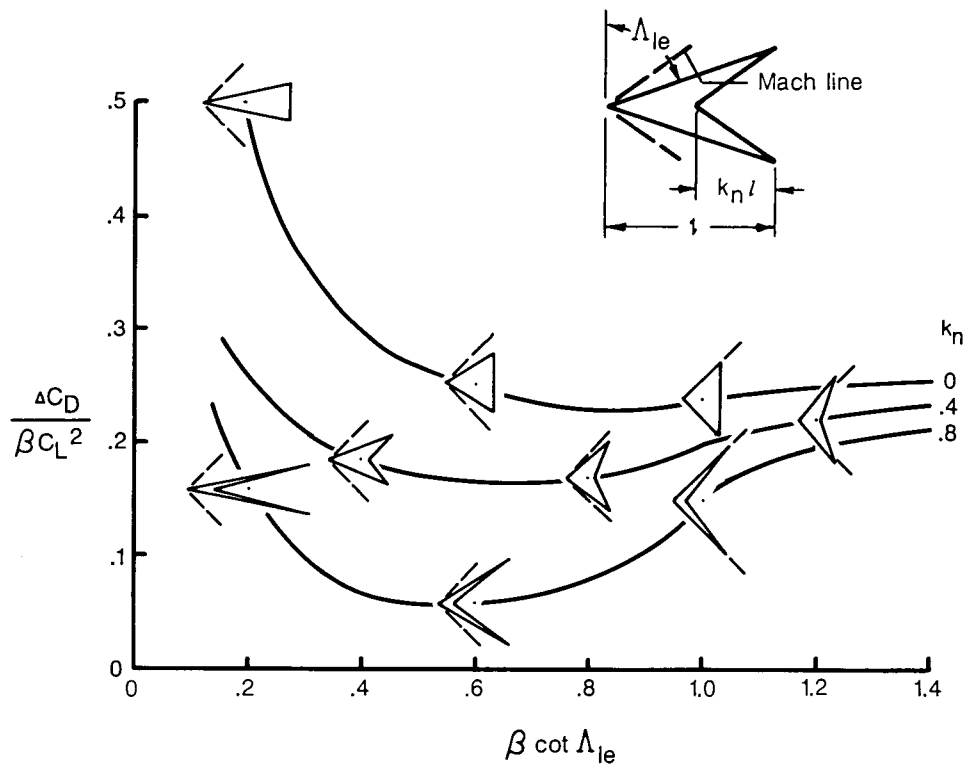

(c) Representative twisted and cambered wing designs.

Figure 1. Concluded.

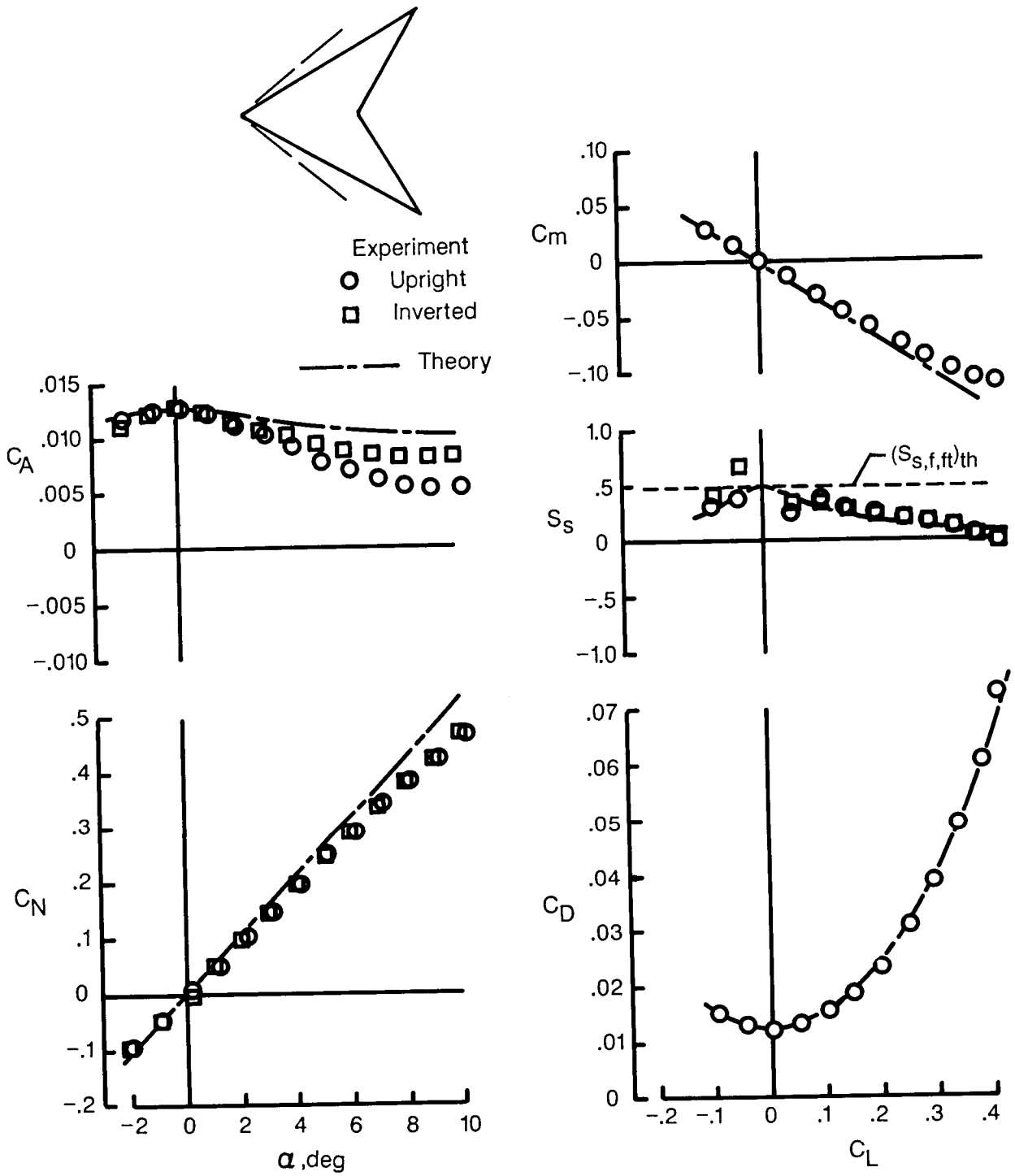

(a) Sharp leading edge; $M = 1.60$; $R = 2.0 \times 10^6$.

Figure 2. Theoretical and experimental data for flat 60° swept arrow wings with various wing sections.

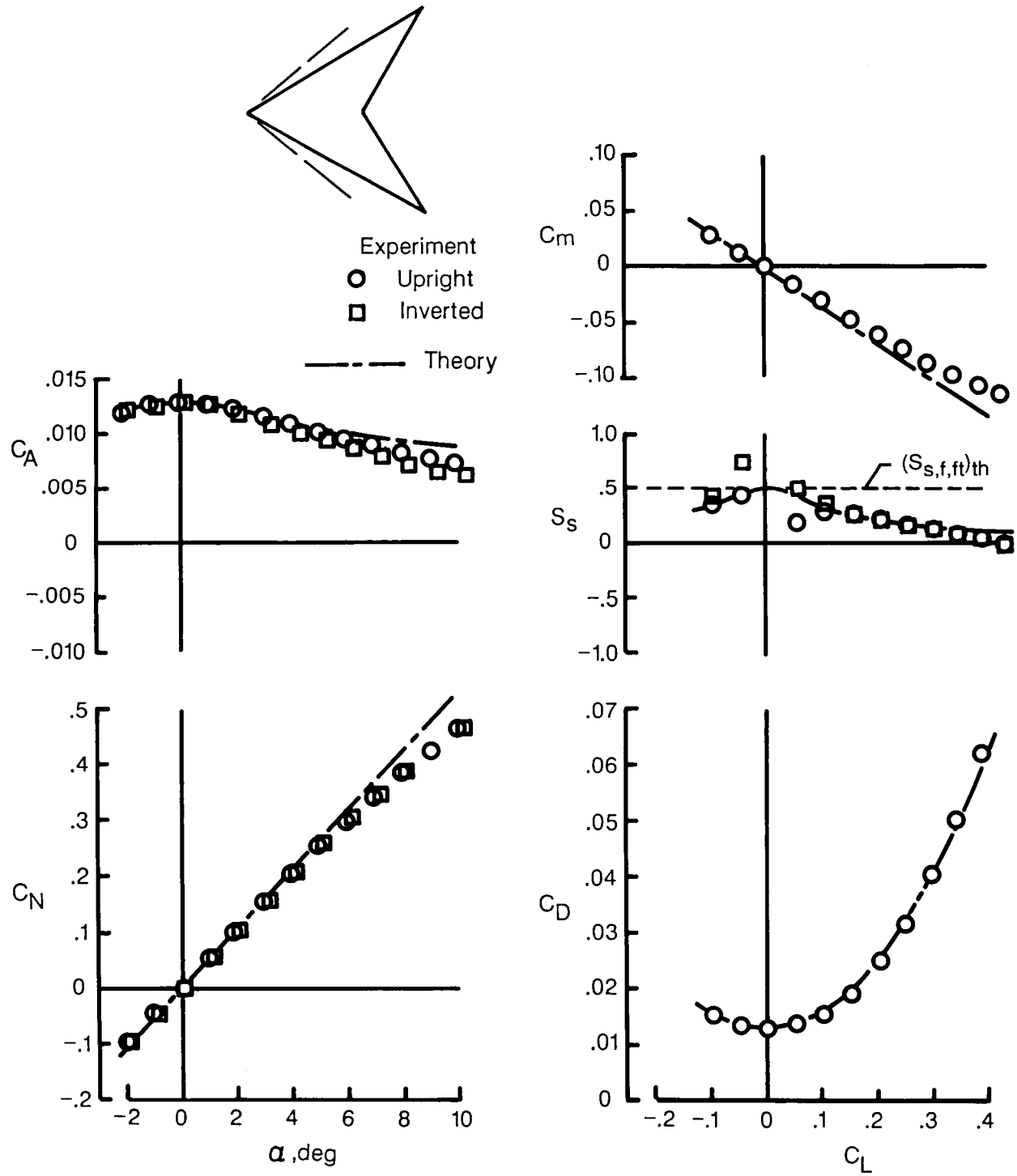

(b) Standard leading edge; $M = 1.60$; $R = 2.0 \times 10^6$.

Figure 2. Continued.

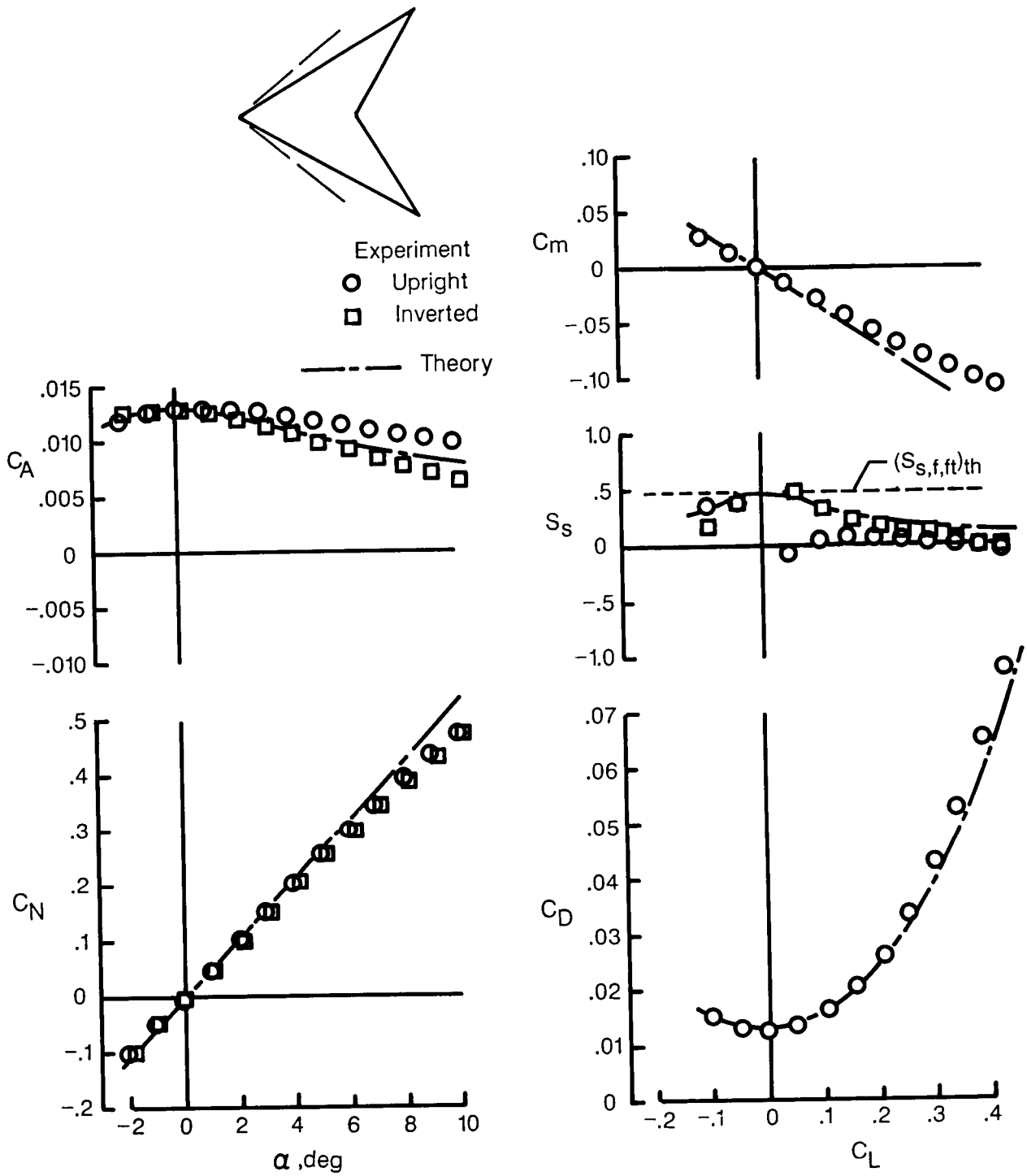

(c) Blunt leading edge; $M = 1.60$; $R = 2.0 \times 10^6$.

Figure 2. Continued.

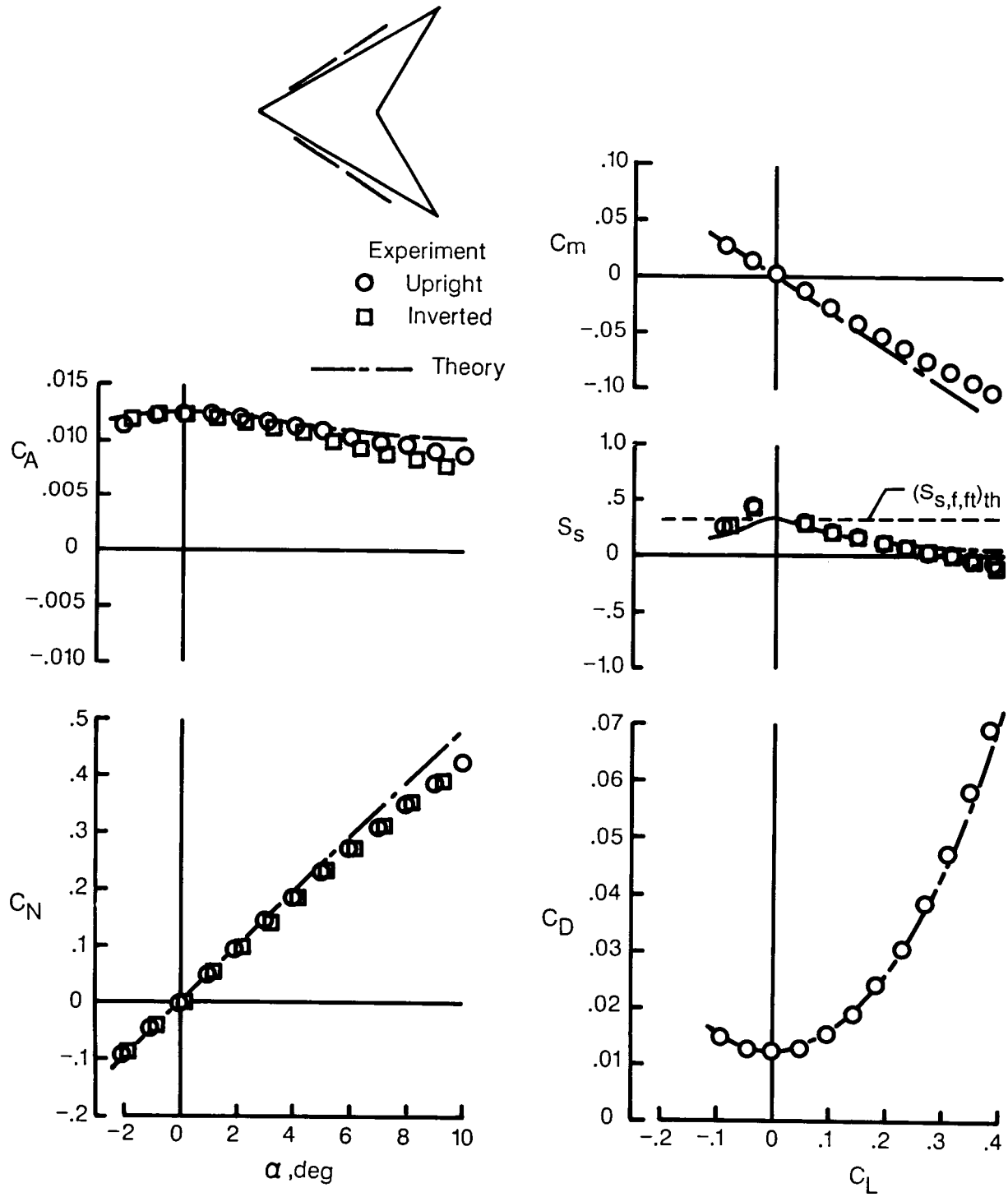

(d) Standard leading edge; $M = 1.80$; $R = 2.0 \times 10^6$.

Figure 2. Continued.

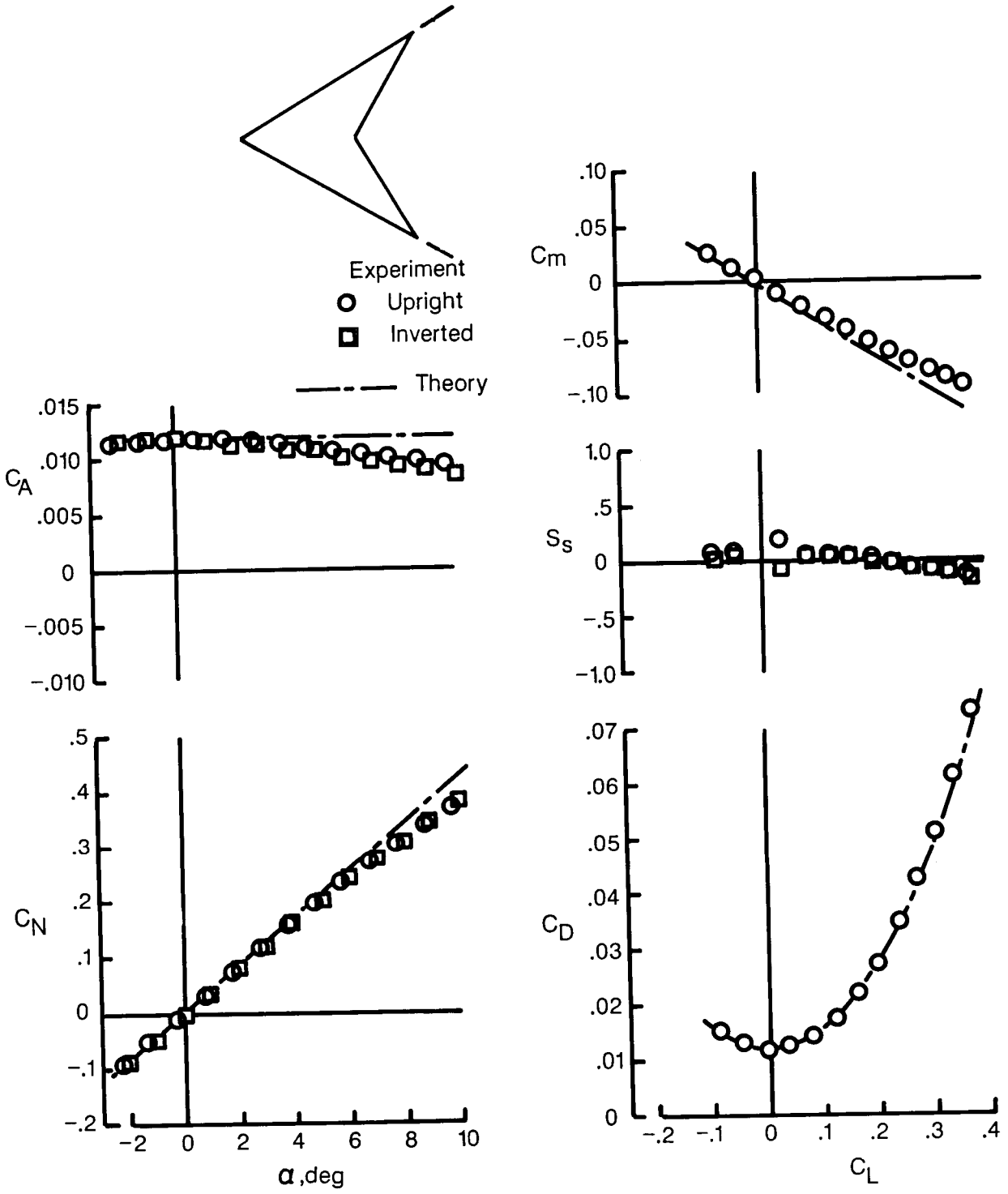

(e) Standard leading edge; $M = 2.00$; $R = 2.0 \times 10^6$.

Figure 2. Continued.

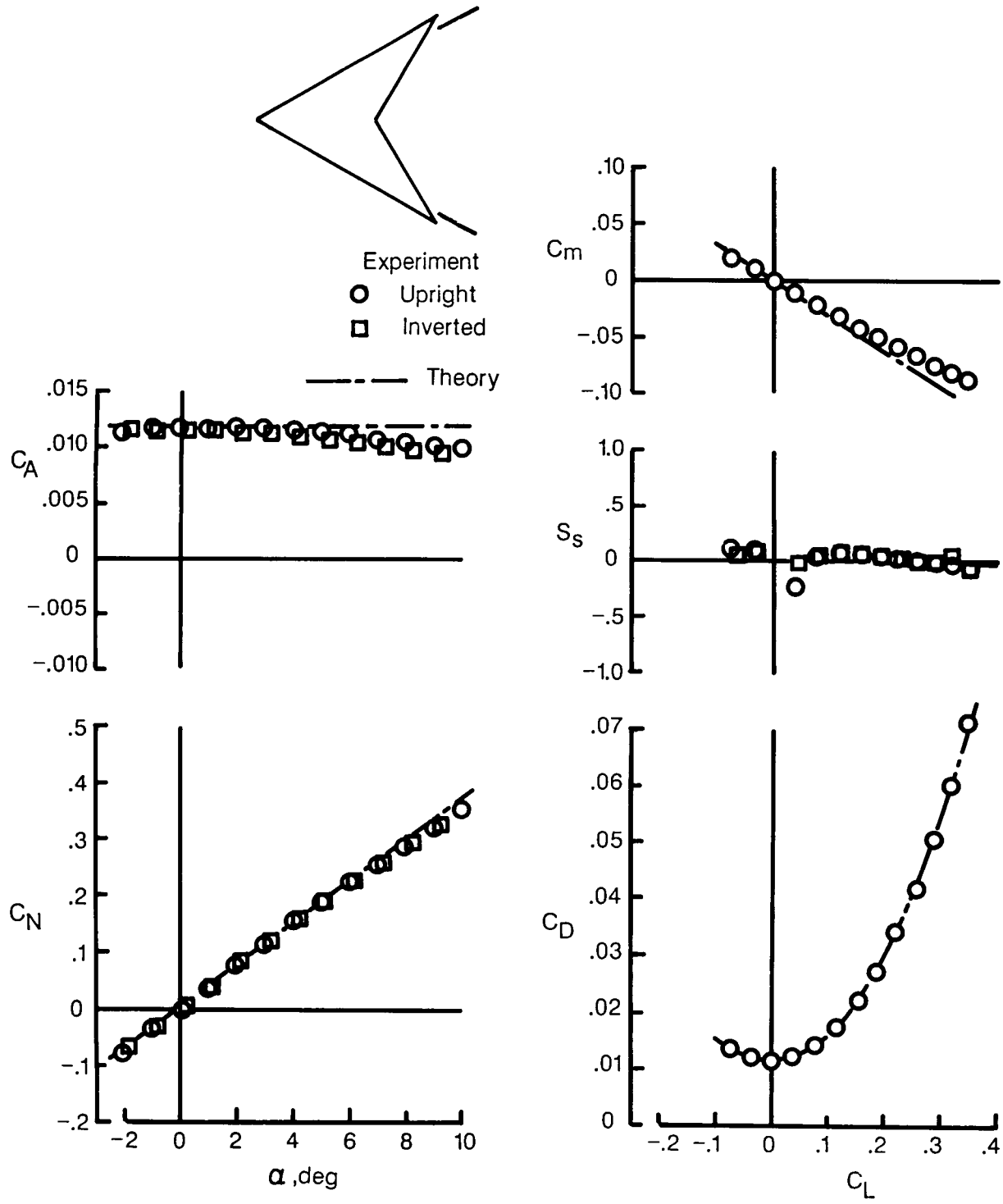

(f) Standard leading edge; $M = 2.16$; $R = 2.0 \times 10^6$.

Figure 2. Concluded.

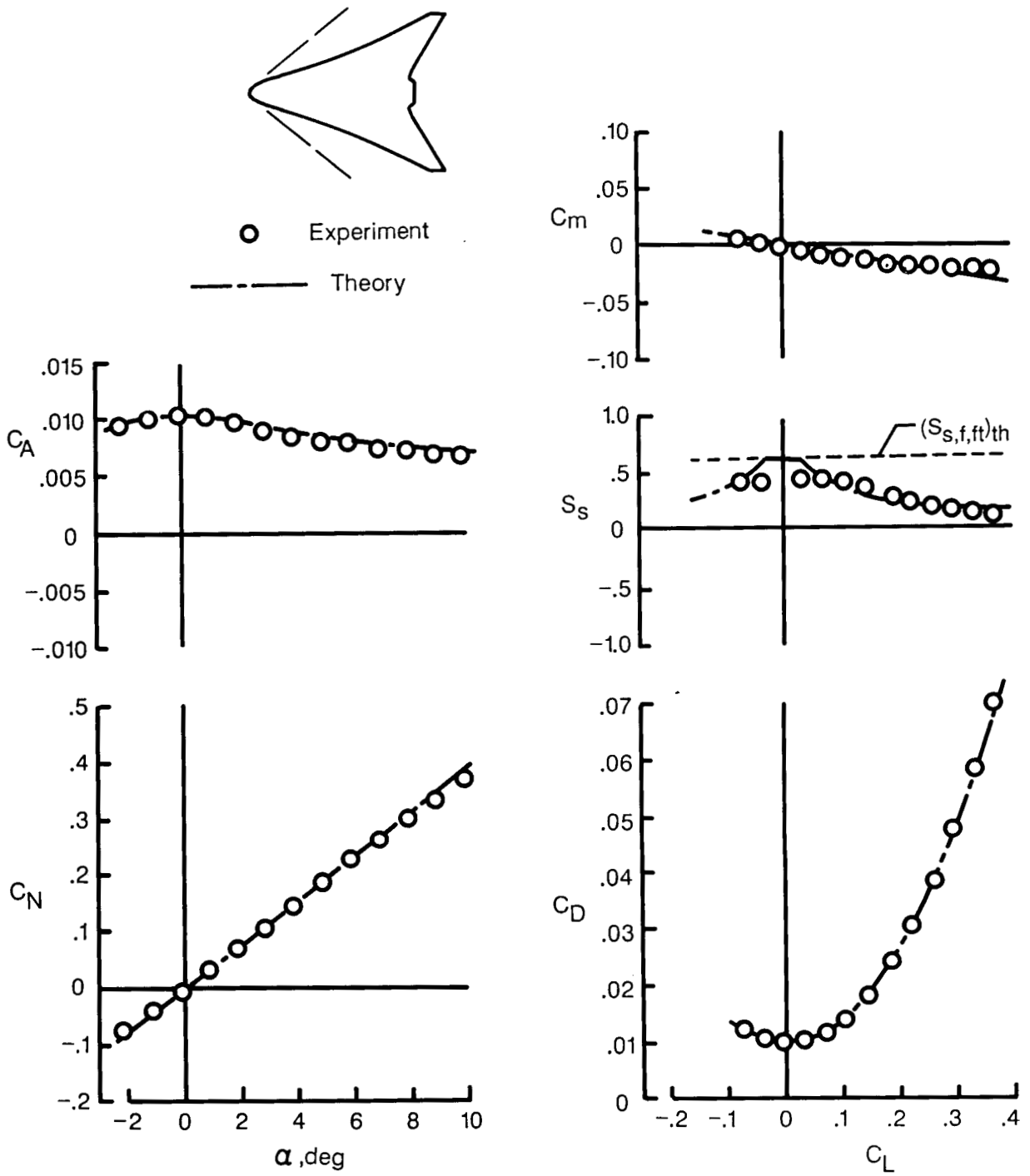

(a) Sharp leading edge; $M = 1.60$; $R = 2.6 \times 10^6$.

Figure 3. Theoretical and experimental data for flat modified arrow wing–body combinations with various wing sections.

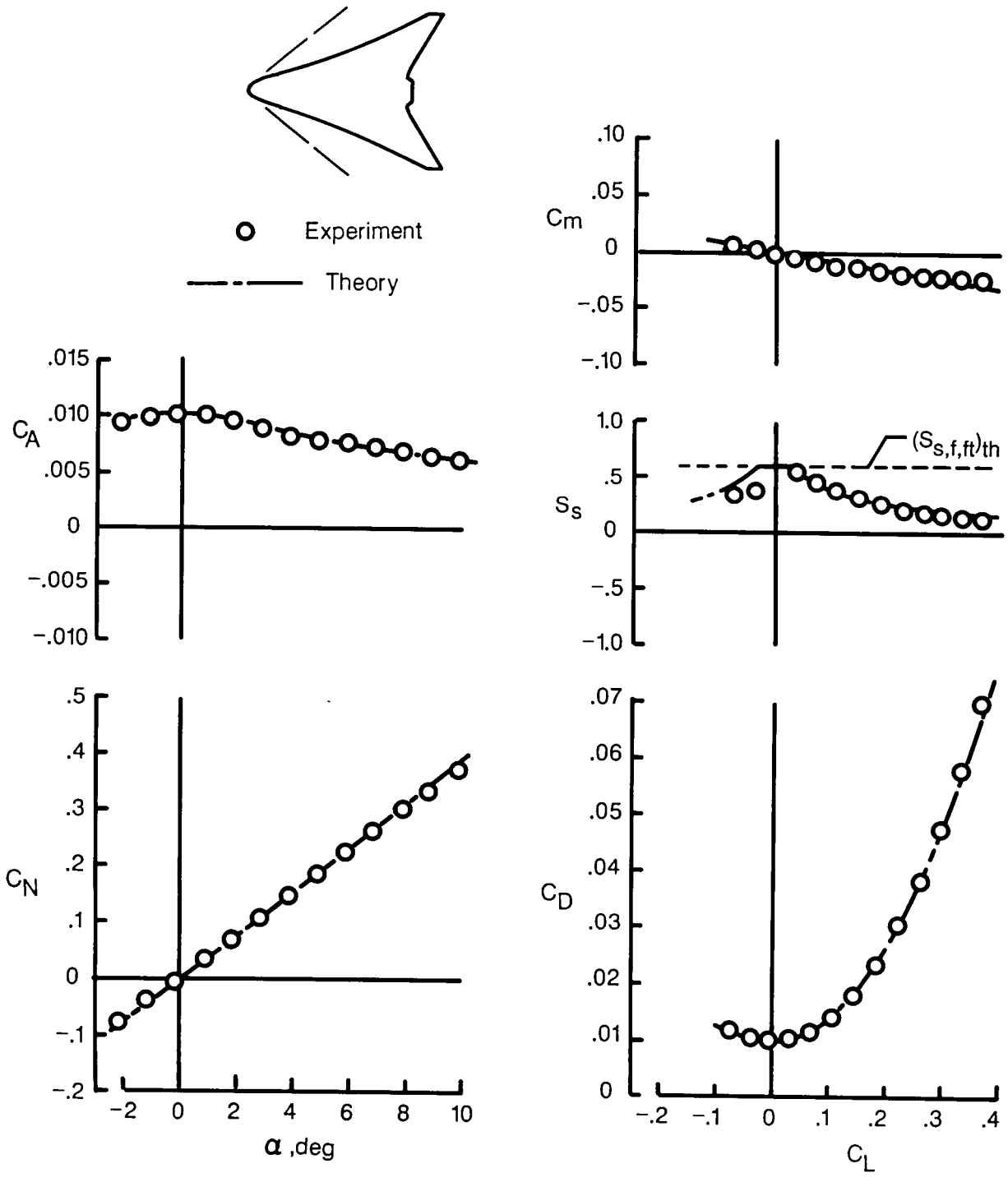

(b) Standard leading edge; $M = 1.60$; $R = 2.6 \times 10^6$.

Figure 3. Continued.

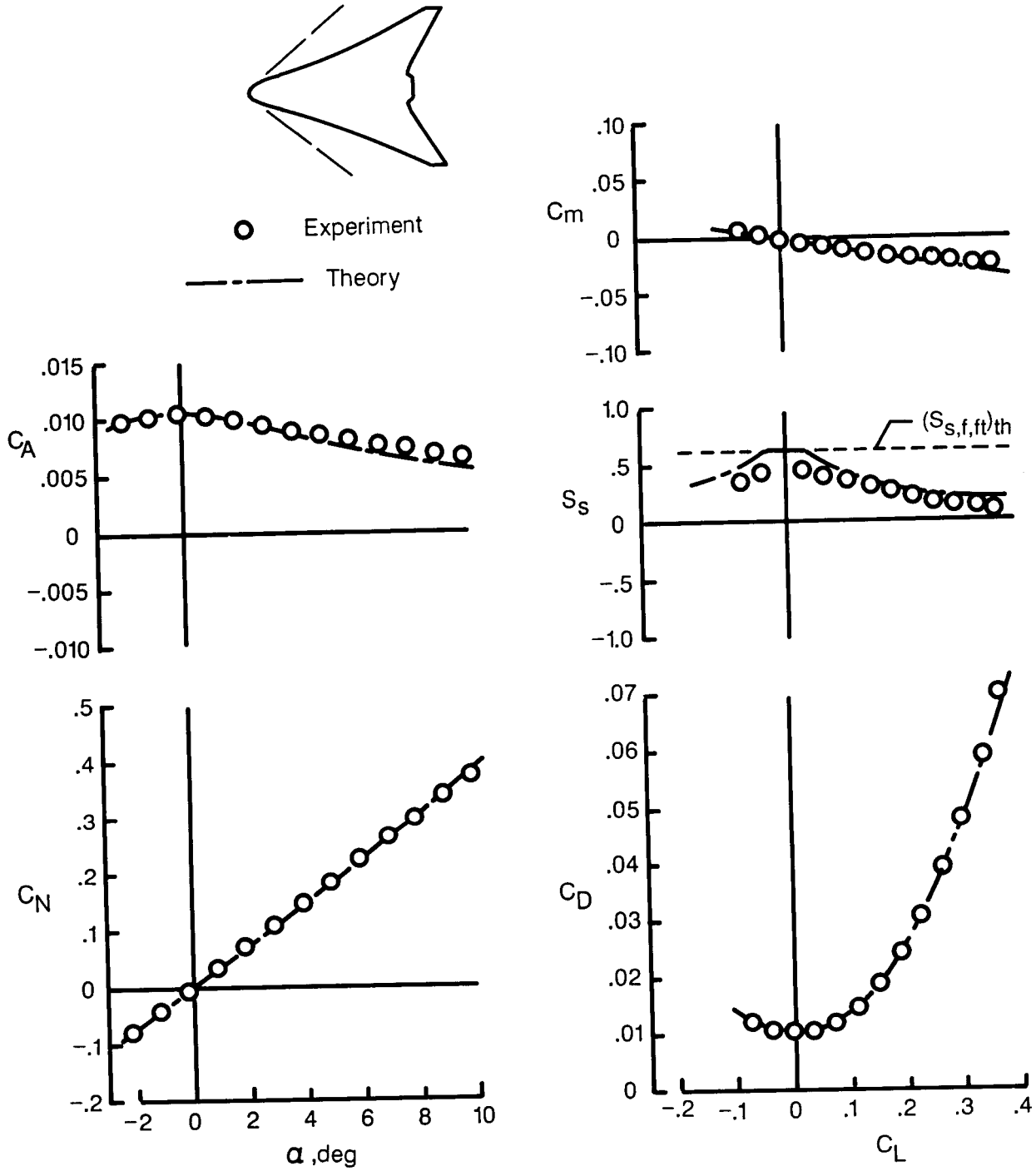

(c) Blunt leading edge; $M = 1.60$; $R = 2.6 \times 10^6$.

Figure 3. Continued.

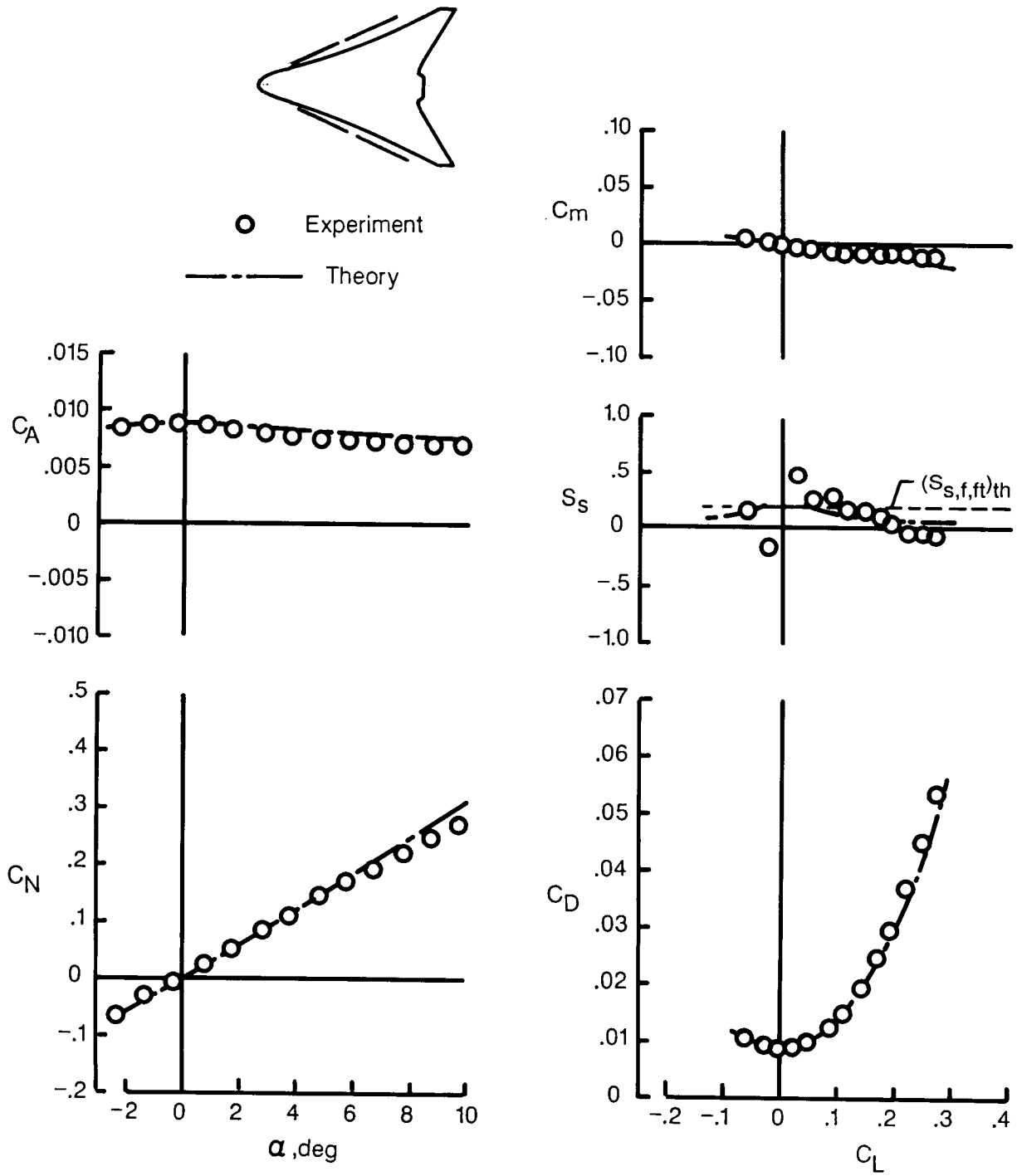

(d) Sharp leading edge; $M = 2.36$; $R = 2.6 \times 10^6$.

Figure 3. Continued.

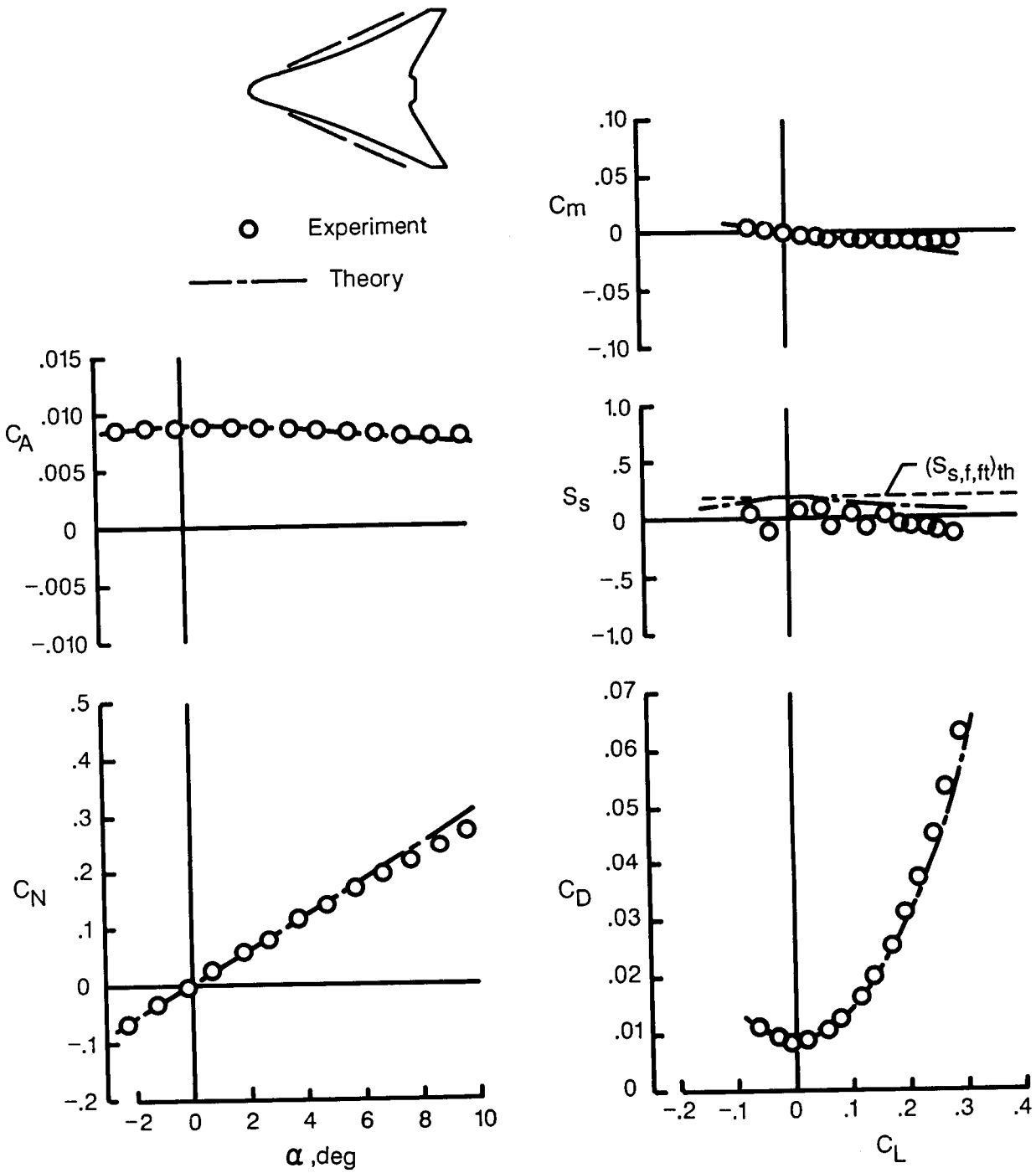

(e) Standard leading edge; $M = 2.36$; $R = 2.6 \times 10^6$.

Figure 3. Continued.

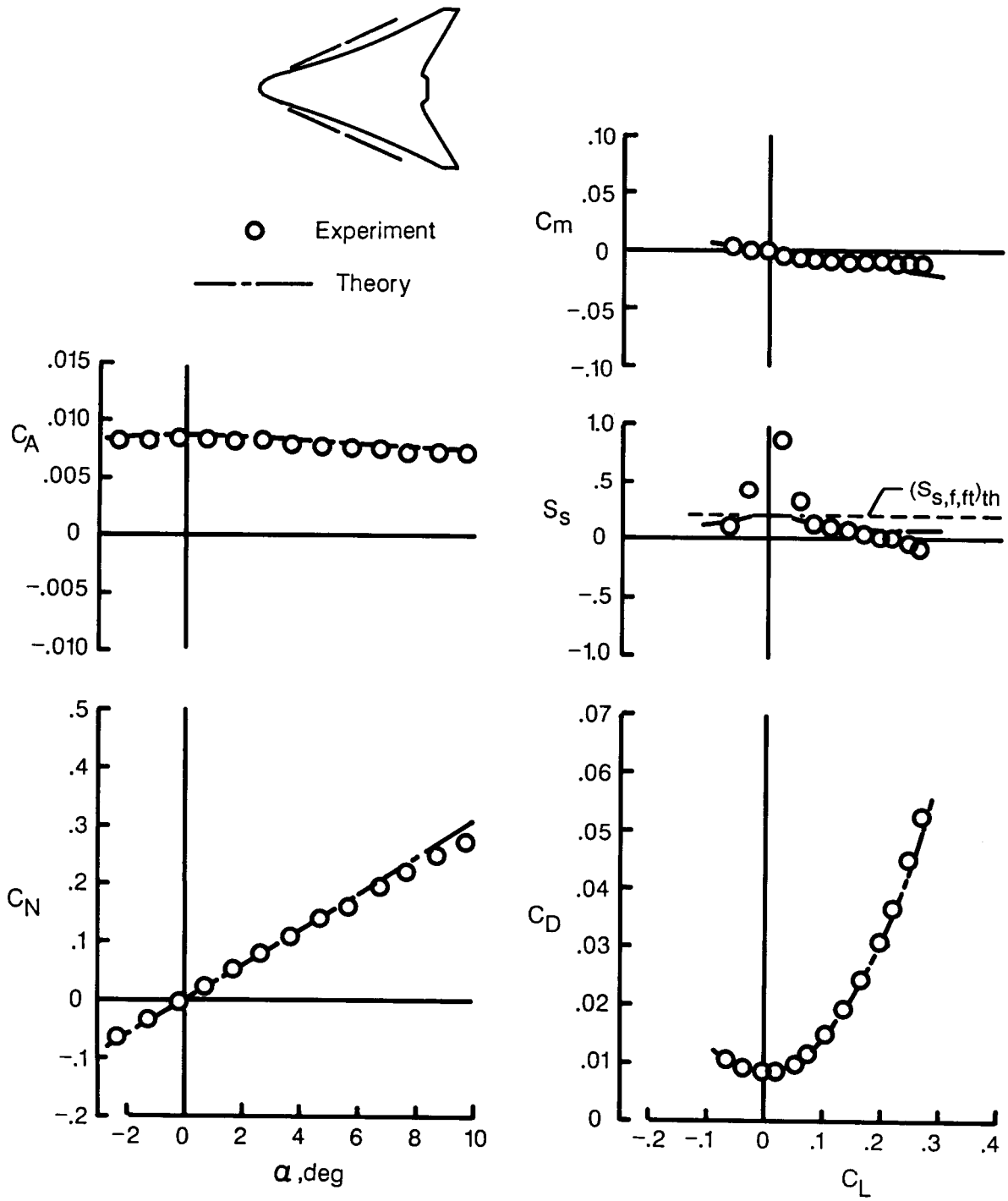

(f) Blunt leading edge; $M = 2.36$; $R = 2.6 \times 10^6$.

Figure 3. Concluded.

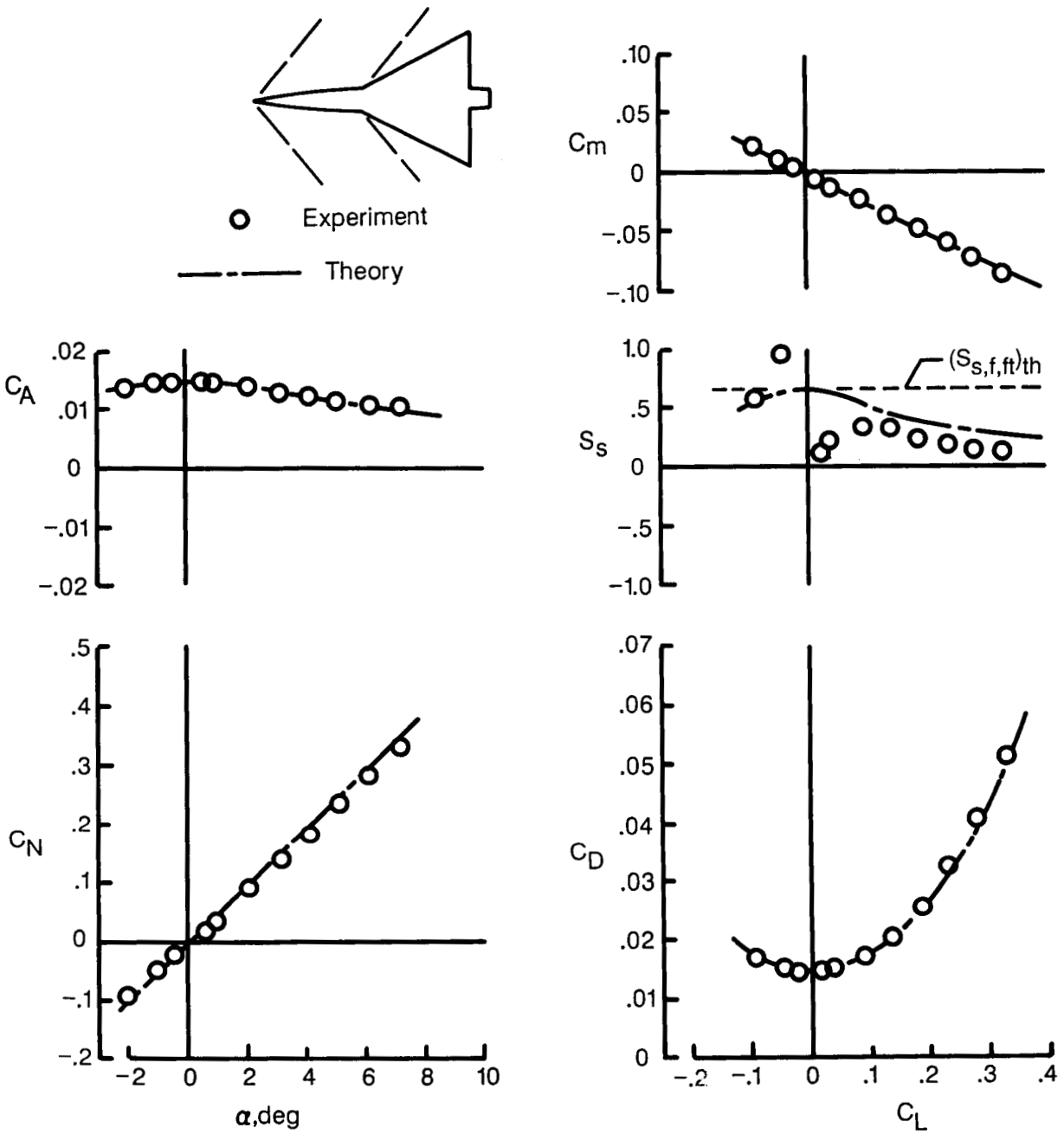

(a) 5-percent-thick airfoil section; $M = 1.30$; $R = 2.8 \times 10^6$.

Figure 4. Theoretical and experimental data for flat aspect ratio 2 wing–body combinations.

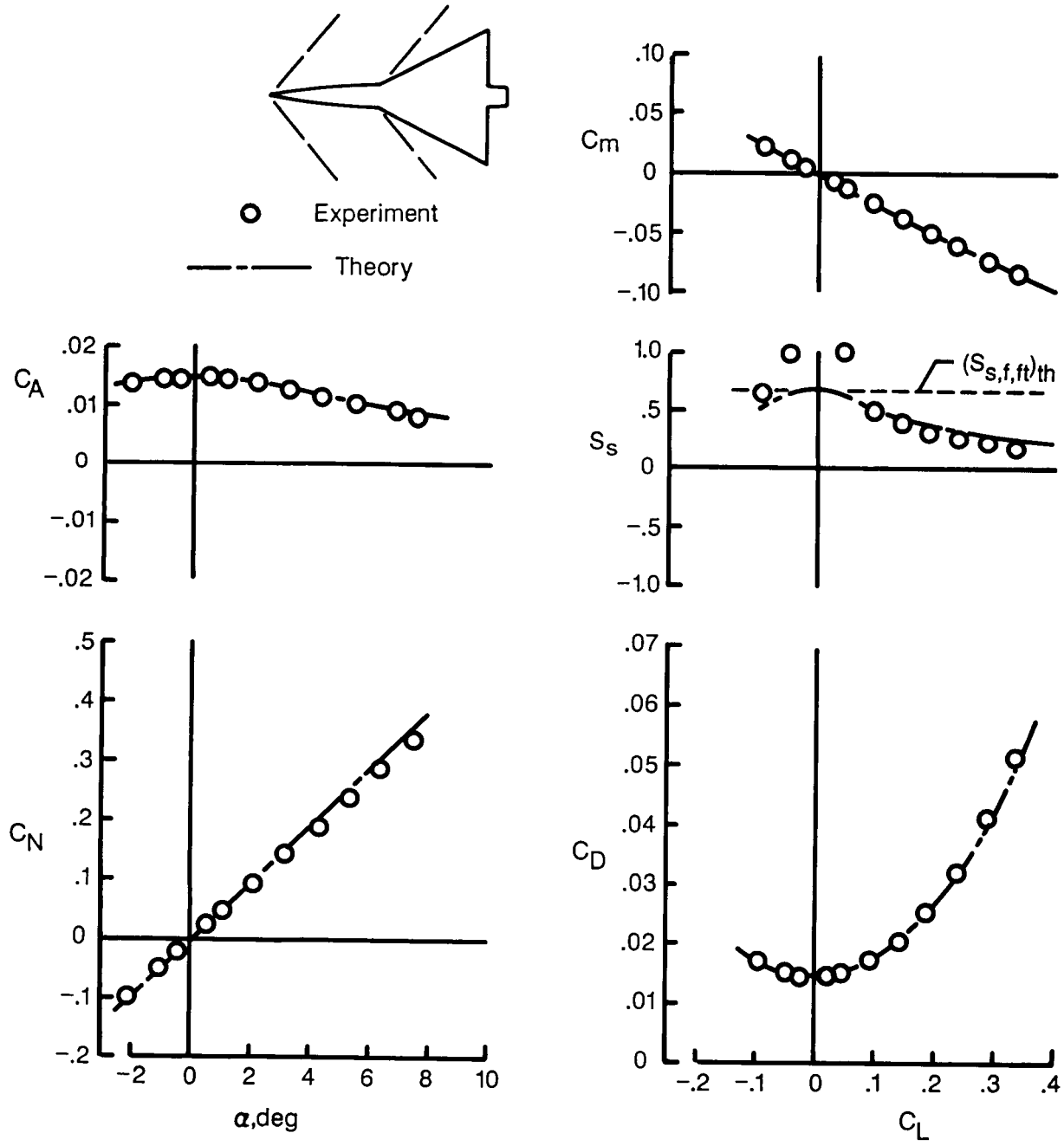

(b) 5-percent-thick airfoil section; $M = 1.30$; $R = 5.6 \times 10^6$.

Figure 4. Continued.

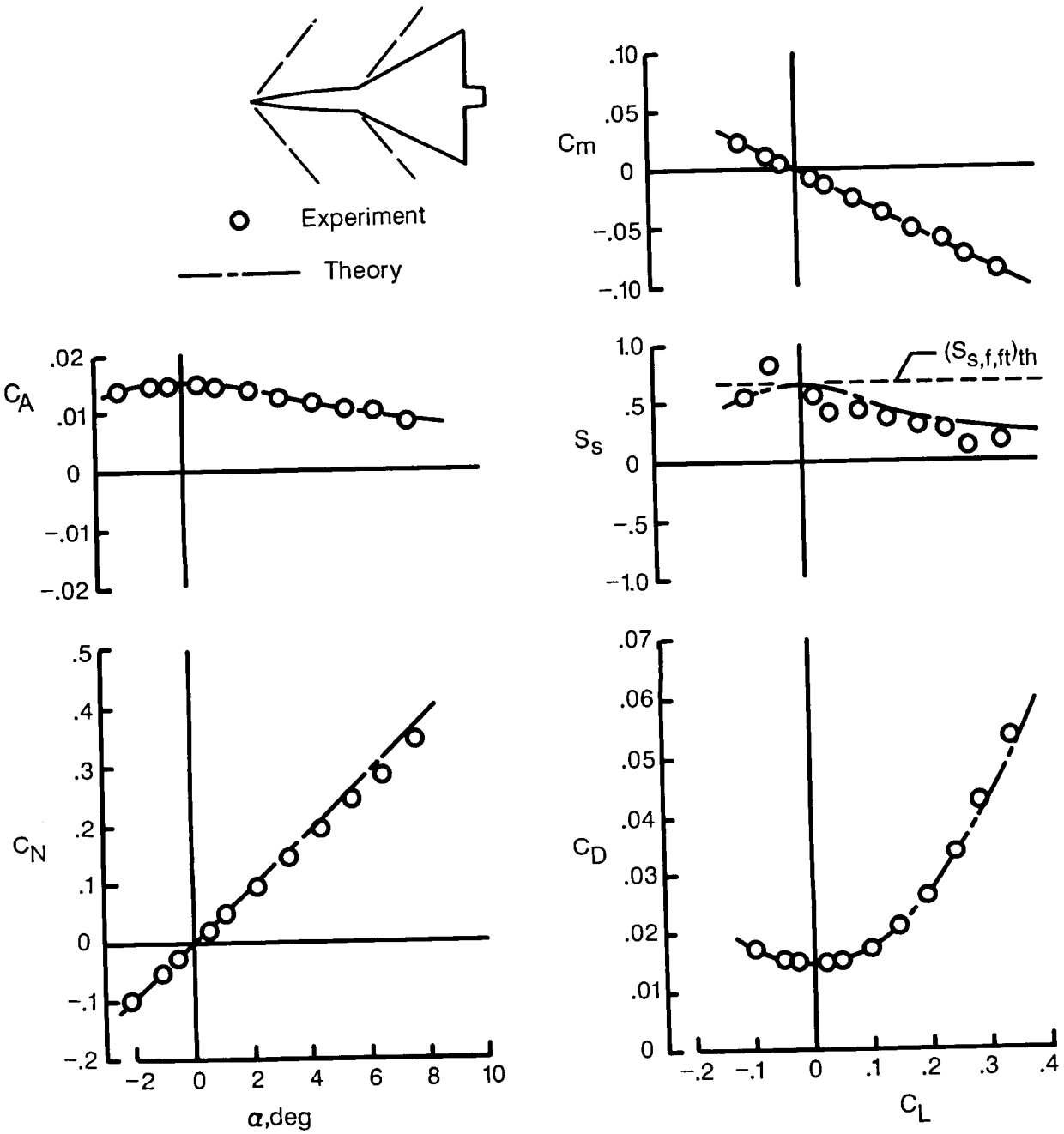

(c) 5-percent-thick airfoil section; $M = 1.30$; $R = 7.7 \times 10^6$.

Figure 4. Continued.

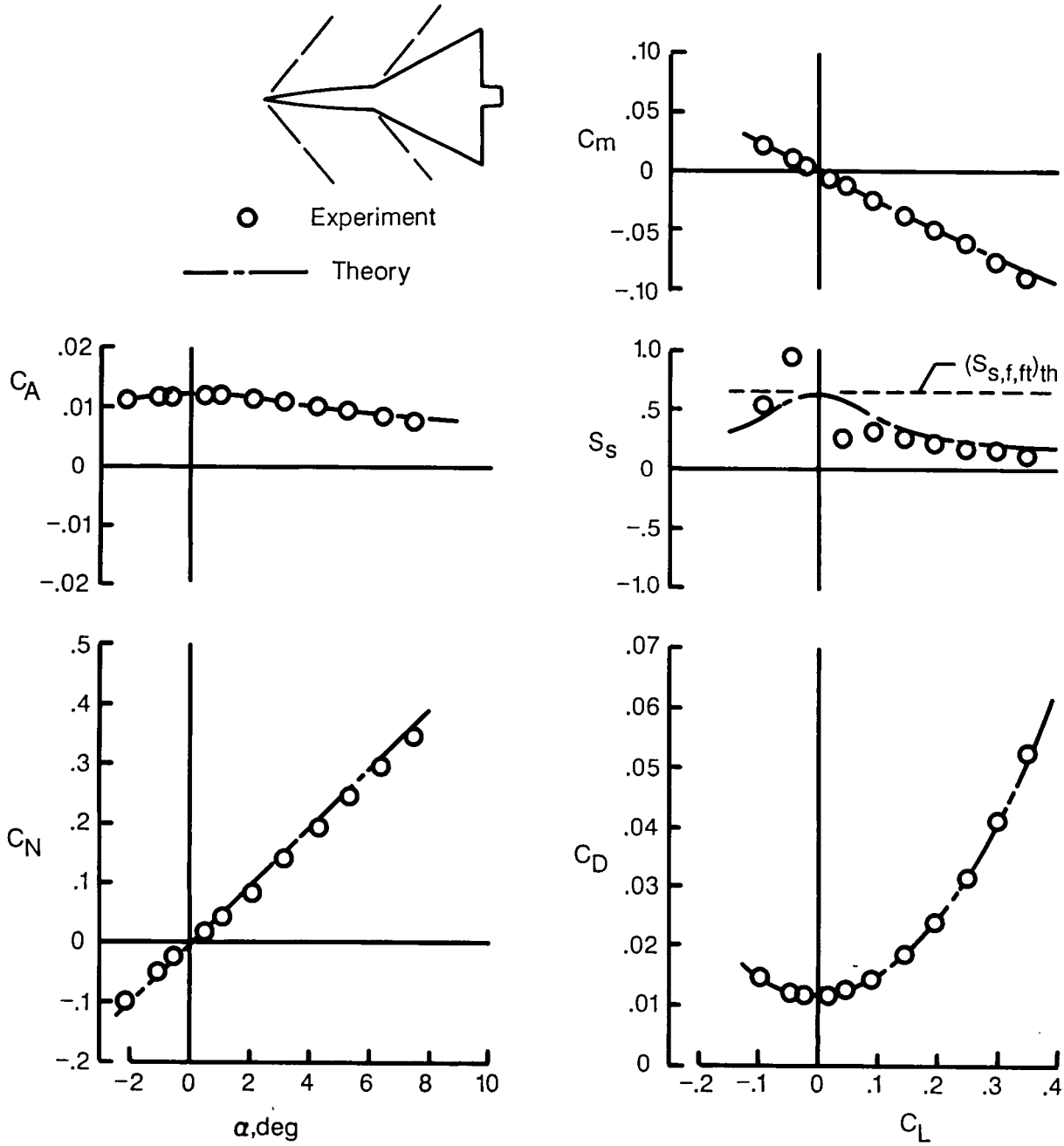

(d) 3-percent-thick airfoil section; $M = 1.30$; $R = 5.6 \times 10^6$.

Figure 4. Continued.

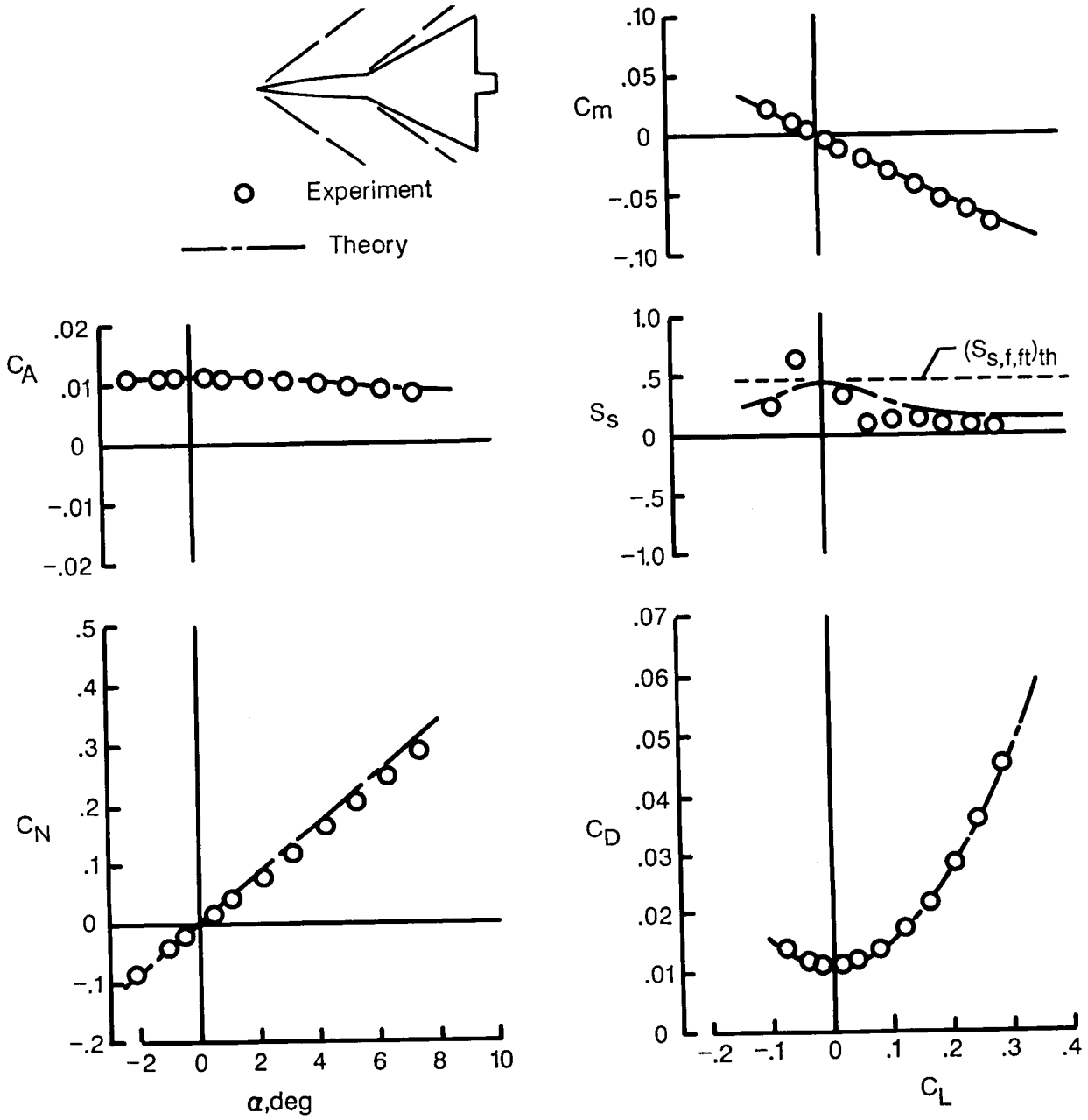

(e) 3-percent-thick airfoil section; $M = 1.70$; $R = 5.6 \times 10^6$.

Figure 4. Concluded.

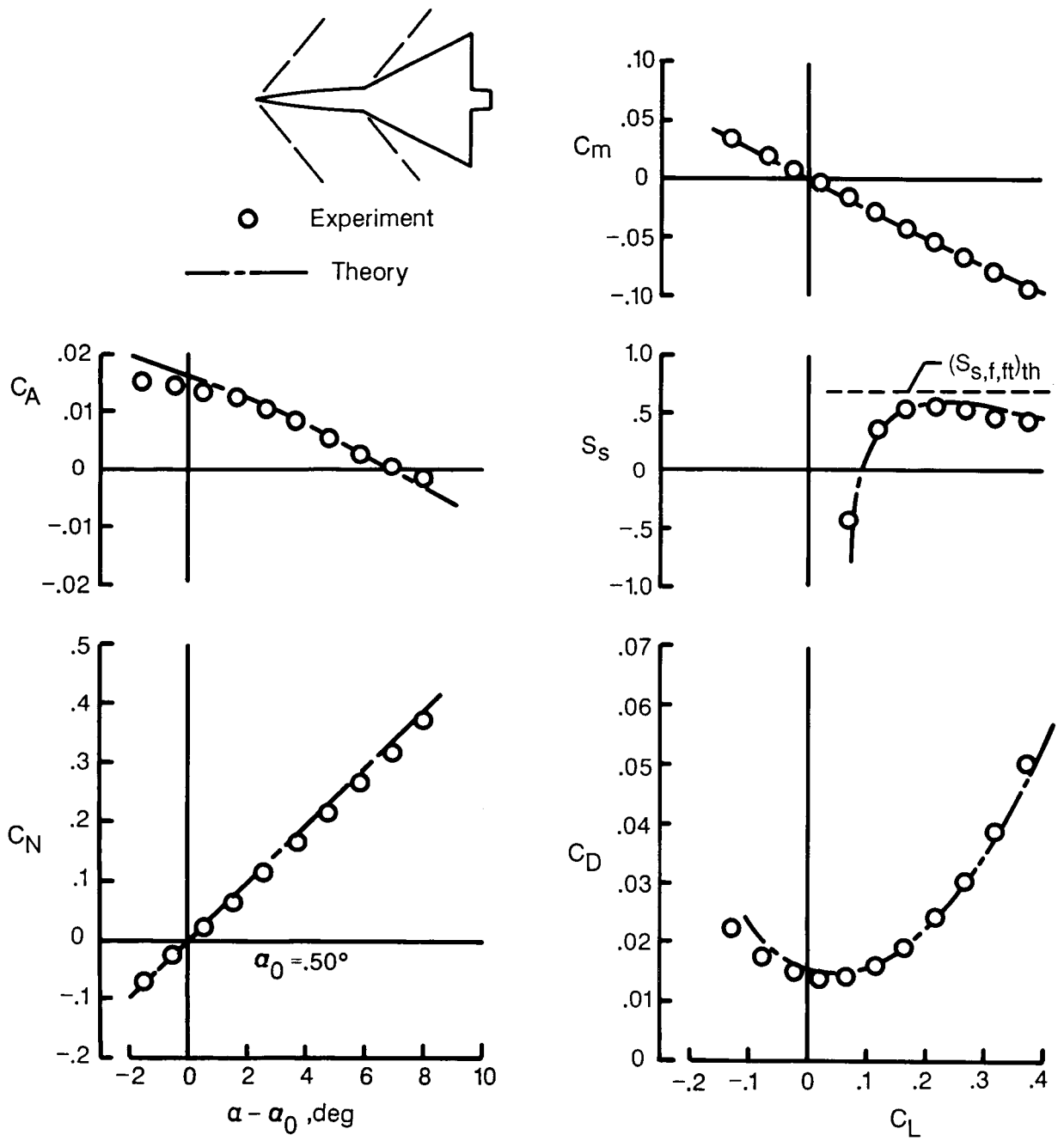

(a) $M = 1.30$; $R = 5.6 \times 10^6$.

Figure 5. Theoretical and experimental data for aspect ratio 2 wing–body combinations with 3-percent-thick airfoil sections and conical camber.

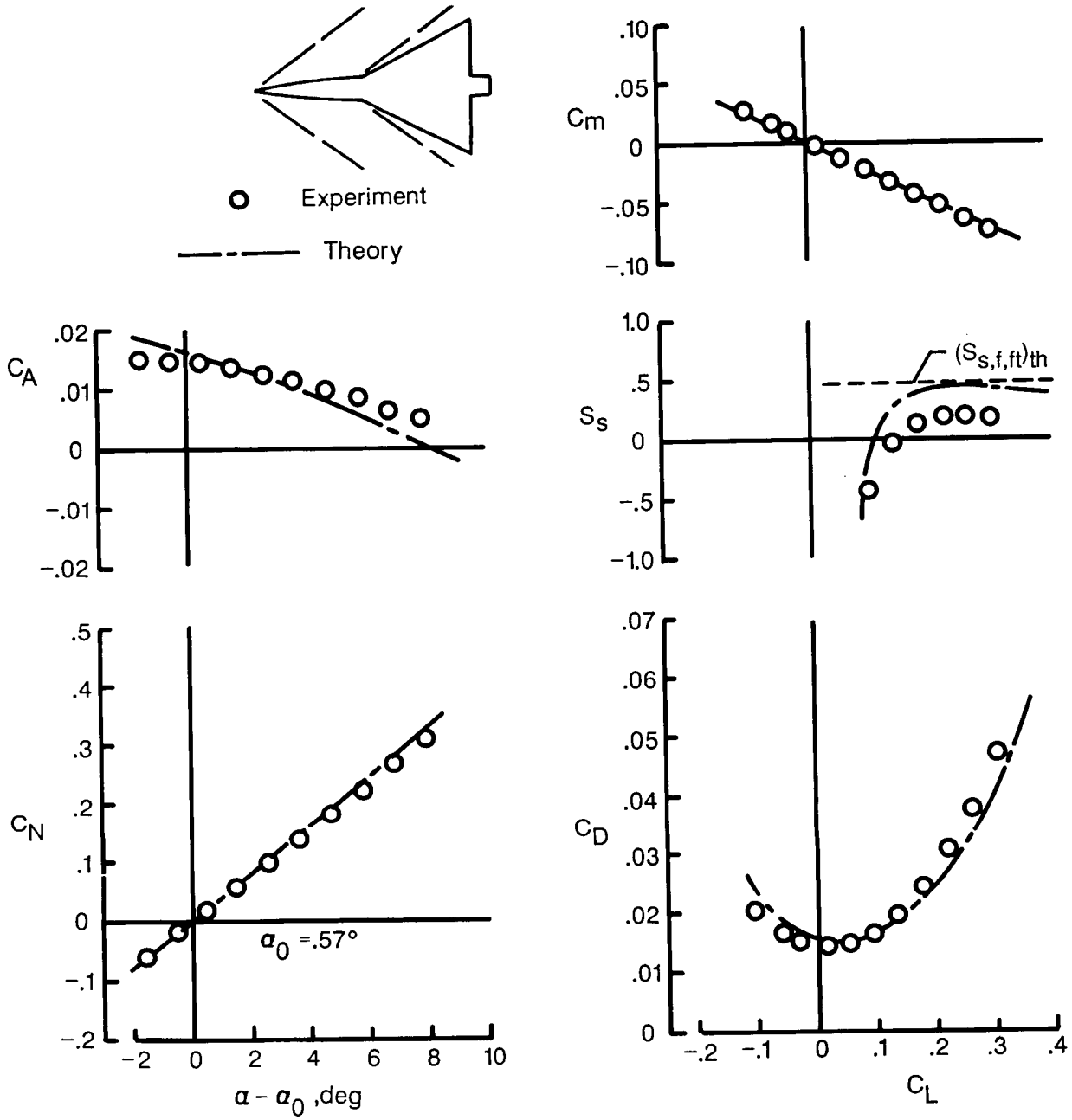

(b) $M = 1.70$; $R = 5.6 \times 10^6$.

Figure 5. Concluded.

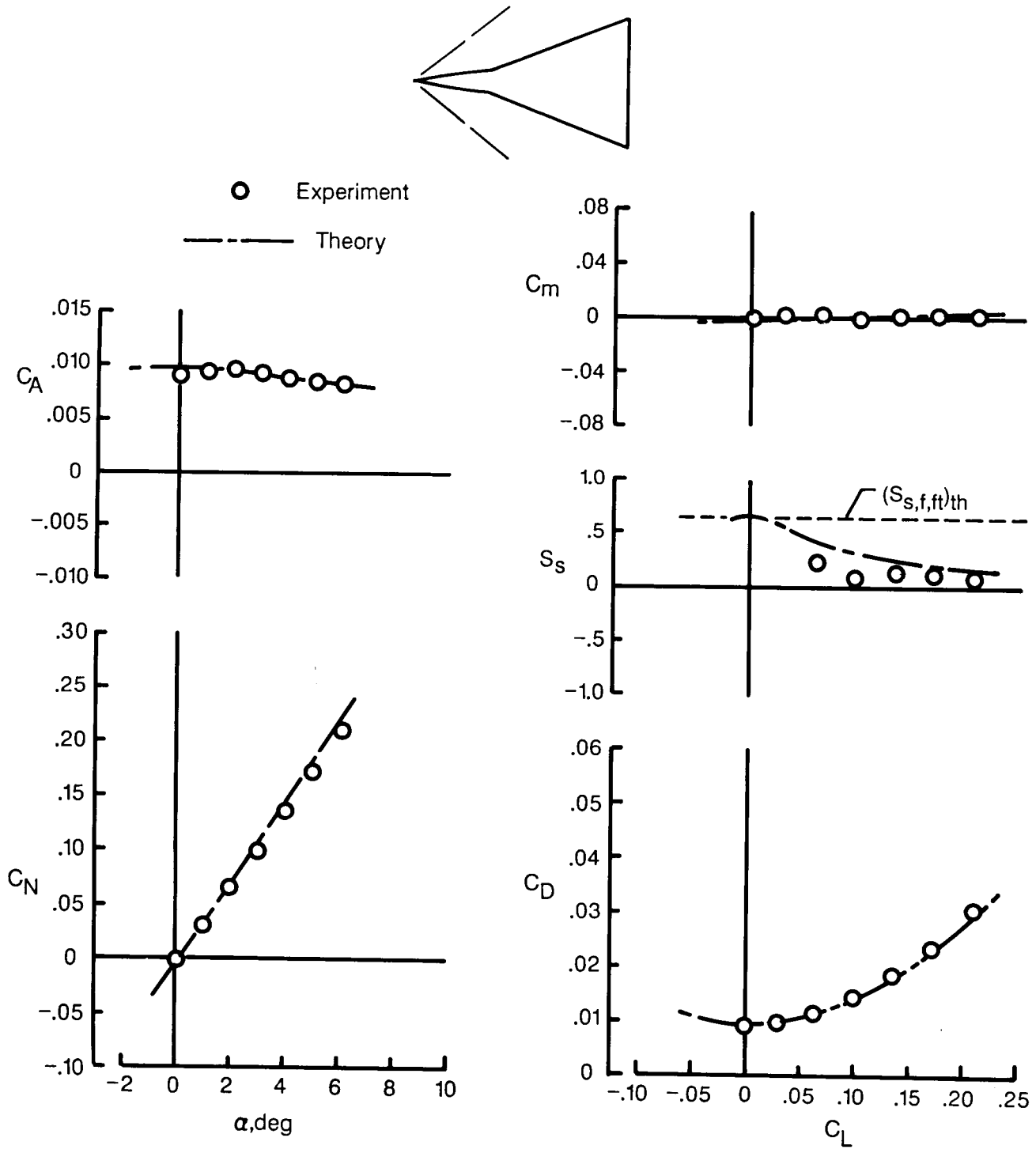

(a) $C_{L,\mathrm{des}} = 0$.

Figure 6. Theoretical and experimental data for aspect ratio 1.57 wing–body combinations twisted and cambered for three design lift coefficients. $M = 1.62$; $R = 1.4 \times 10^6$.

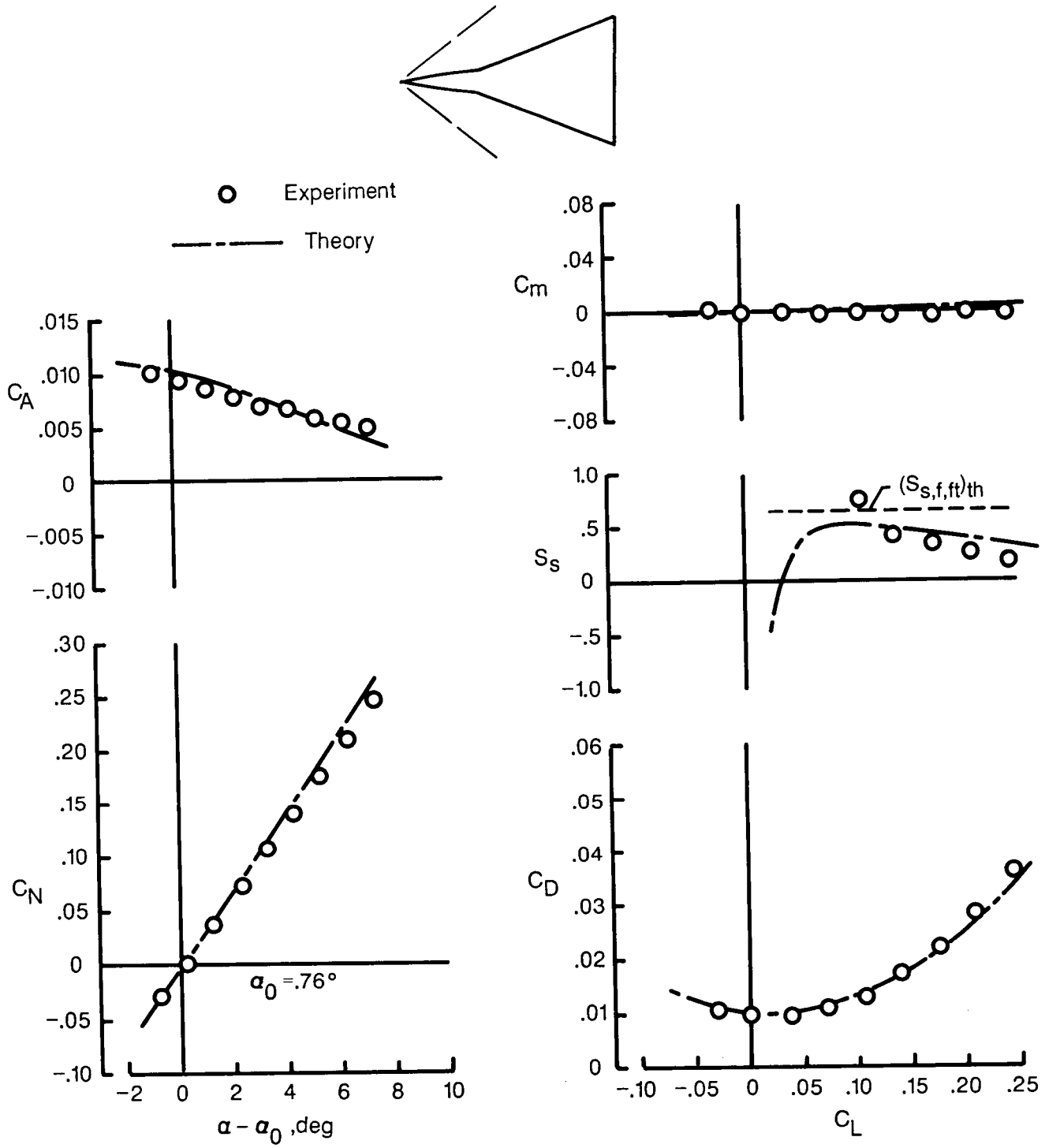

(b) $C_{L,\mathrm{des}} = 0.08$.

Figure 6. Continued.

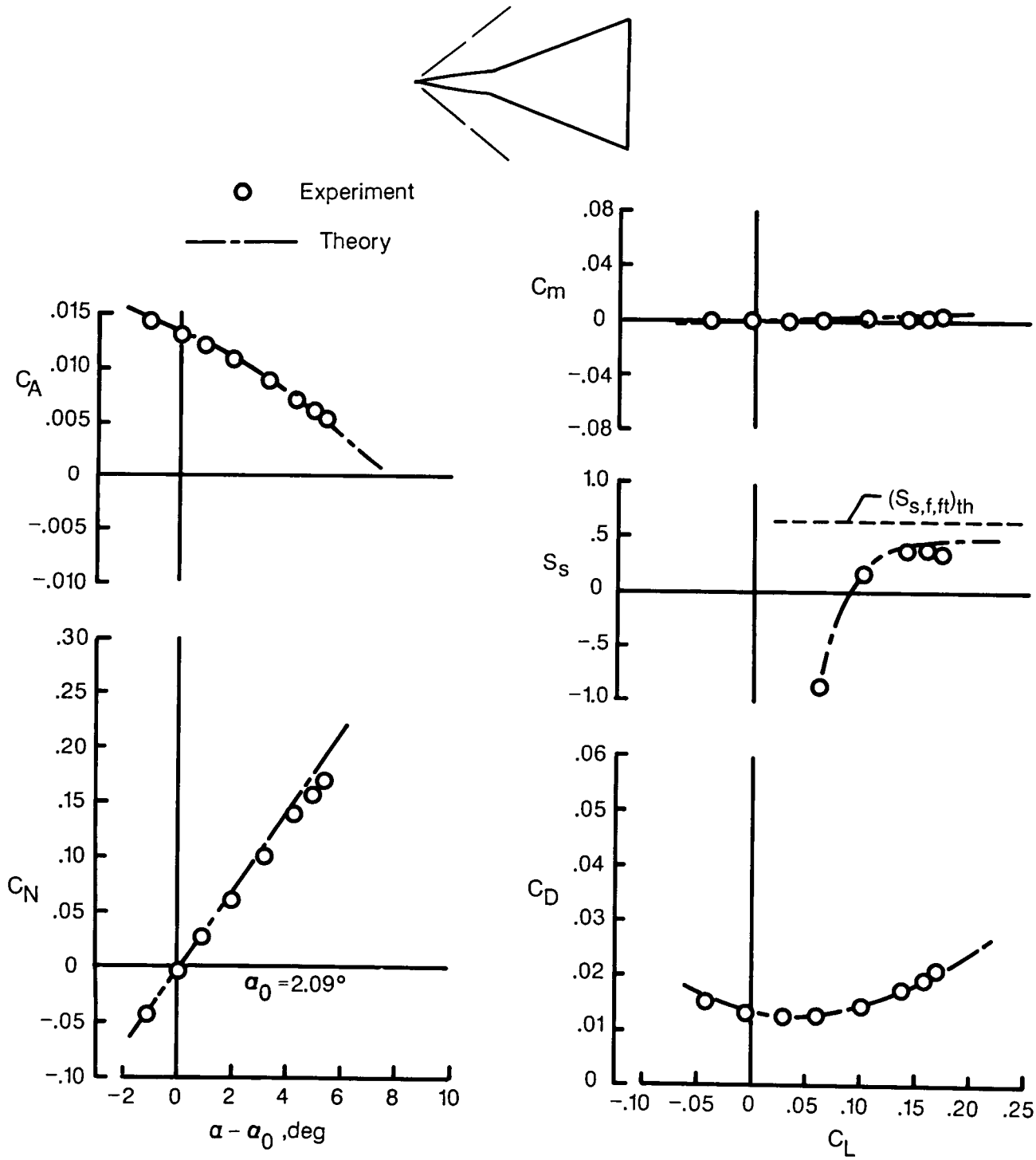

(c) $C_{L,\mathrm{des}} = 0.20$.

Figure 6. Concluded.

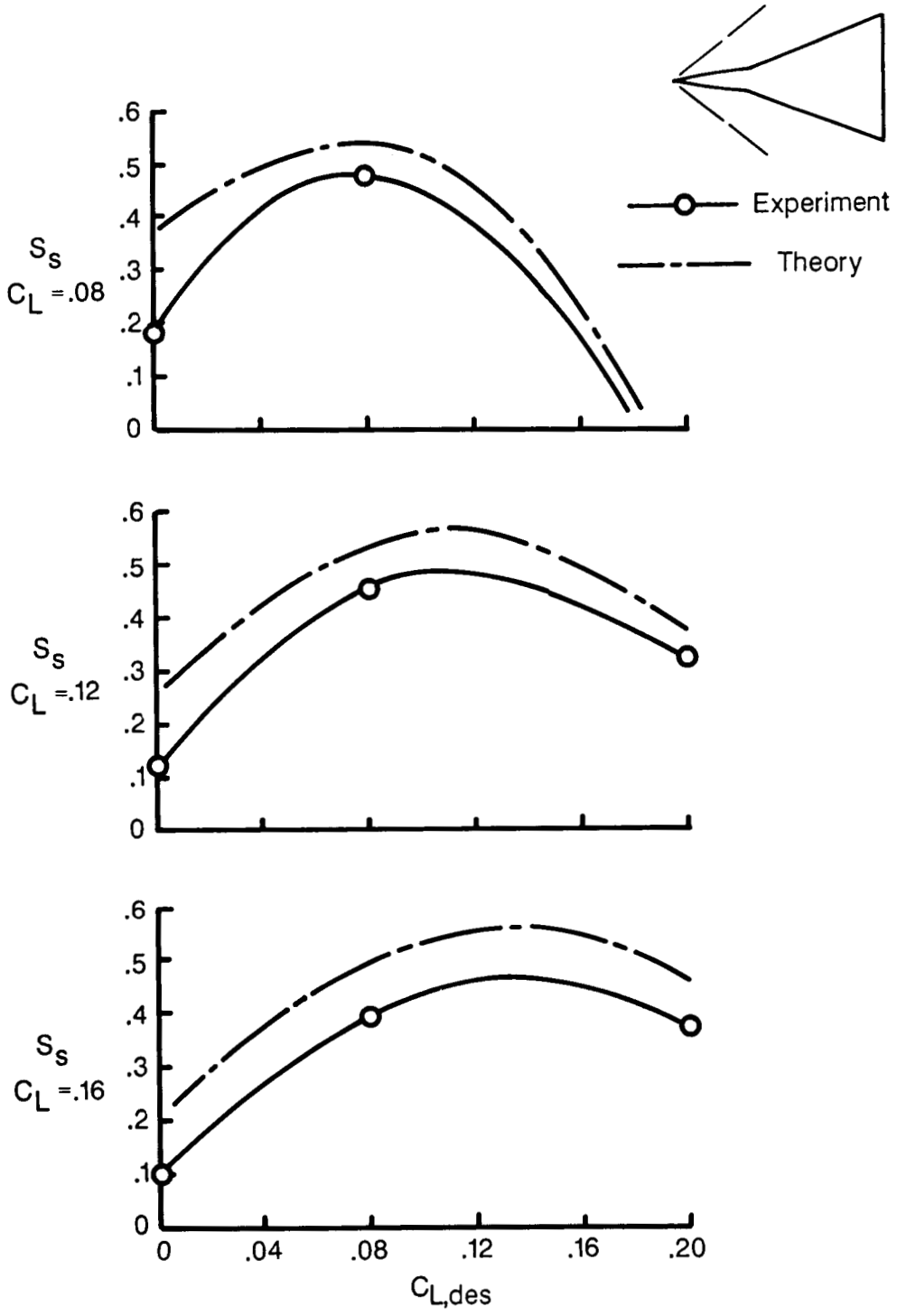

Figure 7. Variation of suction parameter at three cruise lift coefficients with design lift coefficient for aspect ratio 1.57 wing–body combinations. $M = 1.62$; $R = 1.4 \times 10^6$.

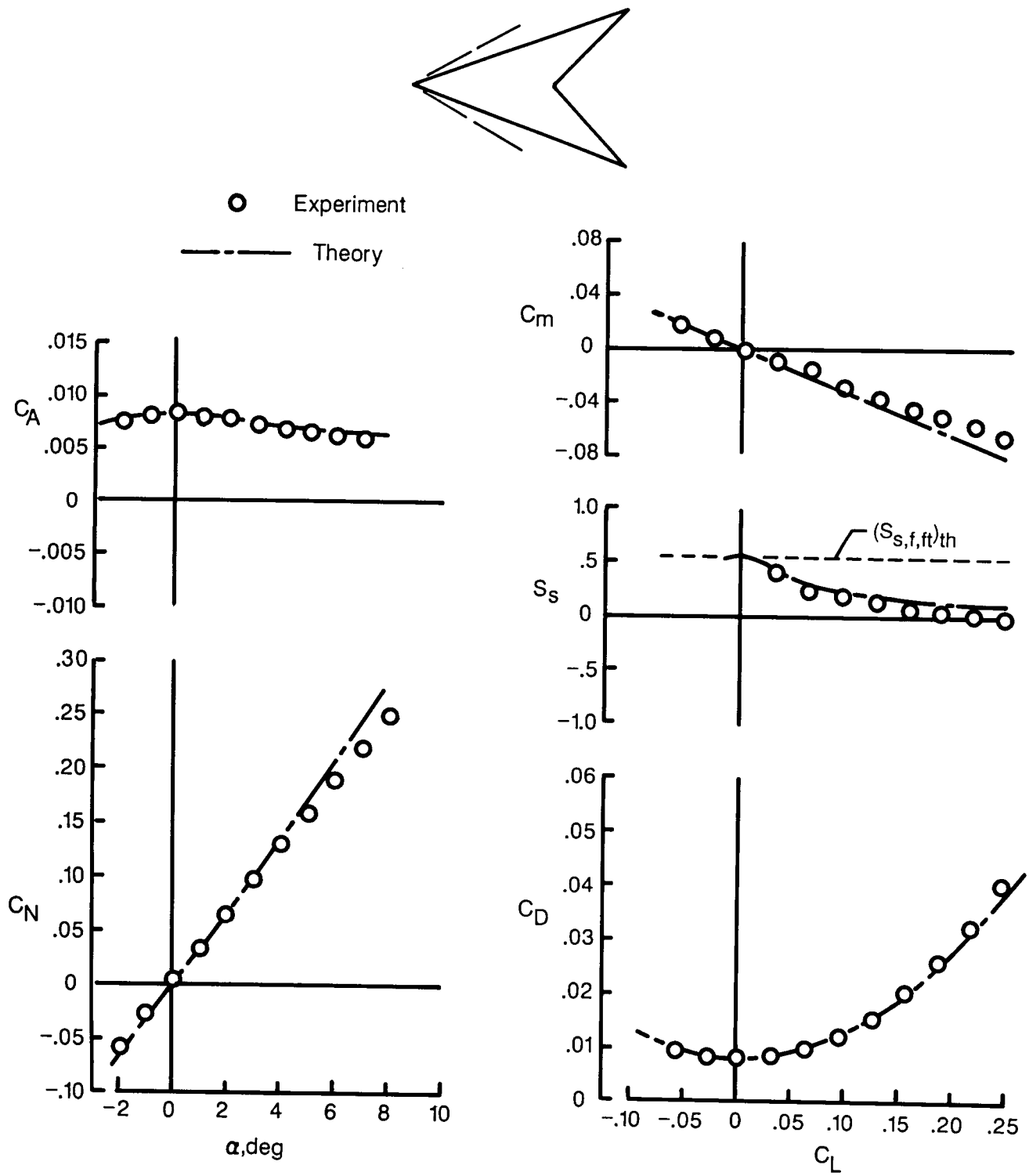

(a) $C_{L,\text{des}} = 0$.

Figure 8. Theoretical and experimental data for 70° swept arrow wings twisted and cambered for three design lift coefficients. $M = 2.05$; $R = 4.4 \times 10^6$.

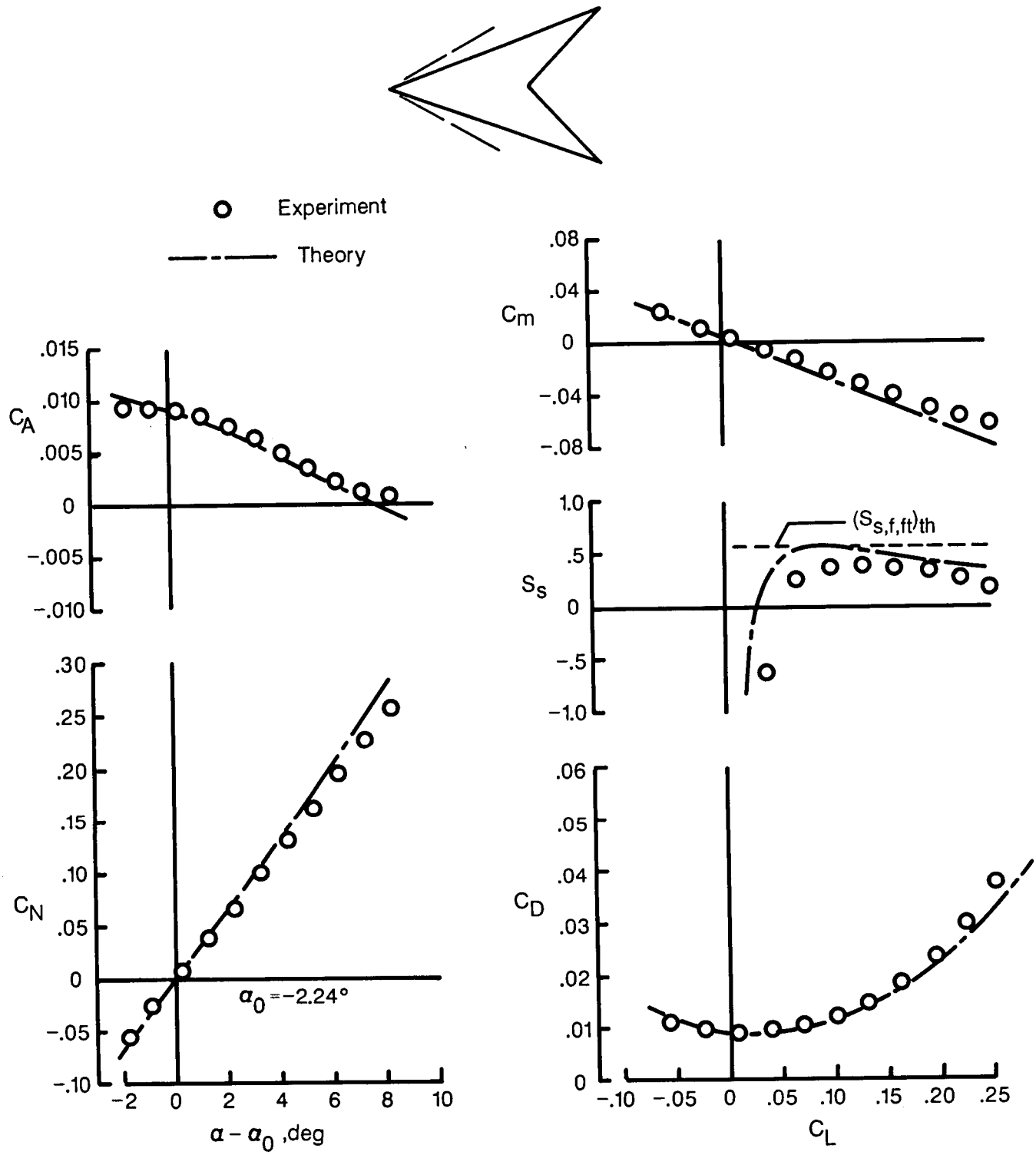

(b) $C_{L,\text{des}} = 0.08$.

Figure 8. Continued.

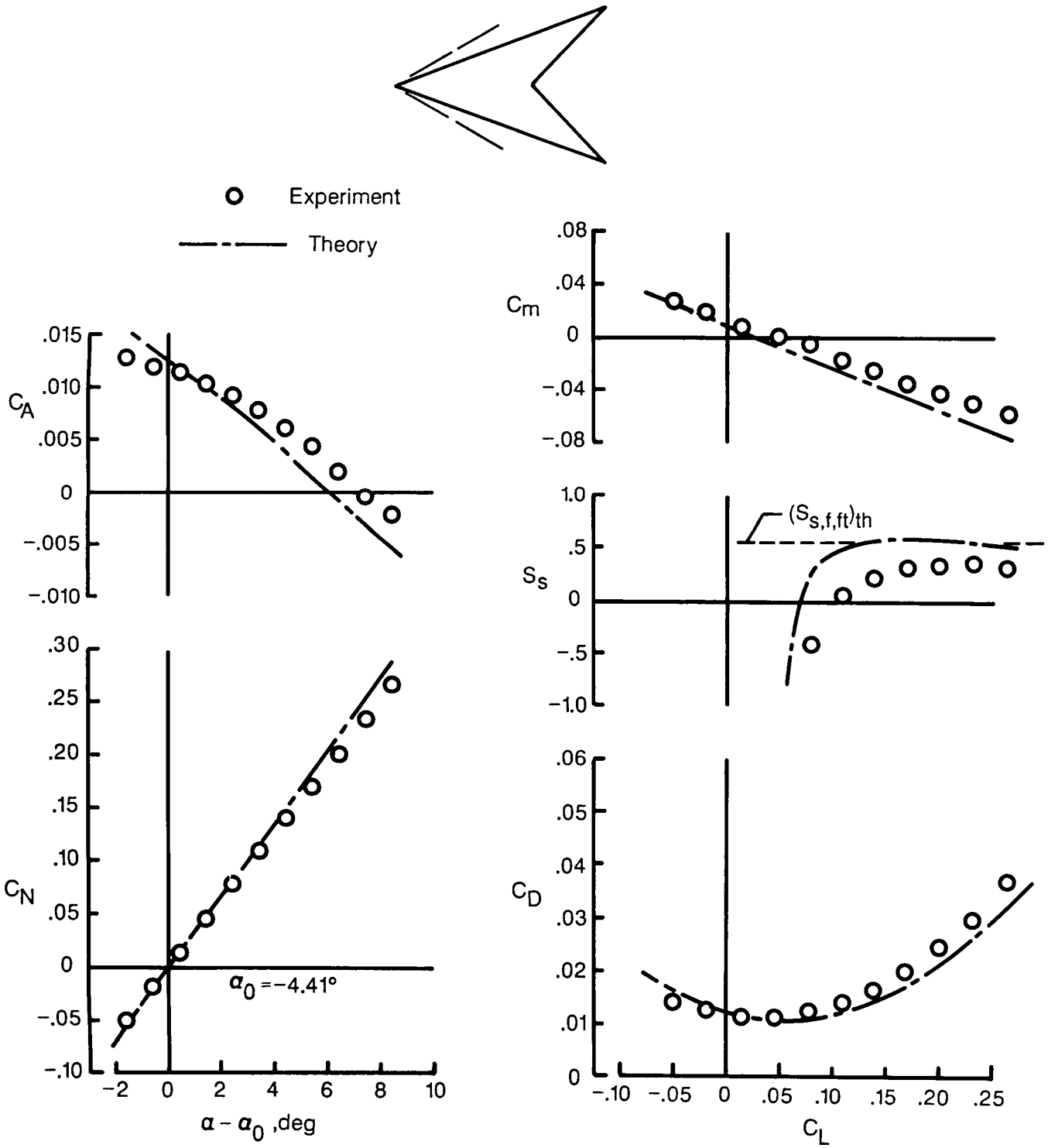

(c) $C_{L_{des}} = 0.16$.

Figure 8. Concluded.

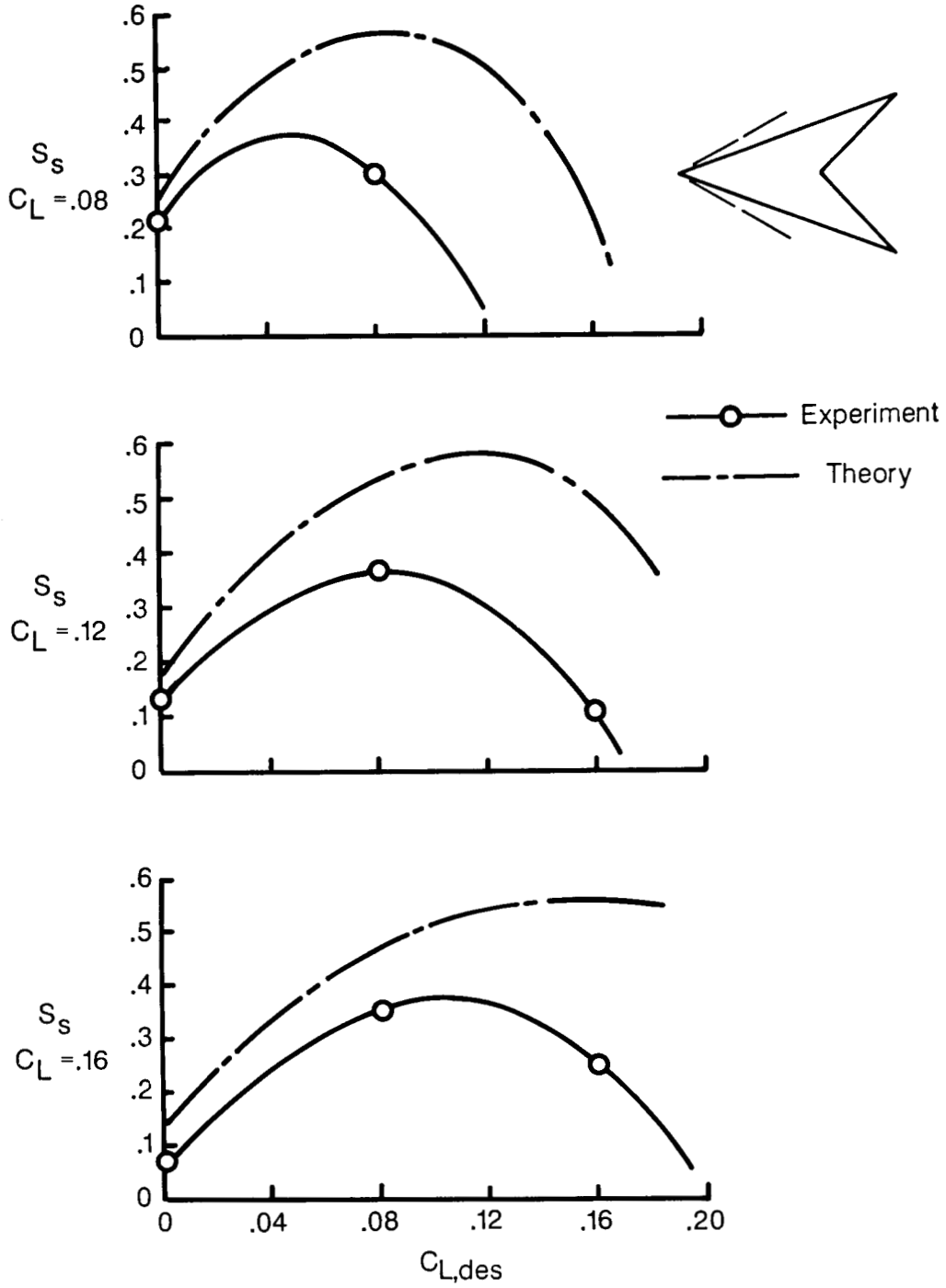

Figure 9. Variation of suction parameter at three cruise lift coefficients with design lift coefficient for 70° swept arrow wing. $M = 2.05$; $R = 4.4 \times 10^6$.

C-2

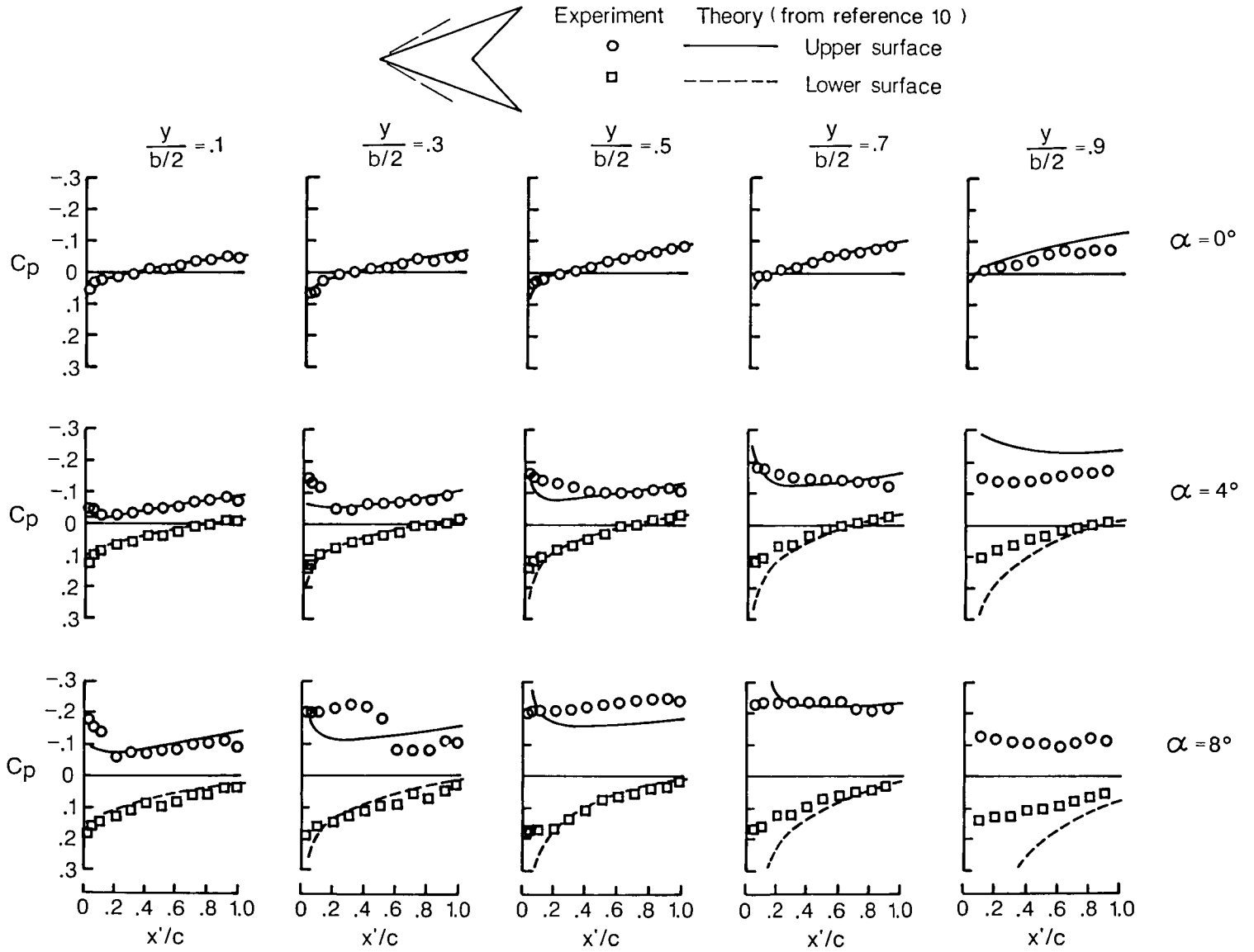

(a) $C_{L,\text{des}} = 0$.

Figure 10. Theoretical and experimental pressure distributions for 70° swept arrow wings. $M = 2.05$; $R = 4.4 \times 10^6$.

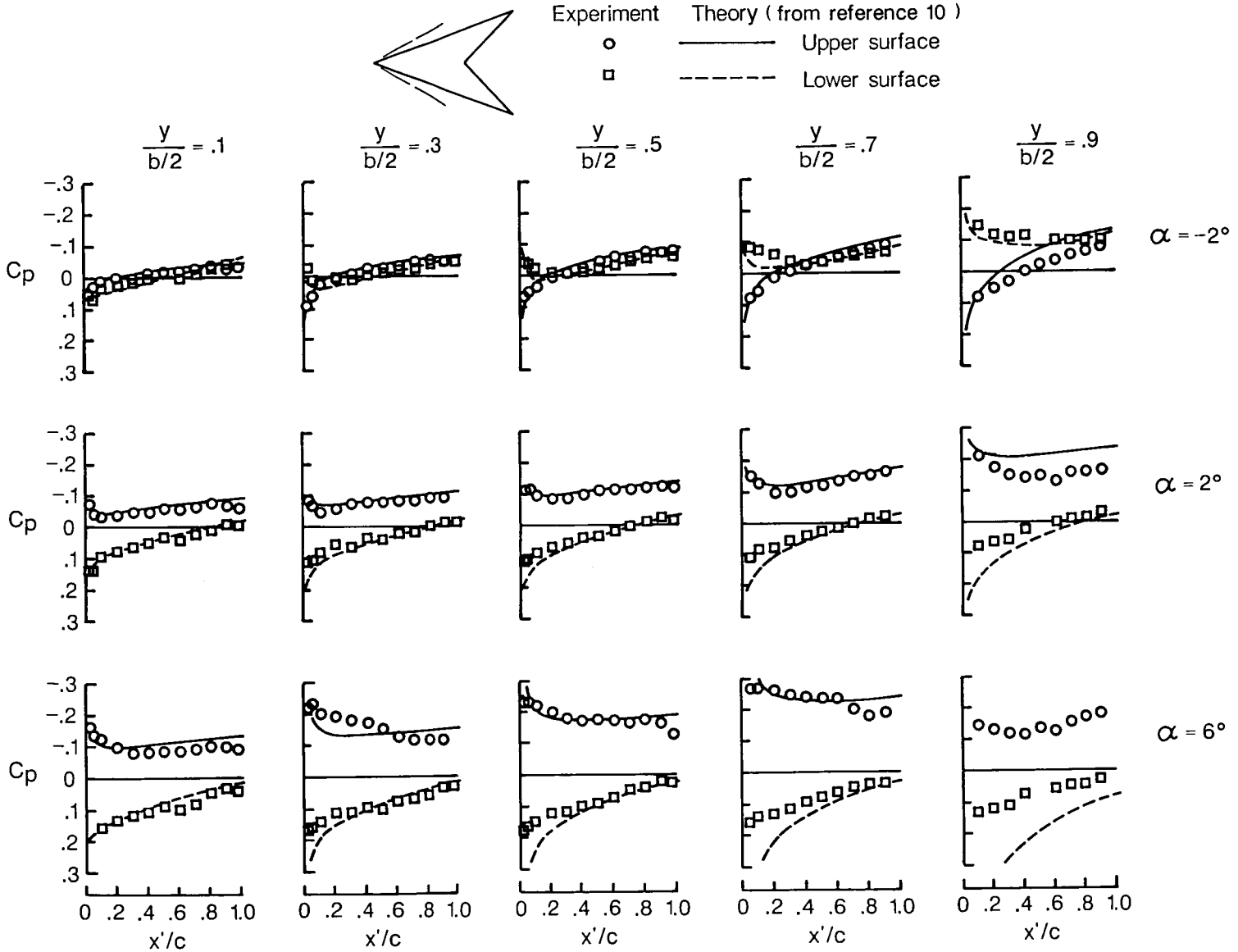

(b) $C_{L,\mathrm{des}} = 0.08$.

Figure 10. Continued.

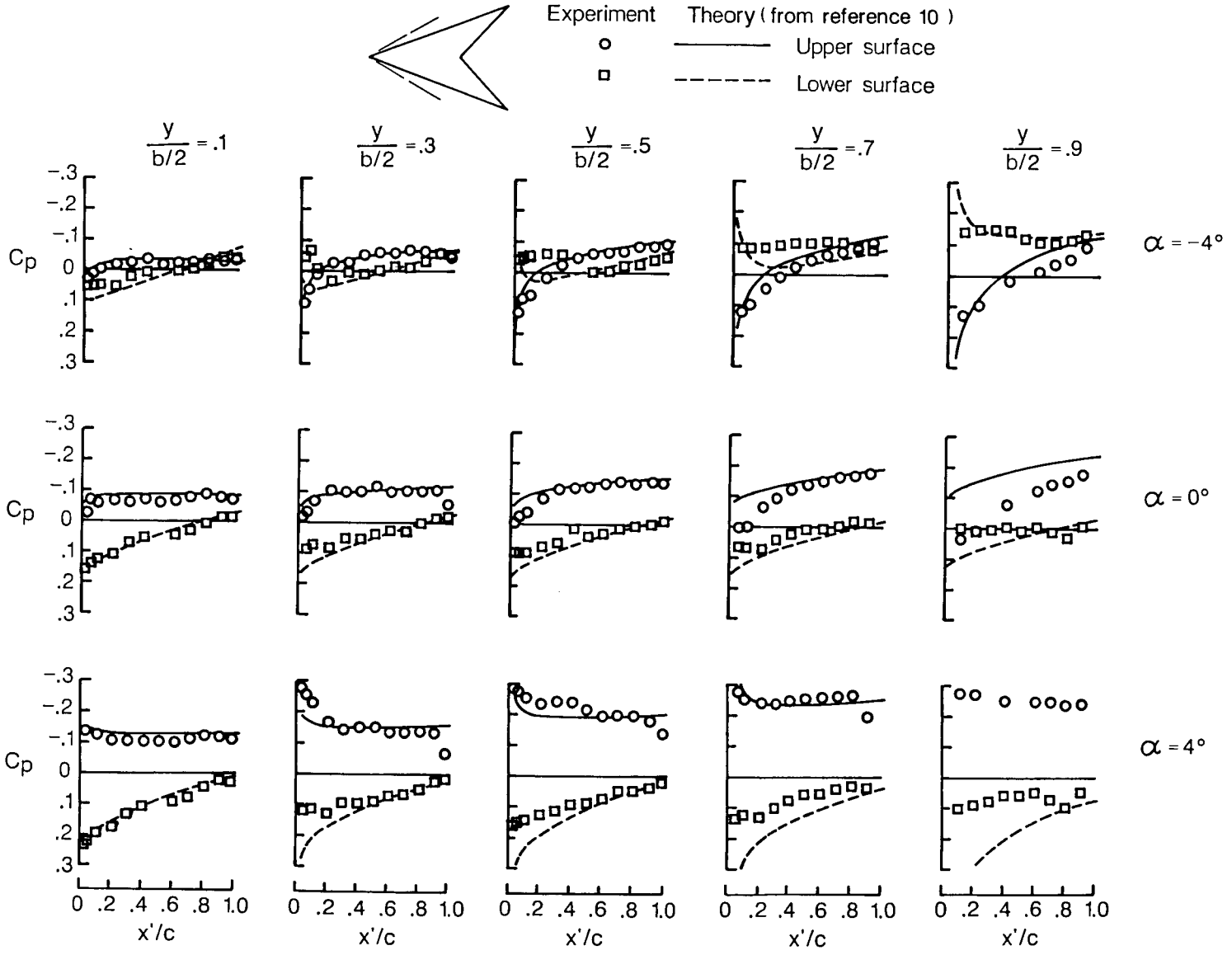

(c) $C_{L,\text{des}} = 0.16$.

Figure 10. Concluded.

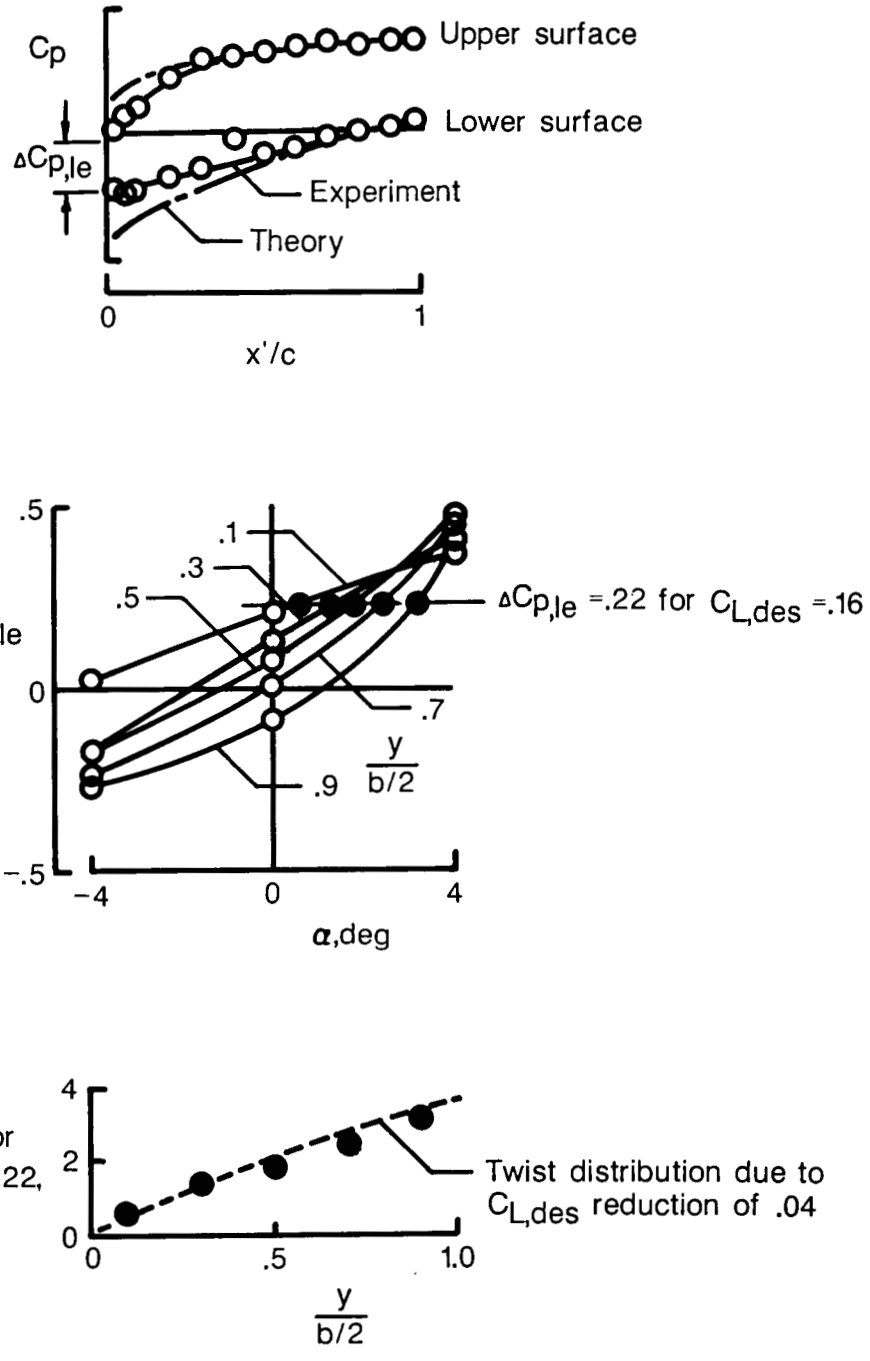

Figure 11. Incremental twist distribution required to meet design leading-edge loading goal for 70° swept arrow wing with $C_{L,\mathrm{des}} = 0.16$. $M = 2.05$; $R = 4.4 \times 10^6$.

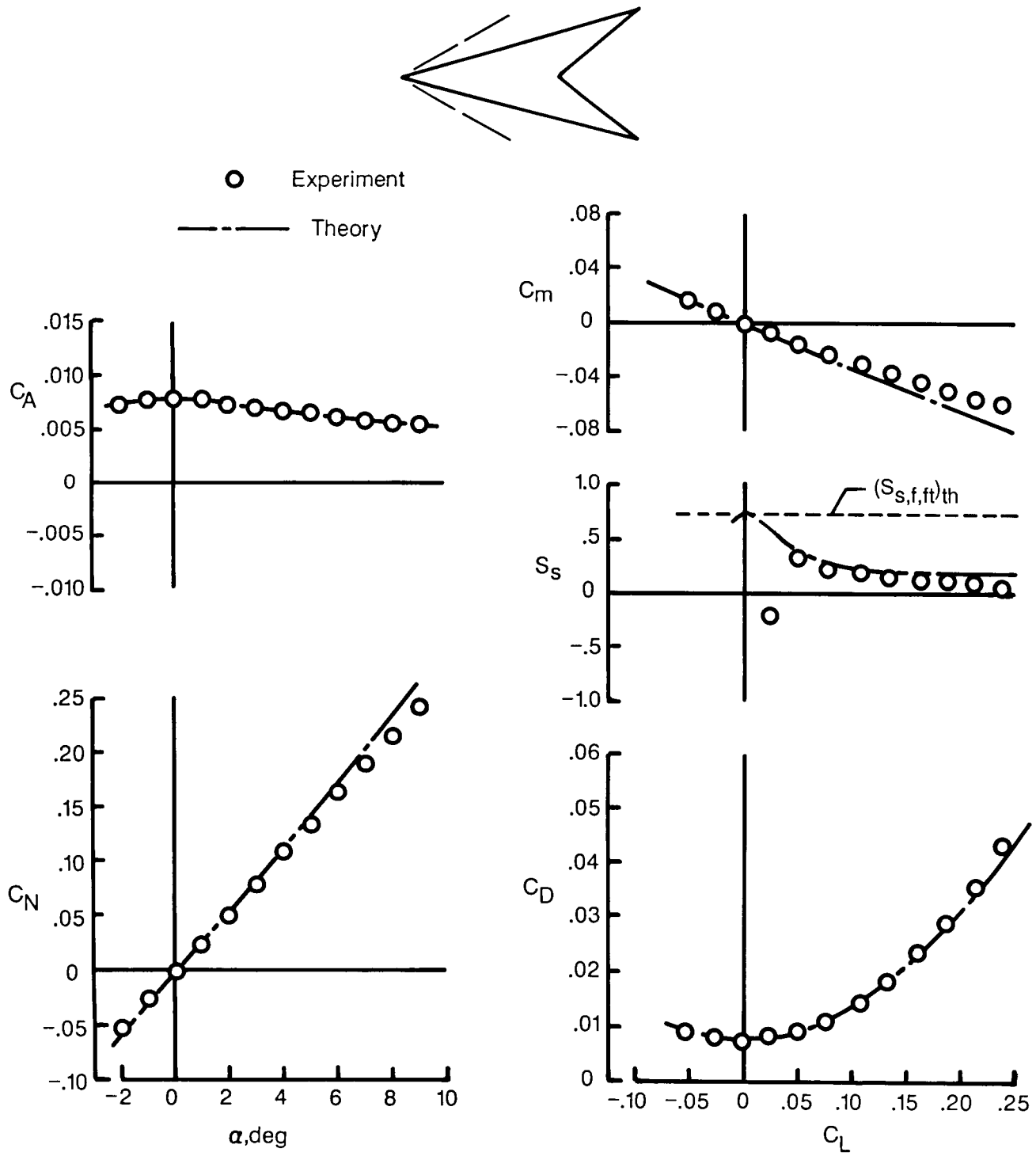

(a) Flat wing.

Figure 12. Theoretical and experimental data for flat and twisted and cambered 75° swept arrow wing. $M = 2.05$; $R = 4.4 \times 10^6$.

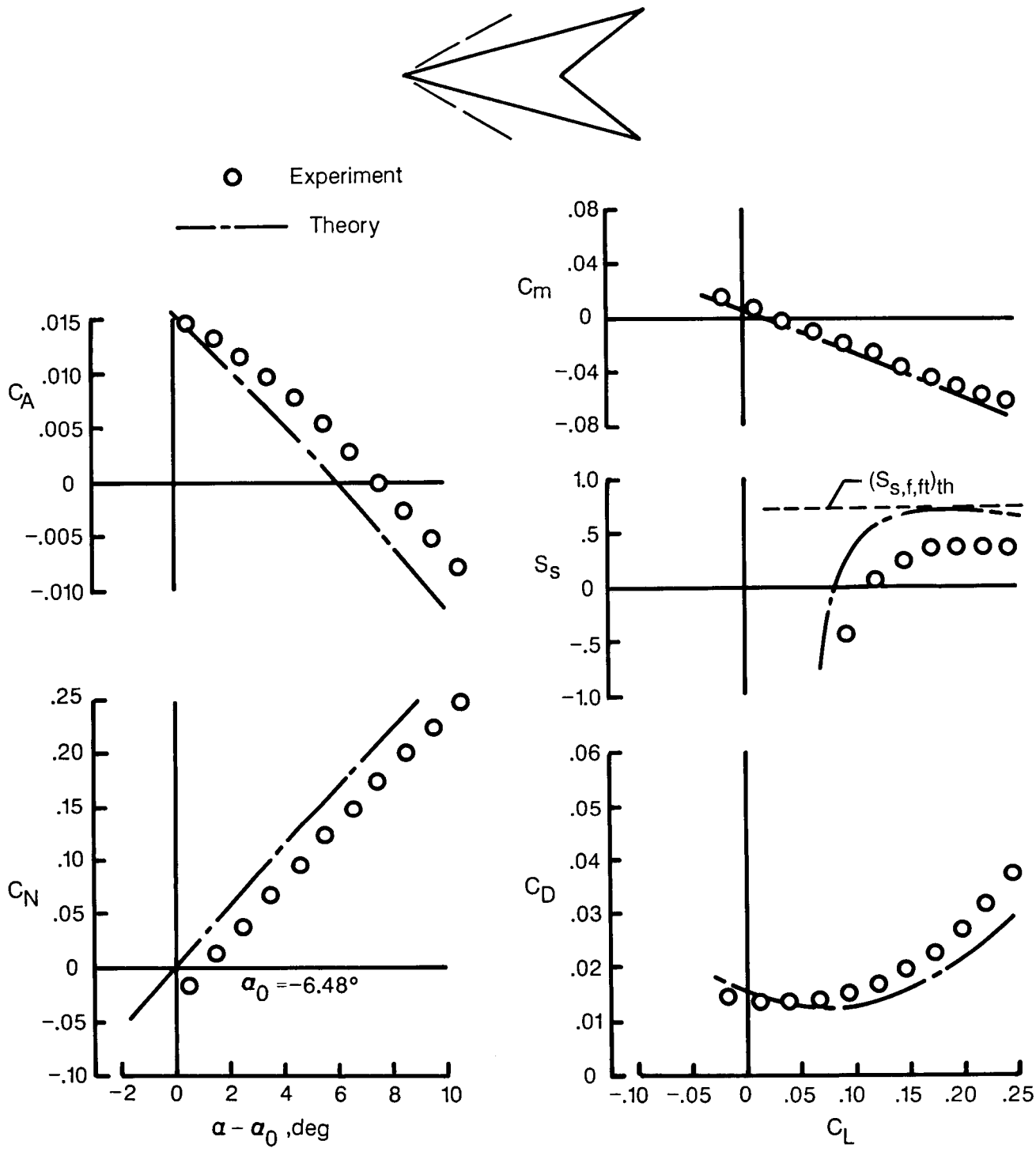

(b) $C_{L,\mathrm{des}} = 0.16$.

Figure 12. Concluded.

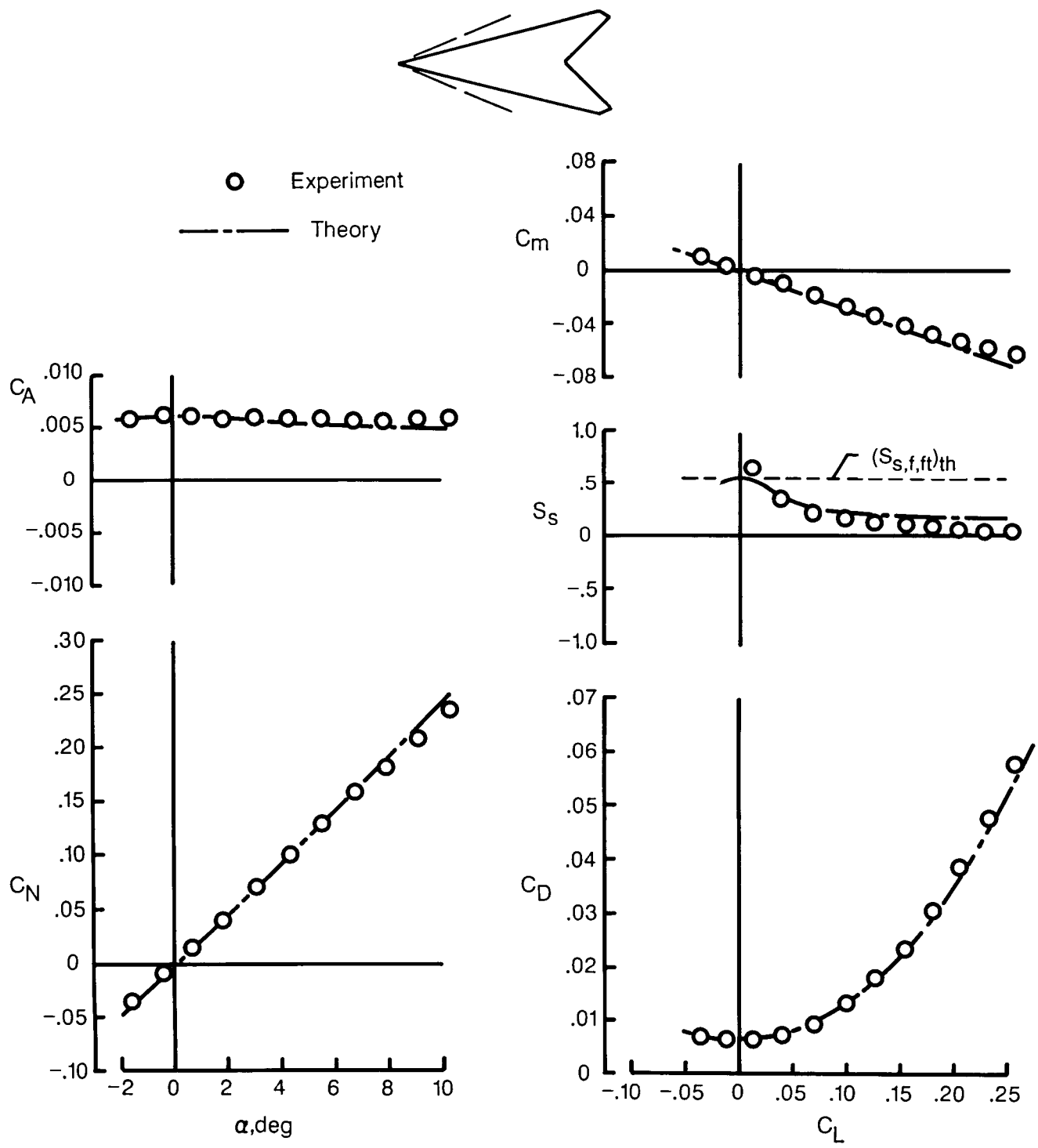

(a) $C_{L,\mathrm{des}} = 0$.

Figure 13. Theoretical and experimental data for 75.96° swept modified arrow wings twisted and cambered for three design lift coefficients. $M = 2.60$; $\beta \cot \Lambda_{le} = 0.60$; $R = 5.1 \times 10^6$.

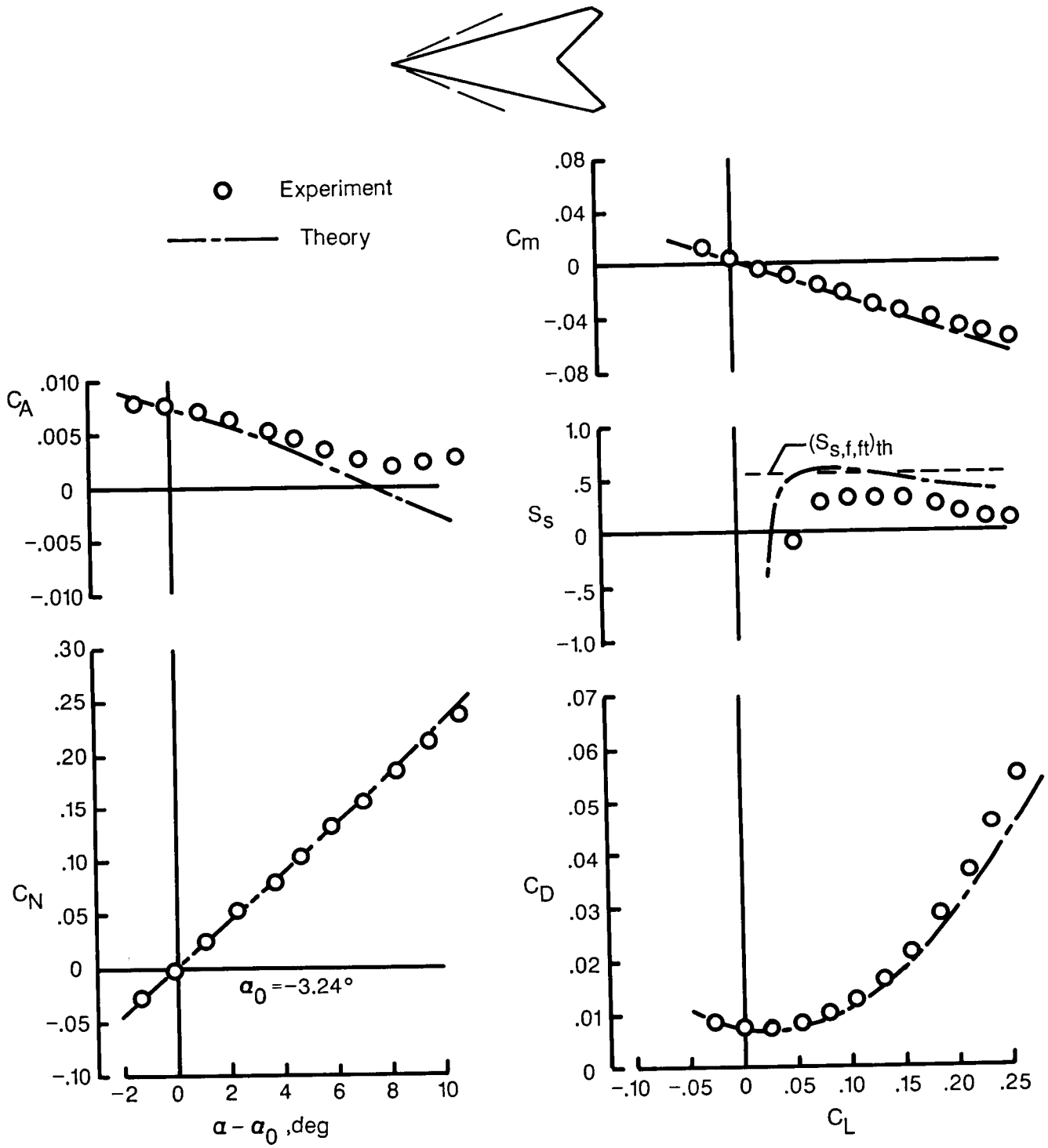

(b) $C_{L,\text{des}} = 0.08$.

Figure 13. Continued.

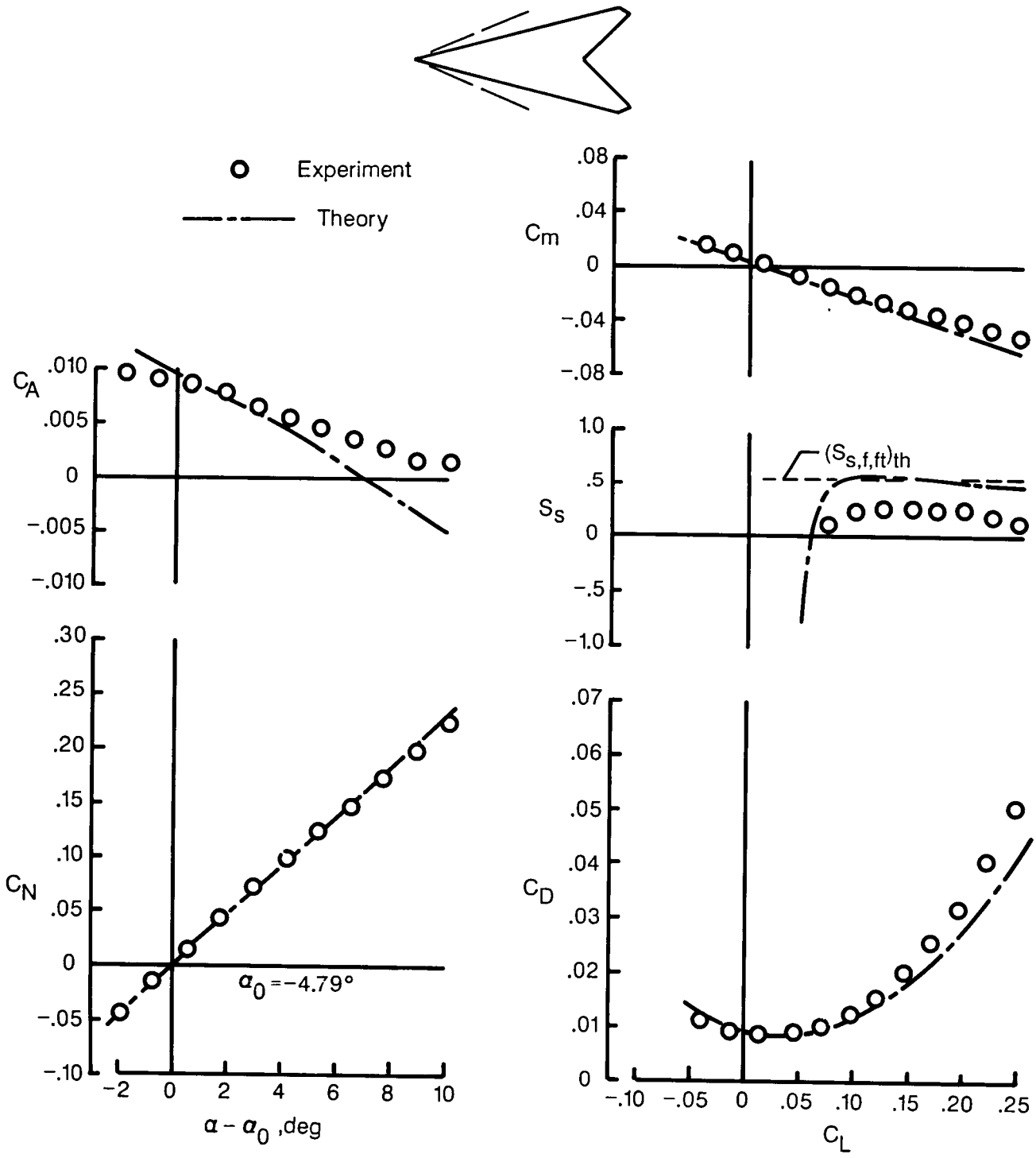

(c) $C_{L,\mathrm{des}} = 0.12$.

Figure 13. Concluded.

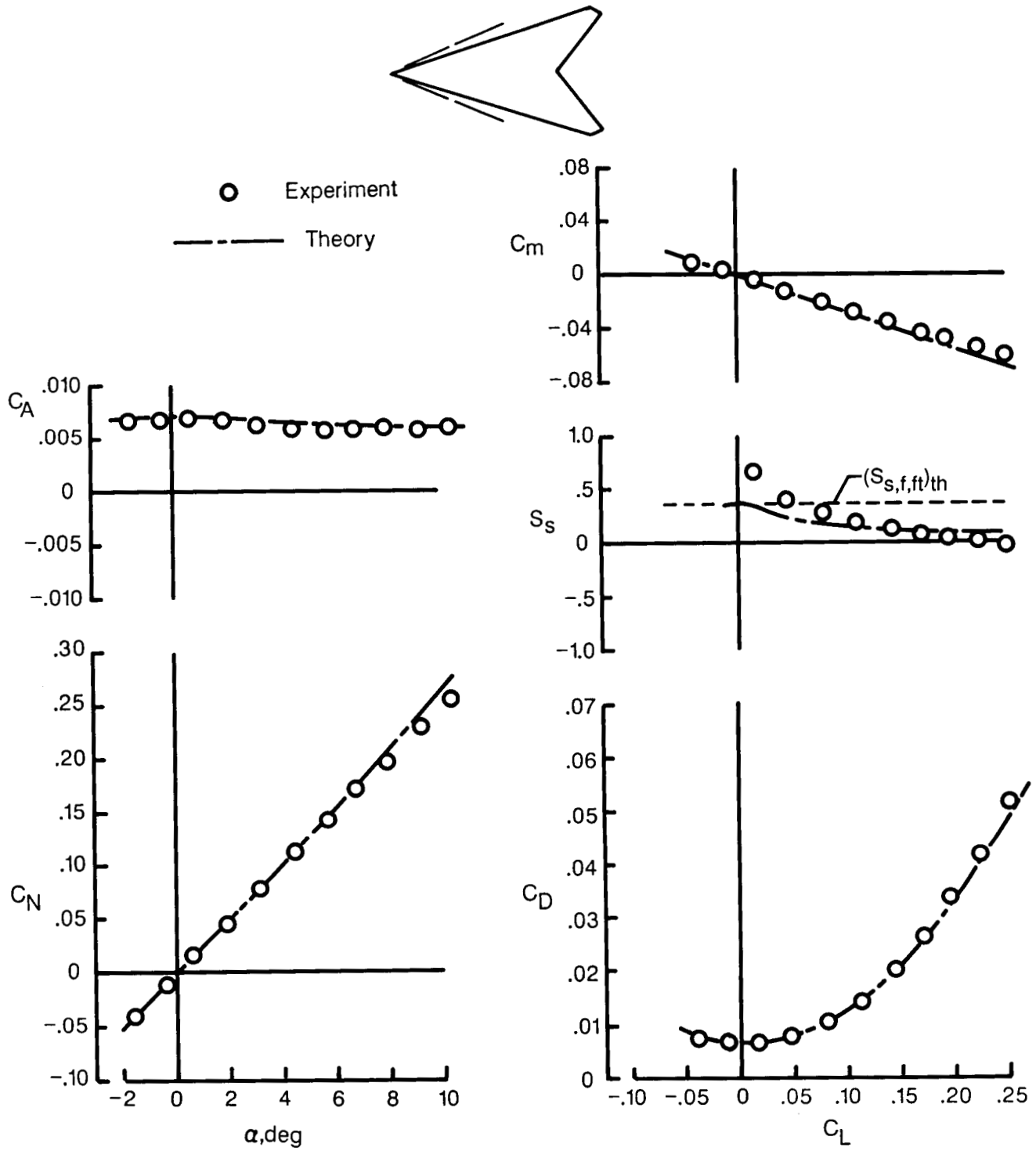

(a) $C_{L,\mathrm{des}} = 0$.

Figure 14. Theoretical and experimental data for 72.65° swept modified arrow wings twisted and cambered for three design lift coefficients. $M = 2.60$; $\beta \cot \Lambda_{le} = 0.75$; $R = 5.1 \times 10^6$.

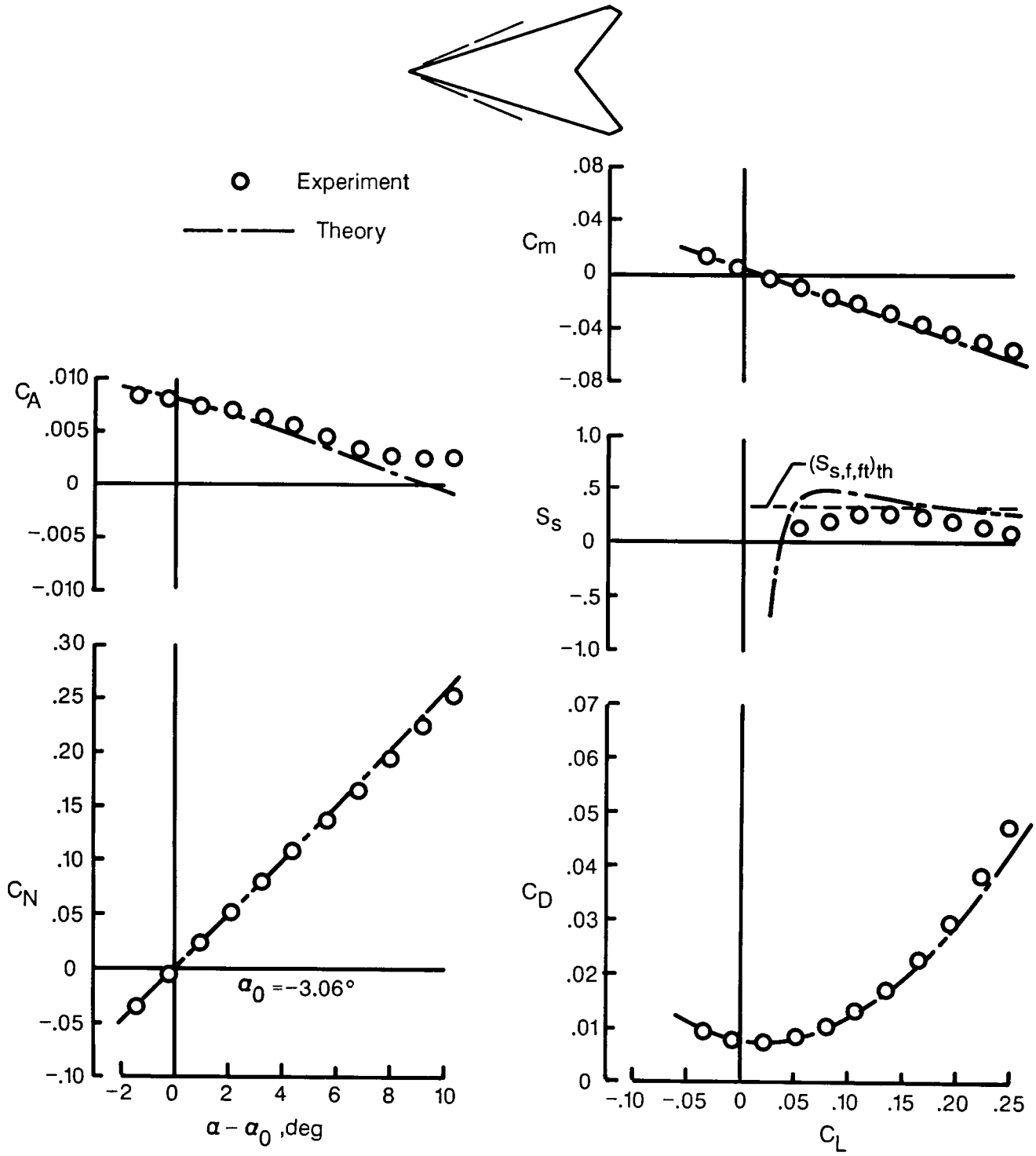

(b) $C_{L,\mathrm{des}} = 0.08$.

Figure 14. Continued.

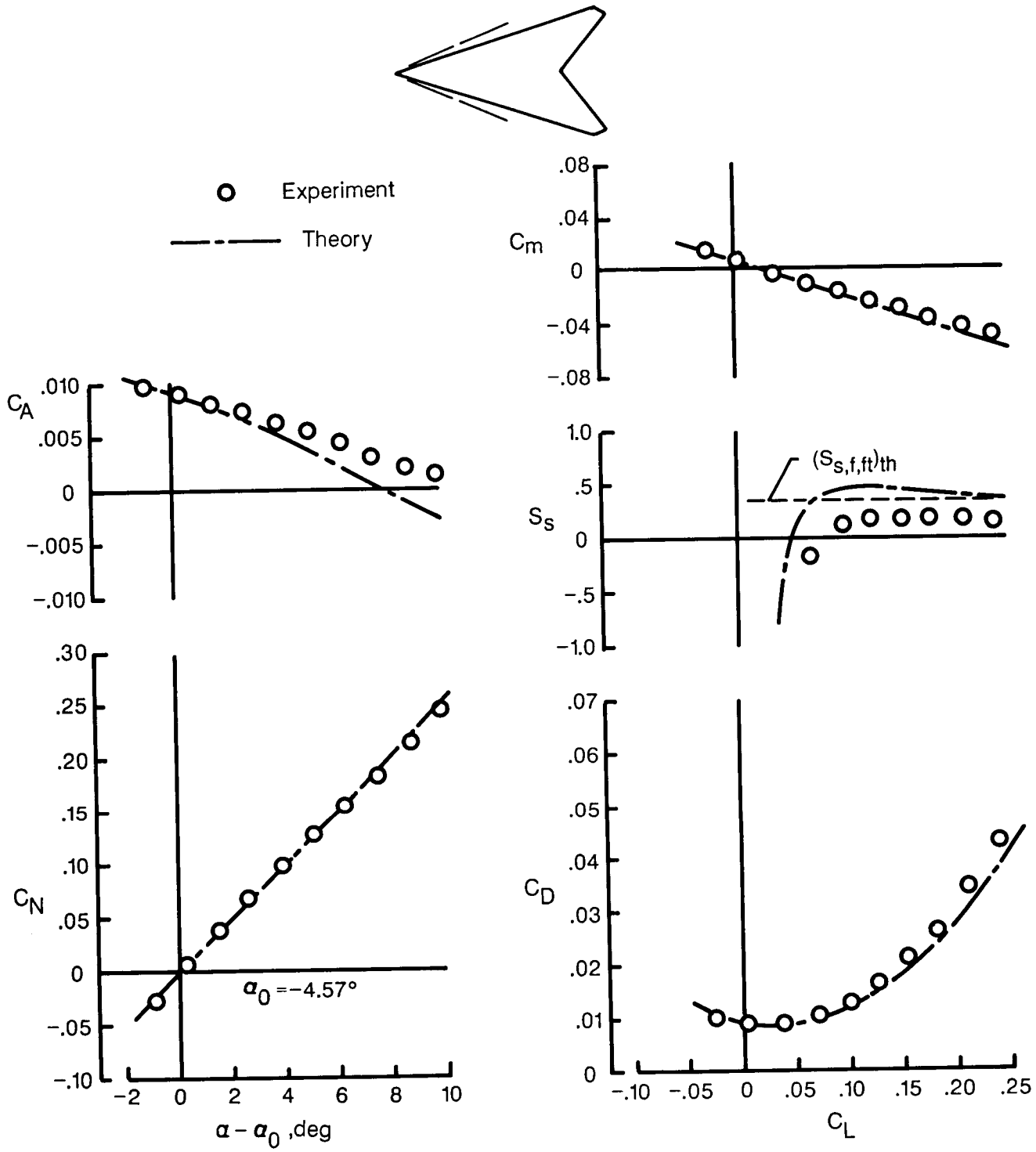

(c) $C_{L,\text{des}} = 0.12$.

Figure 14. Concluded.

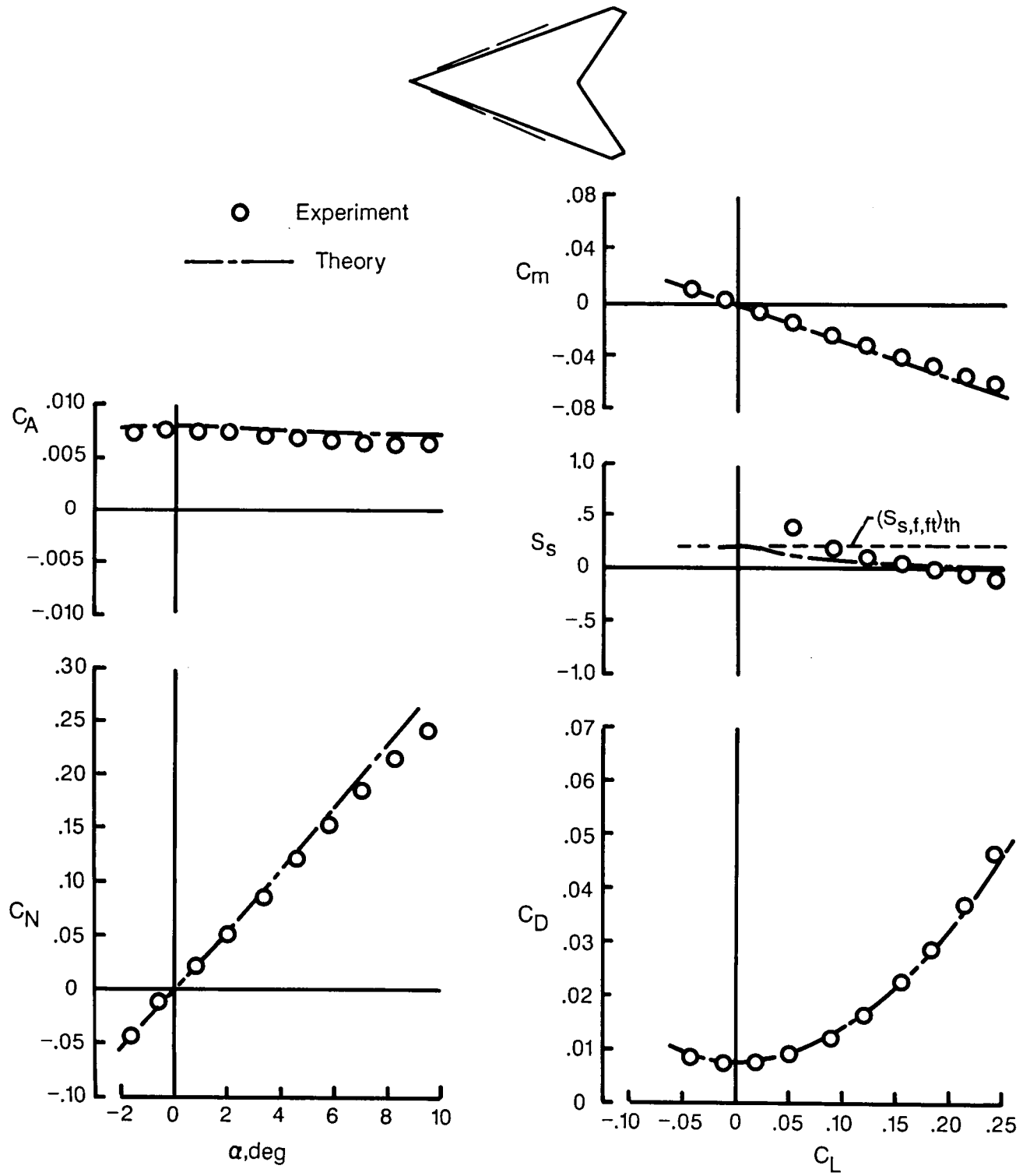

(a) $C_{L,\mathrm{des}} = 0$.

Figure 15. Theoretical and experimental data for 69.44° swept modified arrow wings twisted and cambered for three design lift coefficients. $M = 2.60$; $\beta \cot \Lambda_{le} = 0.90$; $R = 5.1 \times 10^6$.

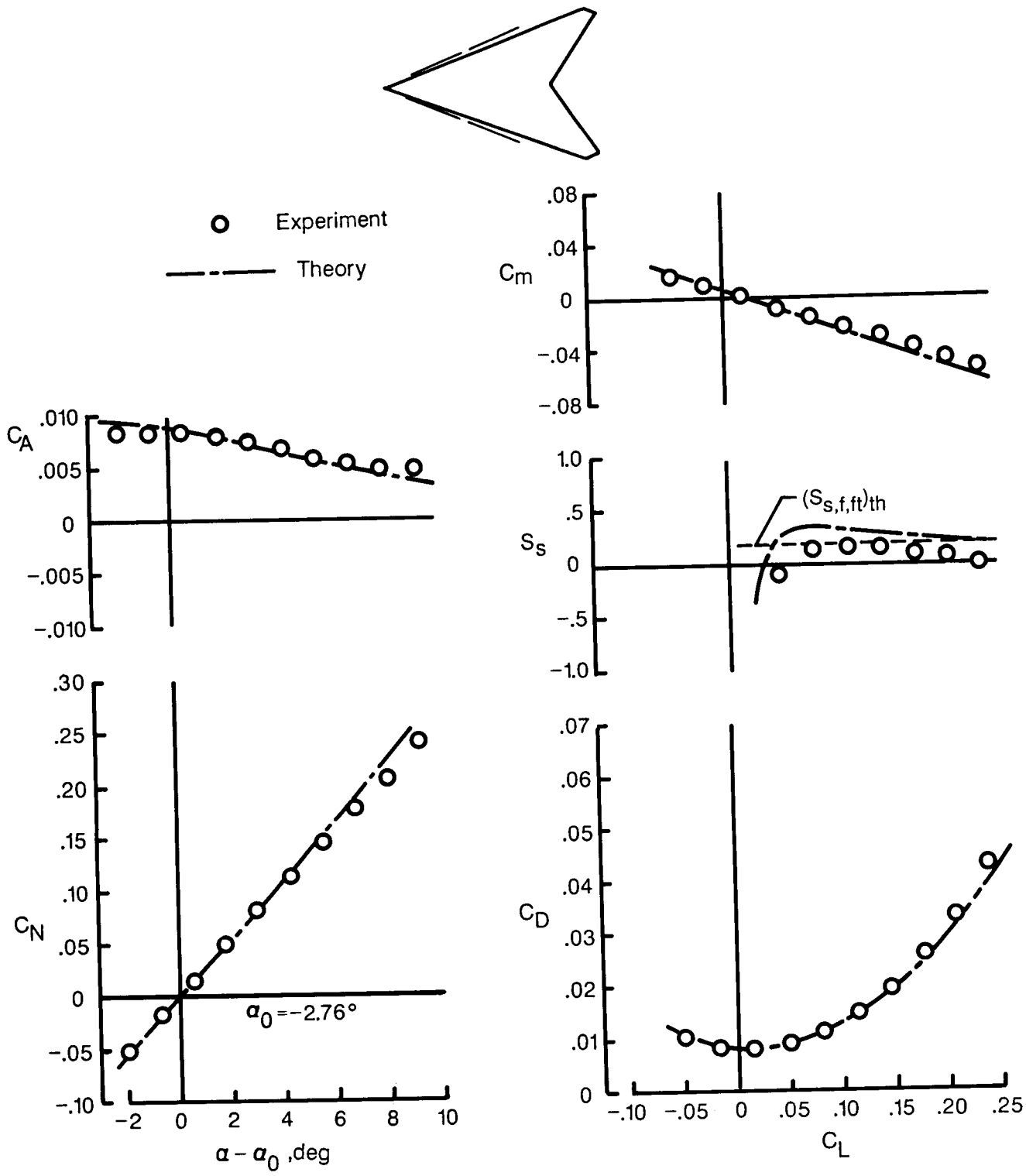

(b) $C_{L,\text{des}} = 0.08$.

Figure 15. Continued.

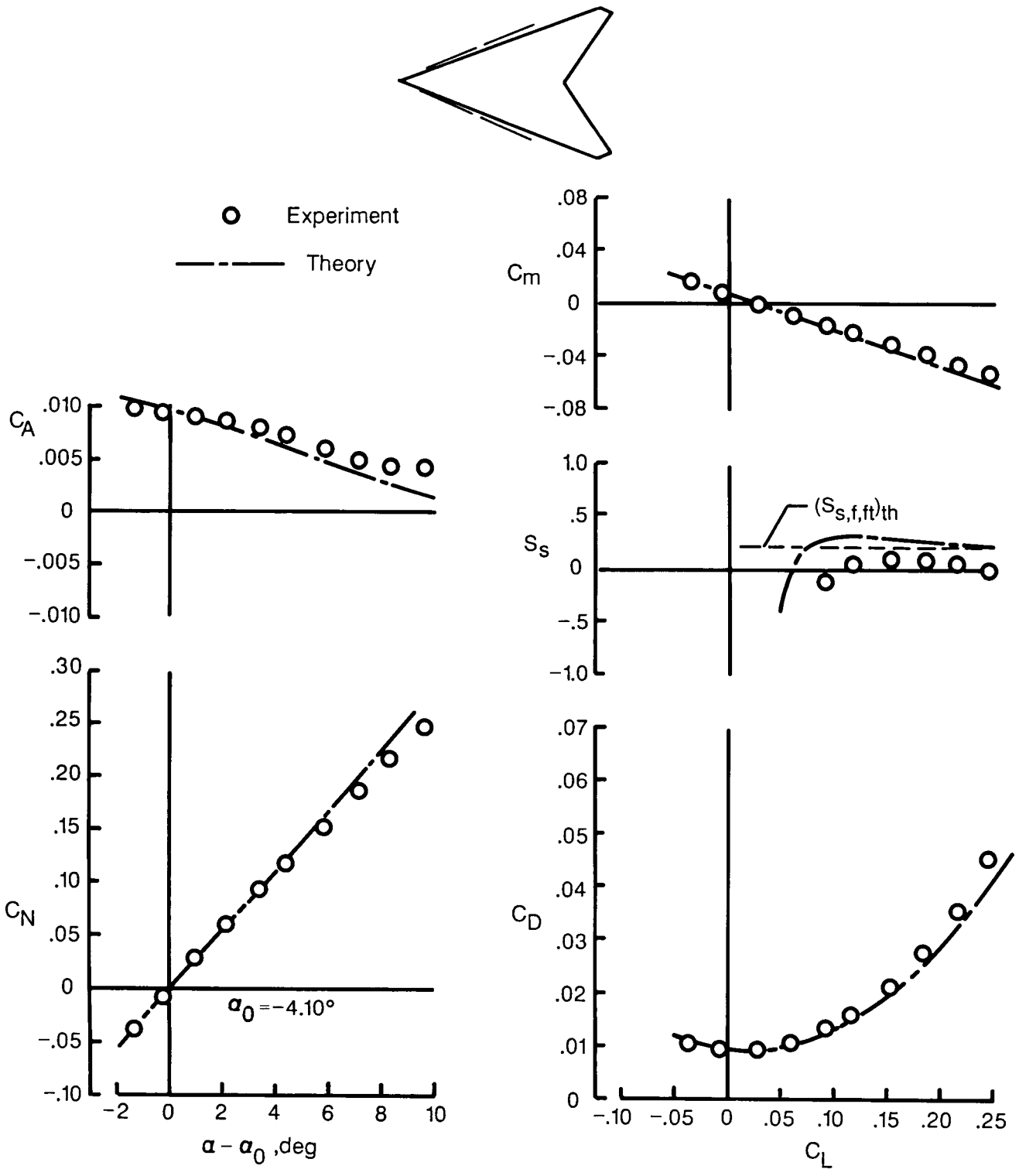

(c) $C_{L,\mathrm{des}} = 0.12$.

Figure 15. Concluded.

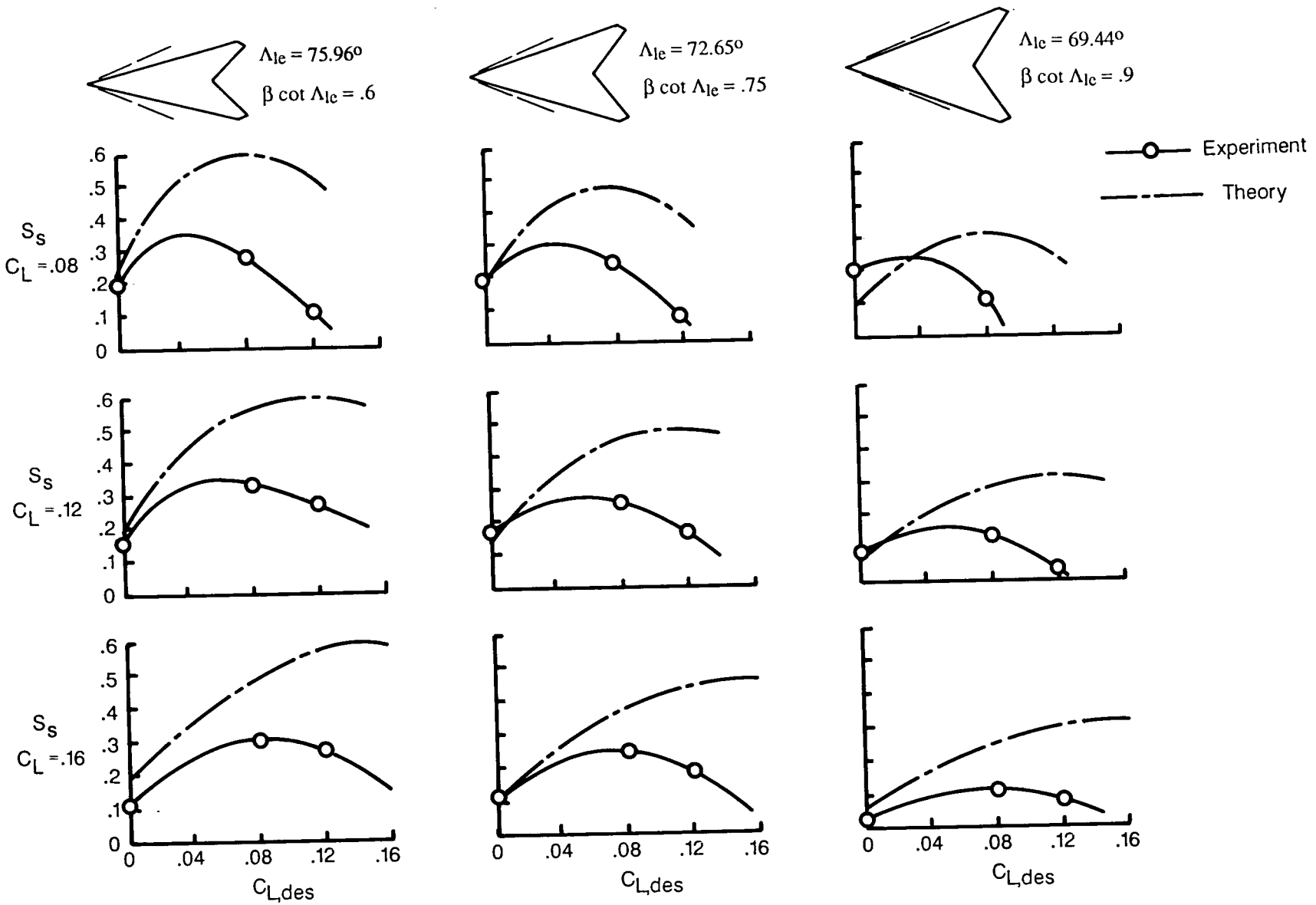

Figure 16. Variation of suction parameter at three lift coefficients with design lift coefficient for 75.96°, 72.65°, and 69.44° swept modified arrow wings.

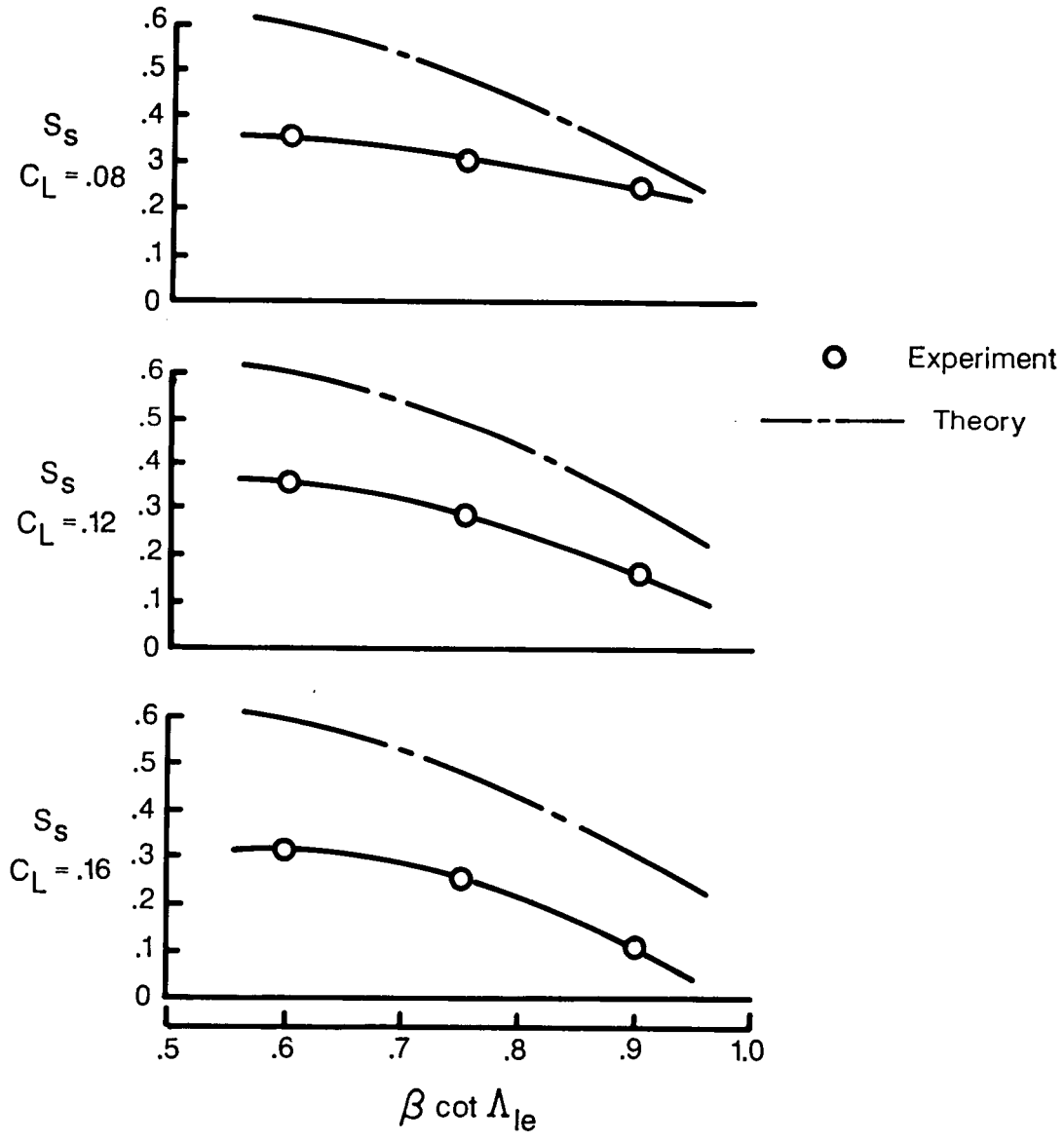

Figure 17. Variation of maximum suction parameter at three lift coefficients with leading-edge sweep angle for 75.96°, 72.65°, and 69.44° swept modified arrow wings.

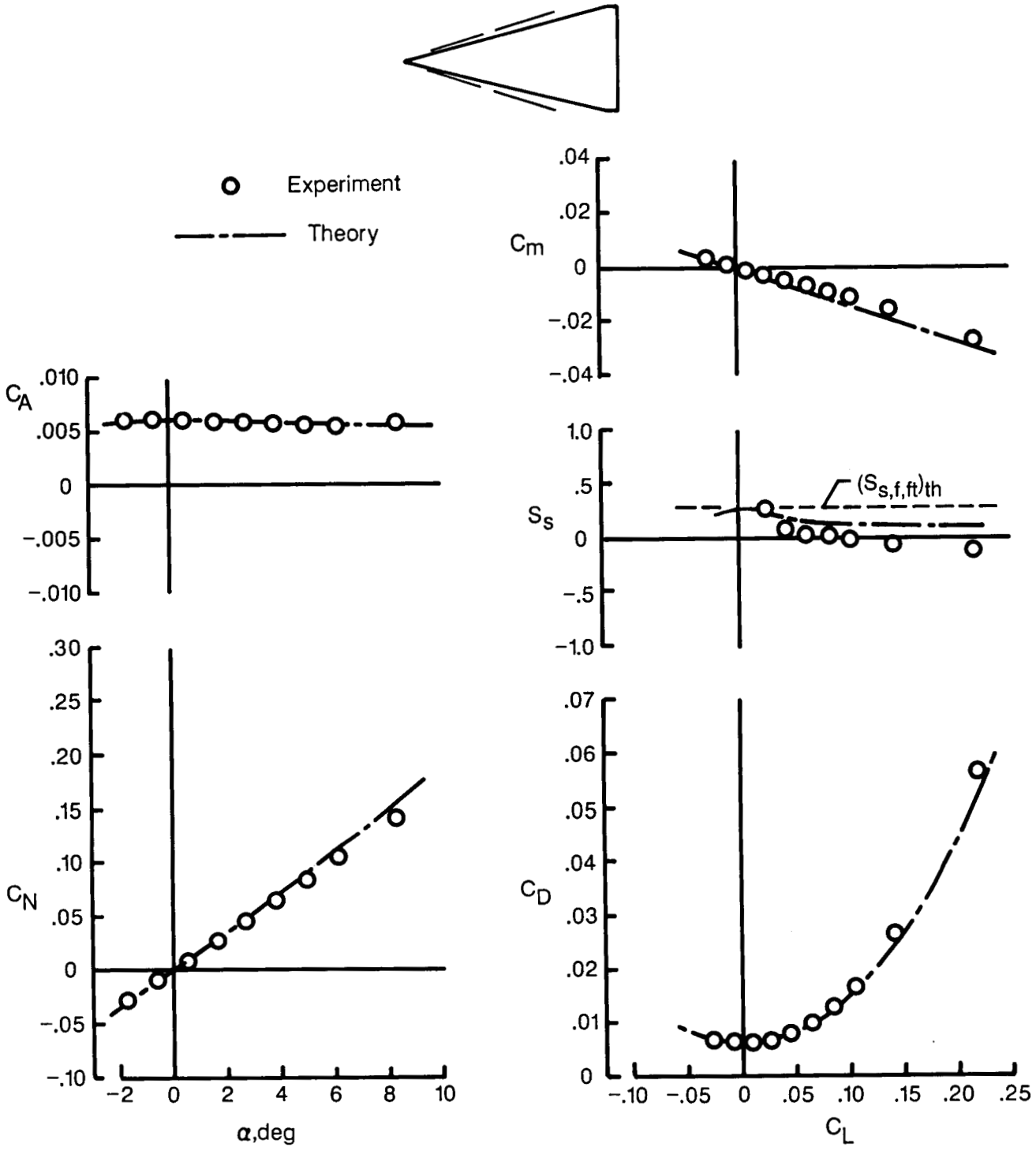

(a) $C_{L,\mathrm{des}} = 0$.

Figure 18. Theoretical and experimental data for 76° swept delta wing–body combinations twisted and cambered for three design lift coefficients. $M = 3.50$; $R = 4.9 \times 10^6$.

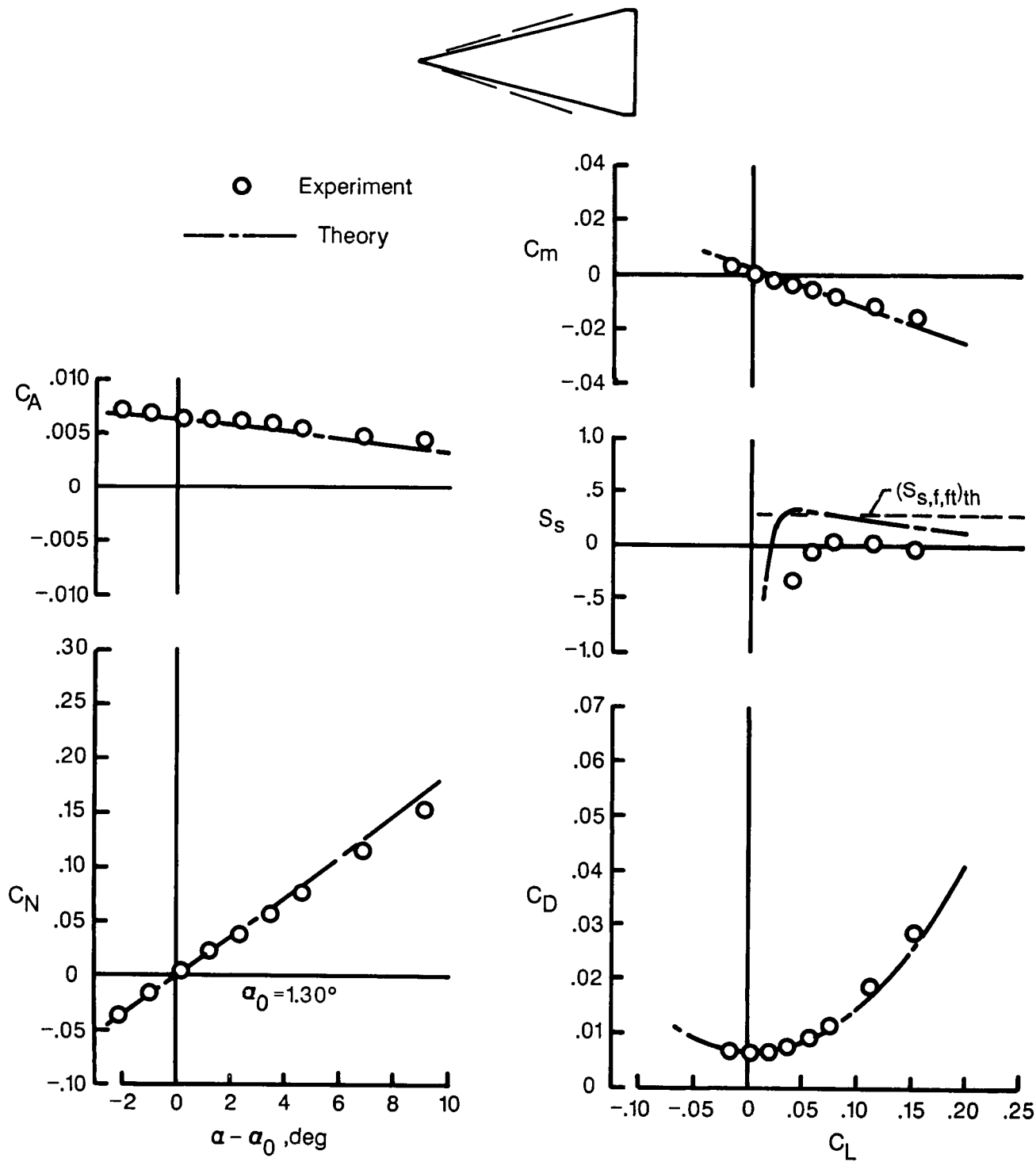

(b) $C_{L,\text{des}} = 0.05$.

Figure 18. Continued.

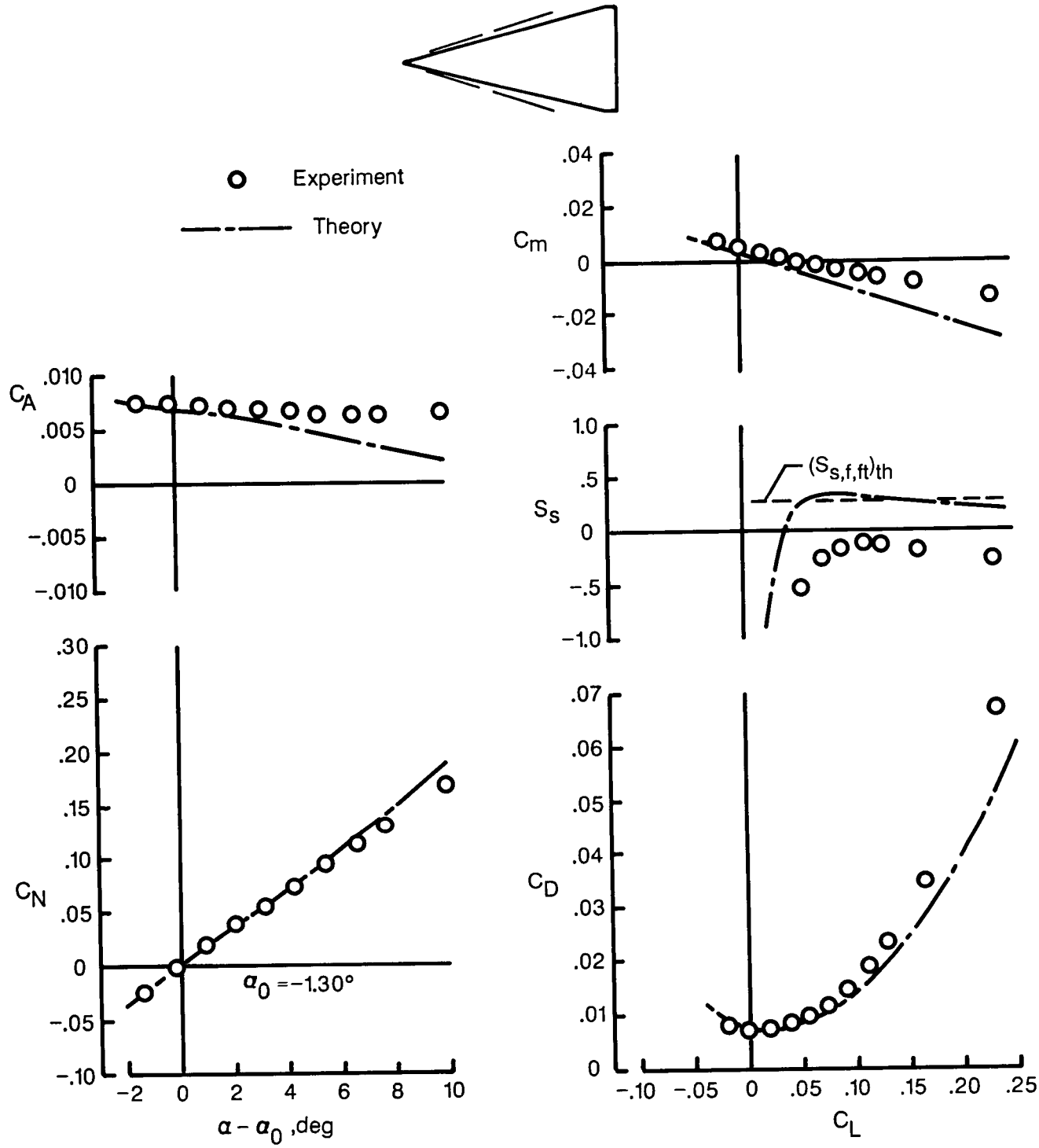

(c) $C_{L,\mathrm{des}} = 0.10$.

Figure 18. Concluded.

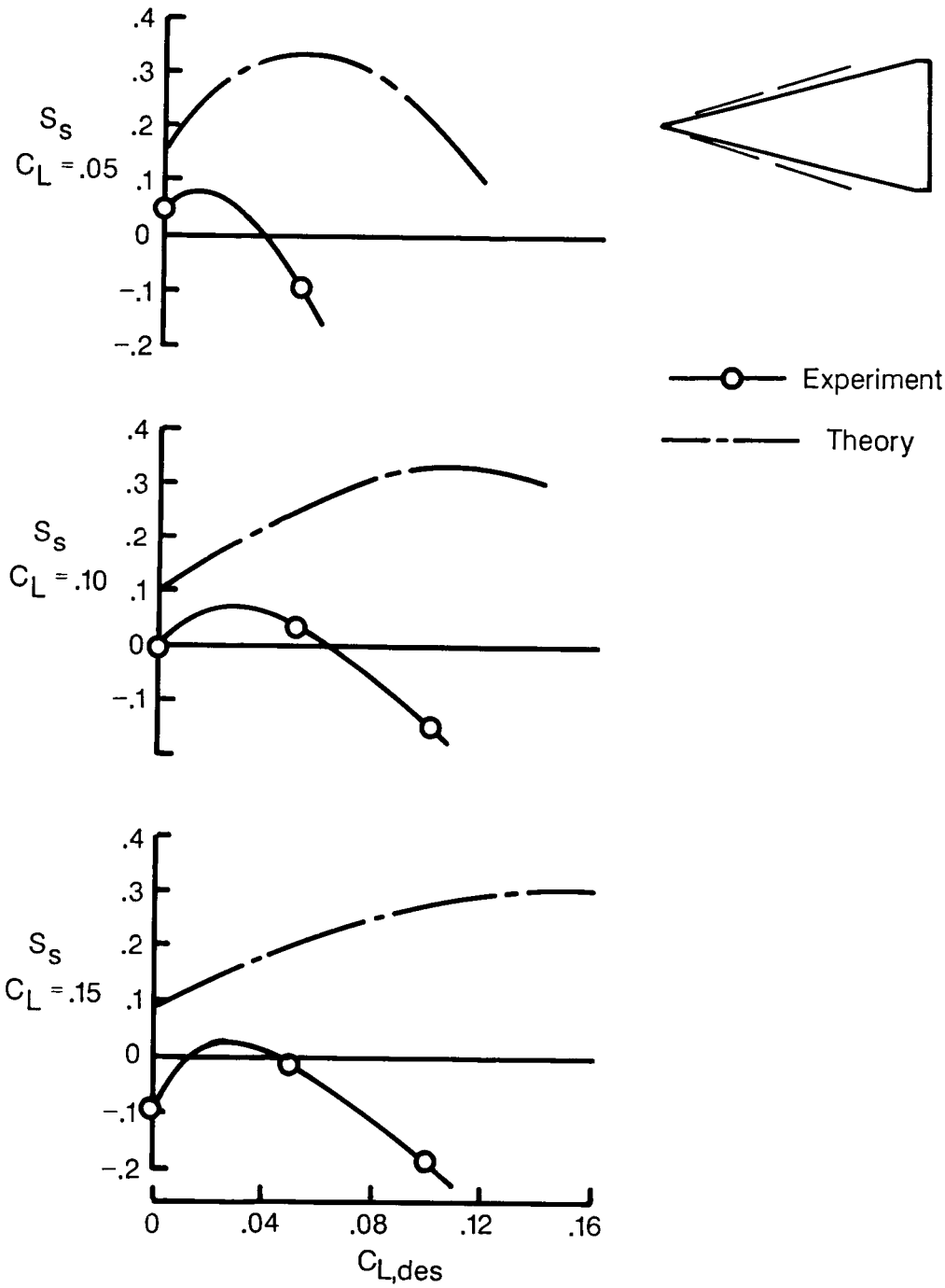

Figure 19. Variation of suction parameter at three cruise lift coefficients with design lift coefficient for the 76° swept delta wing–body combinations. $M = 3.50$; $R = 4.9 \times 10^6$.

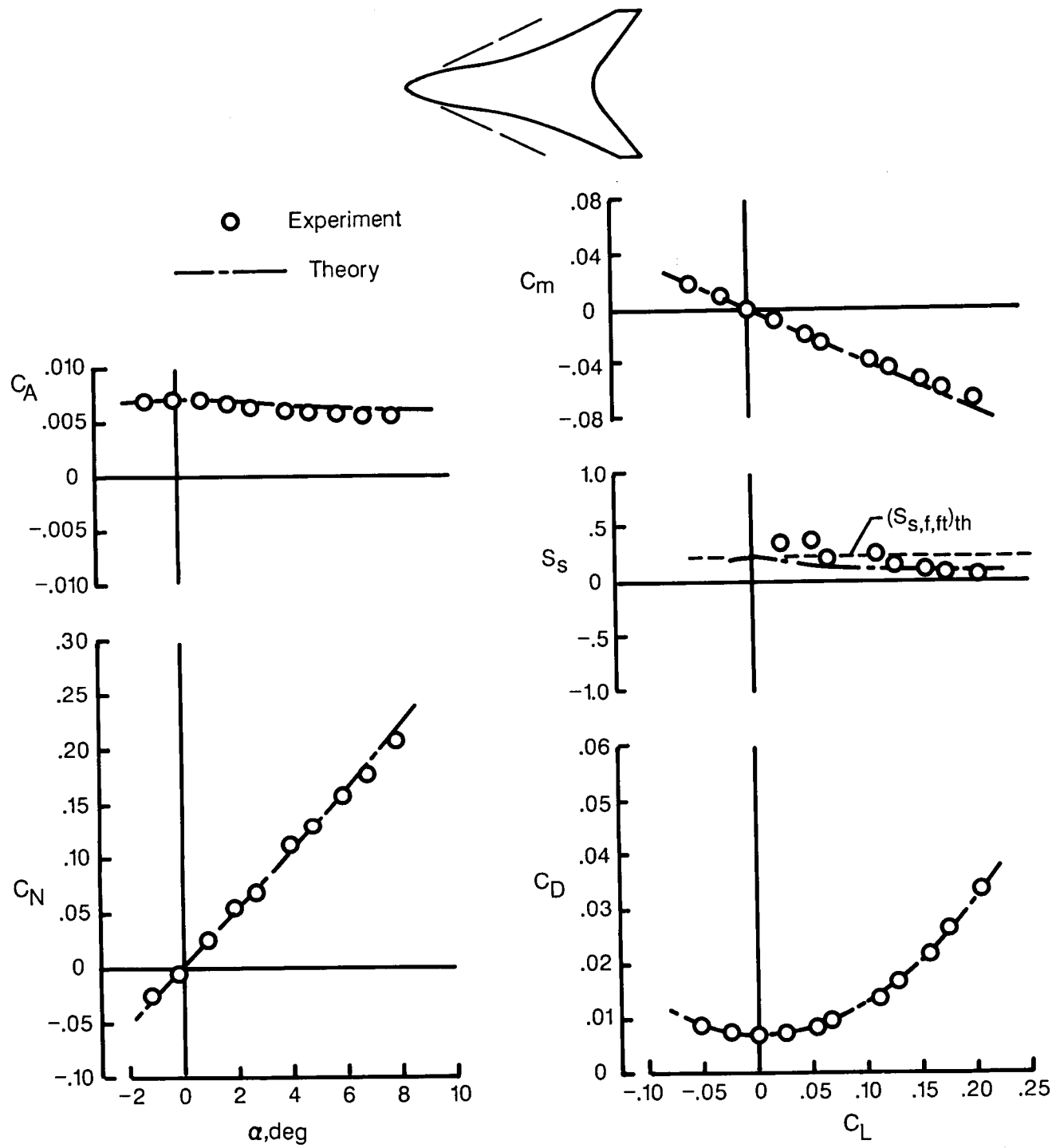

(a) Flat wing.

Figure 20. Theoretical and experimental data for arbitrary planform wing–body combinations with different loading constraints on twisted and cambered wing design. $M = 2.40$; $R = 3.4 \times 10^6$.

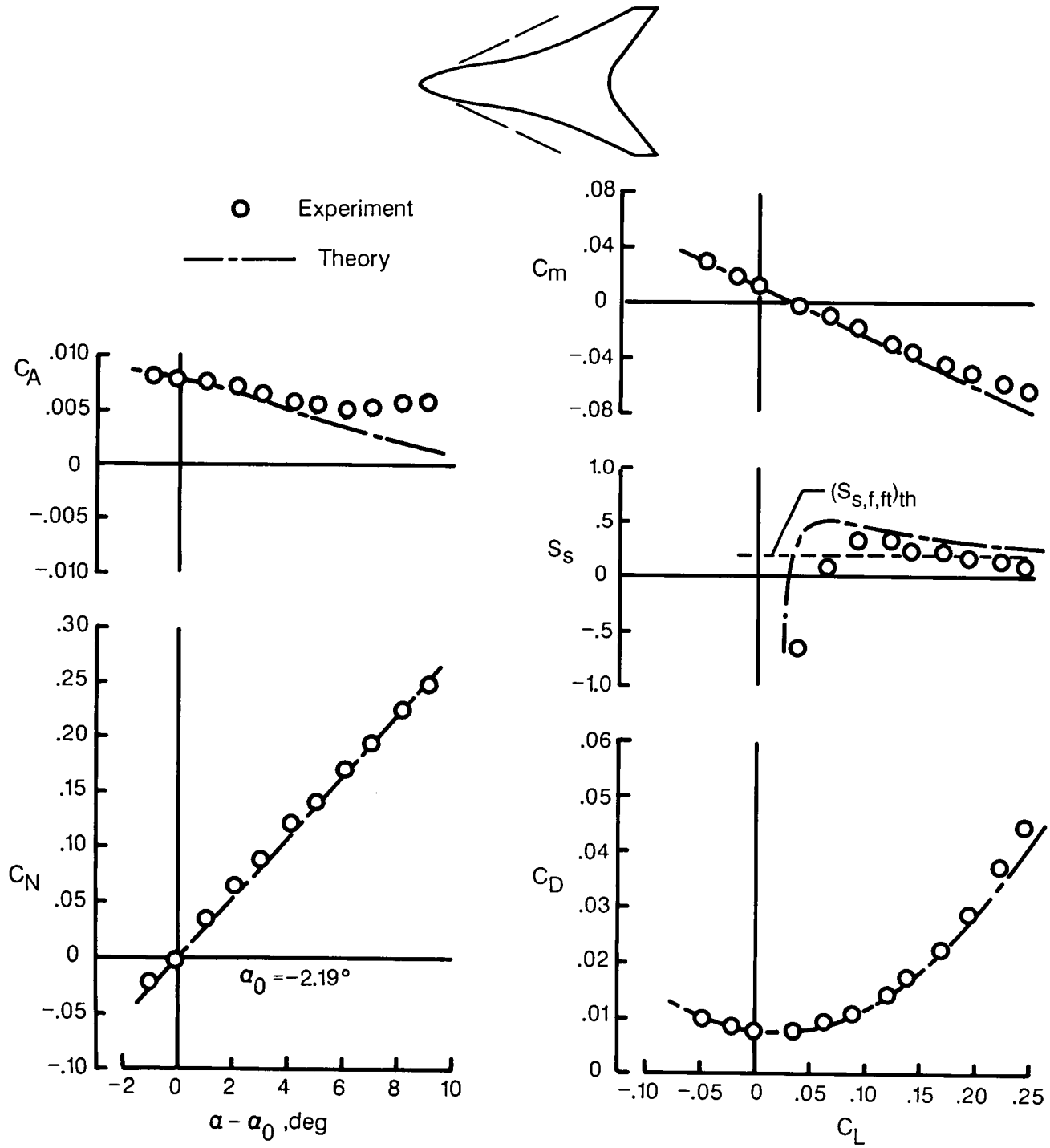

(b) $C_{L,\text{des}} = 0.08$; no constraint.

Figure 20. Continued.

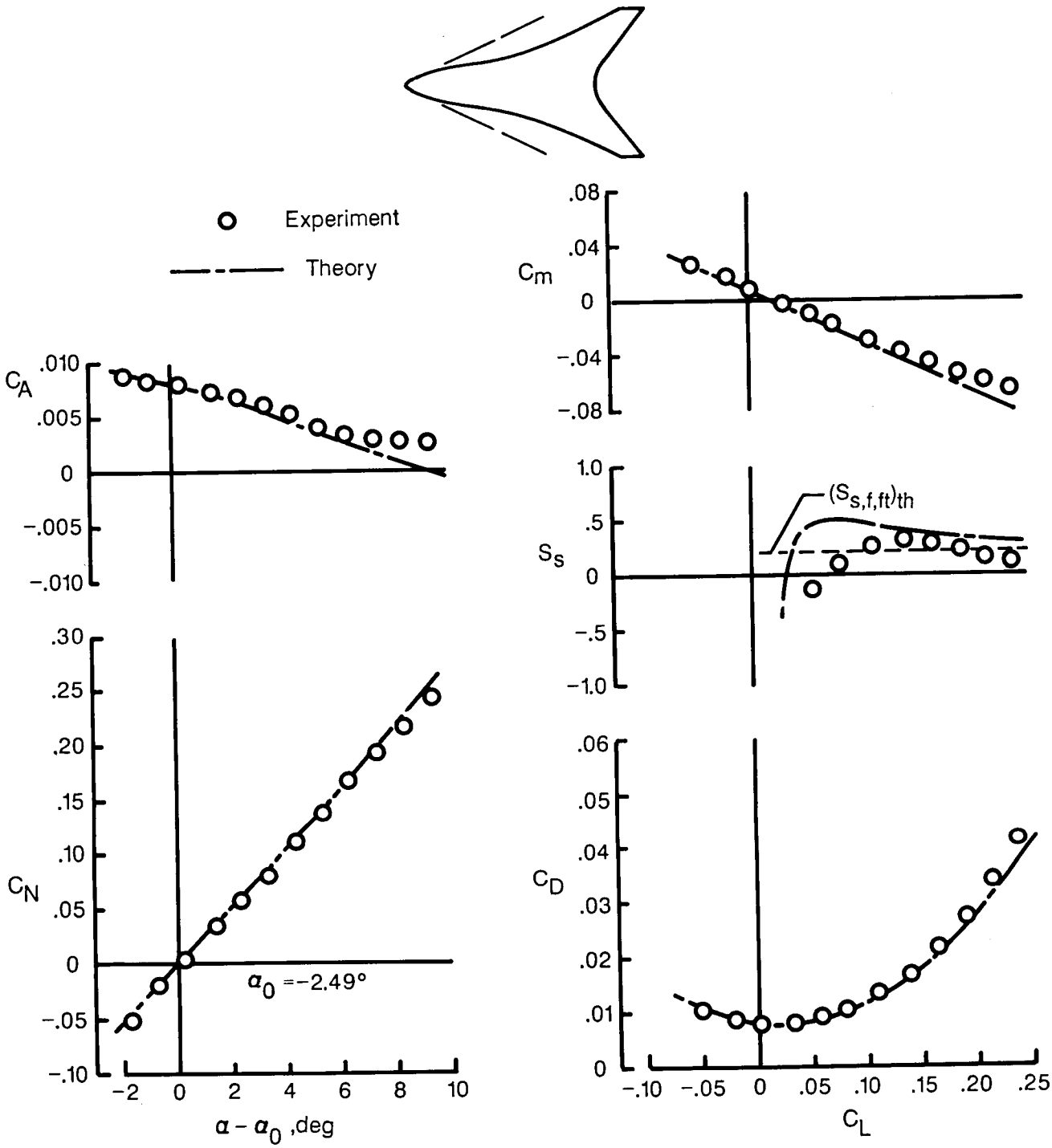

(c) $C_{L,\text{des}} = 0.08$; moderate constraint.

Figure 20. Continued.

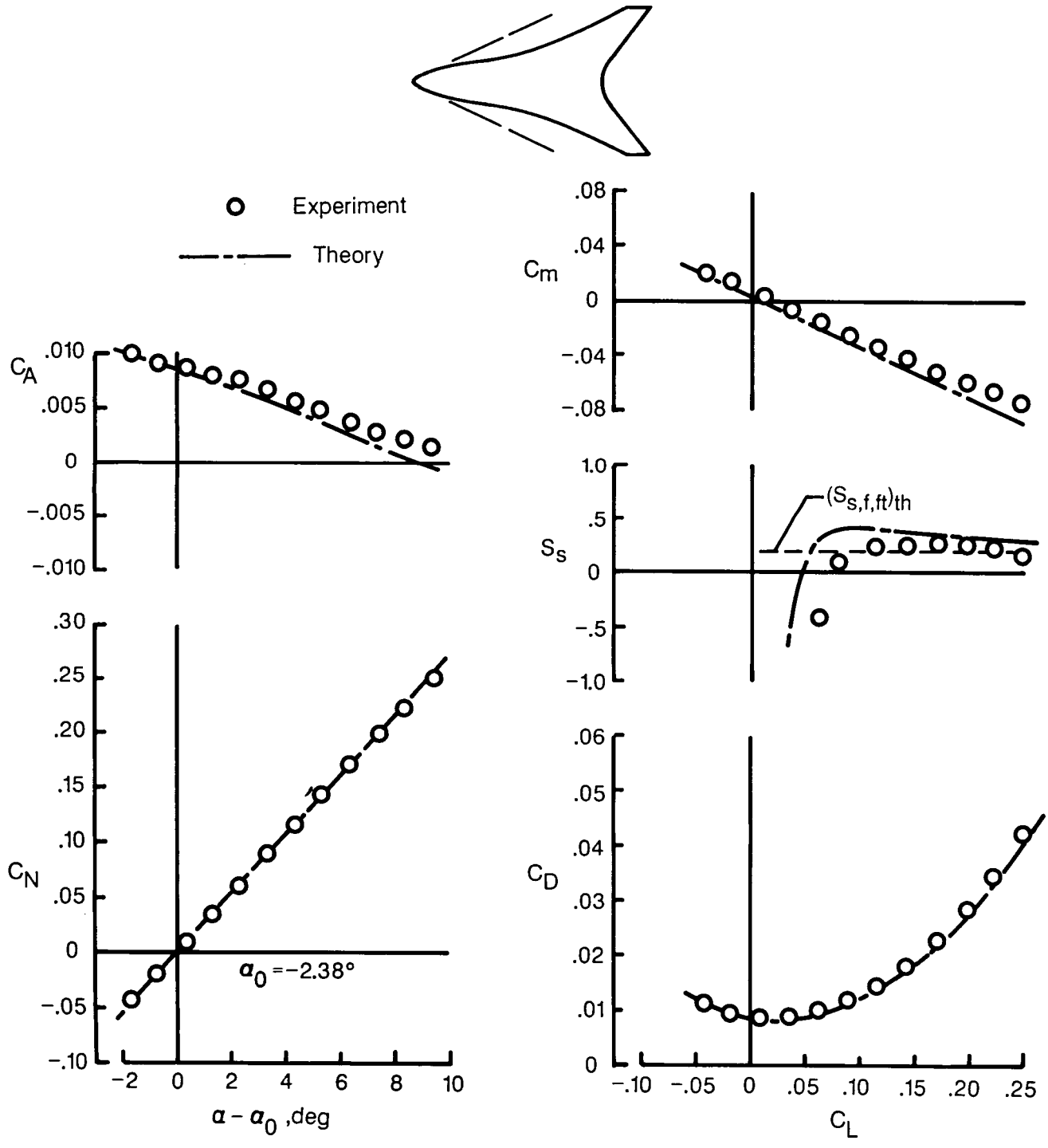

(d) $C_{L,\text{des}} = 0.08$; severe constraint.

Figure 20. Concluded.

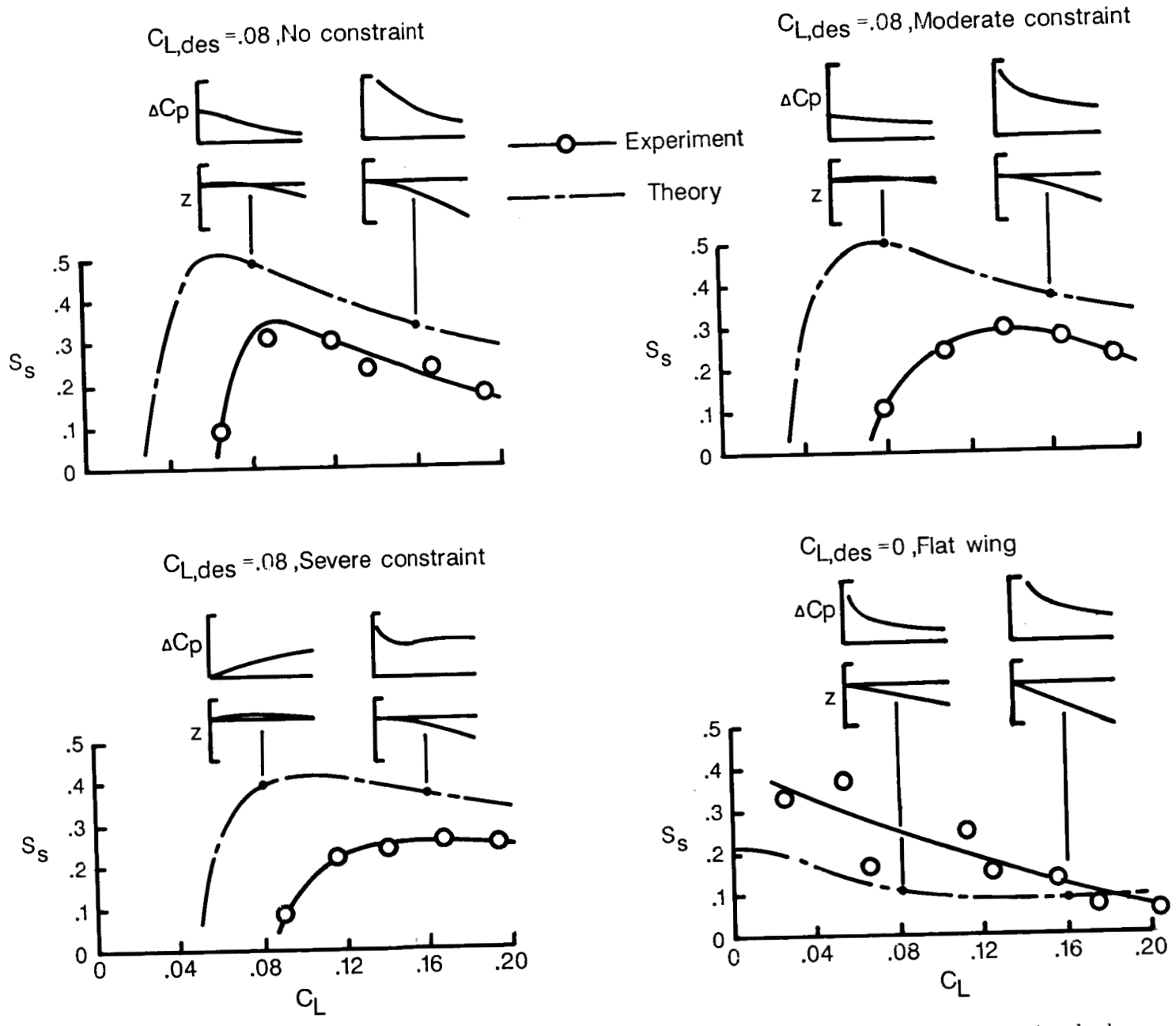

Figure 21. Variation of suction parameter with cruise lift coefficient for arbitrary planform wing–body combinations. $M = 2.40$; $R = 3.4 \times 10^6$; sketches show lifting pressure distributions and section ordinates at mid semispan.

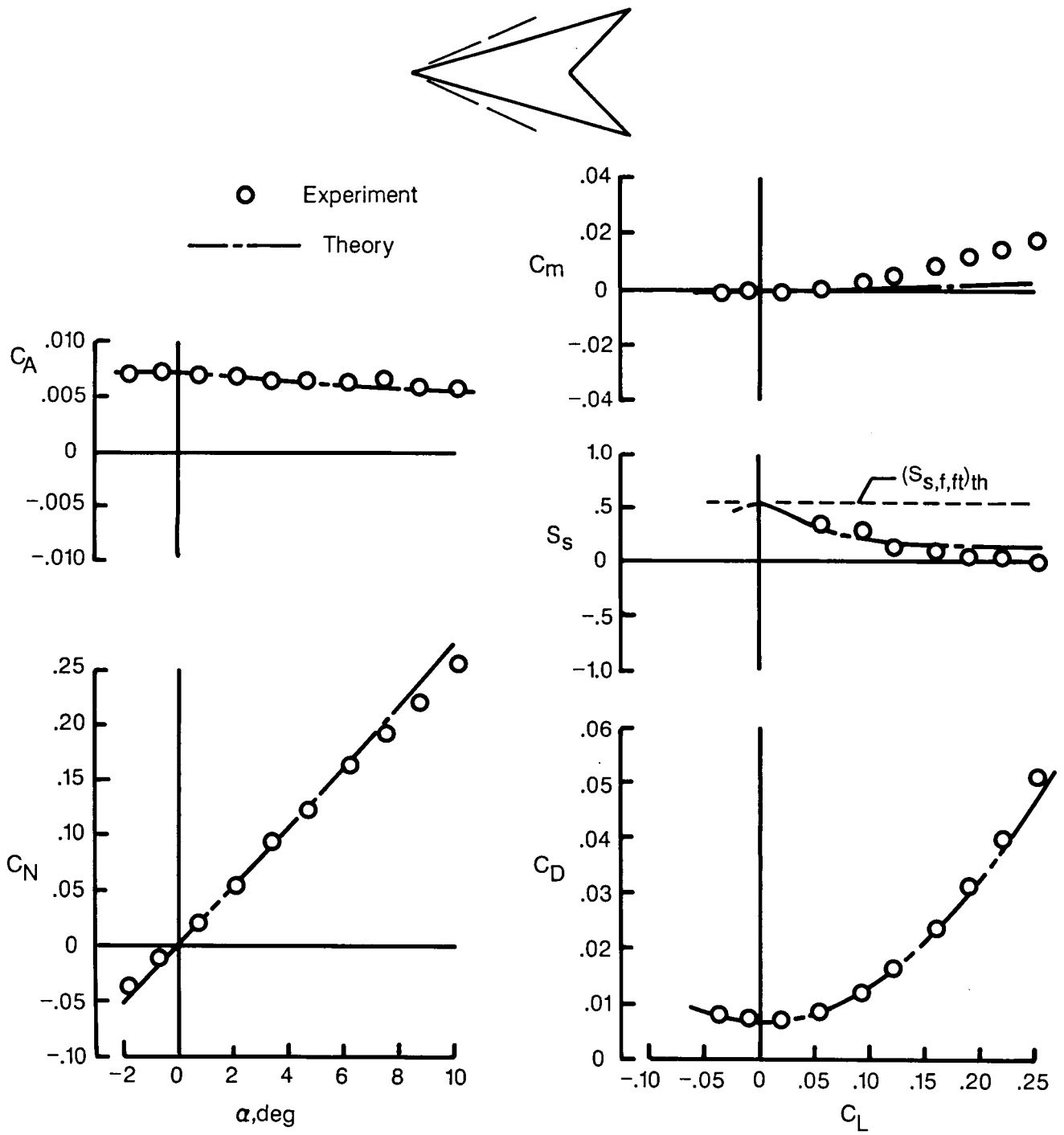

(a) Flat wing.

Figure 22. Theoretical and experimental data for flat and twisted and cambered 74° swept arrow wing–body combinations. $M = 2.50$; $R = 5.0 \times 10^6$.

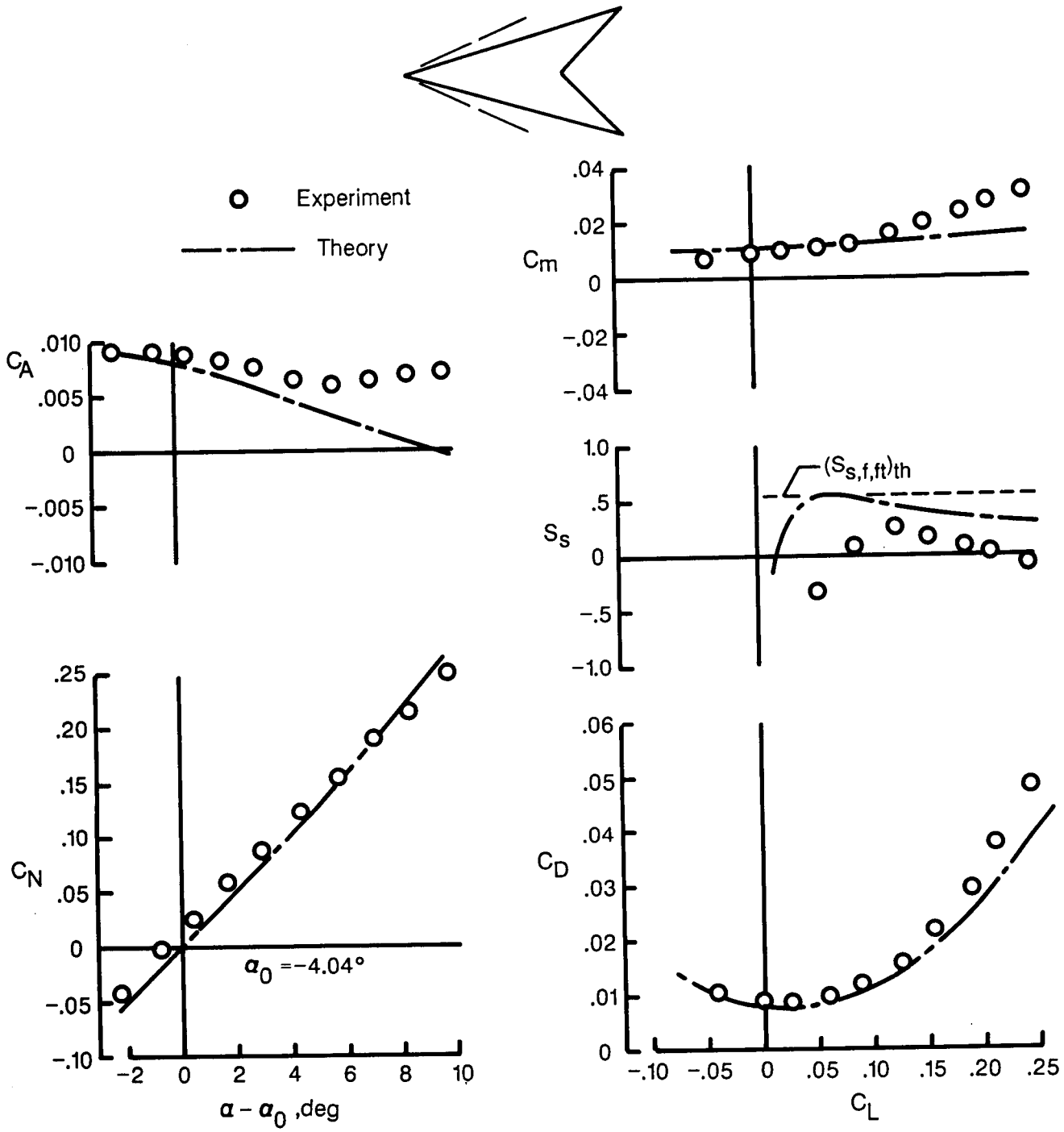

(b) $C_{L,\text{des}} = 0.10$.

Figure 22. Concluded.

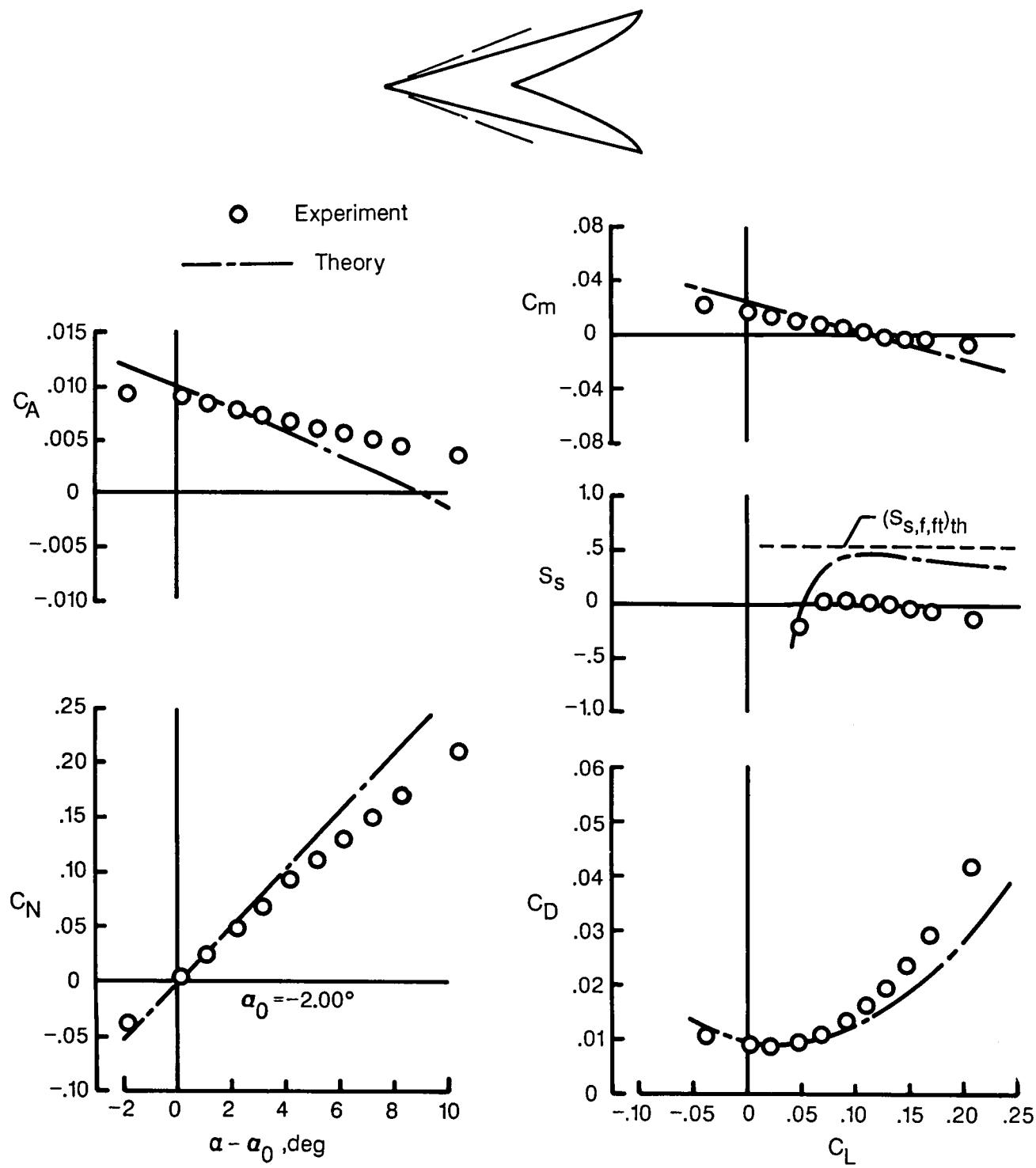

Figure 23. Theoretical and experimental data for 75° swept modified arrow wing–body combination with twist and camber for $C_{L,\text{des}} = 0.10$. $M = 2.87$; $R = 4.2 \times 10^6$.

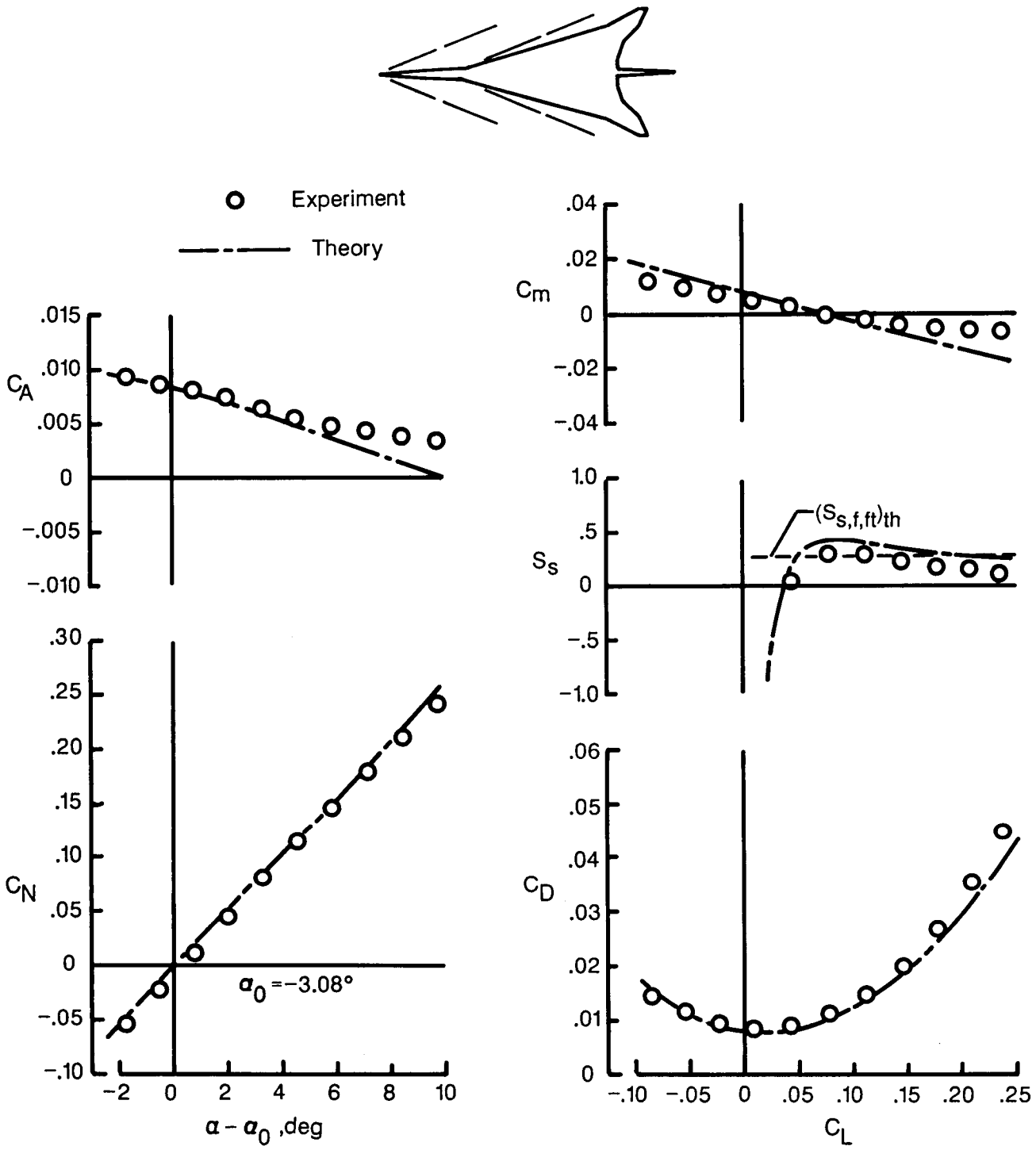

Figure 24. Theoretical and experimental data for supersonic transport wing–body combination with twist and camber for $C_{L,\text{des}} = 0.08$; $M = 2.70$; $R = 3.2 \times 10^6$.

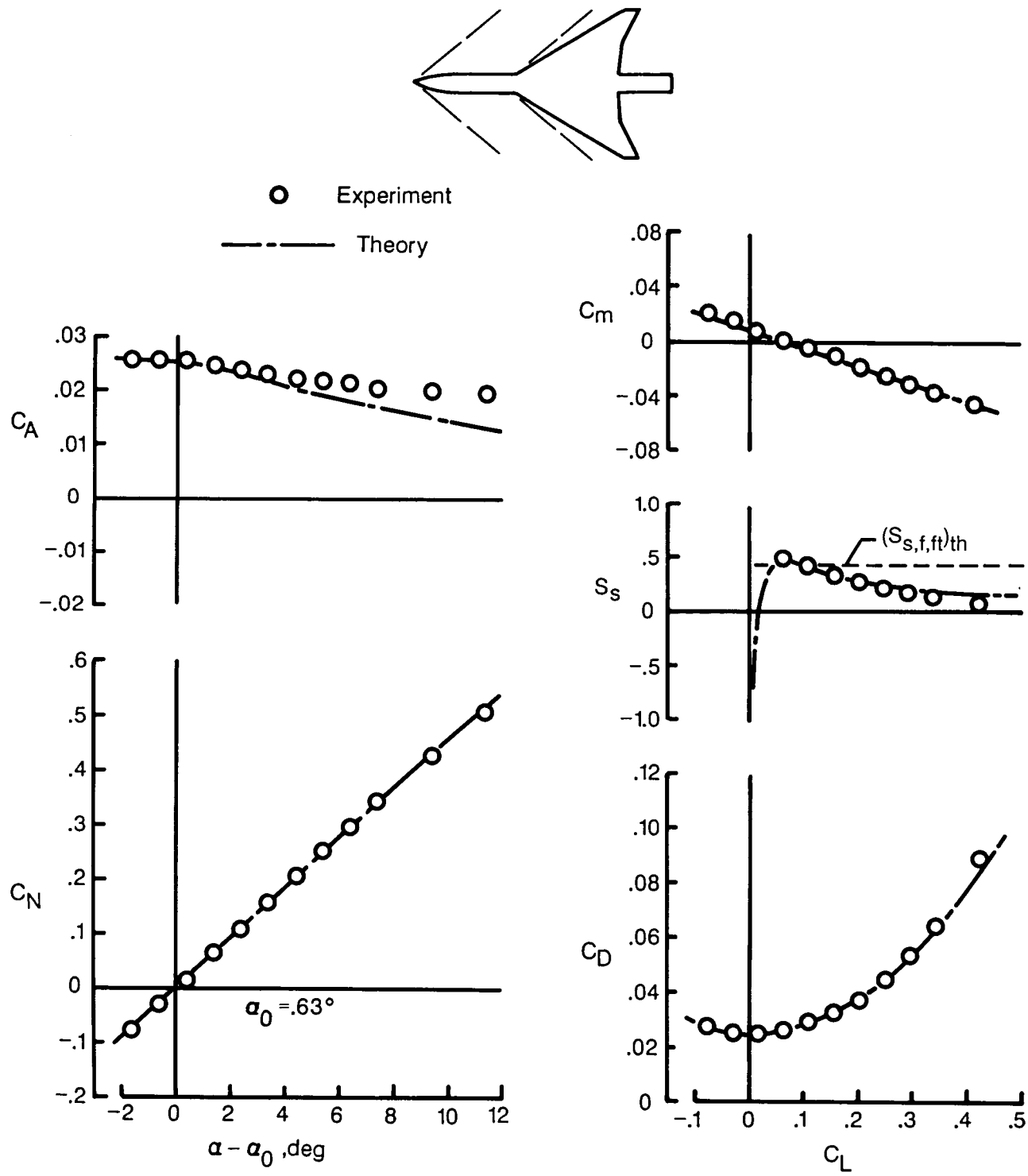

(a) Cruise design; $C_{L,\text{des}} = 0.05$; $M = 1.80$ (data are for $M = 1.60$).

Figure 25. Theoretical and experimental data for 60° swept wing–body combination twisted and cambered for two flight conditions. $M = 1.60$; $R = 1.7 \times 10^6$.

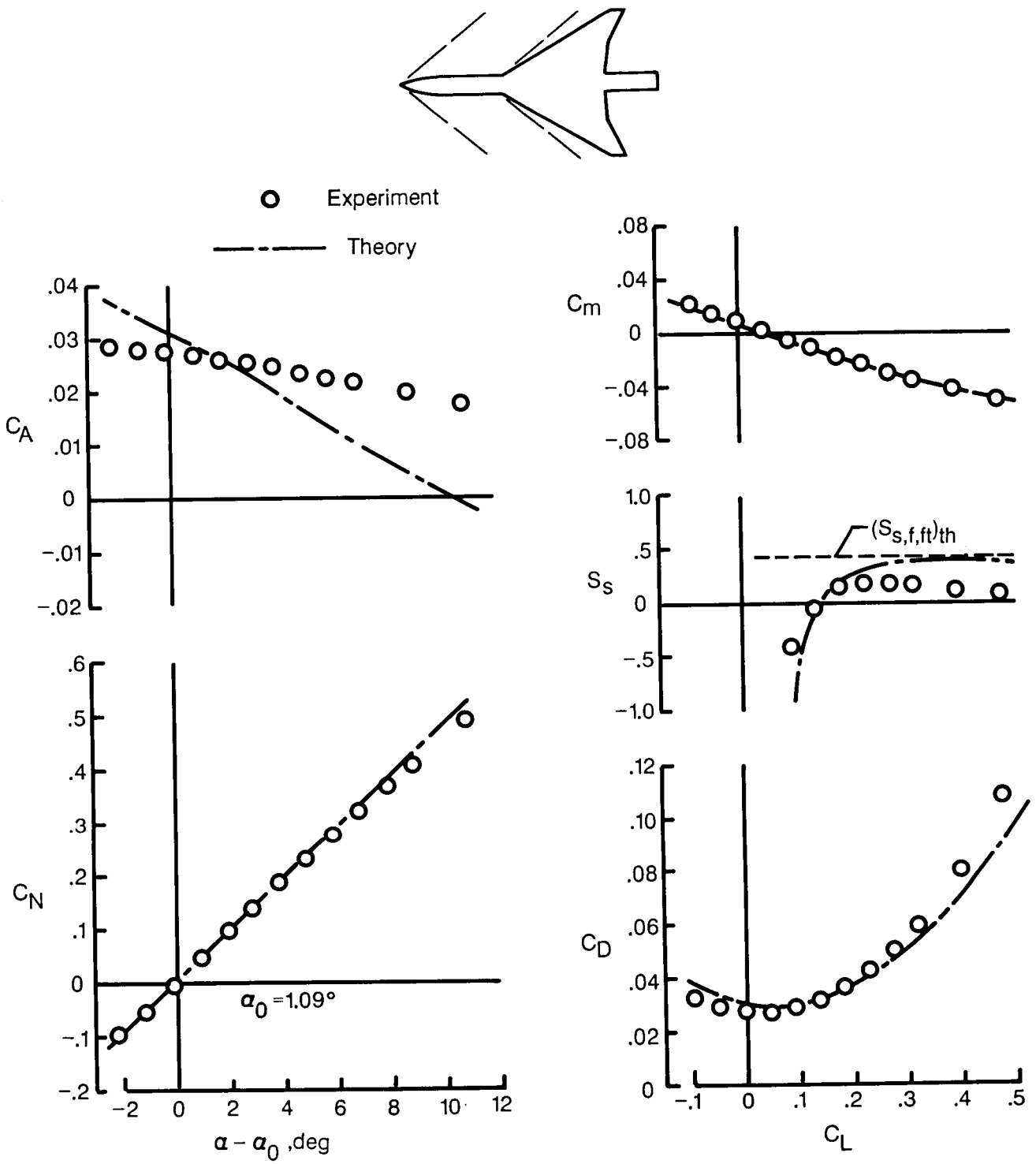

(b) Maneuver design; $C_{L,\text{des}} = 0.30$; $M = 1.60$.

Figure 25. Concluded.

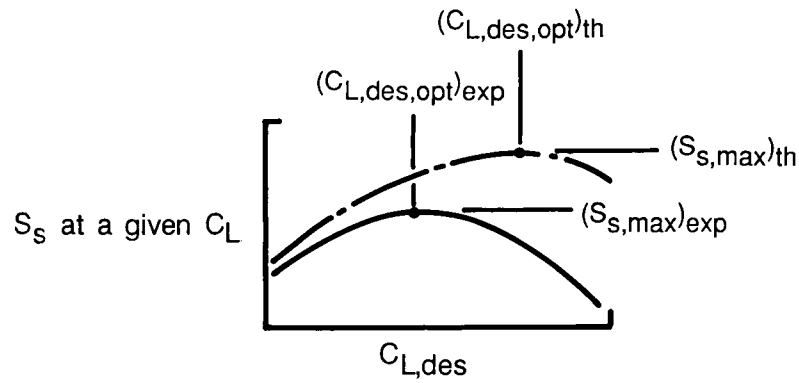

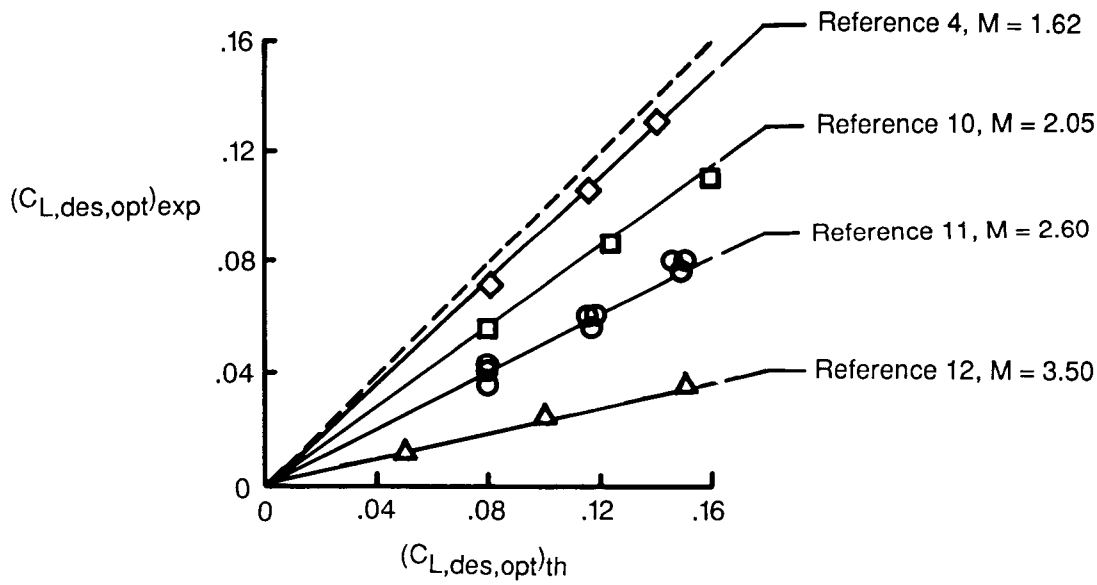

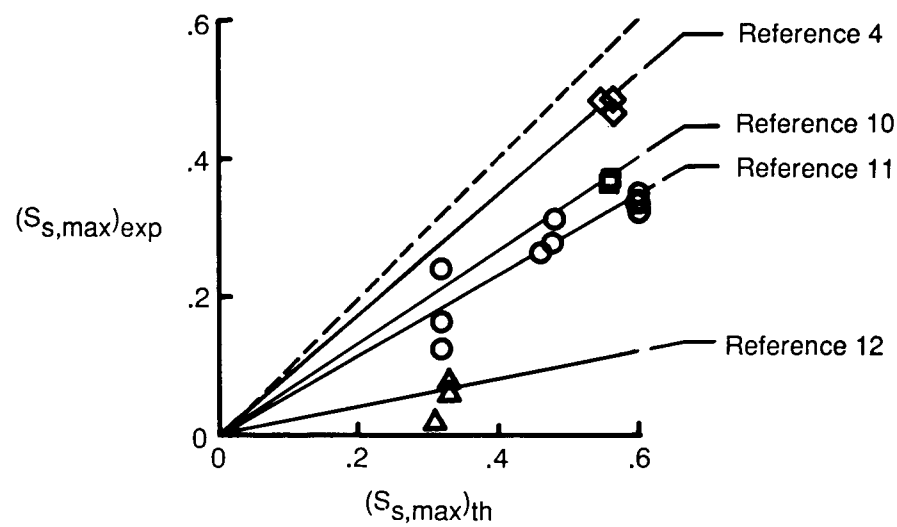

Figure 26. Relationship between experimental and theoretical maximum suction parameters and corresponding lift coefficients.

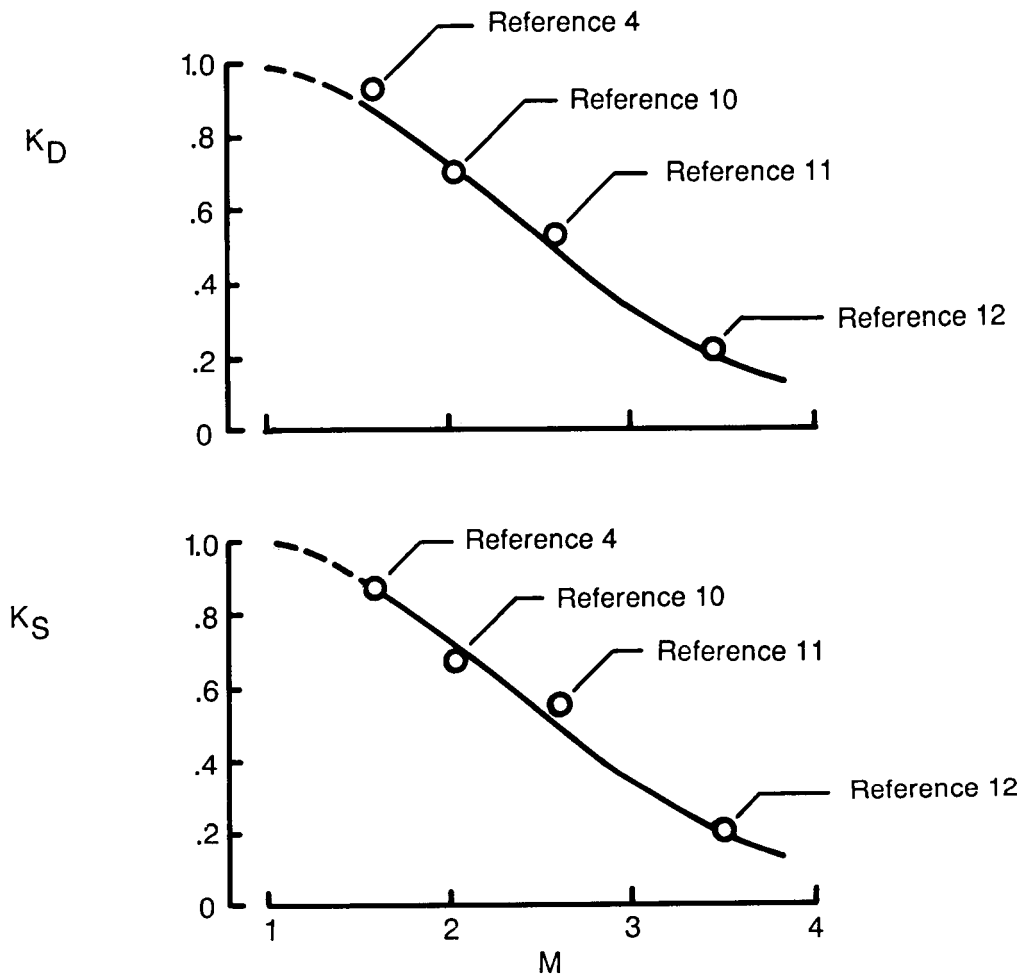

Figure 27. Empirical method factors used to select optimum design lift coefficients and to predict achievable suction parameters.

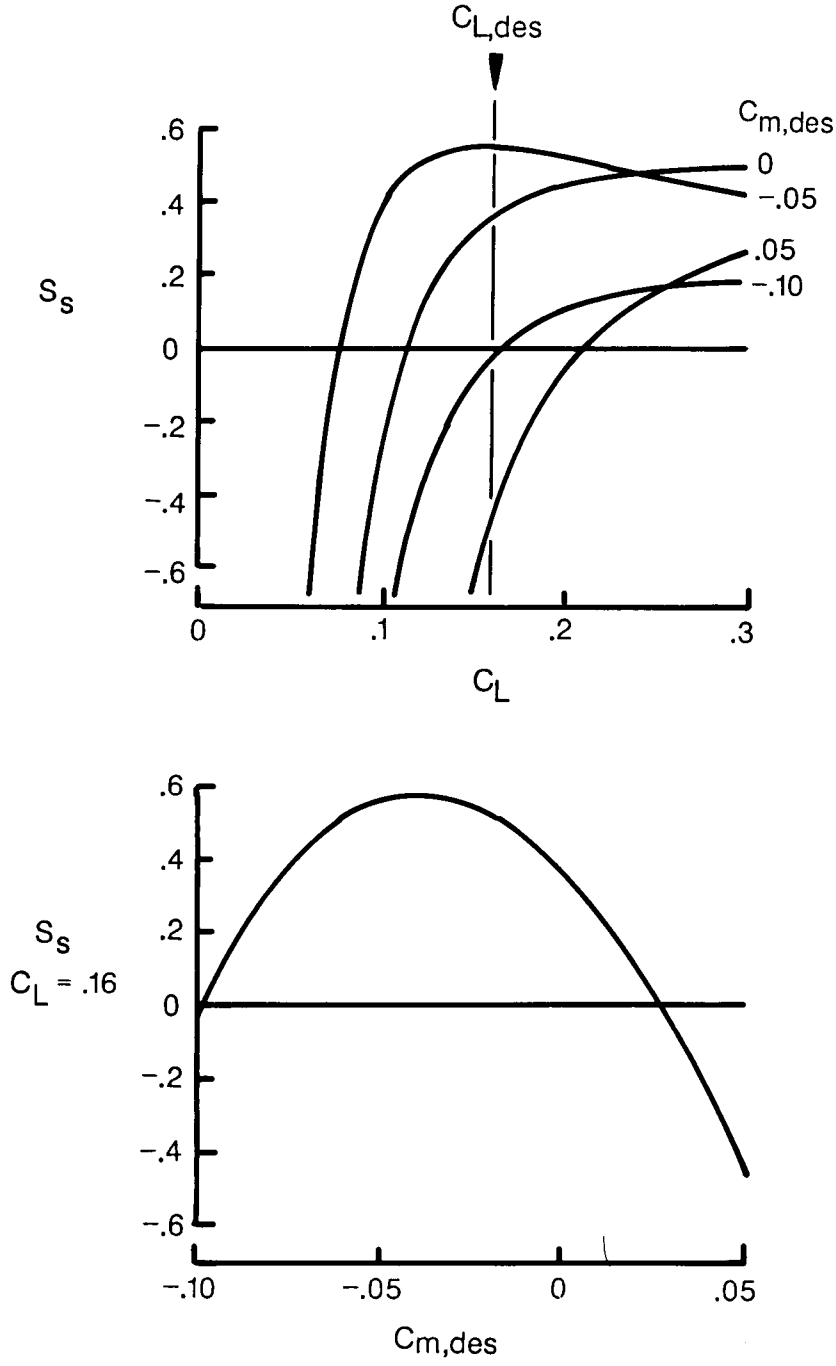

Figure 28. Effect of pitching-moment restraint on suction parameter. 70° swept arrow wing; $M = 2.05$.

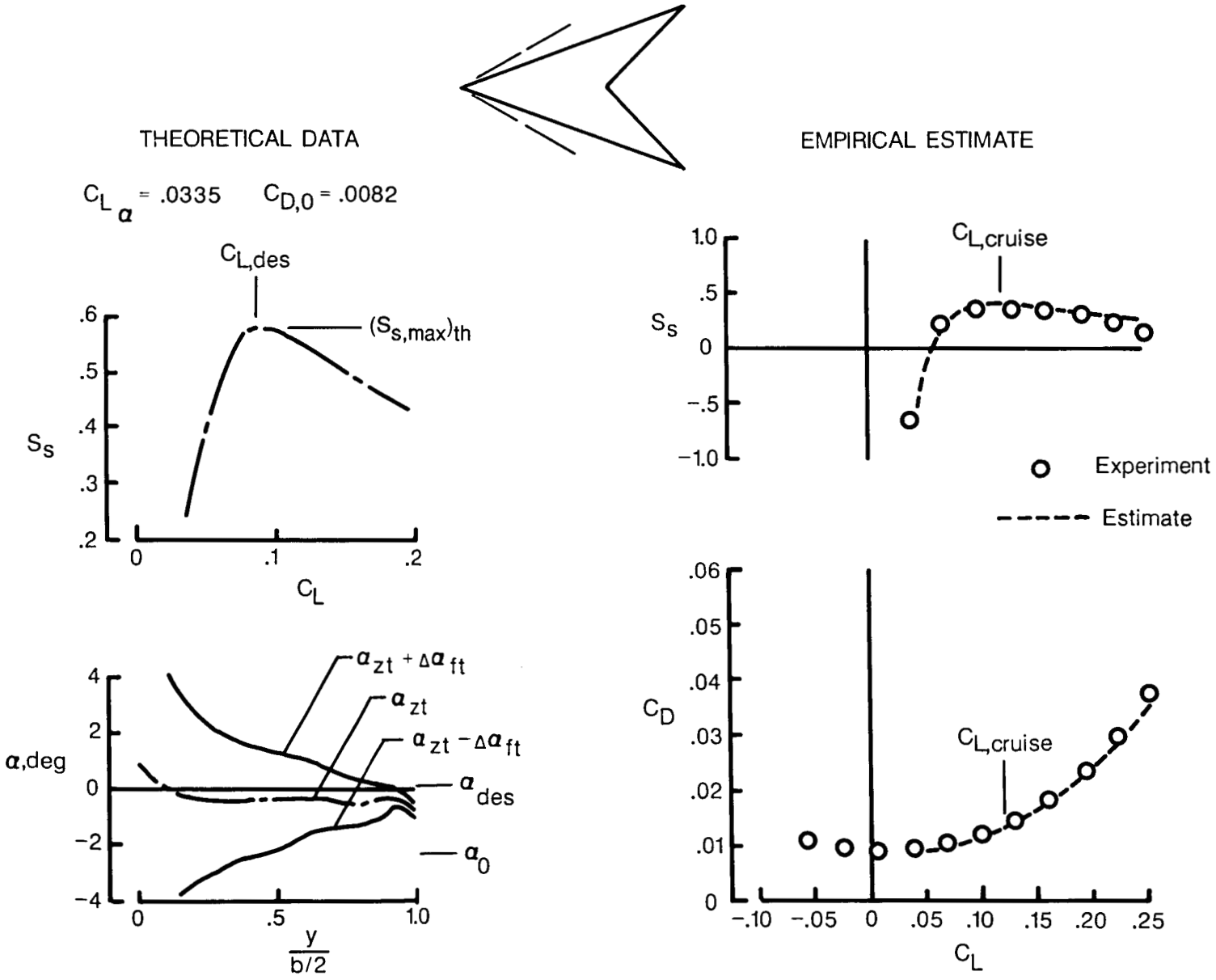

(a) 70° swept arrow wing designed for $C_L = 0.08$ at $M = 2.00$; $M = 2.05$; $R = 4.4 \times 10^6$.

Figure 29. Examples of application of empirical method used to select optimum design lift coefficients and to predict achievable suction parameters.

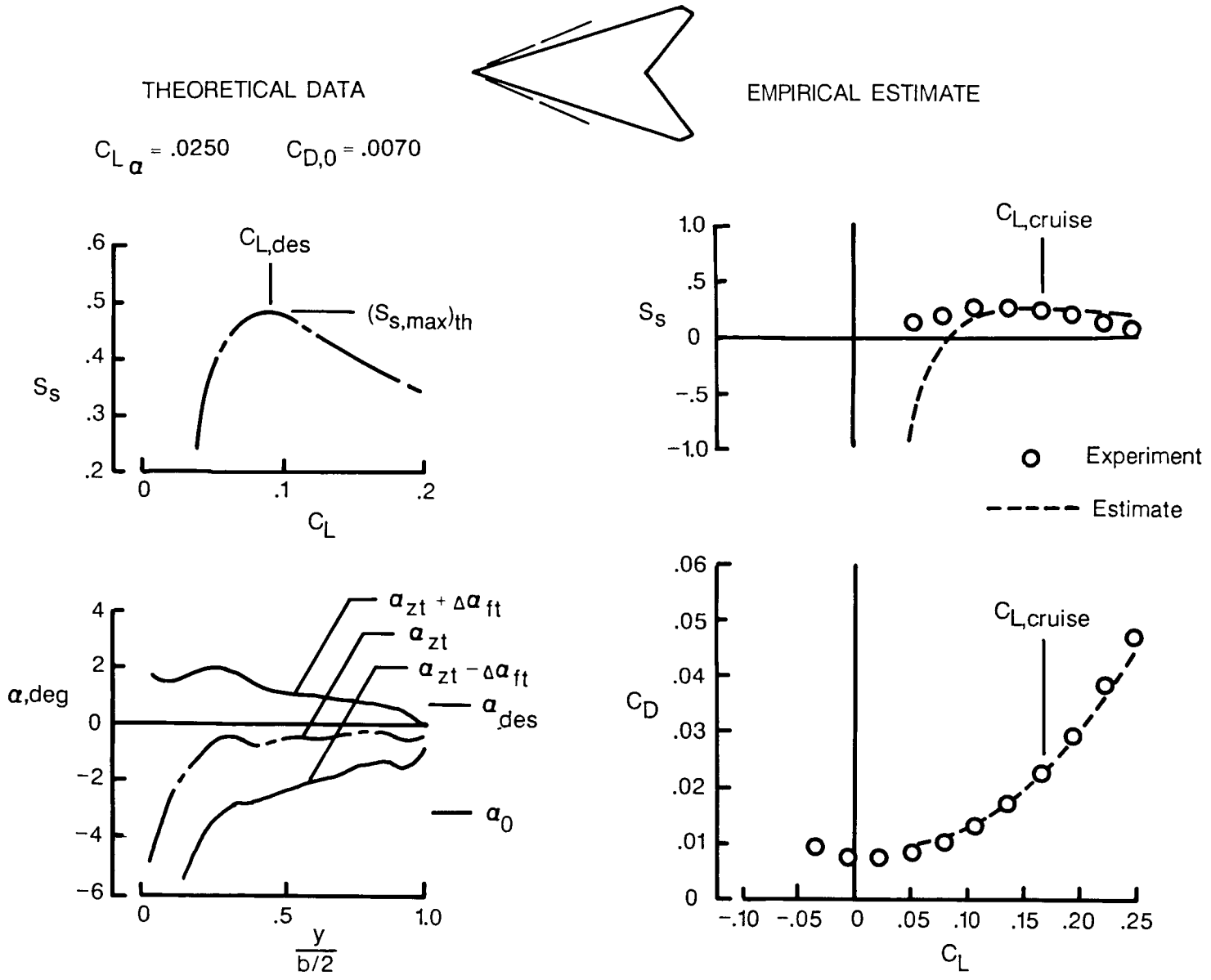

(b) 72.65° swept modified arrow wing designed for $C_L = 0.08$ at $M = 2.60$; $M = 2.60$; $R = 5.1 \times 10^6$.

Figure 29. Continued.

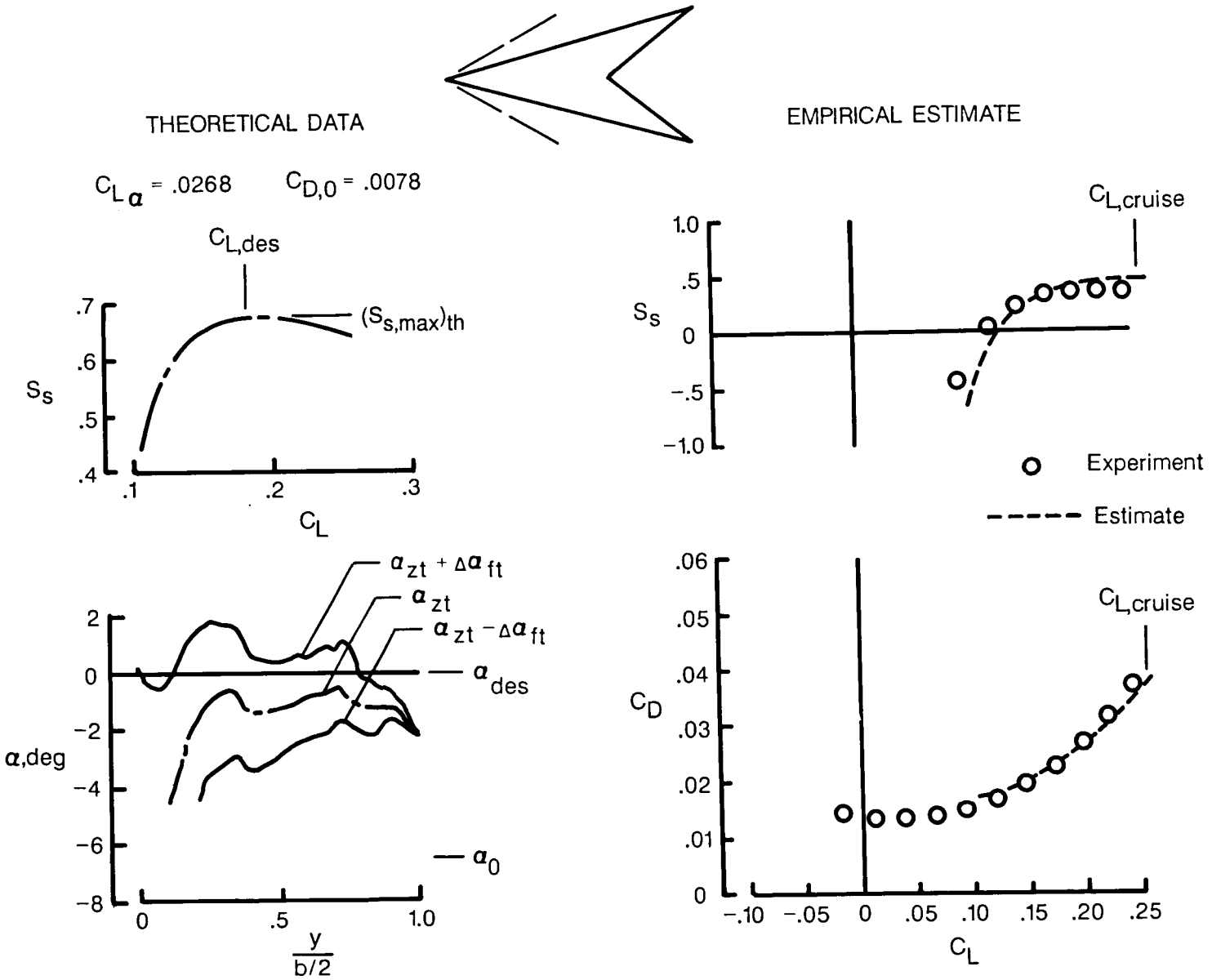

(c) 75° swept arrow wing designed for $C_L = 0.16$ at $M = 2.00$; $M = 2.05$; $R = 4.4 \times 10^6$.

Figure 29. Continued.

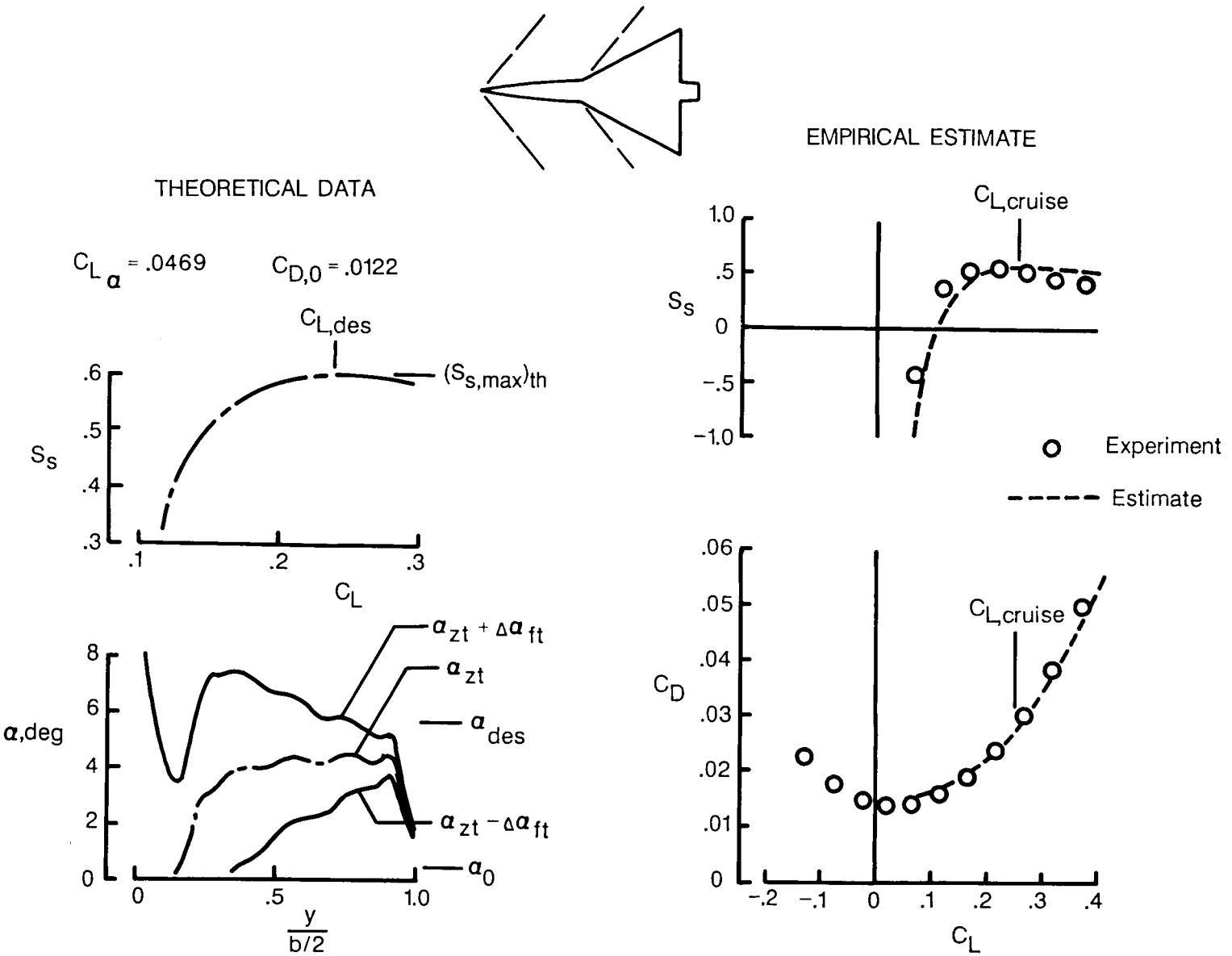

(d) 3-percent-thick aspect ratio 2 wing–body combination designed for $C_L = 0.215$ at $M = 1.00$; $M = 1.30$; $R = 5.6 \times 10^6$.

Figure 29. Continued.

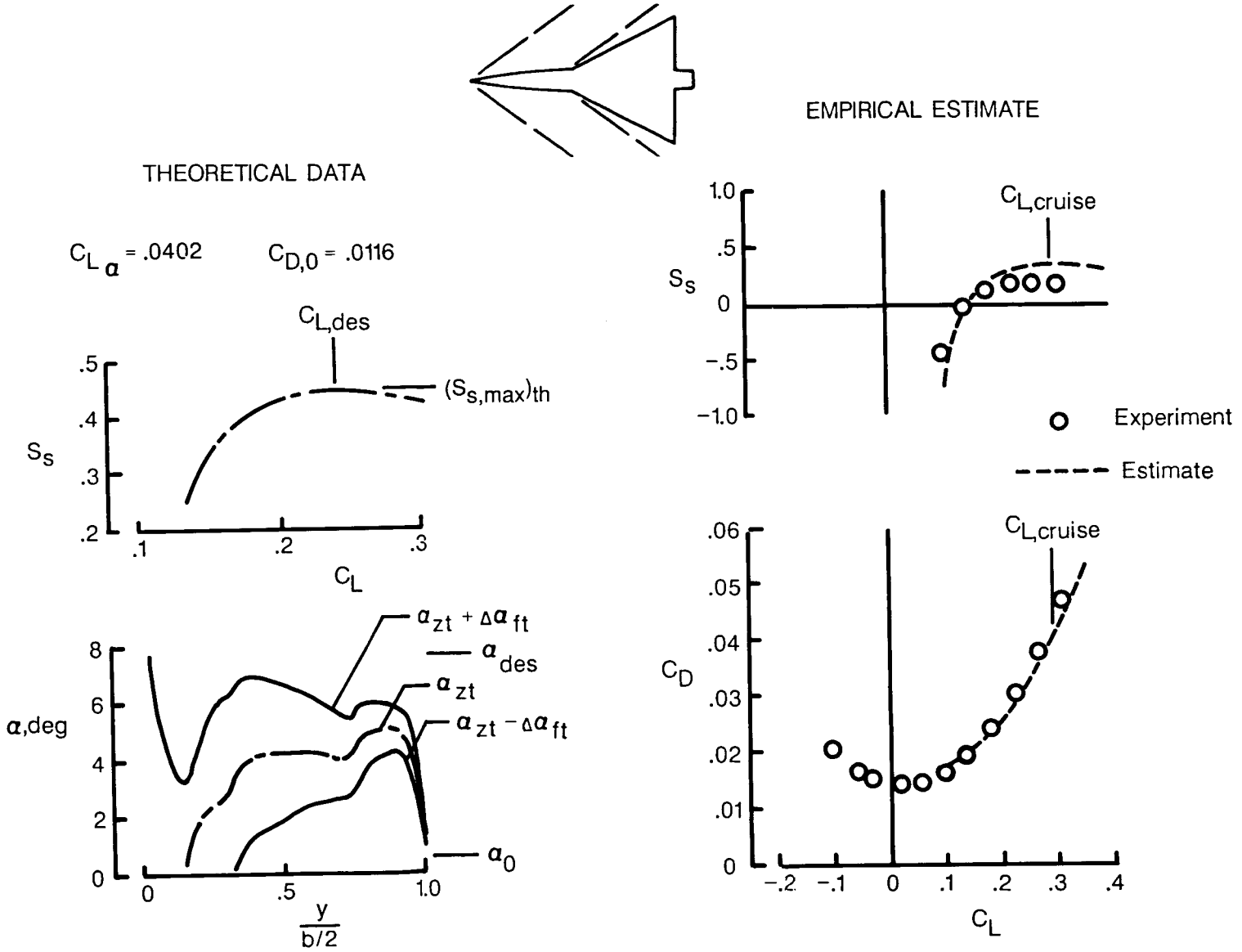

(e) 3-percent-thick aspect ratio 2 wing-body combination designed for $C_L = 0.215$ at $M = 1.00$; $M = 1.70$; $R = 5.6 \times 10^6$.

Figure 29. Continued.

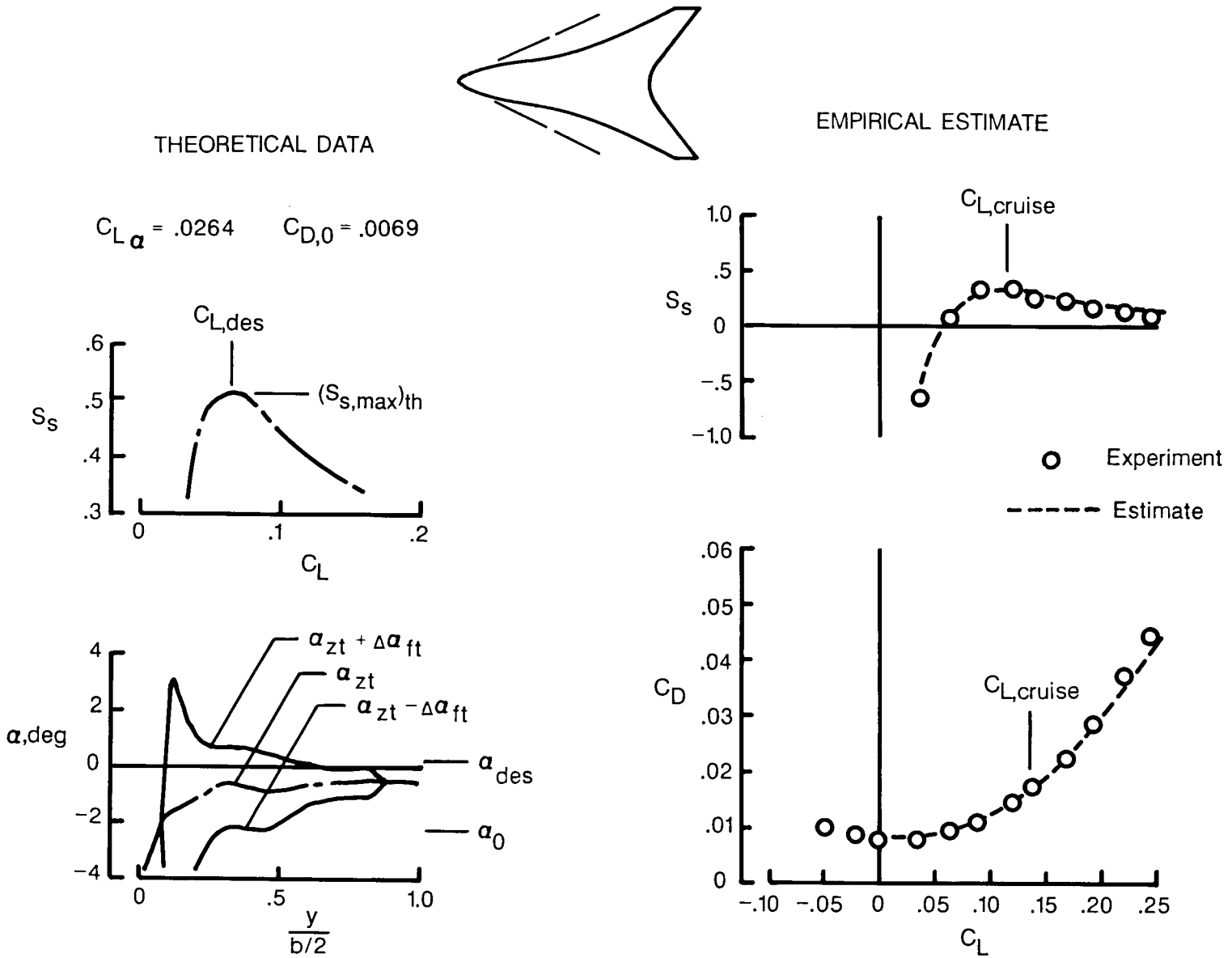

(f) Arbitrary planform wing–body combination designed for $C_L = 0.08$ at $M = 2.40$; $M = 2.40$; $R = 3.4 \times 10^6$; no constraint.

Figure 29. Continued.

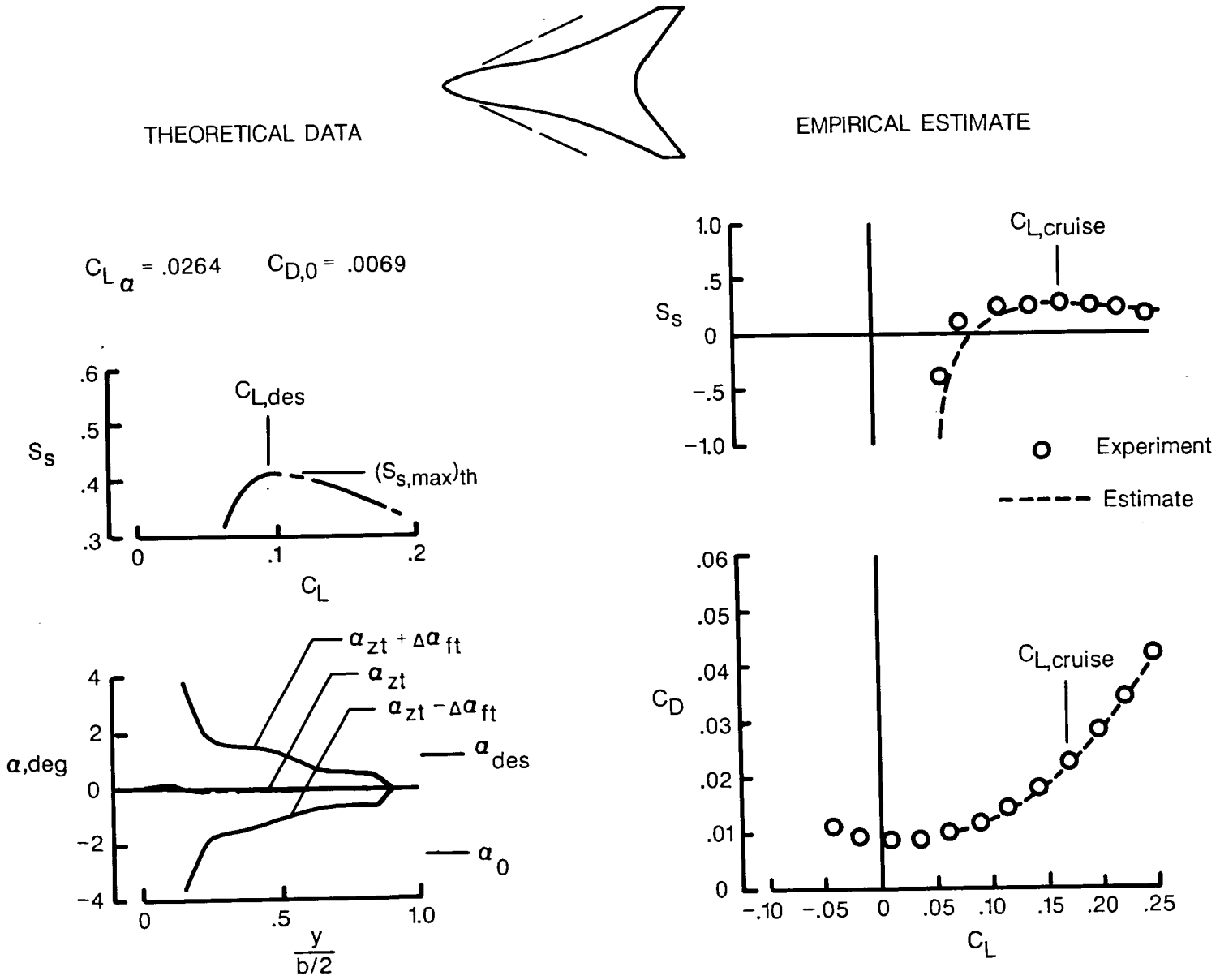

(g) Arbitrary planform wing–body combination designed for $C_L = 0.08$ at $M = 2.40$; $M = 2.40$; $R = 3.4 \times 10^6$; severe constraint.

Figure 29. Continued.

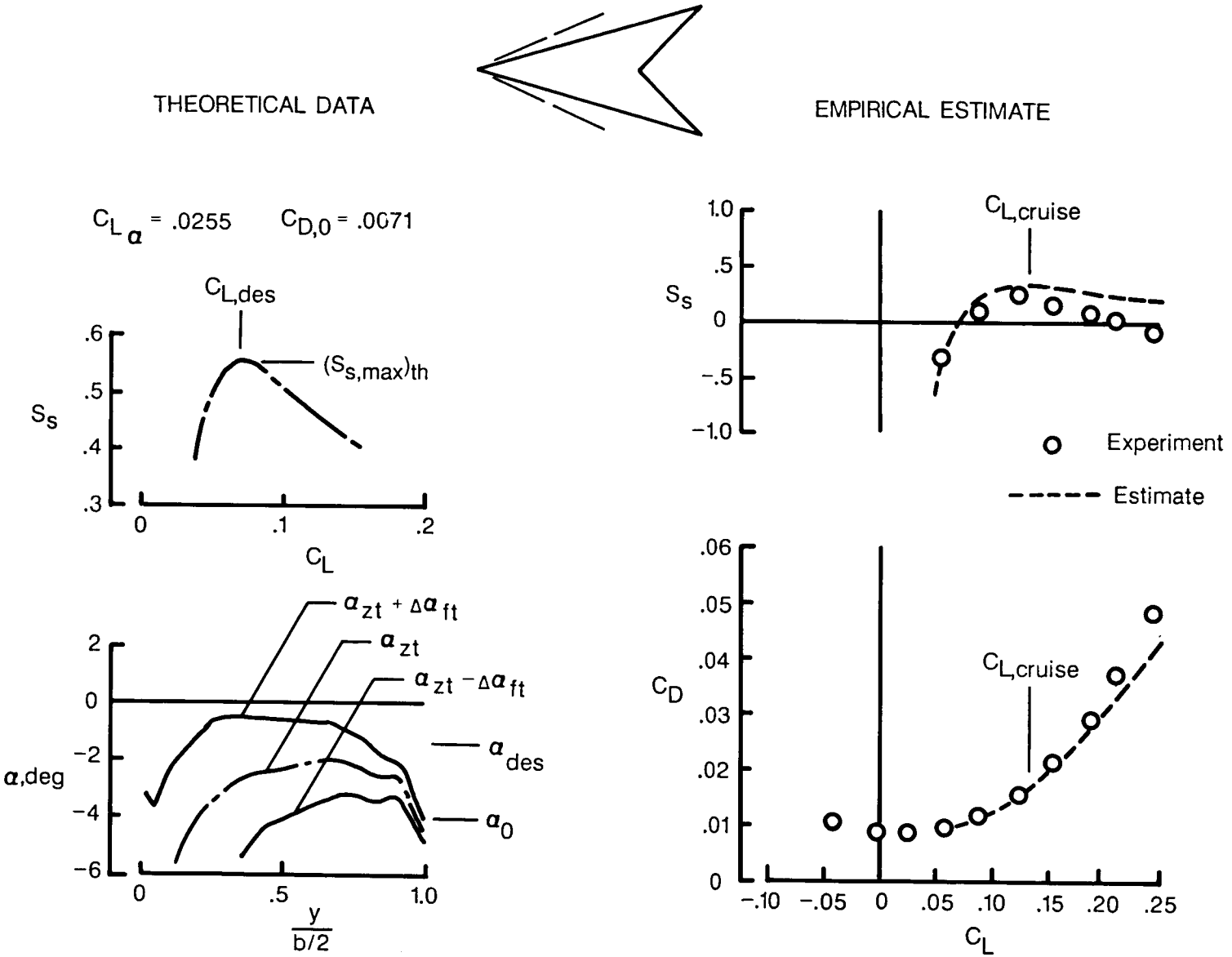

(h) 74° swept arrow wing–body combination designed for $C_L = 0.10$ at $M = 2.50$; $M = 2.50$; $R = 5.0 \times 10^6$.

Figure 29. Continued.

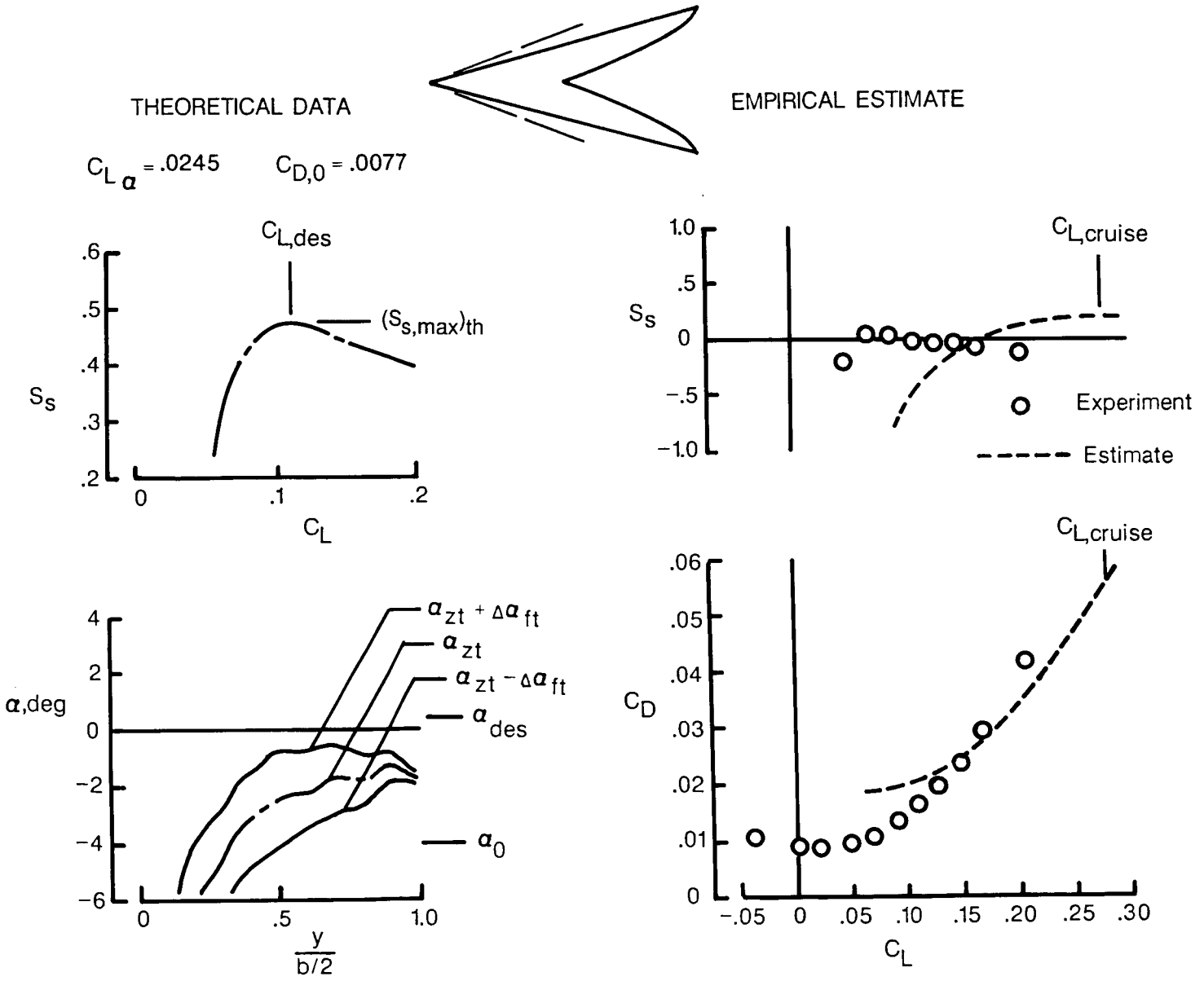

(i) 75° swept modified arrow wing–body combination designed for $C_L = 0.10$ at $M = 3.00$; $M = 2.87$; $R = 4.2 \times 10^6$.

Figure 29. Continued.

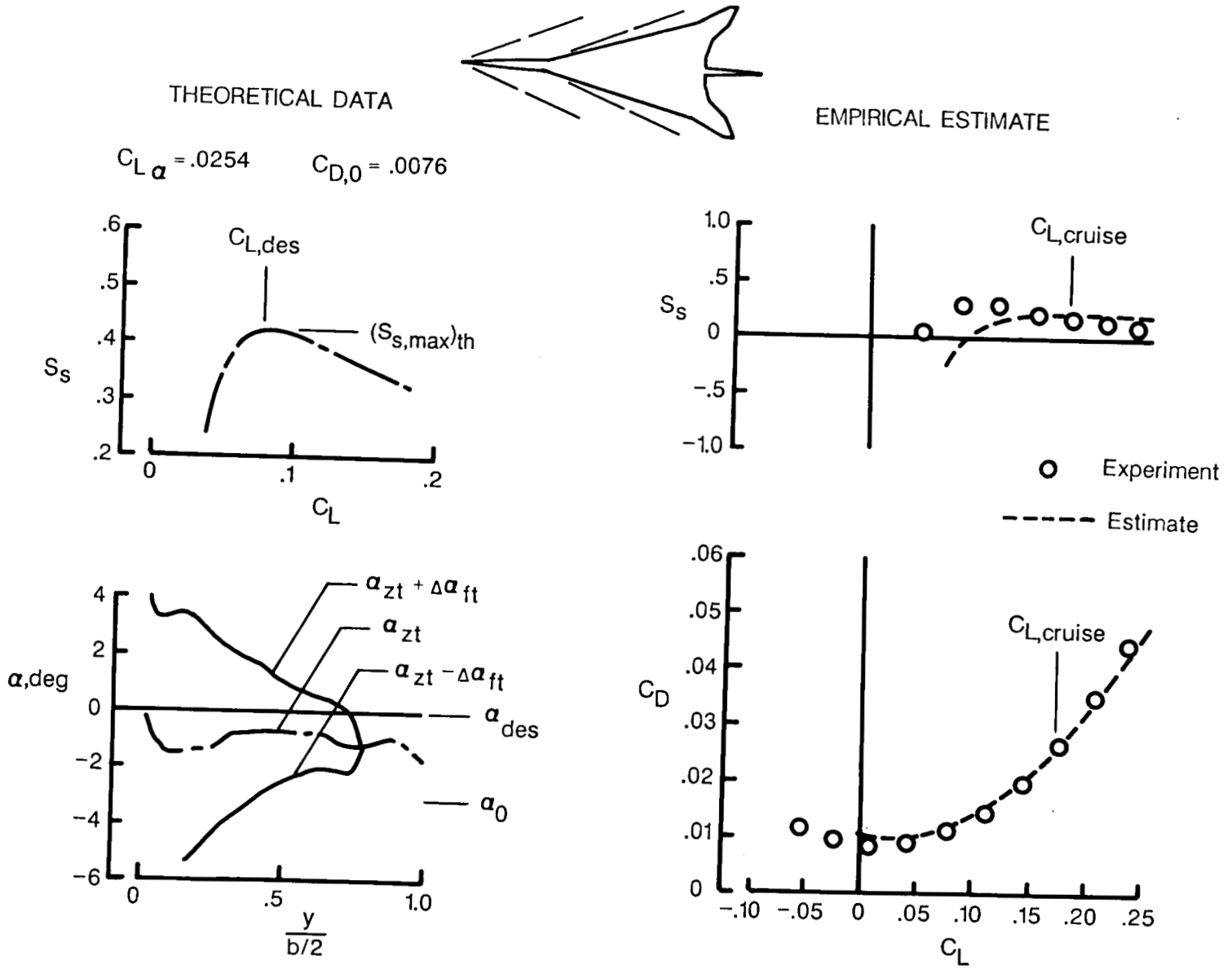

(j) Supersonic transport wing–body combination designed for $C_L = 0.08$ at $M = 2.70$; $M = 2.70$; $R = 3.2 \times 10^6$.

Figure 29. Continued.

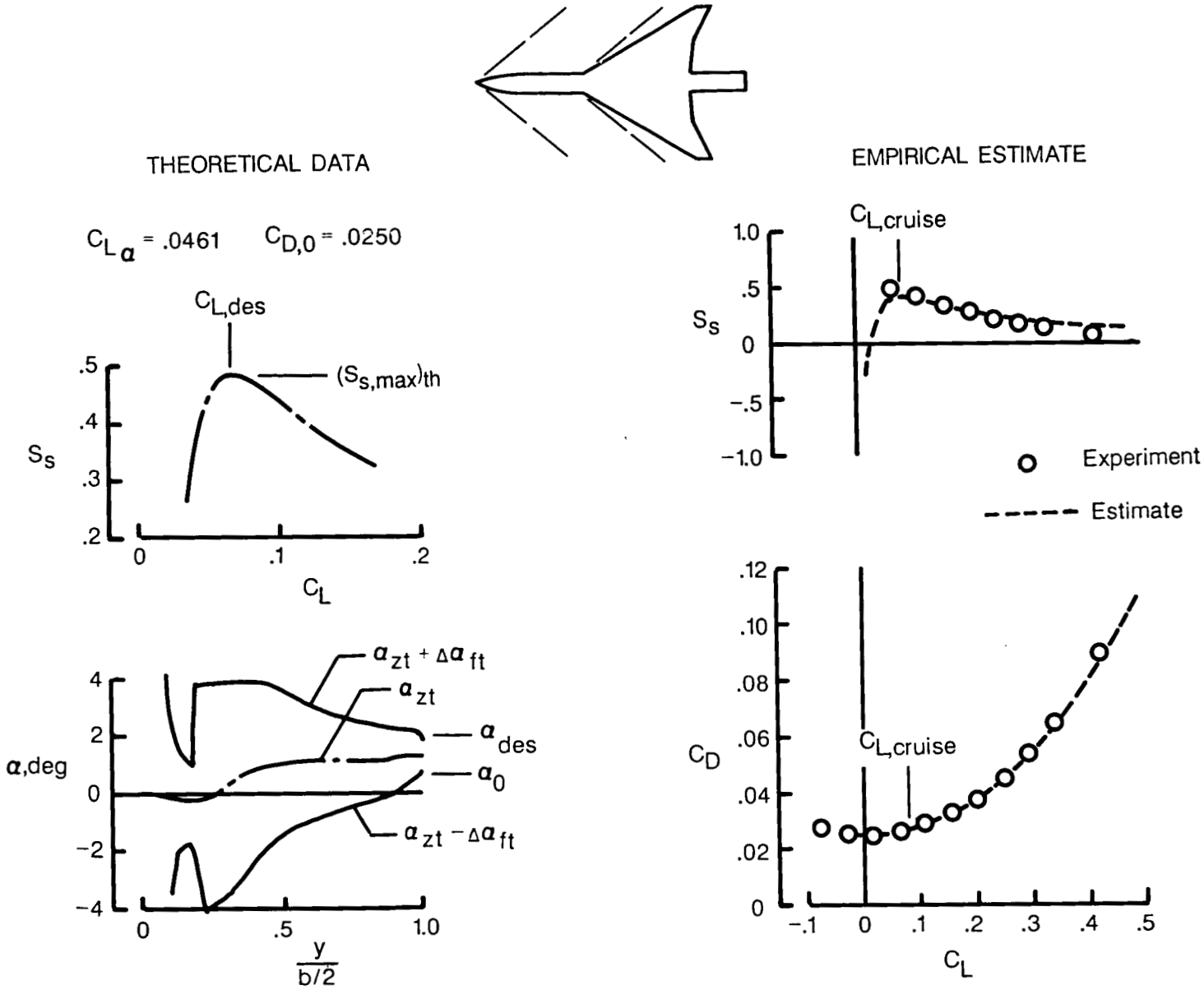

(k) 60° swept wing–body combination designed for $C_L = 0.05$ at $M = 1.80$; $M = 1.60$; $R = 1.7 \times 10^6$; cruise design.

Figure 29. Continued.

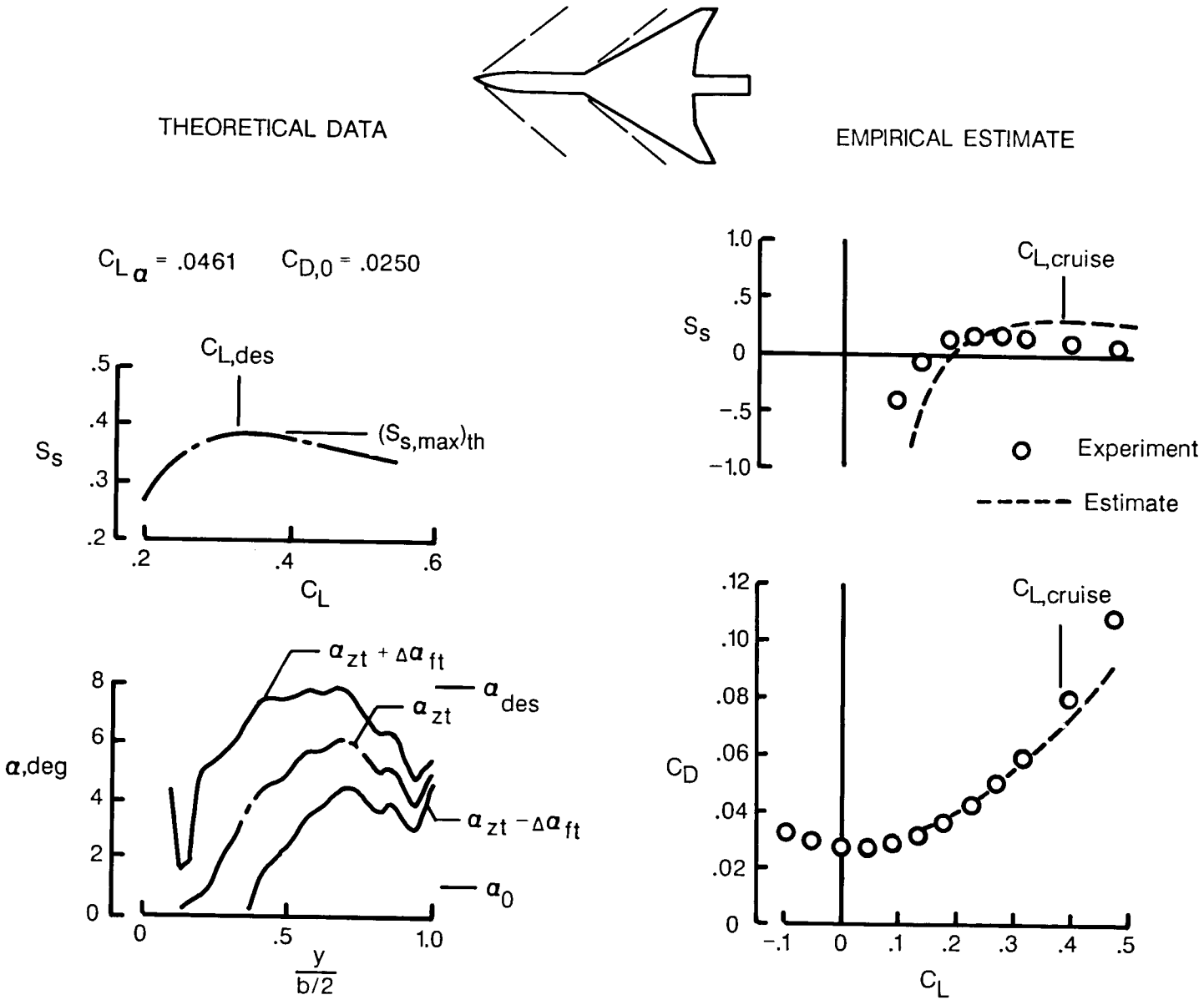

(l) 60° swept wing–body combination designed for $C_L = 0.30$ at $M = 1.60$; $M = 1.60$; $R = 1.7 \times 10^6$; maneuver design.

Figure 29. Concluded.

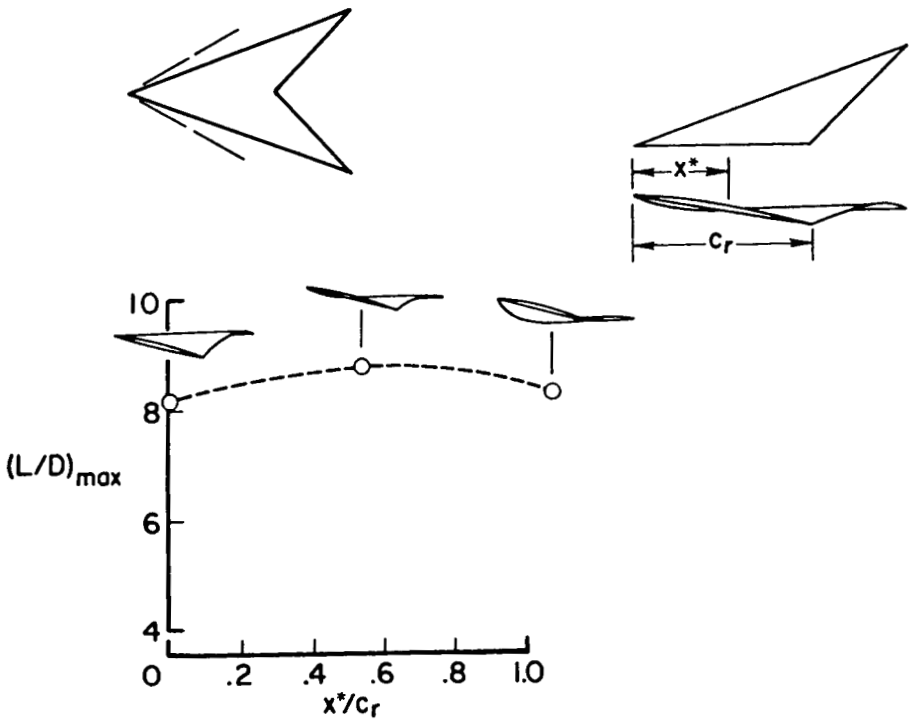

Figure 30. Illustration of the effect of wing shear. $M = 2.03$.

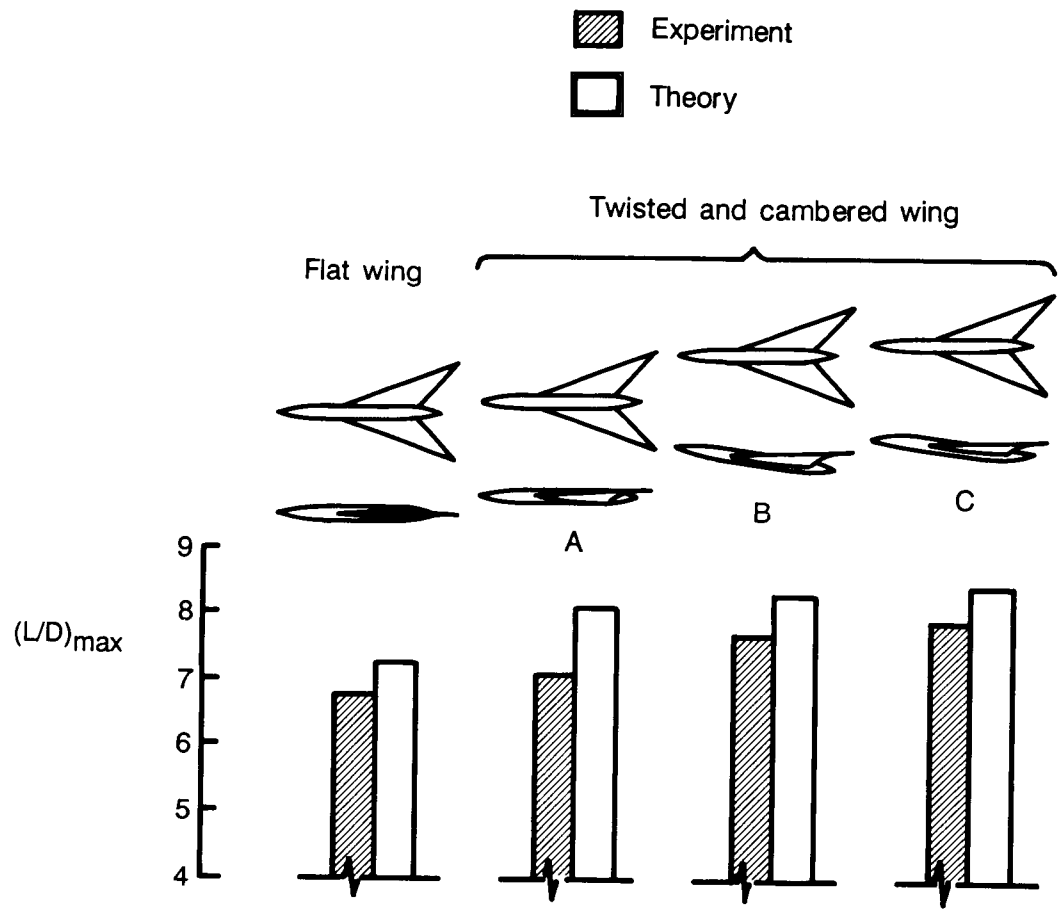

Figure 31. Illustration of the effect of fuselage alignment. $M = 2.02$.

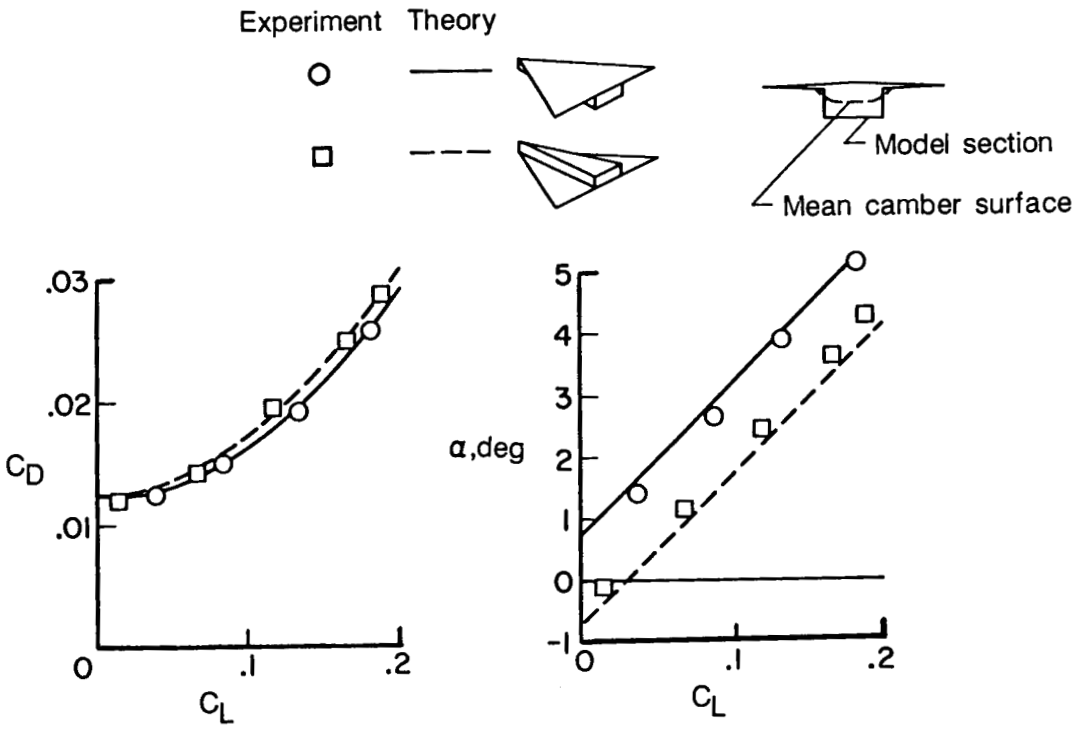

Figure 32. Illustration of mean camber surface analysis. $M = 2.00$.

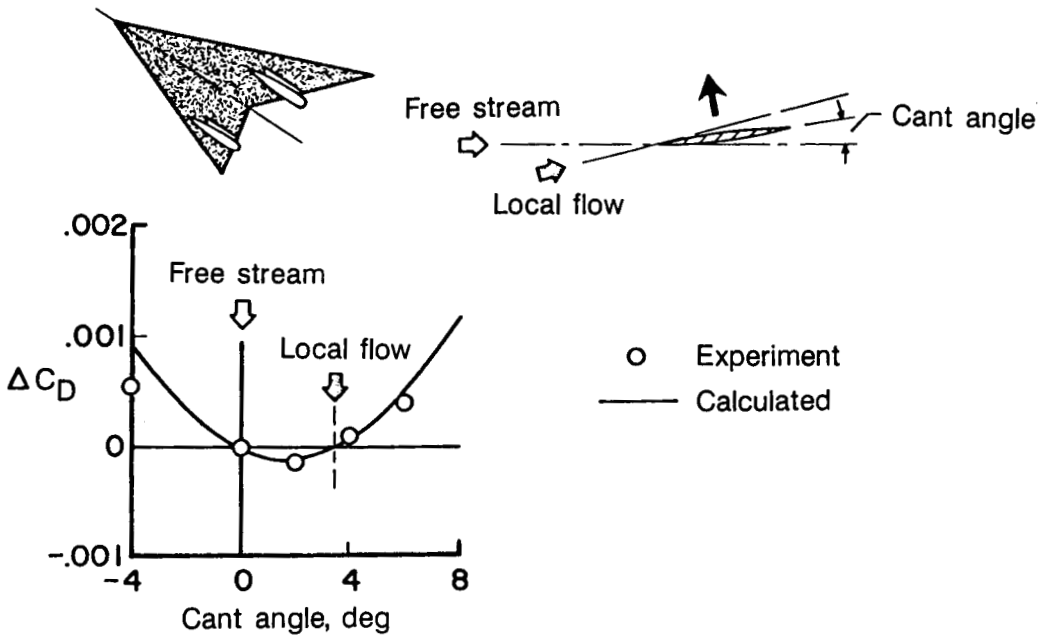

Figure 33. Illustration of the effect of nacelle alignment. $M = 2.03$; $C_L = 0.16$.

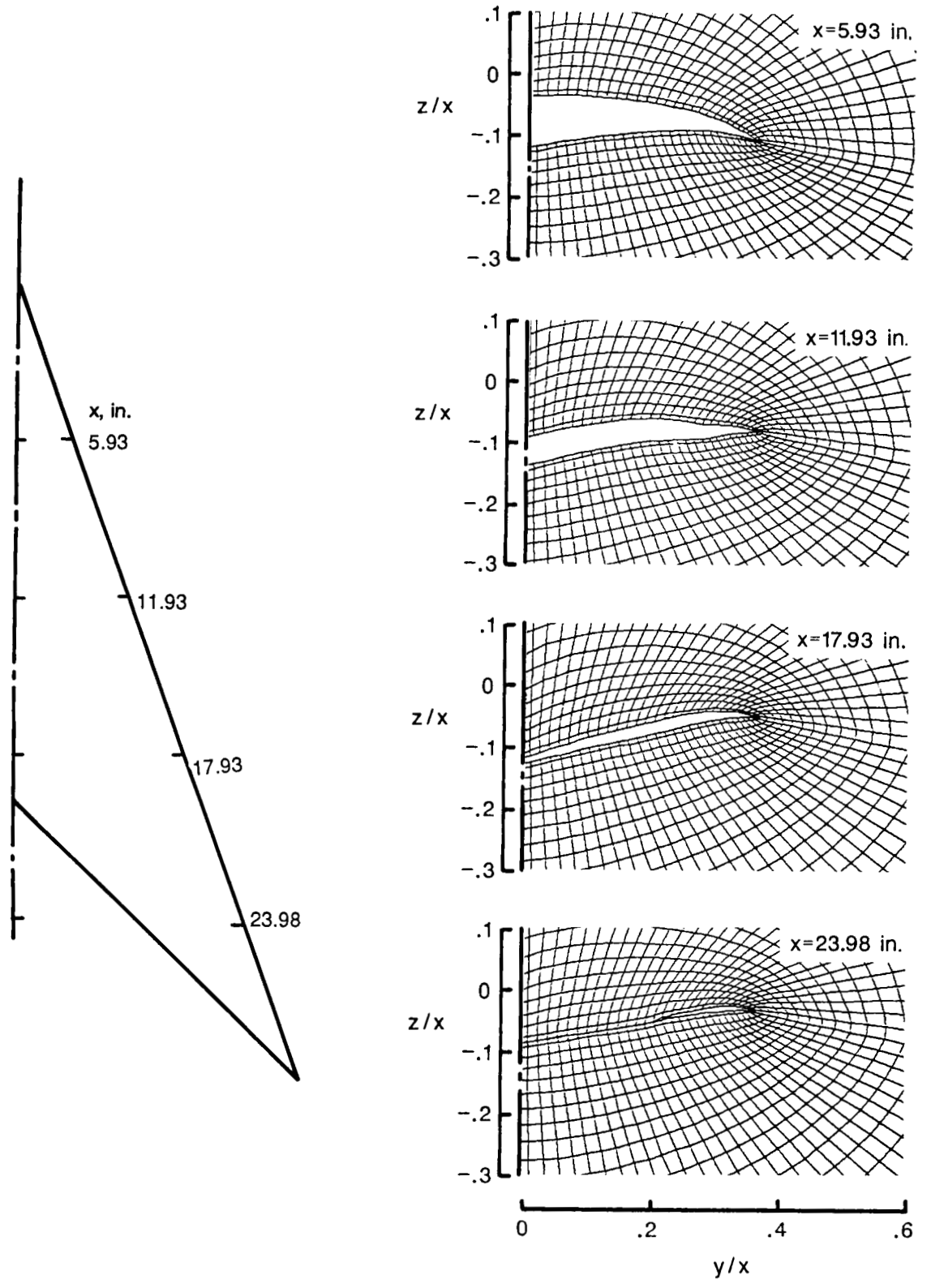

Figure 34. Sample of grid system employed in Euler code solution of 70° swept arrow wing with $C_{L,\text{des}} = 0.16$. $M = 2.05$; $\alpha = 0°$.

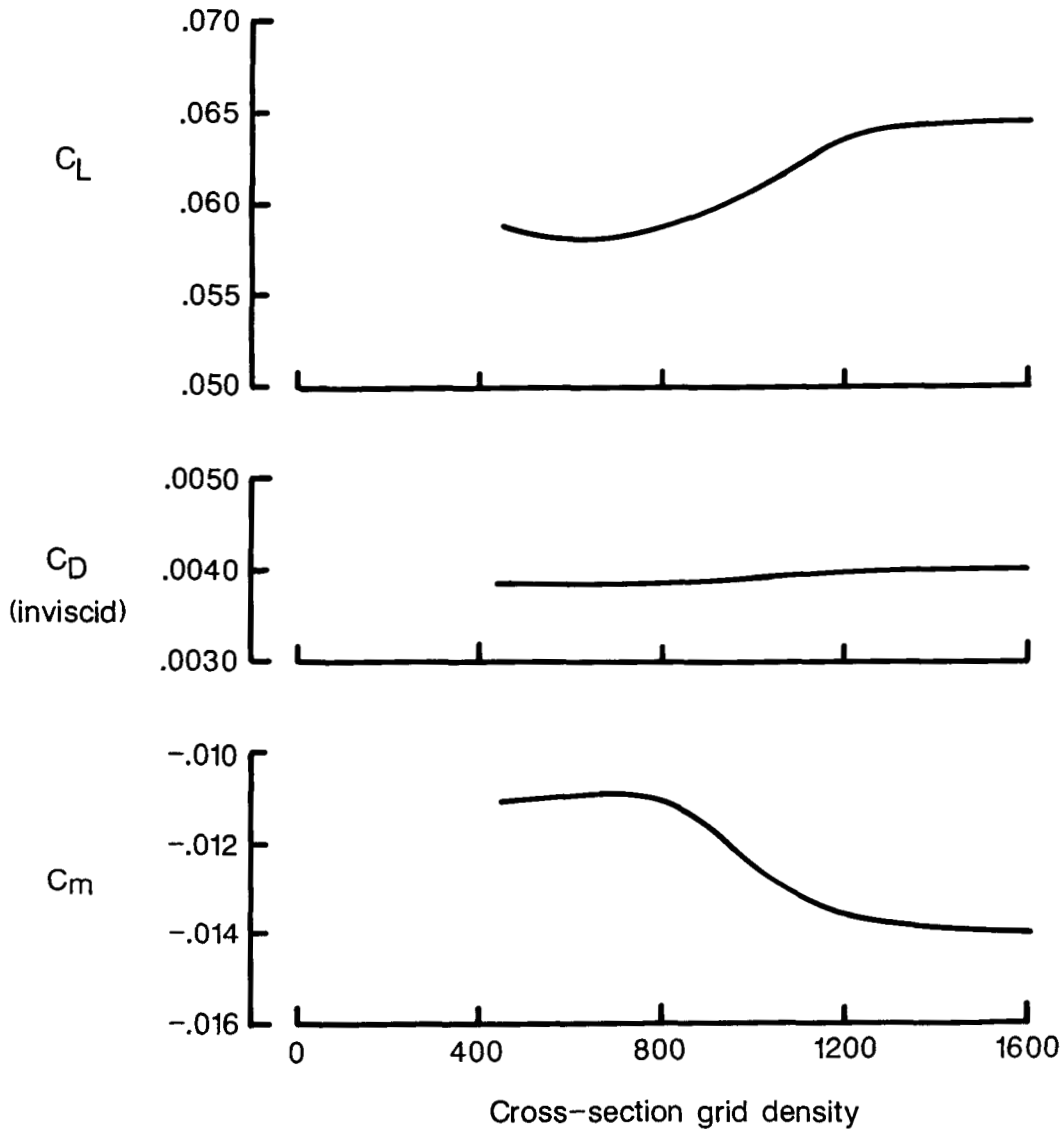

Figure 35. Lift, drag, and pitching-moment coefficients as function of cross-section grid density for Euler code. 70° swept arrow wing; $C_{L,\text{des}} = 0.08$; $M = 2.05$; $\alpha = 0°$.

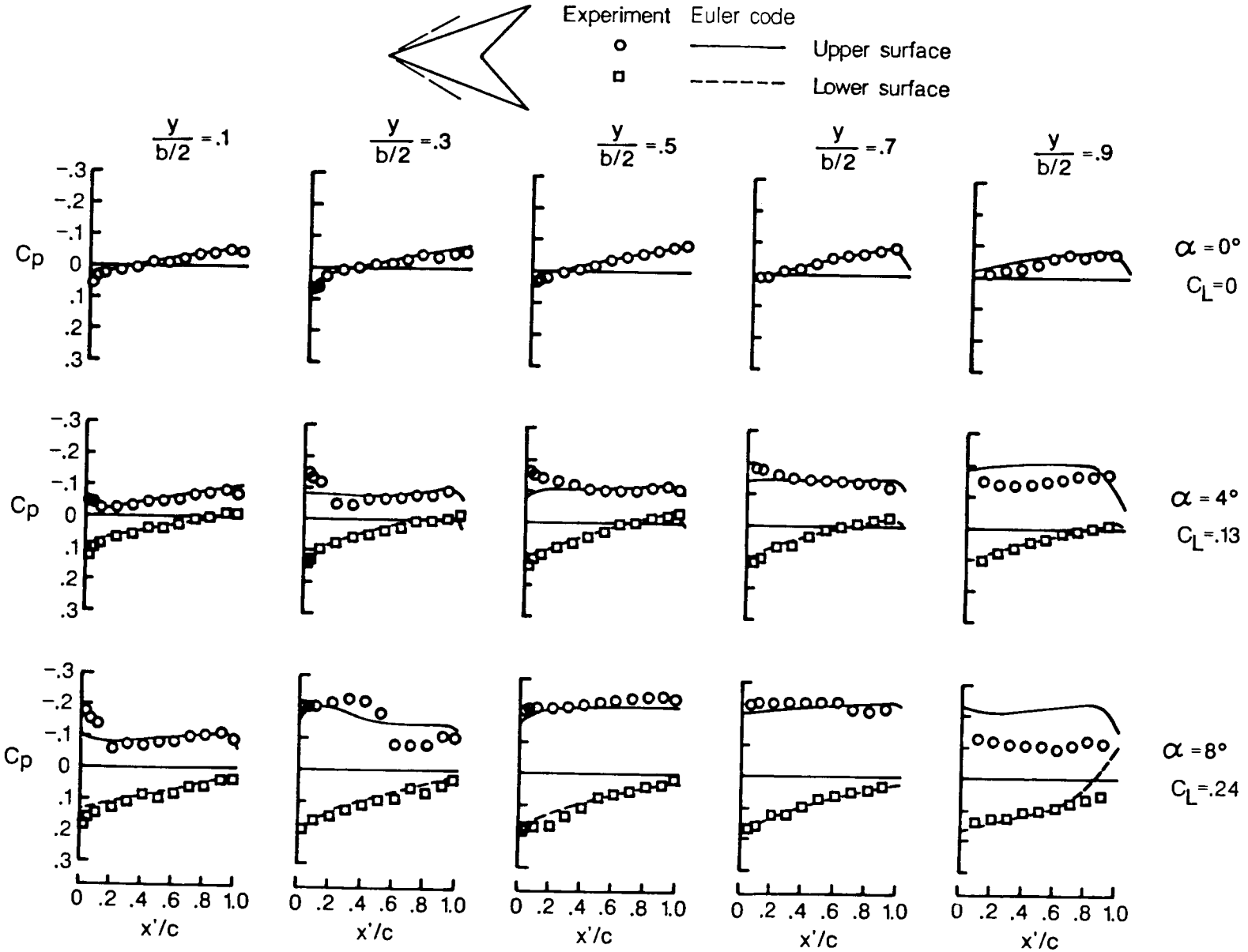

(a) $C_{L,\text{des}} = 0$.

Figure 36. Experimental and Euler code pressure distributions for 70° swept arrow wing. $M = 2.05$; $R = 4.4 \times 10^6$.

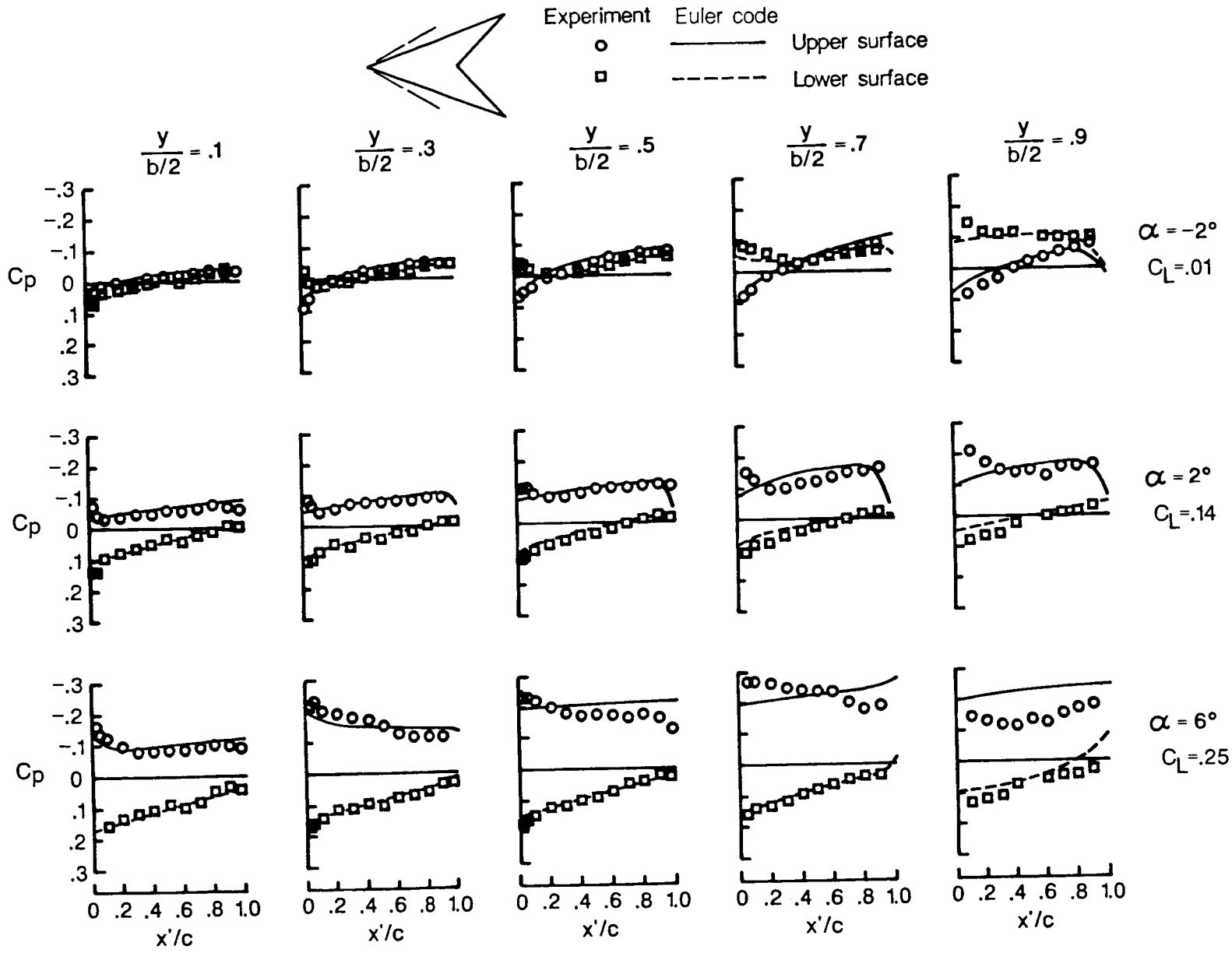

(b) $C_{L,\text{des}} = 0.08$.

Figure 36. Continued.

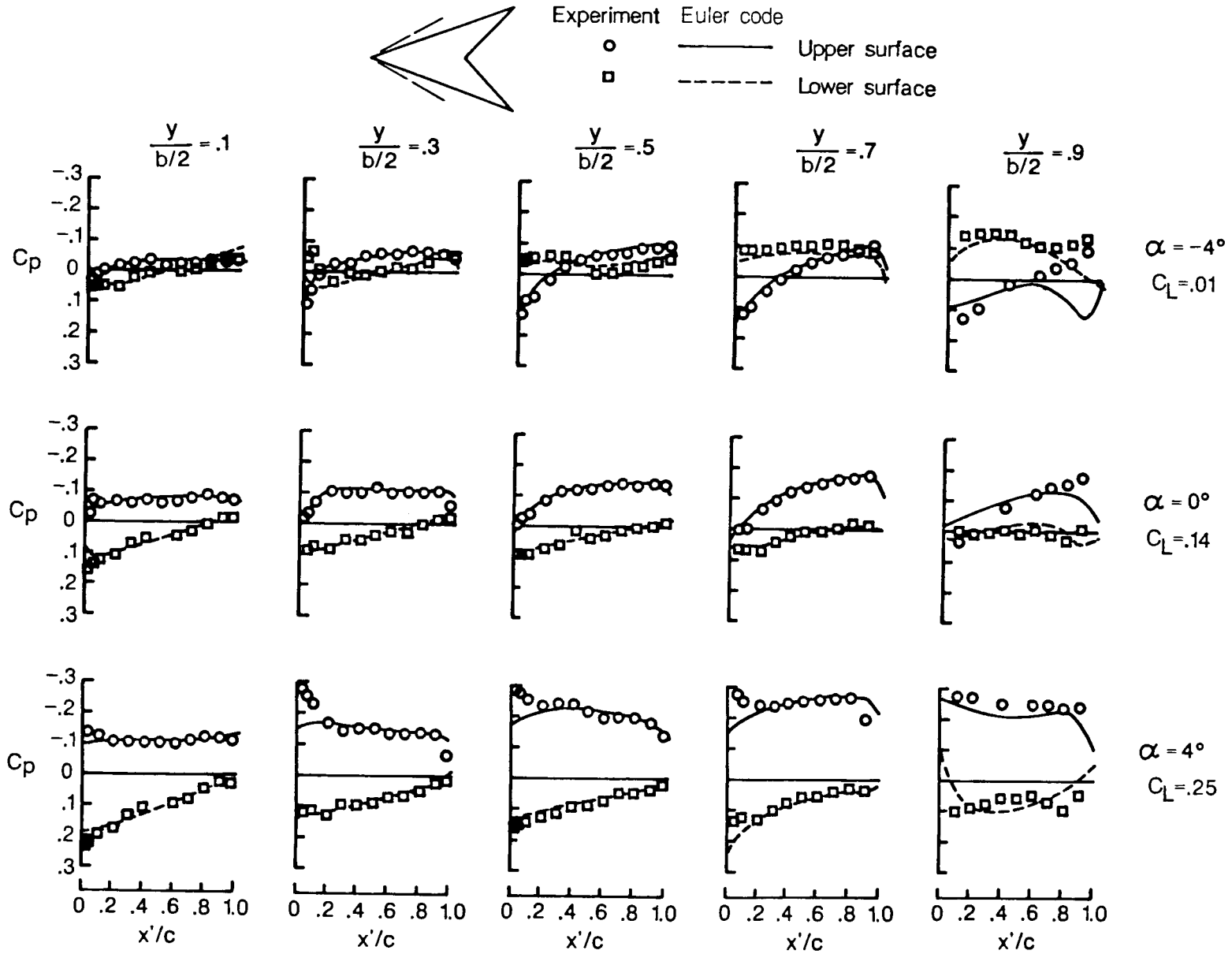

(c) $C_{L,\mathrm{des}} = 0.16$.

Figure 36. Concluded.

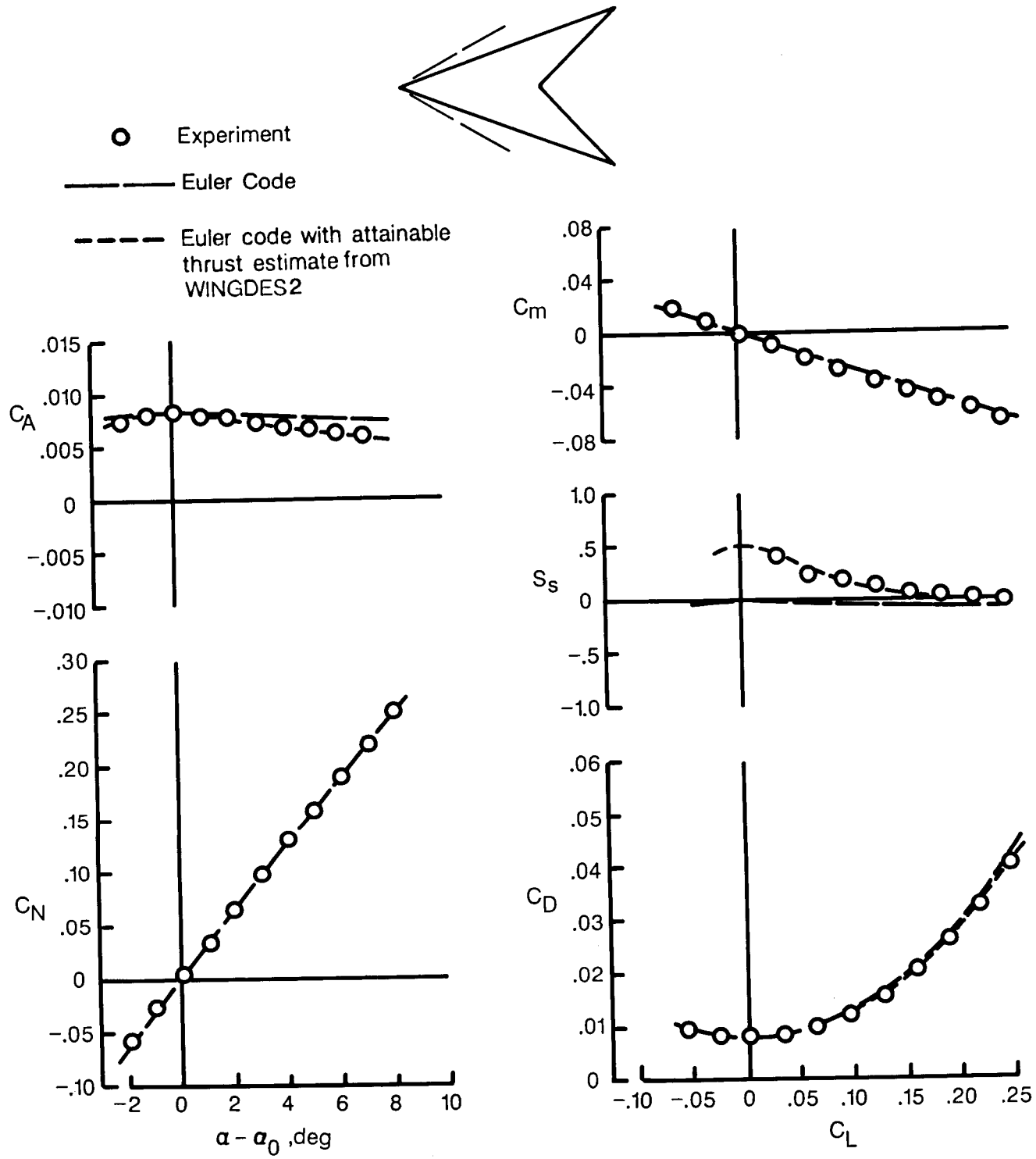

(a) $C_{L,\text{des}} = 0$.

Figure 37. Experimental and Euler code force results. 70° swept arrow wing; $M = 2.05$; $R = 4.4 \times 10^6$.

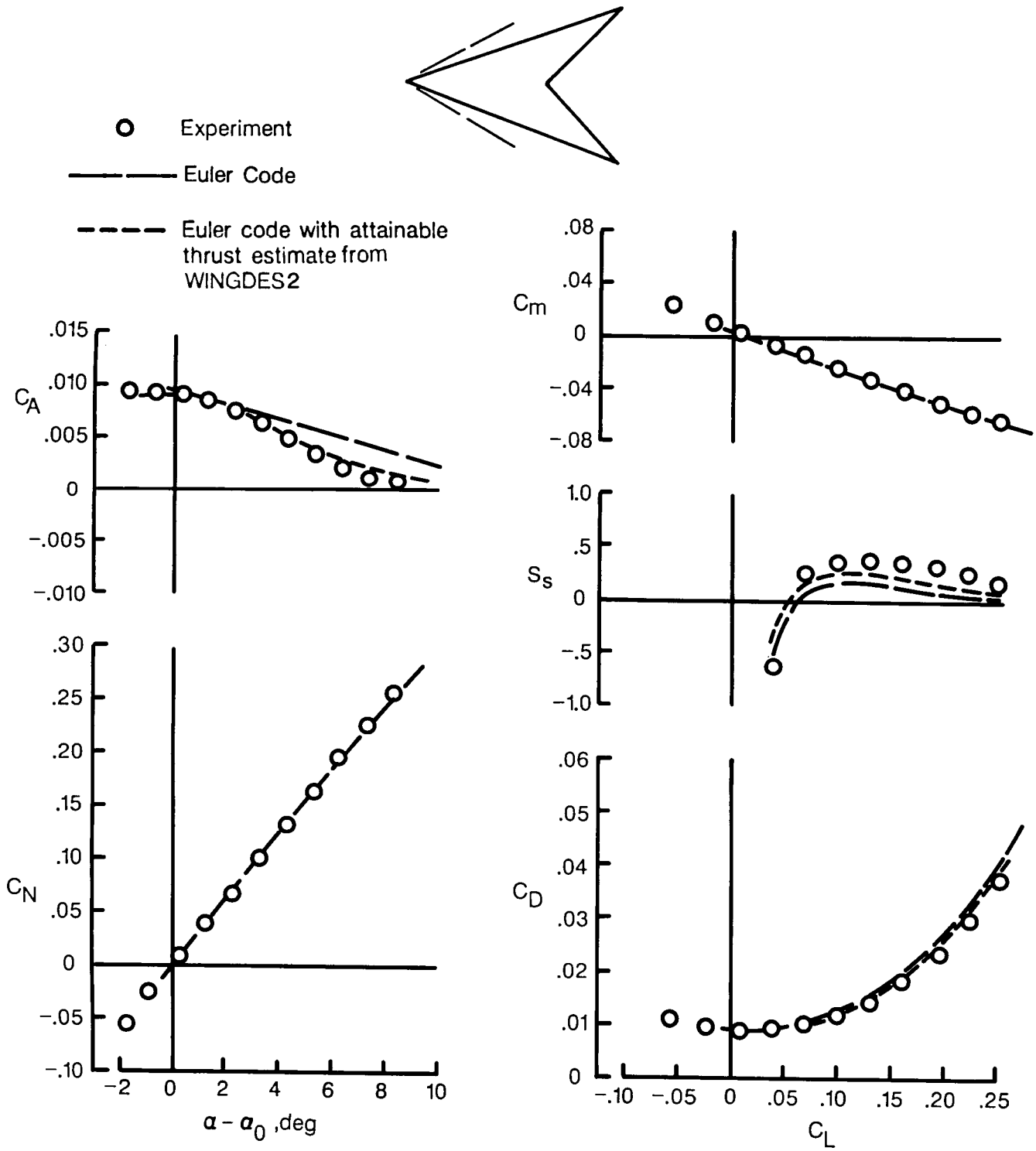

(b) $C_{L,\mathrm{des}} = 0.08$.

Figure 37. Continued.

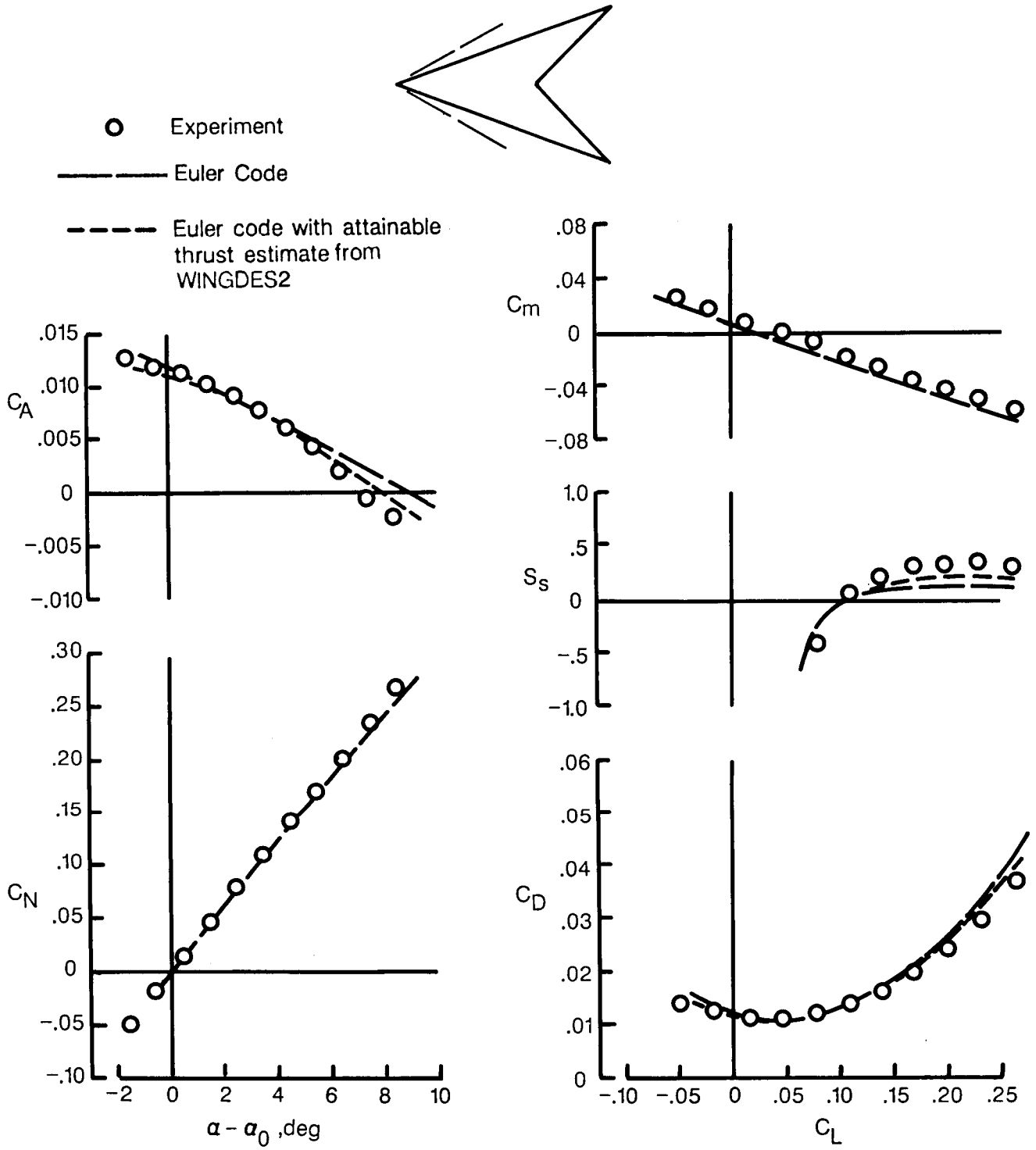

(c) $C_{L,\mathrm{des}} = 0.16$.

Figure 37. Concluded.

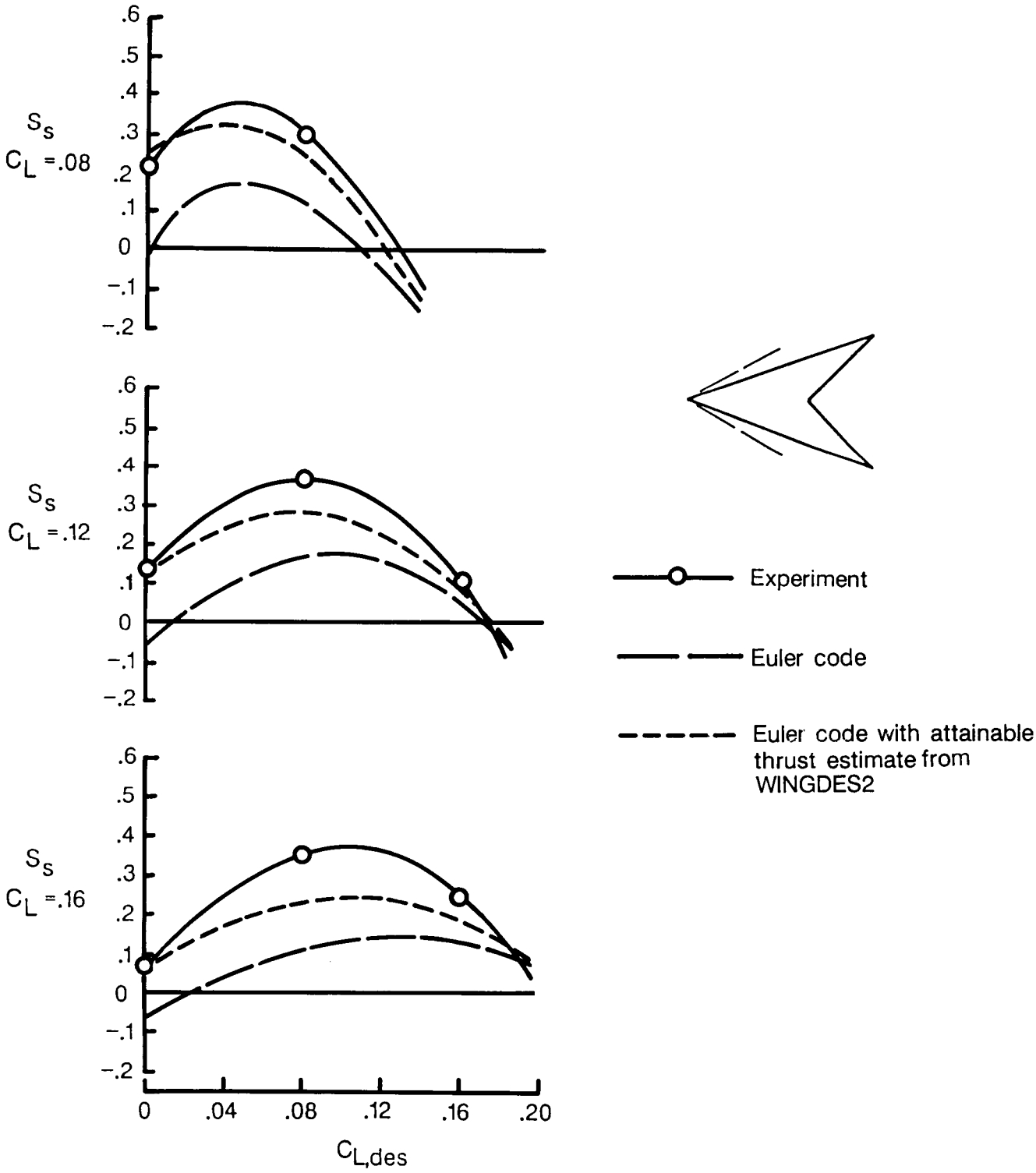

Figure 38. Euler code prediction of variation of suction parameter with design lift coefficient. 70° swept arrow wing; $M = 2.05$; $R = 4.4 \times 10^6$.

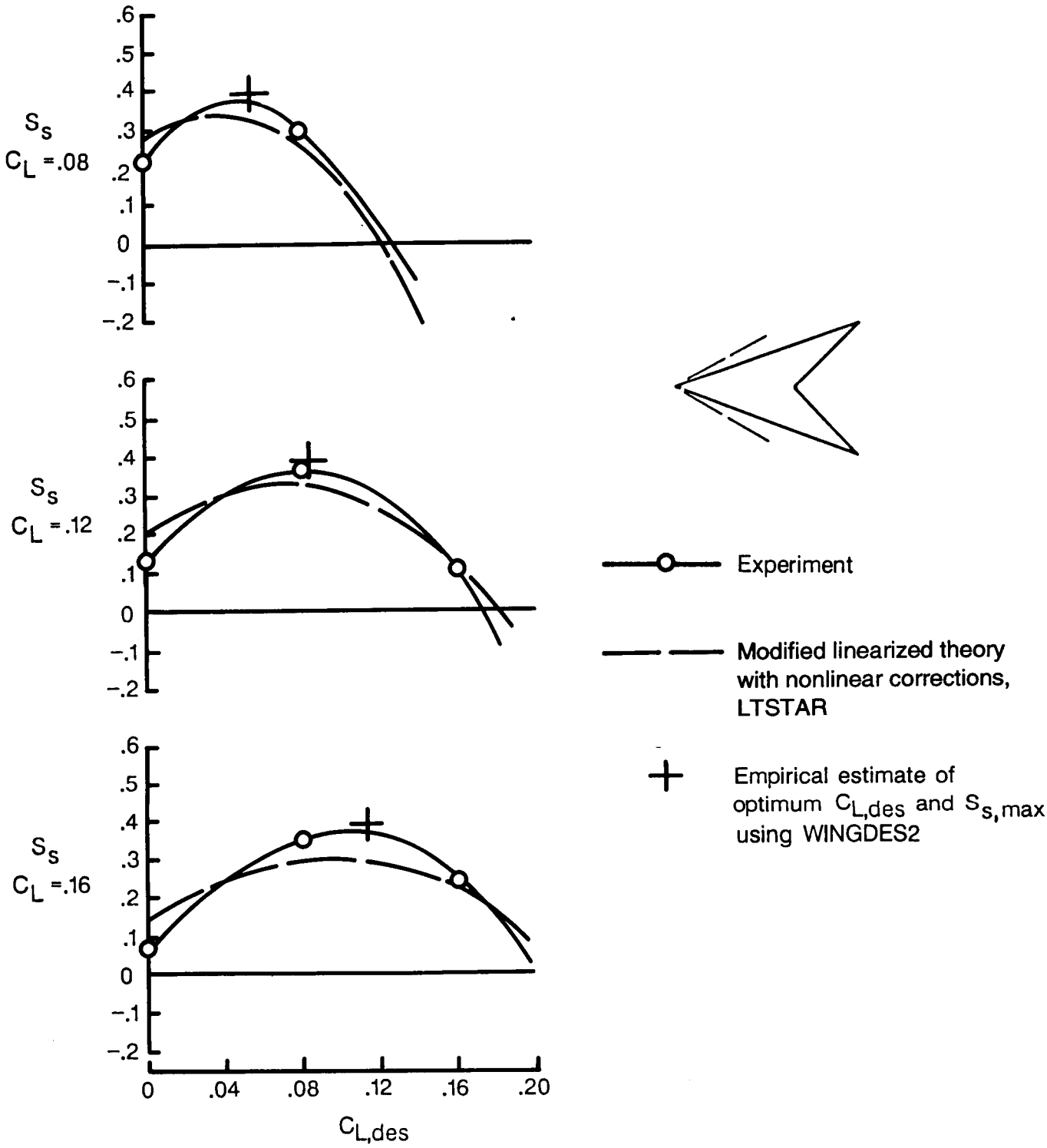

Figure 39. Corrected linearized theory prediction of variation of suction parameter with design lift coefficient. 70° swept arrow wing; $M = 2.05$; $R = 4.4 \times 10^6$.

REPORT DOCUMENTATION PAGE

Form Approved
OMB No. 0704-0188

1. AGENCY USE ONLY *(Leave blank)*	2. REPORT DATE	3. REPORT TYPE AND DATES COVERED
	September 1992	Technical Paper

4. TITLE AND SUBTITLE
Survey and Analysis of Research on Supersonic Drag-Due-to-Lift Minimization With Recommendations for Wing Design

5. FUNDING NUMBERS
WU 505-68-70-02

6. AUTHOR(S)
Harry W. Carlson and Michael J. Mann

7. PERFORMING ORGANIZATION NAME(S) AND ADDRESS(ES)
NASA Langley Research Center
Hampton, VA 23681-0001

8. PERFORMING ORGANIZATION REPORT NUMBER
L-16963

9. SPONSORING/MONITORING AGENCY NAME(S) AND ADDRESS(ES)
National Aeronautics and Space Administration
Washington, DC 20546-0001

10. SPONSORING/MONITORING AGENCY REPORT NUMBER
NASA TP-3202

11. SUPPLEMENTARY NOTES
Carlson: Lockheed Engineering & Sciences Co., Hampton, VA; Mann: Langley Research Center, Hampton, VA.

12a. DISTRIBUTION/AVAILABILITY STATEMENT
Unclassified–Unlimited

Subject Category 02

12b. DISTRIBUTION CODE

13. ABSTRACT *(Maximum 200 words)*

A survey of research on drag-due-to-lift minimization at supersonic speeds, including a study of the effectiveness of current design and analysis methods, has been conducted. The results show that a linearized theory analysis with estimated attainable thrust and vortex force effects can predict with reasonable accuracy the lifting efficiency of flat wings. Significantly better wing performance can be achieved through the use of twist and camber. Although linearized theory methods tend to overestimate the amount of twist and camber required for a given application and provide an overly optimistic performance prediction, these deficiencies can be overcome by implementation of recently developed empirical corrections. Numerous examples of the correlation of experiment and theory are presented to demonstrate the applicability and limitations of linearized theory methods with and without empirical corrections. The use of an Euler code for the estimation of aerodynamic characteristics of a twisted and cambered wing and its application to design by iteration are discussed.

14. SUBJECT TERMS	15. NUMBER OF PAGES
Supersonic drag due to lift; Supersonic wing design	156
	16. PRICE CODE A08

17. SECURITY CLASSIFICATION OF REPORT	18. SECURITY CLASSIFICATION OF THIS PAGE	19. SECURITY CLASSIFICATION OF ABSTRACT	20. LIMITATION OF ABSTRACT
Unclassified	Unclassified		

NSN 7540-01-280-5500

★U.S. GOVERNMENT PRINTING OFFICE: 1992-627-064/66002

Standard Form 298(Rev. 2-89)
Prescribed by ANSI Std. Z39-18
298-102

NASA-Langley, 1992